

---

# Quenching-Induced Changes in the Structural and Electrical Properties of Lead-Free Ferroelectric Ceramics

---

Fachbereich Material- und Geowissenschaften, Technische Universität Darmstadt

Dissertation zur Erlangung des akademischen Grades  
Doktor der Naturwissenschaften (Dr. rer. nat.)

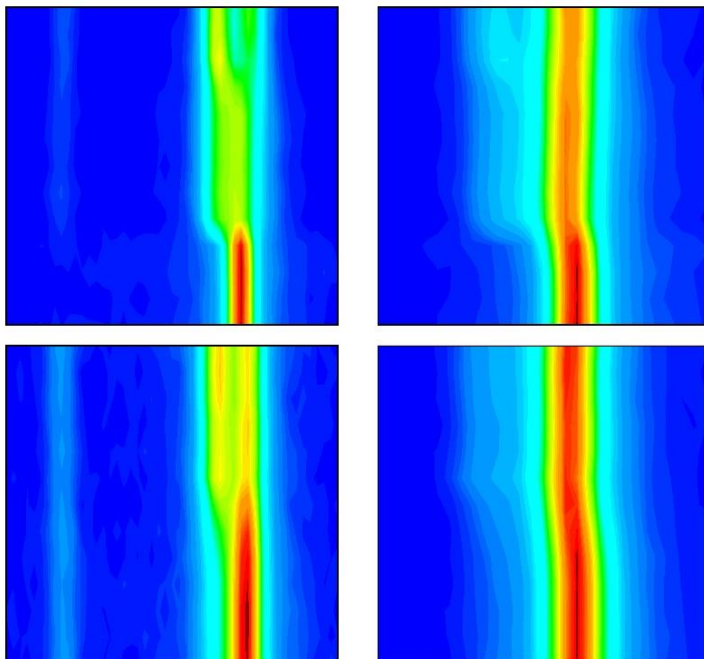
von Andreas Georg Wohninsland

Erstgutachter: Prof. Dr. Jürgen Rödel

Zweitgutachter: Dr. Manuel Hinterstein

Darmstadt, Juni 2023

---



TECHNISCHE  
UNIVERSITÄT  
DARMSTADT

Nichtmetallisch - Anorganische Werkstoffe



---

Dissertation

Quenching-Induced Changes in the Structural and Electrical Properties of Lead-Free Ferroelectric Ceramics

Abschreckungsinduzierte Veränderungen in den Strukturellen und Elektrischen Eigenschaften Bleifreier Ferroelektrischer Keramiken

von Andreas Georg Wohninsland

geboren am 26.08.1993 in Kirchheimbolanden.

Tag der Einreichung: 12. Juni 2023

Tag der Prüfung: 21. Juli 2023

Darmstadt, Technische Universität Darmstadt

Bitte zitieren Sie dieses Dokument als:

urn:nbn:de:tuda-tuprints-243645

<https://tuprints.ulb.tu-darmstadt.de/id/eprint/24364>

Dieses Dokument wird bereit gestellt von tuprints,  
E-Publishing-Service der TU Darmstadt

Die Veröffentlichung steht unter folgender Creative Commons Lizenz:

CC BY-SA 4.0 International

<https://creativecommons.org/licenses/>

---

---

---

## **Declaration of Authorship**

---

### **Thesis Statement pursuant to § 22 paragraph 7 and § 23 paragraph 7 of APB TU Darmstadt**

I hereby formally declare that I, Andreas Georg Wohninsland, have written the submitted thesis independently pursuant to §22 paragraph 7 of APB TU Darmstadt. I did not use any outside support except for the quoted literature and other sources mentioned in the thesis. Furthermore, I state that all passages which have been taken out of publications of all means or unpublished material either whole or in part, in words or ideas, have been marked as quotations in the relevant passage. This thesis has not been handed in or published before in the same or similar form.

In the submitted thesis the written copies and the electronic version for archiving are pursuant to § 23 paragraph 7 APB identical in content.

Darmstadt, June 12<sup>th</sup>, 2023

---

Andreas Georg Wohninsland

---

---

---

## List of Contents

---

Acknowledgements.....	III
Abstract .....	V
Kurzfassung.....	VII
<b>1 Introduction.....</b>	<b>1</b>
<b>2 Theoretical Background and Literature Review .....</b>	<b>3</b>
<b>2.1 Dielectrics .....</b>	<b>3</b>
<b>2.2 Piezo- and Pyroelectrics .....</b>	<b>5</b>
<b>2.3 Ferroelectrics .....</b>	<b>6</b>
<b>2.4 Relaxor Ferroelectrics.....</b>	<b>9</b>
2.4.1 Differences between Relaxor and Ferroelectric Properties.....	10
2.4.2 Theoretical Models of Relaxor Behavior and Polar Nanoregions.....	12
<b>2.5 Lead-free Ferroelectrics .....</b>	<b>14</b>
2.5.1 The $\text{Na}_{1/2}\text{Bi}_{1/2}\text{TiO}_3\text{-BaTiO}_3$ System.....	15
2.5.2 The $\text{BiFeO}_3\text{-BaTiO}_3\text{(-Na}_{1/2}\text{Bi}_{1/2}\text{TiO}_3)$ System .....	20
<b>2.6 Quenching Lead-free Ferroelectrics.....</b>	<b>26</b>
2.6.1 Quenching-induced Changes in $\text{Na}_{1/2}\text{Bi}_{1/2}\text{TiO}_3\text{-BaTiO}_3$ .....	26
2.6.2 Quenching-induced Changes in $\text{BiFeO}_3\text{-BaTiO}_3$ .....	30
<b>3 Aim of the Work.....</b>	<b>34</b>
<b>4 Methodology .....</b>	<b>35</b>
<b>4.1 Powder Processing and Manufacturing of Dense Ceramic Samples.....</b>	<b>35</b>
4.1.1 $\text{Na}_{1/2}\text{Bi}_{1/2}\text{TiO}_3\text{-BaTiO}_3$ Compositions .....	35
4.1.2 $\text{BiFeO}_3\text{-BaTiO}_3\text{(-Na}_{1/2}\text{Bi}_{1/2}\text{TiO}_3)$ Compositions .....	37
<b>4.2 Laboratory X-ray Diffraction .....</b>	<b>38</b>
<b>4.3 Microstructure .....</b>	<b>38</b>
<b>4.4 Density .....</b>	<b>39</b>
<b>4.5 Poling and Piezoelectric Response .....</b>	<b>40</b>
<b>4.6 Dielectric Analysis .....</b>	<b>40</b>
<b>4.7 Ferroelectric Polarization and Strain Analysis.....</b>	<b>41</b>
<b>4.8 Temperature-dependent Young's Modulus and Composite Model .....</b>	<b>41</b>
<b>4.9 Synchrotron X-ray Diffraction.....</b>	<b>45</b>
4.9.1 Deutsches Elektronen-Synchrotron.....	45
4.9.2 Advanced Photon Source .....	46

4.9.3	Processing of Synchrotron X-ray Diffraction Data.....	47
<b>5</b>	<b>Results and Discussion.....</b>	<b>49</b>
5.1	<b>Effect of Quenching on the Structural and Ferroelectric Properties of NBT-BT.....</b>	<b>49</b>
5.1.1	Introduction and Motivation.....	49
5.1.2	Structural Characteristics of Ceramic Powders.....	51
5.1.3	Structural Characteristics of Unpoled and Poled Bulk Ceramics.....	56
5.1.4	Microstructure and Density.....	66
5.1.5	Ferroelectric and Piezoelectric Response.....	68
5.1.6	Short Summary.....	72
5.2	<b>Quenching-induced Changes of Polarized Volume in NBT-BT.....</b>	<b>74</b>
5.2.1	Introduction and Motivation.....	74
5.2.2	Dielectric Analysis.....	75
5.2.3	Temperature-dependent Young's Modulus and PNR Volume Fraction.....	80
5.2.4	Short Summary.....	85
5.3	<b>Electric Field-dependent <i>in situ</i> Diffraction on Quenched NBT-BT.....</b>	<b>86</b>
5.3.1	Introduction and Motivation.....	86
5.3.2	Qualitative Description.....	87
5.3.3	Quantitative Texture and Rietveld Analysis.....	95
5.3.4	Volumetric Strain Calculation for NBT-6BT and NBT-9BT.....	102
5.3.5	Lattice and Domain Switching Strain Calculations for NBT-3BT.....	105
5.3.6	Short Summary.....	109
5.4	<b>Effect of Introducing <math>\text{Na}_{1/2}\text{Bi}_{1/2}\text{TiO}_3</math> and Quenching on <math>\text{BiFeO}_3\text{-BaTiO}_3</math>.....</b>	<b>111</b>
5.4.1	Introduction and Motivation.....	111
5.4.2	Phase Purity, Microstructure and Density.....	112
5.4.3	Structural Analysis of Sintered Ceramics.....	116
5.4.4	Dielectric Analysis.....	120
5.4.5	Ferroelectric Polarization and Strain Analysis and Piezoelectric Properties.....	123
5.4.6	Short Summary.....	127
<b>6</b>	<b>Summary and Perspective.....</b>	<b>129</b>
<b>7</b>	<b>Supplementary Material.....</b>	<b>132</b>
	<b>List of Tables.....</b>	<b>141</b>
	<b>List of Figures.....</b>	<b>142</b>
	<b>List of Abbreviations and Symbols.....</b>	<b>149</b>
	<b>Literature.....</b>	<b>153</b>

---

---

## Acknowledgements

---

During the past four years, many individuals have made direct and indirect contributions to this work and the resulting thesis.

Firstly, I would like to express my gratitude to Prof. Jürgen Rödel for providing me with the opportunity to pursue my PhD in his research group. I am thankful for his guidance throughout the various stages of the project and for his effective management in creating and maintaining a productive atmosphere at NAW. I truly valued our insightful discussions and his openness to new scientific ideas.

I would also like to extend my sincere appreciation to Dr. Lalitha Kodumudi Venkataraman, my direct supervisor from the beginning of my PhD journey, who taught me as much as no one else during this time. Your support has been invaluable, and without it, this research would not have been possible. Thank you immensely, Lalitha!

Additionally, I would like to express my deep gratitude to Prof. Hans-Joachim Kleebe for his helpful discussions and support, particularly regarding microstructure-related inquiries. I would also like to mention Dr. Ann-Katrin Fetzner, who has been a fantastic colleague within the project and has contributed significantly through her exceptional TEM work. Thank you, Ann-Katrin!

My thanks also go to the committee members, Prof. Gerd Buntkowsky and Prof. Wolfgang Donner, for their time and interest in this work.

I extend my gratitude to Dr. Manuel Hinterstein for serving as the second reviewer of this work, for our joint beam time at DESY, and the resulting collaboration.

Special thanks also go to all the external collaborators: Dr. David Hall, Dr. Yizhe Li, Bing Wang, and Ziqi Yang, who warmly welcomed and supported me during my research stay in Manchester. Furthermore, I would like to express my gratitude to Rachel Broughton and Prof. Jacob Jones for their assistance in measuring and discussing synchrotron XRD data, as well as to Dr. Erling Ringgaard and Dr. Kathrin Hofmann.

In addition, I want to thank the entire NAW group for their support in work-related matters and for the enjoyable coffee breaks, barbeques, hiking trips, and the time spent in La Clusaz. Special thanks to Gila, Patrick, Daniel I., and Siegfried for keeping everything running smoothly. I would like to express my appreciation to my (former) PhD colleagues: Lukas, Marion, Mihail, Qaisar, Maohua, An-Phuc, Max, Kuan, Maryam, Michi, Hamed, Mehrzad, Laura, Sophie, Sabrina, Oliver, Carl

---

Philipp, Alexander, Dalu, and an honorable mention to Daniel B. with whom I shared the different stages of the PhD project and had numerous, incredibly valuable discussions. Furthermore, I extend my thanks to Jurij, Till, Xufei, Lovro, Changhao, my office mate Fangping, Shuang, Ahmad, Wolfgang, and the guests who visited NAW during my time there: Quimei, Lei, Mupeng, Dragan, and Alp. I would also like to express my appreciation to my ARL student, Julius Körner. To all of you, thank you very much. It was a truly memorable time!

Thanks to Daniel and Richard, the hosts of GAG. Your podcast made endless hours of lab work and driving much more enjoyable. You helped keep me going!

Furthermore, I extend sincere gratitude to my parents, Monika and Georg, my sisters, Constanze and Irina, Markus, Reinhard, and my niece Alma. Thank you very much for your unwavering support and understanding. Of course, I also want to express my appreciation to my 'extended' family Rebekka, Sabine, Juliane, Steffi, and Christoph.

I would like to thank my friends connected to Heidelberg: Susi, Simon, Eli, Matti, Chris, Urs, Patrycja, Mario, Tobi, and Nils Felix. Also, a big thanks to the Laumersheim group: Jasmin, Yann, Axel, Max H., Michi, Tobias, and Chrissi. And of course, thanks to Max B. I am grateful to all of you for reminding me to engage in non-PhD-related activities from time to time.

Finally, and most importantly, I want to express my heartfelt gratitude to Karoline for her constant encouragement, support, and patience – for everything. Wherever you are, that's where my home is.

Andreas Wohninsland

Darmstadt, June 12<sup>th</sup>, 2023

---

## Abstract

---

Ferroelectrics are an important class of functional materials utilized in various electronic devices, often in the form of polycrystalline ceramics. The most commonly used ferroelectric ceramics are lead-containing  $\text{Pb}(\text{Zr},\text{Ti})\text{O}_3$ -based materials. However, due to the toxicity of lead and the resulting environmental concerns, the EU legislation on the Restriction of Hazardous Substances has emphasized the need to identify lead-free alternatives.  $\text{Na}_{1/2}\text{Bi}_{1/2}\text{TiO}_3$ - $\text{BaTiO}_3$  (NBT-BT) and  $\text{BiFeO}_3$ - $\text{BaTiO}_3$  (BF-BT) solid solutions are among the promising lead-free candidates for high power and high temperature applications, respectively. Both compositions exhibit certain drawbacks, with NBT-BT having a low temperature stability and BF-BT rather low piezoelectric coefficient ( $d_{33}$ ) and resistivity. These disadvantages can be mitigated to some extent by quenching the material from high temperatures.

The present study aims to investigate the quenching-induced changes in the structural and electrical characteristics of lead-free Bi-based ceramics to advance the understanding of the underlying mechanisms. The investigated materials are NBT-BT with 3, 6, 9 and 12 mol% BT, and BF-BT with 30 and 33 mol% BT with and without the addition of 5 mol% NBT.

High-resolution X-ray powder diffraction and synchrotron diffraction experiments on bulk samples confirmed that quenching increases the lattice distortion in NBT-BT. This effect is particularly pronounced for 6 mol% BT, located at the morphotropic phase boundary (MPB). For this composition, which is a non-ergodic relaxor at room temperature, quenching alters the phase fractions, leading to a notable decrease in the volume of the cubic phase. In the poled state, the lattice distortion for the quenched samples is more pronounced in comparison to the furnace cooled counterparts, presumably being the reason for the increased depolarization temperature,  $T_d$ . *In situ* electric field-dependent synchrotron diffraction revealed a shift in the onset of electric field-induced structural changes to higher electric field amplitudes. Further, quenched NBT-BT exhibits strongly reduced volumetric strain compared to the furnace cooled sample. This can be attributed to the stabilized ferroelectric domain state, which limits the possibility for quenching-induced phase transformation. The increase in lattice distortion and spontaneous strain in NBT-BT upon quenching is also reflected in increased polarization, coercive field and total strain as established from ferroelectric hysteresis measurements. However, quenching decreases the  $d_{33}$  in all the investigated NBT-BT compositions. Dielectric characterization revealed an increase in the ferroelectric to relaxor transition temperature, and thus,  $T_d$ . To elucidate the influence of



---

quenching on the nanoscale structure of NBT-BT at elevated temperatures, temperature-dependent Young's modulus and a composite model were used to calculate the volume fraction of polar nanoregions (PNRs). Above the temperature of maximum permittivity, quenching causes an increase in PNR volume fraction at and close to the MPB, likely due to the enhanced non-cubic distortions, which is consistent with the change in phase composition at room temperature.

The addition of 5 mol% NBT into BF-BT with 30 and 33 mol% BT promotes a more cubic structure with a smaller rhombohedral distortion and lower rhombohedral phase fraction. Furthermore, the ternary composition exhibits significantly reduced dielectric losses. BF-BT-NBT demonstrates characteristics of a partially ergodic relaxor material in its ferroelectric response, displaying low remanent polarization and strain, which can be correlated to a decrease in  $d_{33}$  values. Quenching BF-BT-NBT leads to vanishing of the ergodicity and enhanced negative strain and remanent polarization. The  $d_{33}$  value is increased by up to 107 %, and the rhombohedral lattice distortion is enhanced upon quenching.

In both investigated material systems, quenching induces changes in structural and electrical characteristics, yielding beneficial effects on application-relevant properties. The enhanced lattice distortion in quenched NBT-BT results in an increased  $T_d$ , improving the temperature-range for applications. Moreover, the Young's modulus is only marginally lower compared to the furnace cooled material, indicating insignificant deterioration of the mechanical properties. In quenched BF-BT-NBT, the  $d_{33}$  value is greatly improved, and the increase in resistivity upon introducing NBT into BF-BT is maintained. These findings emphasize that quenching Bi-based piezoceramics can help bringing these lead-free materials into application.

---

## Kurzfassung

---

Ferroelektrika sind eine wichtige Klasse funktionaler Materialien, die in verschiedenen elektronischen Geräten verwendet werden, oft in Form von polykristallinen Keramiken. Die am häufigsten verwendeten ferroelektrischen Keramiken sind bleihaltige  $\text{Pb}(\text{Zr,Ti})\text{O}_3$ -basierte Materialien. Aufgrund der Giftigkeit von Blei und den daraus resultierenden Umweltbedenken hat die EU-Gesetzgebung zur Beschränkung gefährlicher Stoffe die Notwendigkeit betont, bleifreie Alternativen zu finden. Die Festkörperlösungen  $\text{Na}_{1/2}\text{Bi}_{1/2}\text{TiO}_3$ - $\text{BaTiO}_3$  (NBT-BT) und  $\text{BiFeO}_3$ - $\text{BaTiO}_3$  (BF-BT) gehören zu den vielversprechendsten bleifreien Kandidaten für Hochleistungs- und Hochtemperaturanwendungen. Beide Zusammensetzungen weisen bestimmte Nachteile auf; dies ist bei NBT-BT eine geringe Temperaturstabilität und bei BF-BT ein eher niedriger piezoelektrischer Koeffizient ( $d_{33}$ ) und ein geringer spezifischer Widerstand. Diese Nachteile können in gewissem Maße durch das Abschrecken des Materials von hohen Temperaturen verringert werden.

Die vorliegende Studie zielt darauf ab, die durch das Abschrecken verursachten Veränderungen in den strukturellen und elektrischen Eigenschaften von bleifreien Bi-basierten Keramiken zu untersuchen, um das Verständnis der zugrunde liegenden Mechanismen zu verbessern. Die untersuchten Materialien sind NBT-BT mit 3, 6, 9 und 12 mol% BT sowie BF-BT mit 30 und 33 mol% BT mit und ohne Zugabe von 5 mol% NBT.

Hochauflösende Röntgenpulverdiffraktometrie und Synchrotronbeugungsexperimente an nicht-zerkleinerten Keramikproben haben bestätigt, dass das Abschrecken die Gitterverzerrung in NBT-BT erhöht. Dieser Effekt ist besonders ausgeprägt für 6 Mol% BT, das sich an der morphotropen Phasengrenze (MPB) befindet. Bei dieser Zusammensetzung, die bei Raumtemperatur ein nicht-ergodischer Relaxor ist, verändert das Abschrecken die Phasenanteile, was zu einer deutlichen Verringerung des Volumenanteils der kubischen Phase führt. Im polarisierten Zustand ist die Gitterverzerrung für die abgeschreckten Proben im Vergleich zu den im Ofen abgekühlten Referenzproben stärker ausgeprägt, was vermutlich der Grund für die erhöhte Depolarisationstemperatur ( $T_d$ ) ist. *In-situ*-Beugungsexperimente mit elektrischem Feld haben eine Verschiebung des Beginns der durch elektrisches Feld induzierten strukturellen Veränderungen zu höheren elektrischen Feldamplituden gezeigt. Darüber hinaus weist abgeschrecktes NBT-BT im Vergleich zu im Ofen abgekühlten Proben eine deutlich reduzierte Änderung der Phasenanteile auf. Dies kann auf den stabilisierten ferroelektrischen Domänenzustand zurückgeführt werden, der die Möglichkeit einer abschreckungsinduzierten

---

Phasentransformation begrenzt. Die Zunahme der Gitterverzerrung und der spontanen Dehnung in NBT-BT durch das Abschrecken spiegelt sich auch in einer erhöhten Polarisierung, Koerzitivfeldstärke und Gesamtdehnung wider, wie sie aus ferroelektrischen Hysterese-Messungen festgestellt wurden. Allerdings verringert das Abschrecken den  $d_{33}$ -Wert bei allen untersuchten NBT-BT-Zusammensetzungen. Dielektrische Charakterisierung ergab eine Erhöhung der Übergangstemperatur von Ferroelektrikum zu Relaxor und damit von  $T_d$ . Um den Einfluss des Abschreckens auf die nanoskalige Struktur von NBT-BT bei erhöhten Temperaturen zu untersuchen, wurden der temperaturabhängige Elastizitätsmodul und ein Verbundmodell verwendet, um den Volumenanteil polarer Nanoregionen (PNRs) zu berechnen. Über der Temperatur mit maximaler Permittivität führt das Abschrecken zu einem Anstieg des Volumenanteils der PNRs an der MPB und in ihrer Nähe, wahrscheinlich aufgrund der verstärkten nicht-kubischen Verzerrungen, was mit der Veränderung der Phasenzusammensetzung bei Raumtemperatur korreliert.

Die Zugabe von 5 Mol% NBT zu BF-BT mit 30 und 33 Mol% BT fördert eine stärker kubische Struktur mit geringerer rhomboedrischer Verzerrung und geringerem Anteil an rhomboedrischer Phase. Zusätzlich weist die ternäre Zusammensetzung deutlich reduzierte dielektrische Verluste auf. BF-BT-NBT zeigt Merkmale eines teilweise ergodischen Relaxormaterials in seinen ferroelektrischen Eigenschaften, mit geringer Remanenzpolarisation und Dehnung, was wiederum mit verringerten  $d_{33}$ -Werten korreliert. Durch das Abschrecken von BF-BT-NBT verschwindet die Ergodizität und es kommt zu einer verstärkten negativen Dehnung und Remanenzpolarisation. Der  $d_{33}$ -Wert steigt um bis zu 107 % und die rhomboedrische Gitterverzerrung wird durch das Abschrecken vergrößert.

In beiden untersuchten Materialsystemen führt das Abschrecken zu Veränderungen der strukturellen und elektrischen Charakteristika, die sich positiv auf anwendungsrelevante Eigenschaften auswirken. Die erhöhte Gitterverzerrung in abgeschrecktem NBT-BT führt zu einer erhöhten Depolarisationstemperatur, was den Temperaturbereich für Anwendungen verbessert. Darüber hinaus ist der Elastizitätsmodul nur geringfügig niedriger im Vergleich zum im Ofen abgekühlten Material, was auf eine vernachlässigbare Verschlechterung der mechanischen Eigenschaften hinweist. In abgeschrecktem BF-BT-NBT wird der  $d_{33}$ -Wert erheblich verbessert, und der Anstieg des spezifischen Widerstands beim Hinzufügen von NBT in BF-BT bleibt erhalten. Diese Erkenntnisse betonen, dass das Abschrecken von Bi-basierten Piezokeramiken dazu beitragen kann, diese bleifreien Materialien zur Anwendung zu bringen.

---

# 1 Introduction

---

Ferroelectric materials represent a subgroup of piezoelectrics within the category of dielectrics and are characterized by a spontaneous and switchable polarization [1]. The phenomenon of ferroelectricity was first described in 1921 for Rochelle salt and discovered in the 1940s in BaTiO<sub>3</sub> (BT), which can be considered as the prototype ferroelectric and exhibits a perovskite structure [2]. Today, lead zirconate titanate, which shares the characteristic of a perovskite structure with BT, is the most frequently utilized piezoelectric material in application, often in the form of polycrystalline bulk ceramics or thin films [3]. Typical applications include piezoelectric sensors and transducers, capacitors, energy harvesting, or memory devices.

However, due to growing environmental concerns about the toxicity of lead and the resulting EU legislation on the Restriction of Hazardous Substances (RoHS) in 2002, the scientific community has shifted its focus towards lead-free alternatives for ferroelectric materials [4]. Until now, no single material system can replace lead-based ferroelectrics in all varieties of usages, but different systems have been identified as promising candidates for certain applications. These are barium titanate-, alkaline bismuth titanate-, alkaline niobate- and bismuth ferrite-based materials [5]. Bismuth ferrite (BF) and its solid solutions exhibit extensive temperature stability and are therefore suitable for high-temperature environments [6], while sodium bismuth titanate (NBT)-based ferroelectrics are mainly utilized for high-power applications [7]. Nevertheless, both of these systems present difficulties in handling, such as high conductivity and the formation of secondary phases in the case of BF [6] and a high coercive field for NBT [8]. Introducing BT into the material is beneficial for both BF and NBT to partly mitigate the mentioned complications.

The solid solution Na<sub>1/2</sub>Bi<sub>1/2</sub>TiO<sub>3</sub>-BaTiO<sub>3</sub> (NBT-BT) exhibits non-ergodic relaxor properties depending on the composition. Relaxors are a special type of ferroelectrics with a disordered structure characterized by polar nanoregions (PNRs) instead of micrometer-sized ferroelectric domains. In the case of a non-ergodic relaxor, the domain structure can be irreversibly transformed into a normal ferroelectric by the application of an electric field [9]. NBT-BT has a morphotropic phase boundary (MPB) at 6-7 mol% BT, at which the electrical properties are most suited for high power applications such as transducers or ultrasonic devices. A severe drawback of NBT-BT is its rather low depolarization temperature,  $T_d$ , of about 100 °C. Different approaches have been made to increase  $T_d$ . These are chemical modification [10], forming composites [11] and rapidly cooling the material from high temperatures, also known as quenching [12]. Besides increasing  $T_d$ , quenching NBT-BT enhances the lattice distortion from the ideal cubic perovskite

---

structure and stabilizes the ferroelectric state, leading to less pronounced relaxor characteristics [13]. However, a complete understanding of how quenching affects phase assemblage and field-dependent structural and electrical properties for different regions of the phase diagram has not been established yet.

In the case of  $\text{BiFeO}_3\text{-BaTiO}_3$  (BF-BT), rapid cooling from high temperatures has been found to increase its resistivity and piezoelectric properties, as well as induce structural changes similar to those observed in NBT-BT, further underlining the usefulness of quenching [14]. The quenching method is frequently used on the well investigated pure or e.g. Mn-doped BF-BT. However, many ternary compositions based on BF-BT exhibit improved properties, particularly in terms of conductivity and piezoelectricity. One such ternary system is BF-BT-NBT [15]. Given the beneficial impact of quenching on the properties of both BF-BT and NBT-BT, it is plausible that quenching has a similar effect on BF-BT-NBT and could serve as a useful method to further improve the material characteristics.

The main objective of this study is to deepen the understanding of quenching-induced changes in lead-free Bi-based ferroelectric ceramics, with a specific focus on their electrical properties and structural characteristics such as lattice parameters and phase composition. To achieve this, multiple laboratory and synchrotron diffraction experiments were conducted on four different compositions of quenched and furnace cooled (as-sintered) NBT-BT. These experimental results were then correlated with the dielectric, piezoelectric, and ferroelectric characteristics of the material. Additionally, the temperature-dependent Young's modulus was utilized in conjunction with a composite model to assess the influence of quenching NBT-BT on the PNR volume fraction at elevated temperatures, providing further insight into the nanoscale structural changes.

The second part of the study focuses on BF-BT, investigating the changes in electrical and structural properties upon the formation of a ternary composition with NBT, and subsequent quenching. By correlating the findings from different experiments conducted on the two material systems and considering recent literature, this study aims to provide a more comprehensive understanding of how quenching affects lead-free Bi-based ferroelectrics. The ultimate goal is to facilitate the application of these materials by elucidating the role of quenching in improving their properties.

---

## 2 Theoretical Background and Literature Review

---

In the following chapters, the theoretical background necessary to describe and understand the presented study is provided. Physical fundamentals of dielectric materials and their subgroups are presented, followed by a thorough description and literature review of the investigated material systems. Furthermore, the concept and known effects of quenching on lead-free piezoelectric materials are outlined.

---

### 2.1 Dielectrics

---

The following descriptions in chapters 2.1-2.3 are based on the textbooks by Moulson & Herbert [16], Lines & Glass [1], Uchino [17] and Newnham [18] and on the review article by Damjanovic [19].

A dielectric material is defined as an insulator that can be polarized by the application of an electric field. Applying an electric field causes the charge carriers within the material to shift, leading to a macroscopic polarization,  $P_i$ , which is the sum of all dipole moments.  $P_i$  of a linear dielectric is proportional to the external electric field,  $E_j$ , and coupled by the susceptibility,  $\chi_{ij}$ , given in equation (1):

$$P_i = \varepsilon_0 \cdot \chi_{ij} \cdot E_j \quad (1)$$

where  $\varepsilon_0$  is the permittivity of free space ( $8.8542 \cdot 10^{-12}$  F/m). The dielectric displacement,  $D_i$ , is the sum of the macroscopic polarization and the electric field strength multiplied with the permittivity of free space, as shown in equation (2):

$$D_i = \varepsilon_0 \cdot E_i + P_i \quad (2)$$

The relative permittivity or dielectric constant  $\varepsilon_r$  describes a material's capacity to store electric energy and can be written as:

$$\varepsilon_r = \frac{\varepsilon'}{\varepsilon_0} \quad (3)$$

The dielectric permittivity is defined as a complex quantity to account for a phase shift between the applied alternating electric field and the response of the dielectric, as described in equation (4):

$$\epsilon_r = \epsilon' + \epsilon'' \quad (4)$$

with  $\epsilon'$  and  $\epsilon''$  being the real and imaginary part of the permittivity, respectively.

Different mechanisms contribute to the macroscopic polarization of a dielectric under an applied electric field. These are electronic, ionic, orientation or dipole and space charge polarization (Figure 1). In the case of a ferroelectric material, this list can be extended by domain wall polarization as a specific case of space charge polarization. All dielectrics can exhibit electronic polarization, which means that the negatively charged electrons are displaced with respect to the positively charged core. Ionic polarization can be observed in ionic crystals, in which the charged sublattices are displaced. In the case of a dipole material, said dipoles are oriented with respect to the direction of the applied electric field. Dielectrics with an inhomogeneous distribution of charge carriers show space charge polarization. Charge carriers migrate through the material and accumulate at a potential barrier e.g. a grain boundary. The contribution of the listed mechanisms to the polarization of a dielectric depends on the frequency of the applied alternating electric field. There are upper frequency limits for electrons, ions and dipoles to be able to follow an alternating electric field, which are  $10^{12}$ - $10^{15}$  Hz,  $10^9$ - $10^{12}$  Hz and  $10^6$ - $10^9$  Hz, respectively [17].

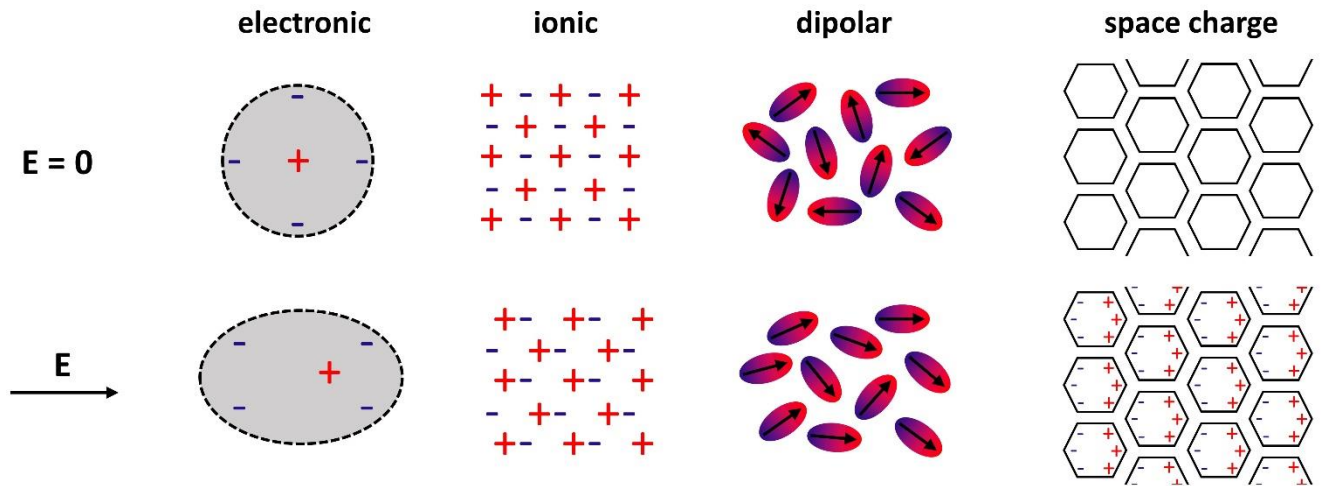


Figure 1: Different polarization processes in dielectric materials under applied electric field: electronic, ionic, dipolar and space charge polarization (redrawn after [16]).

In the following sections, the subcategories of dielectric materials, including piezo-, pyro-, and ferroelectrics (Figure 2), and their unique properties will be discussed.

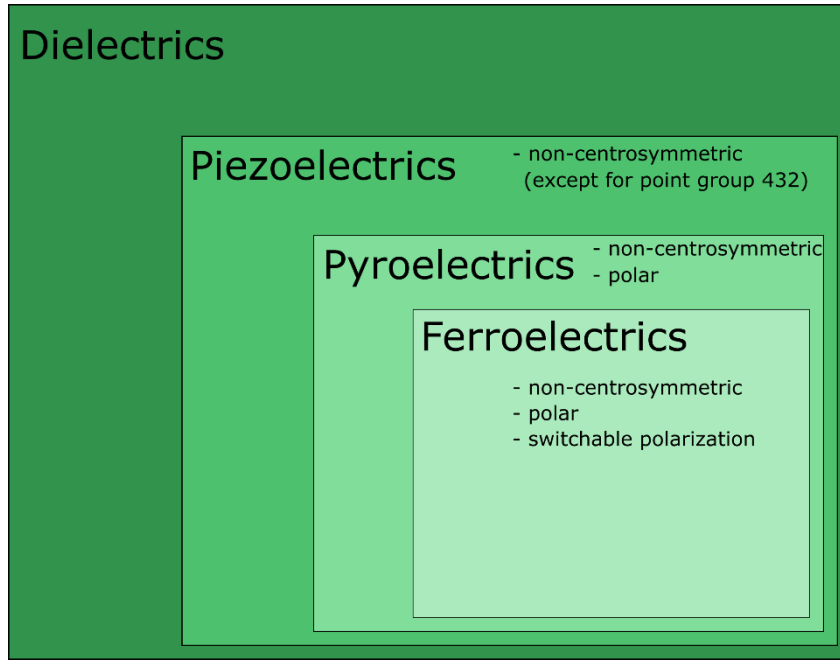


Figure 2: Classification of dielectrics and their subgroups with respective relevant properties.

## 2.2 Piezo- and Pyroelectrics

Piezoelectric materials are a subgroup of dielectric materials while pyroelectric materials are a subgroup of piezoelectric materials (Figure 2). Piezoelectrics can be polarized by the application of mechanical stress or by the application of an electric field. The direct piezoelectric effect refers to the accumulation of charges on a material's surface when a mechanical stress is applied. The linear relationship between applied stress,  $\sigma_{jk}$ , and resulting charge density,  $D_i$ , is coupled by the piezoelectric coefficient,  $d_{ijk}$  (C/N), which is a third-rank tensor:

$$D_i = d_{ijk} \cdot \sigma_{jk} \quad (5)$$

Piezoelectric materials also exhibit the converse piezoelectric effect, which means applying an electric field causes the material to expand or contract. The linear relationship between applied electric field,  $E_k$ , and strain,  $x_{ij}$ , is coupled by the converse piezoelectric coefficient, with the index  $t$  denoting the transposed matrix:

$$x_{ij} = d_{kij} \cdot E_k = d_{ijk}^t \cdot E_k \quad (6)$$

The piezoelectric coefficients of the direct and converse effects are thermodynamically equivalent. Units of the direct and converse piezoelectric coefficients are C/N and m/V, respectively.



In order to show a piezoelectric response, a material has to be non-centrosymmetric. A centrosymmetric point group contains a center of inversion as one of its symmetry elements. Out of the 32 crystallographic point groups, 21 are non-centrosymmetric and 20 of them exhibit piezoelectricity, while the point group 432 is the only exception. The piezoelectric groups can be subdivided into 10 non-polar and 10 polar or pyroelectric point groups with a unique polar axis.

Pyroelectric materials are characterized by a permanent temperature-dependent dipole without being exposed to an external electric field or stress. Temperature changes cause the lattice of the material to expand or contract, which induces a change in the spontaneous polarization  $\Delta P_i$ . A linear relationship exists between  $\Delta T$  and  $\Delta P_i$  coupled by the pyroelectric constant  $p_i$ :

$$\Delta P_i = p_i \cdot \Delta T \quad (7)$$

Similar to the piezoelectric effect, a converse effect exists for pyroelectricity which is the electrocaloric effect. This means an electric or stress field applied to a pyroelectric material causes a change in temperature.

---

## 2.3 Ferroelectrics

---

Ferroelectric materials are pyroelectrics characterized by a spontaneous polarization that can be switched by the application of an electric field. Therefore, the material must have at least two energetically equivalent orientations of polarization.

The structures of the ferroelectric materials studied in this thesis are distorted cubic unit cells with the generic perovskite structure  $ABX_3$ . Barium titanate ( $BaTiO_3$ , BT) can be considered as a prototype ferroelectric material and will be used as an example to describe ferroelectric characteristics in the following.

The unit cell of BT is built up by  $Ba^{2+}$ -ions on the A-site, located at the corners, a  $Ti^{4+}$ -ion in the center, meaning on the B-site, and  $O^{2-}$ -ions located on the center of the six faces of the unit cell (Figure 3). The oxygen ions are located at the corners of an octahedron with the  $Ti^{4+}$ -ion being placed in its center. At temperatures above the Curie Temperature,  $T_C$ , BT is in the cubic state and therefore paraelectric. In the paraelectric state, the dielectric permittivity follows the Curie-Weiss law [19]:

$$\varepsilon = \varepsilon_0 + \frac{C}{T - T_0} \approx \frac{C}{T - T_0} \quad (8)$$

where  $C$  is the Curie Constant and  $T_0$  is the Curie-Weiss temperature.

Cooling the material below  $130\text{ }^\circ\text{C}$ , which is the  $T_C$  of BT, is associated with a first order phase transition to a ferroelectric tetragonal (T) state [16]. The tetragonal distortion arises from a displacement of the B-site cation from the center position and is accompanied with a jump of the spontaneous polarization from zero to a finite value. Further cooling results in phase transitions to orthorhombic at  $0\text{ }^\circ\text{C}$  and to rhombohedral (R) at  $-90\text{ }^\circ\text{C}$  (Figure 3).

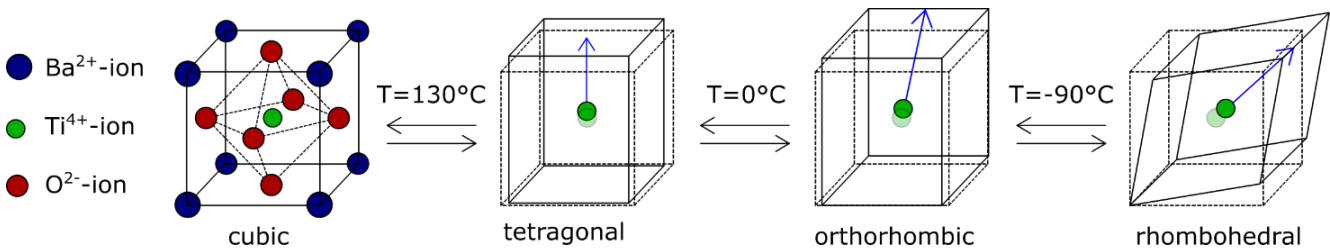


Figure 3: Temperature-dependent distortions of a perovskite-structured BaTiO<sub>3</sub> unit cell. All ions of the unit cell are displayed for the cubic state, while for the lower symmetries only the displacement of the Ti<sup>4+</sup>-ion and one possible polarization vector are given. Distortions are exaggerated for better visibility (modified after [16]).

In order to compensate for the depolarization field induced by the spontaneous polarization in a ferroelectric, the polarization vectors do not align into the same direction. Certain volumes within the material bulk with equal polarization directions are called domains and different domains exhibit different polarization vectors. Domain walls separate neighboring domains with differing polarization directions.

Since all ferroelectrics exhibit at least two equivalent orientations of polarization, the polarization vector of unit cells, and thus the ferroelectric domains, can be reoriented by external stimuli such as an electric field or mechanical stress. Figure 4 displays the hysteretic macroscopic polarization and strain response of an idealized ferroelectric crystal alongside the associated domain configuration – both as a function of a bipolar electric field. In the initial virgin state at point A, polarization vectors are randomly oriented leading to zero net polarization. Upon application of an electric field, macroscopic polarization and strain set in (point B). This is accompanied with unit cell reorientation and the resulting growth of ferroelectric domains which have the polarization vector aligned parallel to the electric field. This growth occurs at the expense of the volume of domains with a less favorable orientation. It is associated with domain wall motion, and labeled as the extrinsic contribution to the field-induced strain. At a certain field amplitude, a monodomain state is introduced in an ideal single crystal while a polycrystalline material would

---

reach a saturated domain configuration but not a single-domain state. Further increase of the applied electric field will result in a linear response in polarization due to further lattice extension without additional domain reorientation (point C to D). This is referred to as the linear, lattice or intrinsic contribution to polarization and strain. Upon decrease of the electric field to zero, domains partially reorient and the polarization and strain drop to  $P_{\text{rem}}$  and  $S_{\text{rem}}$ , respectively, however, not to the initial zero field state (point E). Applying an electric field in the opposite direction (negative electric field) results in further decrease in polarization and strain. At the electric field amplitude of the negative coercive field,  $-E_c$ , polarization drops to zero and the domain configuration resembles the initial virgin state. The strain response exhibits a minimum at  $-E_c$ , but does not necessarily drop to zero. Increasing the electric field amplitude in the opposite direction leads to a symmetrical response in polarization and strain when moving from point F to J, similar to the development from point B to E (Figure 4). At point J, the material exhibits a negative remanent polarization,  $-P_{\text{rem}}$  and positive remanent strain closing both the hysteretic polarization and strain curves.

In order to exploit the large piezoelectric response of polycrystalline ferroelectric materials for the application in electrical devices, a remanent net polarization needs to be introduced. After fabrication, the net polarization, and therefore net piezoelectric response, of polycrystalline ferroelectrics is zero. Hence, the material is subjected to a DC (direct current) poling process, similar to the stages of applying an electric field from point A to E in Figure 4. Depending on the material, the time, field amplitude and temperature of the poling routine are chosen for optimal results.

The electric field-induced changes in lattice parameters and domain orientation during poling and possible subsequent cycling process directly reflect in the diffraction pattern of a ferroelectric material. Therefore, X-ray diffraction (XRD) is considered a viable method to detect structural changes after the poling process (*ex situ*) or as a function of electric field (*in situ*) and will be discussed in upcoming chapters.

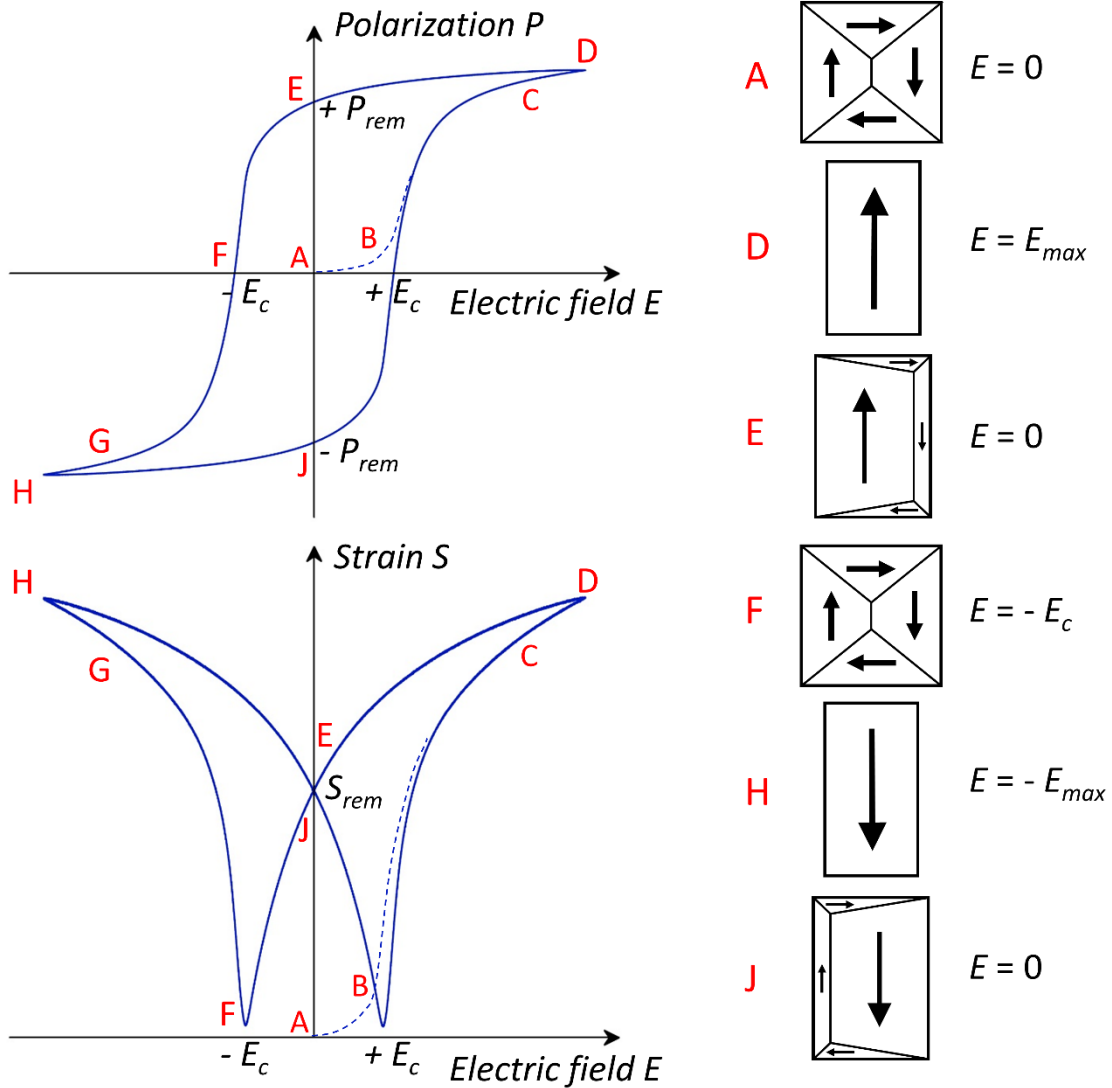


Figure 4: Schematic of the hysteretic ferroelectric behavior of polarization and strain as a function of bipolar electric field. Different idealized stages of the electric field-dependent domain configuration for a tetragonal ferroelectric material are given with the black arrows indicating the direction of the polarization vector for the respective domains (modified after [20]).

## 2.4 Relaxor Ferroelectrics

Relaxor ferroelectrics or relaxors are a subgroup of ferroelectrics. They were firstly described by Smolenskii and Isupov in 1954 [21]. The name relaxor relates to the relaxation processes in the dielectric response, which are responsible for giving the materials their unique properties and differentiate relaxors from normal ferroelectrics [22]. Well-known lead-based relaxor ferroelectrics are  $\text{Pb}(\text{Mg}_{1/3}\text{Nb}_{2/3})\text{O}_3$  (PMN) and  $\text{Pb}_{1-x}\text{La}_x(\text{Zr}_{1-y}\text{Ti}_y)_{1-x/4}\text{O}_3$  (PLZT) [23, 24]. Relaxors are interesting from an application point of view due to their large strain response and high

---

dielectric constants. Information given in this chapter originates from the review articles by Cross [25], Samara [26], Shvartsman & Lupascu [27] and Bokov & Ye [23] and the text book by Tilley [28], unless otherwise specified.

---

### 2.4.1 Differences between Relaxor and Ferroelectric Properties

---

Relaxor ferroelectrics with a perovskite structure have either at least two differently charged cations occupying the same site in the lattice, resulting in a long-range disorder to maintain charge neutrality, or equally-charged cations with different sizes at the same lattice site, also hindering long-range order. These chemical heterogeneities cause some characteristic features in relaxors, with the dielectric behavior being one of the most prominent.

Starting at high temperatures, both ferroelectric and relaxors are in a paraelectric, cubic state. Upon further cooling, the properties of the two material groups differ. The temperature-dependent real part of the permittivity ( $\epsilon'(T)$ ) of relaxors deviates from the Curie-Weiss law at the so-called Burns Temperature,  $T_B$ . This is connected to a frequency dispersion in permittivity for relaxor materials in contrast to ferroelectrics (Figure 5a and d). Ferroelectrics exhibit a frequency-independent maximum in the permittivity response at  $T_c$ . In contrast, relaxors have a broadened maximum with the temperature at which  $\epsilon'$  exhibits a maximum,  $T_m$ , being a function of measurement frequency (Figure 5d). The absence of a sharp phase transition as a function of temperature in relaxors is connected to the presence of short-range polar regions or polar nanoregions (PNRs). These regions persist above  $T_m$  up to  $T_B$ , where the frequency dispersion in permittivity vanishes. Depending on the temperature and material, PNRs can either be in a dynamic or static state. Below a certain temperature, either the PNRs dynamics freeze, meaning they remain in a static state or the material transforms in a ferroelectric and develops a ferroelectric domain state. These characteristics describe the differences between canonical and non-canonical relaxors, respectively.

The temperature-dependent polarization response is also affected by the absence of a sharp phase transition in relaxors. In ferroelectrics, the spontaneous polarization develops or vanishes when the material is cooled below or heated above  $T_c$ , respectively (Figure 5b). In relaxors, the polarization decreases continuously with increasing temperature but persists also above  $T_m$  due to the presence of PNRs (Figure 5e). While ferroelectrics typically exhibit a saturated, open polarization loop in response to an applied bipolar electric field, a subgroup of relaxors, so-called

ergodic relaxors show a slim polarization loop instead (Figure 5c and f). The applied electric field induces a long-range ferroelectric domain order, but in ergodic relaxors, this field-induced state is reversible and the initial relaxor state is reestablished once the electric field is removed. Contrastingly, in non-ergodic relaxors, the field-induced ferroelectric state does not transform back spontaneously upon field removal, but the material stays in a remanent ferroelectric state until being heated above the ferroelectric to relaxor transition temperature,  $T_{F-R}$ . The same holds true for mechanical stress as the external stimulus instead of an electric field. The dashed green lines in Figure 5d give the temperature-dependent permittivity response of a poled non-ergodic relaxor material. Below  $T_{F-R}$ , the material exhibits weak frequency dispersion comparable to ferroelectrics. Above  $T_{F-R}$ , the typical relaxor behavior is reestablished, resulting in the same permittivity response of the initially poled and initially unpoled material and, therefore, in an overlap of the dashed and the solid green lines above  $T_{F-R}$  in Figure 5d.

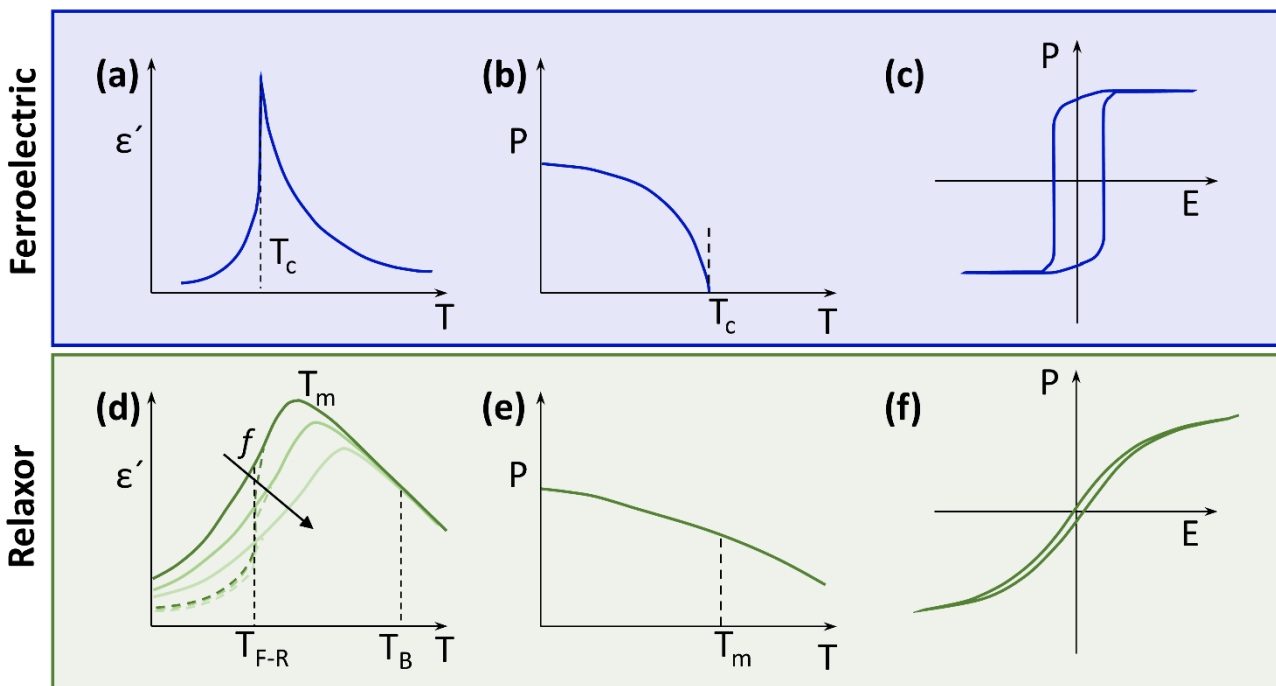


Figure 5: Schematic drawing outlining the differences in electric field- and temperature-dependent polarization and temperature-dependent permittivity in normal ferroelectrics (a-c) and relaxors (d-e). Dashed green lines in (d) indicate the dielectric behavior of a poled non-ergodic relaxor (redrawn and modified after [26]).

---

## 2.4.2 Theoretical Models of Relaxor Behavior and Polar Nanoregions

---

During the decades of studying relaxor materials, several models explaining the peculiar properties of relaxors have been established, refuted and reworked. A comprehensive overview over the different proposed models is provided in the review article by Ahn et al. [9].

Already in the early years of research in relaxors, Smolenksii and coworkers connected the broad permittivity maximum and frequency dispersion in permittivity to the compositional fluctuations of ions with different valences. These compositional heterogeneities result in ordered polar and disordered non-polar regions within the material, namely PNRs (polar) in a cubic matrix (non-polar). It was proposed that the Curie points of the different regions depend on the respective size and therefore differ from region to region due to the different dimensions, resulting in a broad maximum in permittivity [21, 29, 30]. This description is referred to as the diffuse phase transition model and was mathematically described by Kirillov and Isupov [31], however, parts of it are considered to be outdated.

The B-site disorder being connected to the relaxor properties was proven experimentally by Setter and Cross in 1980 and picked up by Cross to develop the superparaelectric model [22, 32]. The name originates from superparamagnetism and the core idea of the model is when the volume of the polar region becomes small enough, the energy barrier of polarization switching becomes comparable to the thermal energy. This assumption is based on Landau-Ginzburg-Devonshire type analysis and leads to randomization of the polarization direction. In this model, the aspect of the diffuse phase transition model explaining the broad permittivity maximum as a result from a distribution of Curie points is contradicted. Despite being helpful to understand the polarity-based properties of relaxors, the superparaelectric model fails to explain the frequency dispersion in the permittivity response of relaxors.

Based on the assumption of spontaneous polarization switching of nano-scale polar volumes, the dipolar glass model was proposed, which compares the dielectric relaxation phenomena in relaxors to spin glass and states a slowing down and eventual freezing of these phenomena [9, 33]. Cooling from the high-temperature state causes the polar nanoregions to grow in size and interact with each other (Figure 6). It was argued, a Vogel-Fulcher relation holds true to describe this thermally-activated process and can be used to extract the respective relaxation times of the dielectric response. Vogel-Fulcher fitting of the measurement frequency of the temperature-

dependent maximum of the imaginary part of permittivity can be applied to determine the static freezing temperature,  $T_{VF}$ , using equation (9):

$$f = f_0 \exp\left(\frac{E_a}{k_B(T_m'' - T_{VF})}\right) \quad (9)$$

where  $f$  is the measurement frequency,  $f_0$  the cut-off frequency of the distribution of relaxation time,  $E_a$  the activation energy for dipole reorientation,  $k_B$  the Boltzmann constant and  $T_m''$  the temperature of the maximum of the imaginary part of permittivity [33]. Studies on heat capacity were used to prove glass-like behavior in non-ergodic relaxor PMN single crystals, supporting the dipolar glass model [34]. The dipolar glass model allows to explain the dynamic and freezing processes of PNRs, but does not provide an explanation for why some materials exhibit ferroelectric and others relaxor behavior upon cooling from the paraelectric cubic state [9].

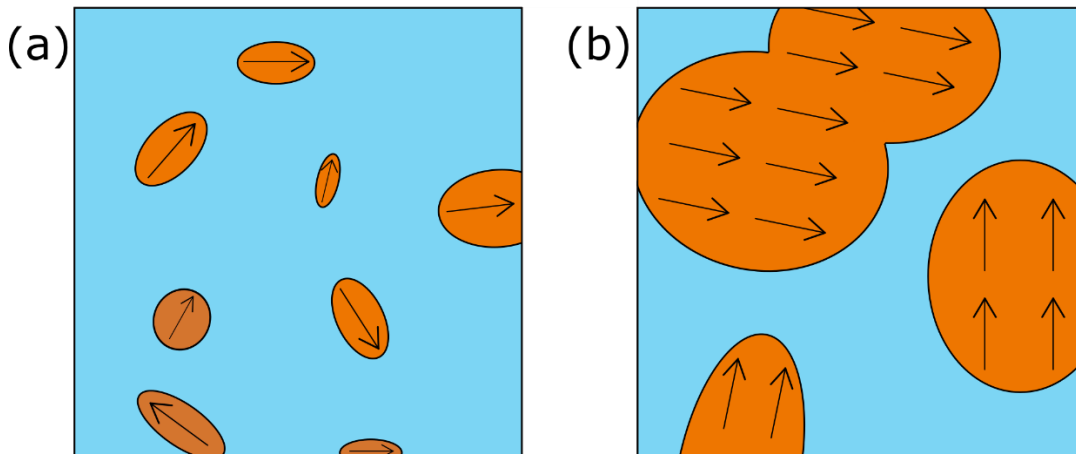


Figure 6: PNRs (orange) embedded in non-polarized matrix (blue) as proposed by the dipolar glass model. (a) Temperature is slightly below  $T_B$ . The PNRs have a short coherence length and do not interact. (b) Upon further cooling the PNRs grow and interact partly (redrawn after [35]).

Another more recent and still discussed model is the random field model [36]. The main difference to the older models is the proposed domain structure in non-ergodic relaxors. Instead of imagining the nanodomains to be surrounded by a non-polar matrix, the random field model describes the PNRs to be only separated by domain walls, so basically as a ferroelectric domain configuration but with domain sizes in the nanometer range. Furthermore, the presence of Barkhausen jumps (discontinuities in polarization change) due to orientation and size change of domains during poling contradicts the ‘glassiness’ proposed in the dipolar glass model [36]. The random field model is based on the assumption that large systems can be unstable against small static random



---

fields [37]. These random fields are influenced by different ions occupying the same site in the lattice. This was shown for  $\text{Sr}_x\text{Ba}_{1-x}\text{Nb}_2\text{O}_6$  and explains the composition-dependent relaxor to ferroelectric transition of the material when starting with a  $\text{Ba}^{2+}$ -rich composition and introducing more  $\text{Sr}^{2+}$  into the lattice, which induces random local fields hindering the formation of large ferroelectric domains [38].

In 2017, Takenaka and coworkers proposed a slush-like domain structure in single crystal  $\text{Pb}(\text{Mg}_{1/3}\text{Nb}_{2/3})\text{O}_3\text{-PbTiO}_3$  (PMN-PT) relaxors [39]. They describe the domain structure as consisting of nanometer-sized polar regions separated by a high density of domain walls. The name relates to the slush state of water and the findings are based on diffuse scattering and molecular dynamic simulations.

Due to the complex structure and nanometer-sized domains of relaxors, a complete and coherent understanding is yet to be developed. Further complications arise from the fact that many different materials are described with the term relaxor (ferroelectric) but do not necessarily share all the same structural features and properties. This is, for example, the case for the well-known lead-based relaxor materials in contrast to lead-free relaxors. Two lead-free systems exhibiting relaxor characteristics at certain compositions are  $\text{Na}_{1/2}\text{Bi}_{1/2}\text{TiO}_3\text{-BaTiO}_3$  and  $\text{BiFeO}_3\text{-BaTiO}_3\text{(-Na}_{1/2}\text{Bi}_{1/2}\text{TiO}_3)$  which will be discussed in the following chapters.

---

## 2.5 Lead-free Ferroelectrics

---

Lead-free ferroelectrics have been extensively studied during the last two decades because of the toxicity of lead, the resulting environmental issues and pending governmental legislation on the Restriction of Hazardous Substances (RoHS) [4]. Due to the superior properties of lead-based piezoceramics, the current understanding is that there will not be one substituting material for all purposes of application, but specifically tailored lead-free materials are able to come close and sometimes even outperform their lead-based competitors in certain fields of application. Four different classes of lead-free materials, all with a perovskite structure have emerged: alkaline niobates, barium titanate-, bismuth ferrite-based compositions and alkali-bismuth titanates [40, 41]. The last two groups are especially interesting due to a multiferroic nature combined with a high Curie temperature and excellent high-power properties, respectively [42-44].

---

### 2.5.1 The $\text{Na}_{1/2}\text{Bi}_{1/2}\text{TiO}_3\text{-BaTiO}_3$ System

---

The perovskite  $\text{Na}_{1/2}\text{Bi}_{1/2}\text{TiO}_3\text{-BaTiO}_3$  or short NBT-BT was first introduced by Takenaka et al. in 1991 [8]. The solid solution between the relaxor end member NBT and the well-known tetragonal ferroelectric  $\text{BaTiO}_3$  is interesting for high-power applications [7, 45, 46].

Smolensky et al. described the relaxor ferroelectric  $\text{Na}_{1/2}\text{Bi}_{1/2}\text{TiO}_3$  (NBT) for the first time in 1961 as exhibiting a perovskite structure with rhombohedral  $R3c$  space group [29]. In the following decades, the structure of NBT was highly debated in literature and reported to be of monoclinic  $Cc$  symmetry at room temperature with a small distortion from the average rhombohedral symmetry [47, 48]. The locally complex structure of NBT results from the A-site disorder, different characteristics of Na-O and Bi-O bonds, and the displacement of the  $\text{Bi}^{3+}$ -ion [49, 50]. This manifests in a shortening of the Bi-O bonds as evident from X-ray absorption fine structure, differentiating the local from the global structure [51]. Adding to the structural complexity, tetragonal platelets with  $P4bm$  symmetry embedded in the monoclinic or rhombohedral matrix were evidenced using transmission electron microscopy (TEM) [52]. As characteristic for relaxor materials, NBT shows a strong frequency dispersion in the dielectric permittivity with a maximum at about 320 °C [53].

Adding BT into NBT causes the structure of the material to change as displayed in the very recent phase diagram of Adhikary et al. (Figure 7) [54]. While NBT-xBT with  $x = 0\text{-}3$  (given in mol% if not indicated otherwise) exhibits  $Cc$  symmetry, the structure changes to a mixture of  $R3c$  and  $P4bm$  with  $3 < x < 6.5$  [54-56]. At room temperature, NBT-BT possesses a morphotropic phase boundary (MPB) around 6-7 mol% BT, at which the material exhibits strong relaxor features, the most promising properties from an application point of view, and an average pseudo-cubic (PC) crystal structure [57]. However, the depolarization temperature,  $T_d$ , at which the material loses its poling-induced net polarization is lowest at the MPB with 107 °C [8]. The MPB separates regions with rhombohedral symmetry at lower BT contents and tetragonal symmetry at higher BT contents. Due to the weak distortions of the coexisting phases and the short correlation lengths of ferroelectric nanodomains at the MPB, the global structure appears to be cubic in the unpoled material [58]. The MPB compositions are often reported to exhibit cubic  $Pm\bar{3}m$  space group since the correlation lengths of the polar entities, meaning regions with uniform symmetry, are not sufficient to be detected when the structure is investigated with regular X-ray diffraction [59, 60]. However, different techniques which allow probing of the local structure were applied to prove

---

the coexistence of rhombohedral and tetragonal phases. Electron diffraction patterns recorded with TEM reveal two types of superlattice reflections (SR).  $a^0a^0c^+$  tilting of the oxygen octahedral results in  $\frac{1}{2} \{00e\}$  SR which can be associated with the tetragonal  $P4bm$  phase. The coexisting rhombohedral  $R3c$  phase is characterized by  $\frac{1}{2} \{00o\}$  SR caused by  $a^-a^-a^-$  anti-phase tilting [61, 62]. The same phase composition was reported based on Raman spectroscopy [63]. Pforr et al. specified NBT-3.6BT to be built up of tetragonal platelets embedded in a rhombohedral matrix utilizing diffuse and quasielastic neutron scattering [64, 65]. This description fits to older findings by Daniels et al. reporting the structure of NBT-4BT single crystals to consist of rhombohedral nanoregions separated by a most likely tetragonal phase [66]. Utilizing *in situ* X-ray synchrotron diffraction, Lalitha K.V. and coworkers claim a coexistence of dominant tetragonal and rhombohedral phases in NBT-9BT [67]. Ma and coworkers reported the  $P4bm$  phase to be stable in NBT-xBT in a composition range from  $6 < x < 11$  together with the ferroelectric  $P4mm$  phase based on TEM findings [62]. However, a recent study claims a phase coexistence of  $P4bm$  and  $P4mm$  up to 18 mol% BT [54]. At even higher BT contents, NBT-BT exhibits single phase  $P4mm$  symmetry [68]. This  $P4mm$  phase that is dominant at  $> 12$  mol% is associated with a spontaneous ferroelectric order.

Depending on the composition, NBT-BT undergoes several phase transitions with increasing temperature (Figure 7a). Early reports assign two temperature-dependent phase transitions to the pure NBT end member, namely at  $\sim 255$  °C from  $R3c$  to  $P4bm$  and at 540 °C from  $P4bm$  to  $Pm\bar{3}m$  based on powder neutron diffraction [69] which was confirmed recently [54]. However, the current understanding is, that pure unpoled NBT exhibits  $Cc$  instead of higher  $R3c$  symmetry at room temperature [48], meaning there might be a transition from  $Cc$  to  $R3c$  (+  $P4bm$ ) between room temperature and  $\sim 255$  °C (Figure 7a). The  $R3c$  phase, which coexists with the  $P4bm$  phase in the MPB composition NBT-6BT, gradually disappears in the temperature range from 130 to 170 °C resulting in a single  $P4bm$  phase. Upon further increase in temperature, the characteristic SRs of  $P4bm$  phase that are visible in the electron diffraction pattern obtained with TEM, become weaker at 335 °C. However, even above 500 °C, very weak  $\frac{1}{2} \{00e\}$  spots remain, indicating local distortions in NBT-6BT [70]. The recently updated phase diagram by Adhikary et al. suggests the described phase transitions to take place at lower temperatures [54]. The authors claim that the  $R3c$  phase vanishes at  $\sim 60$  °C and the material is assumed to be of single phase  $Pm\bar{3}m$  symmetry already above 300 °C. At higher BT contents where  $P4bm$  and  $P4mm$  phases coexist, the transitions to a (globally) entirely cubic structure also happens over a temperature range, e.g. for  $x = 10$  between 170 and about 265 °C, while the  $P4mm$  phase vanishes at 220 °C [54].

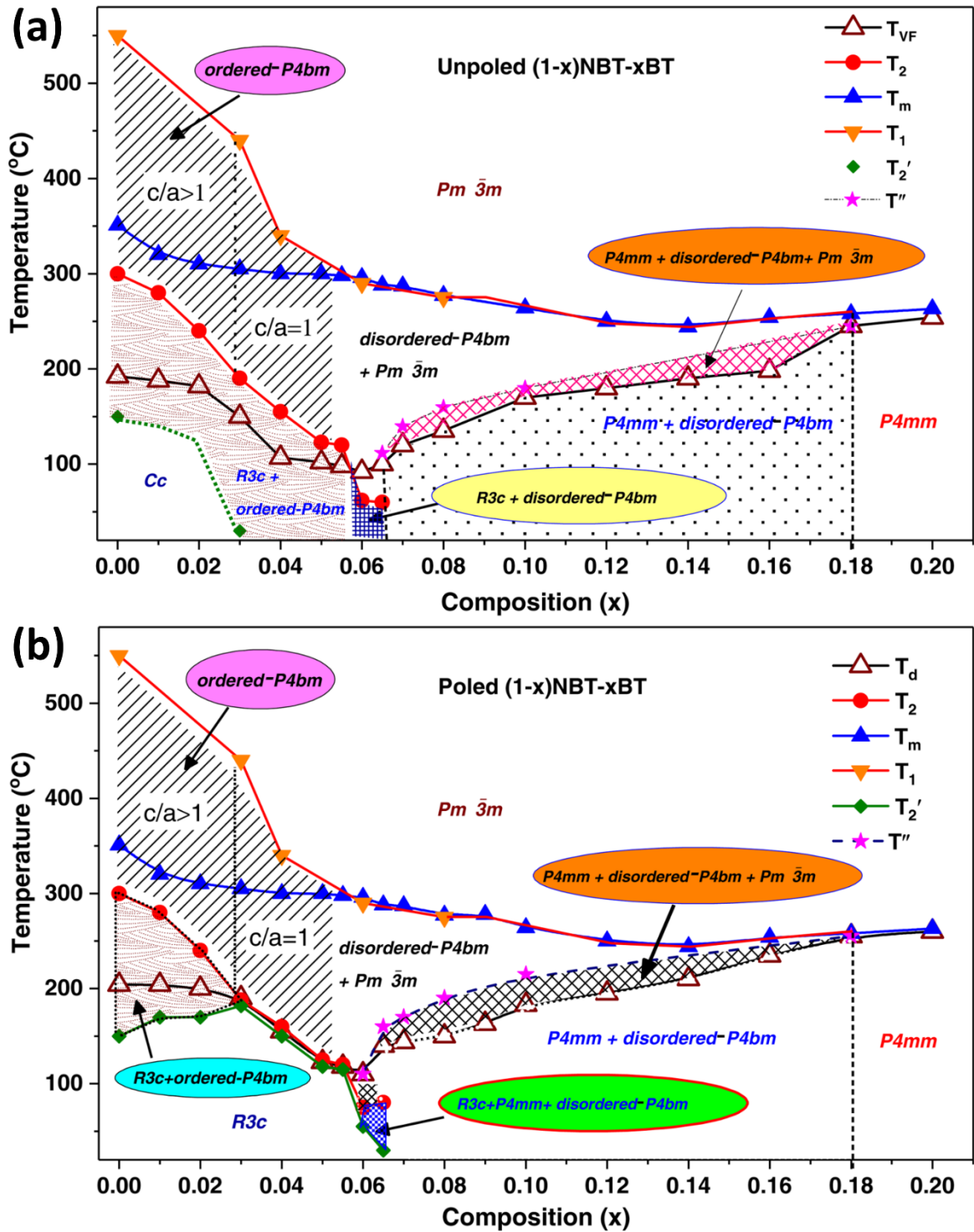


Figure 7: The temperature-dependent phase diagram of NBT-xBT with  $x$  being the absolute amount BT in moles in the unpoled (a) and in the poled state (b). Besides the present phase, several material-specific temperatures are marked with  $T_{VF}$ : freezing or Vogel-Fulcher temperature,  $T_2$ : rhombohedral  $R3c$  to tetragonal  $P4bm$  phase transition temperature,  $T_m$ : temperature of the dielectric permittivity maximum,  $T_1$ : tetragonal  $P4bm$  to cubic  $Pm\bar{3}m$  transition temperature,  $T_2'$ : temperature corresponding to the onset of in-phase octahedral tilt,  $T''$ : tetragonal ( $P4mm$ ) to cubic ( $Pm\bar{3}m$ ) transition temperature,  $T_d$ : depolarization temperature (reprinted from [54] with permission from the American Physical Society).

---

An extensive overview of electric field-induced changes in NBT and its solid solutions is given by Viola and coworkers [71]. Since NBT-xBT is a non-ergodic relaxor material, it transforms from the relaxor to a ferroelectric state upon application of an electric field or stress resulting in a fundamental change in the structural properties (Figure 7b) [54, 72, 73]. For  $x < 6$ , poling suppresses the non-rhombohedral disorder of the A-site cations causing the poled material to exhibit phase pure  $R3c$  symmetry instead of  $Cc$  or  $R3c + P4bm$  as in the unpoled state, respectively [74, 75]. Furthermore, poling suppresses the  $a^0a^0c^+$  in-phase octahedral tilting of the  $P4bm$  phase over the whole composition range of  $3 < x < 6$  [54, 62]. Directly at the MPB, poled NBT-BT is expected to be a phase mixture of  $R3c$  and  $P4mm$  phases with  $R3c$  being the dominant phase for 6 mol% BT [62]. However, Hinterstein et al. report a coexistence of  $R3m$  and  $P4mm$  phases with tetragonal phase fractions of 17 and 66 % for poled NBT-6BT and NBT-7BT, respectively [76]. The recent study by Adhikary et al. claims that for  $x > 6.5$ , the material exhibits coexisting  $P4mm$  and  $P4bm$  symmetries in the poled state with an increasing volume fraction of  $P4mm$  phase with increasing BT content [54].

Upon heating, NBT-BT transforms back from the poled ferroelectric state to an unpoled relaxor state [77]. The temperature at which this transition takes place,  $T_{F-R}$ , is depending on the composition and exhibits a minimum at the MPB. This transition is evident as the first anomaly in the temperature-dependent permittivity (Figure 5d dashed green lines and Figure 8b). In NBT-based materials,  $T_{F-R}$  dictates the depolarization temperature  $T_d$  [77]. However, a deviation between  $T_{F-R}$  and  $T_d$  is possible, depending on the techniques used to characterize the respective temperatures [78].

The temperature-dependent evolution of PNRs within NBT-BT is expected to be similar to the description given in chapter 2.4.2, meaning that PNRs form when the material is cooled below  $T_B$ , grow in size upon further cooling and lose their dynamic characteristics at  $T_{VF}$ . However, the coexistence of two types of PNRs at the MPB with rhombohedral  $R3c$  and tetragonal  $P4bm$  symmetries with different thermal stabilities complicate the picture. This coexistence is directly connected to the material's temperature-dependent dielectric behavior (Figure 8) [79]. In the unpoled state, MPB compositions of NBT-BT exhibit a strong frequency dispersion in dielectric permittivity. Due to the non-ergodic relaxor character of the material, poling induces a long-range ferroelectric order, accompanied by a significant decrease in frequency dispersion of  $\epsilon'$  and  $\epsilon''$  (Figure 8b). Above  $T_{F-R}$ , the frequency-dispersive unpoled relaxor state is restored. Between  $T_{F-R}$  and roughly 200 °C, NBT-BT exhibits its first anomaly as a shoulder in the dielectric response with strong frequency dependence [80] which is connected to the decrease in volume fraction of PNRs

with  $R3c$  symmetry [79]. At around 270 °C, the permittivity of NBT-BT exhibits its maximum. The position of this maximum also depends on the measurement frequency. Above this temperature, only PNRs with  $P4bm$  symmetry are present. NBT-BT compositions with 3 or  $\geq 12$  mol% BT exhibit significantly smaller frequency dispersion at room temperature in the unpoled state, indicating a ferroelectric order in these materials [81]. Above  $T_{F-R}$ , the before mentioned compositions possess ergodic relaxor properties.

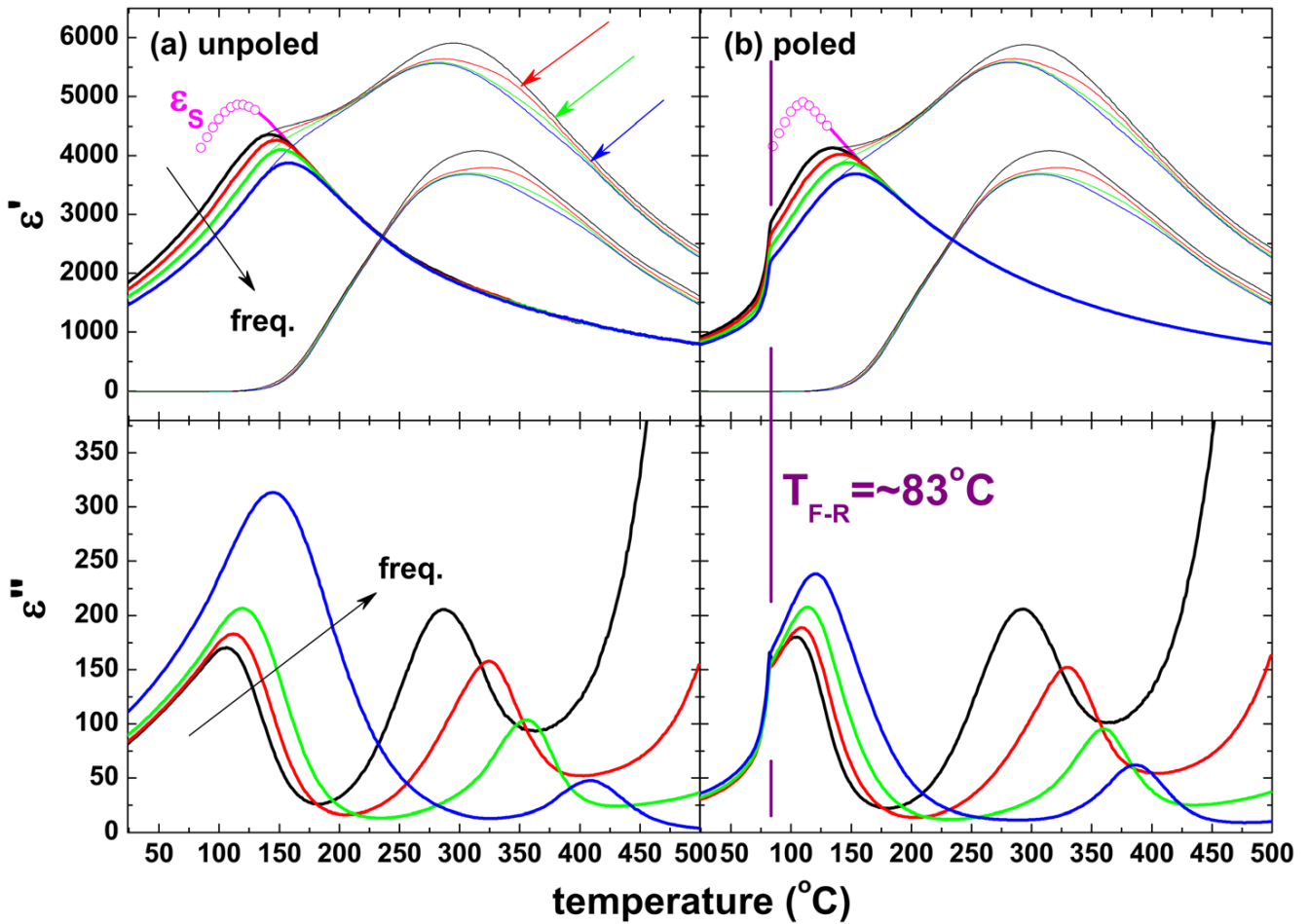


Figure 8: Temperature-dependent real ( $\epsilon'$ ) and imaginary parts ( $\epsilon''$ ) of permittivity of NBT-6BT in the unpoled (a) and poled state (b).  $\epsilon'$  is deconvoluted based on the assumption of two processes being related to the two types of PNRs being present. The colors denote measurement frequencies: black = 100 Hz, red = 1 kHz, green = 10 kHz, blue = 100 kHz (reprinted from [79] with the permission from AIP Publishing).

Even though the existence of PNRs in NBT-BT was proven using different techniques [61, 64], the quantification of the polarized volume remains challenging and the available methods are rather limited. Utilizing  $^{23}\text{Na}$  solid-state nuclear magnetic resonance (NMR), Groszewicz and coworkers established a cubic volume fraction of about 25 % in unpoled NBT-6BT at room temperature, and

---

thus, a fraction of polarized volume of 75 % [82]. Another option to quantify the polar volume is to exploit the sensitivity of mechanical properties to temperature-dependent structural changes even on a nanoscale using resonance frequency damping analysis (RFDA) [83]. By measuring the Young's modulus as a function of temperature and applying a simple model assuming tetragonal inclusions (PNRs) in a cubic matrix, the volume fraction of PNRs at elevated temperatures was established.

Due to its structural and overall phenomenological complexity combined with decent application-relevant properties, NBT-BT offers manifold opportunities for future research and industrial application. However, one of its main drawbacks is the low depolarization temperature at the MPB of  $\pm 100$  °C. Different approaches have been made to increase  $T_d$ , which are chemically modifying the material [10, 84, 85], forming composites [46, 86] and thermally quenching the material from high temperatures [12, 87]. The consequences of quenching NBT-BT are discussed in detail in chapter 2.6.

---

## 2.5.2 The BiFeO<sub>3</sub>-BaTiO<sub>3</sub>(-Na<sub>1/2</sub>Bi<sub>1/2</sub>TiO<sub>3</sub>) System

---

Pure BiFeO<sub>3</sub> (BF) is a multiferroic material with strong ferroelectric behavior, but it has the immense problem of high conductivity due to the oxygen vacancies created during sintering. The creation of oxygen vacancies is connected to Bi<sub>2</sub>O<sub>3</sub> loss and due to the multivalence of the Fe-ions [88, 89]. Furthermore, difficulties with achieving a phase-pure material free of secondary phases are often described in literature [6]. Therefore, forming solid solutions was used to ease phase-pure synthesis and to tailor the material's properties for certain applications, where significantly lower conductivity is needed. One of the possible substitutions is BaTiO<sub>3</sub>.

The lead-free ferroelectric BiFeO<sub>3</sub>-BaTiO<sub>3</sub> (BF-BT or BF-xBT) solid solution with perovskite structure has been intensely investigated because of its tremendously high depolarization temperature of about 470 °C [90] and decent switchable polarization in proximity to its MPB around 33 mol% BT [91]. Similar to pure BF, BF-BT exhibits ferromagnetic behavior [92], however, this will not be further discussed in this thesis due to the focus on ferroelectrics.

At room temperature, the structure of pure BF has been reported to be of rhombohedral  $R3c$  symmetry [88, 93]. The same is true for the BF-BT solid solution from 0 to 25 mol% BT as apparent from the phase diagram in Figure 9 [90]. In the composition range  $x = 0.25-0.40$ , the material

exhibits a pseudo-cubic symmetry but also ferroelectric properties [90]. Due to the ferroelectricity of the material in that composition range, it cannot be truly cubic, and therefore it is described as pseudo-cubic, comparable to the MPB compositions of NBT-BT. Other studies reported the material to still exhibit a rhombohedral distortion at 30 mol% BT in X-ray diffraction patterns [94, 95]. This difference in the reported structural properties might be due to differences in processing route, precursor powders and resolution of the XRD measurement. Upon further increase in BT content, the material remains pseudo-cubic up to high BT concentrations. Above 95 mol% BT, the solid solution exhibits tetragonal symmetry [96]. Even though a region with coexisting rhombohedral and tetragonal phases does not exist, the compositions ranging from 25 to 33 mol% BT are by some authors considered to form an MPB or exhibit MPB-like behavior due to the coexistence of rhombohedral and pseudo-cubic symmetries [89]. This composition range is the most investigated one in BF-BT because it is characterized by the most promising ferro- and piezoelectric properties.

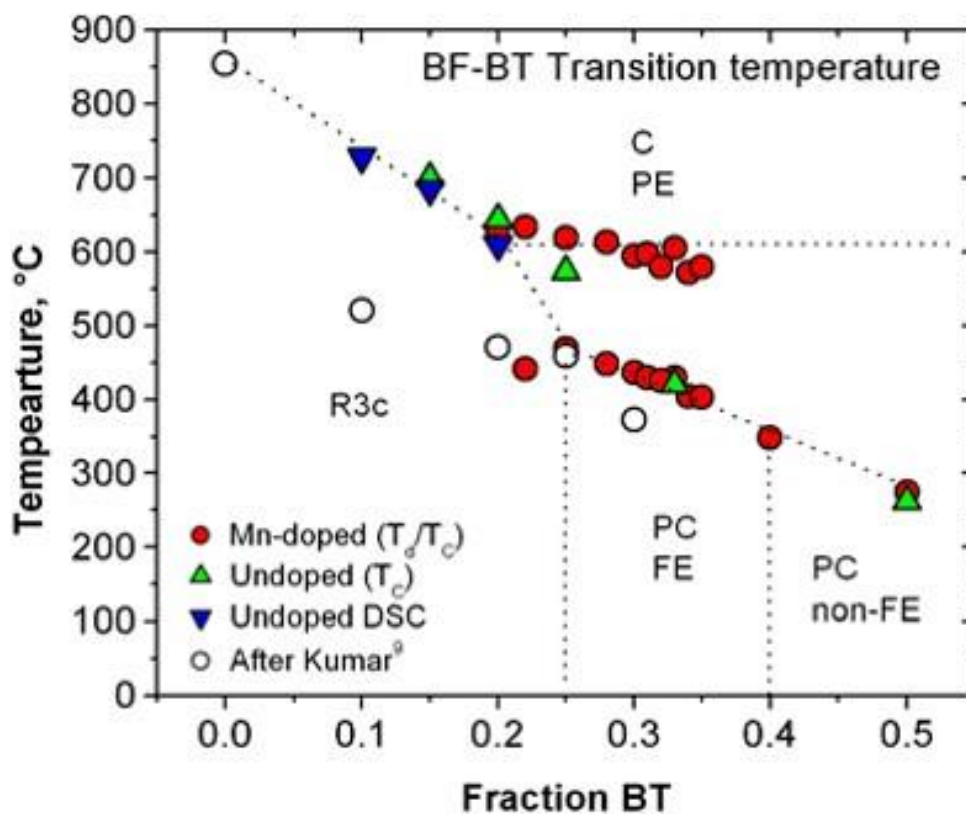


Figure 9: Temperature- and composition-dependent phase diagram of the BF-BT solid solution based on dielectric and differential scanning calorimetry measurements. PE stands for paraelectric. (reprinted from [90] with the permission from John Wiley and Sons).



The temperature at which BF-BT transforms into the paraelectric, cubic state,  $T_c$ , strongly depends on the composition. With increasing amount of BT,  $T_c$  declines monotonously (Figure 10a). This was confirmed by structural and dielectric studies [97]. The dielectric spectrum exhibits a maximum at  $T_c$ , which is shifted to lower temperatures upon introducing more BT into the solid solution [98]. Furthermore, with increasing BT content, the temperature-dependent maximum in dielectric permittivity becomes broader and rather resembles some aspects of the dielectric behavior of a relaxor ferroelectric than from a normal ferroelectric (Figure 11). Therefore, some authors do not report the maximum in permittivity as  $T_c$  but as  $T_m$  [98], however, the existence of an entirely cubic state above this maximum is widely accepted. Please note, that neither  $T_c$  nor  $T_m$  coincides with the depolarization temperature of BF-BT, since the material depolarizes at temperatures below the dielectric maximum. Comparing the dielectric results from different literatures reveals significant differences, especially in absolute values [14, 90, 98], which further underlines the materials' sensitivity towards processing conditions.

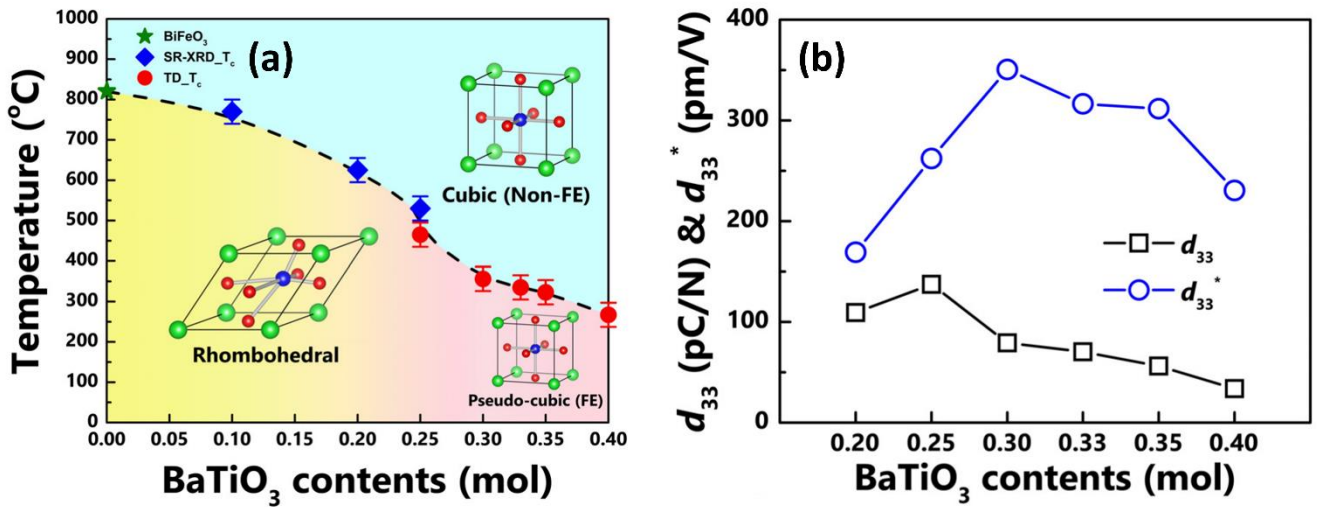


Figure 10: (a) Phase diagram of BF-BT with  $T_c$  established from synchrotron X-ray diffraction and dielectric data and (b) composition-dependent direct ( $d_{33}$ ) and converse ( $d_{33}^*$ ) piezoelectric constants (reprinted from [97] with the permission from AIP Publishing).

Especially in the BF-rich compositions of the pure BF-BT system, the high leakage current causes difficulties in measuring electric-field dependent polarization hysteresis [89, 99]. To reduce the leakage current and also to improve other relevant properties like the piezoelectric constant or to reduce the sintering temperature, many different doping strategies have been investigated (Table 1 and references therein). Many works report that doping small amounts of Mn in the range of about 0.1-1 mol% is beneficial to reduce the leakage current significantly [90, 100], making it

probably the most common doping strategy for BF-BT. Other doping elements are used to achieve high energy storage performance of the material, such as Nb or Sm [101, 102]. Table 1 provides an overview of reported doping elements improving some properties of BF-BT with the respective qualitative changes.

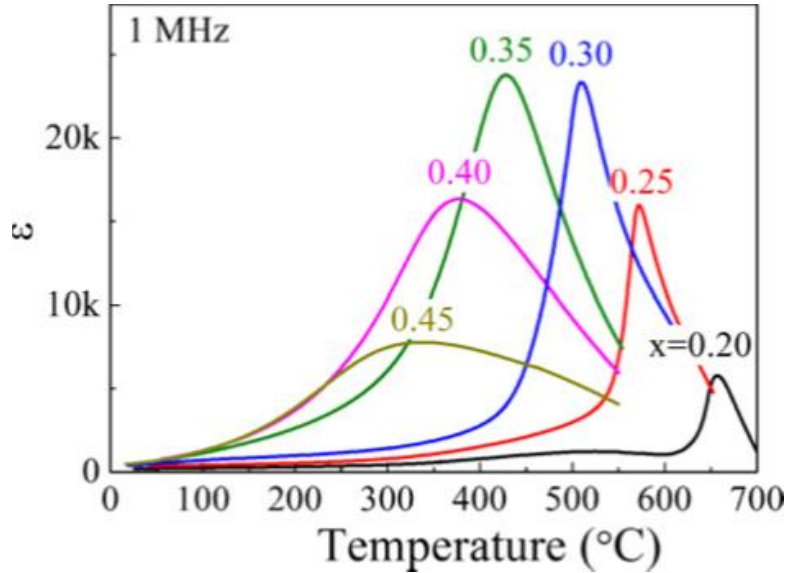


Figure 11: Temperature-dependent dielectric permittivity  $\epsilon'$  for different  $(1-x)\text{BF}-x\text{BT}$  compositions measured at 1 MHz (reprinted from [98] with permission from John Wiley and Sons).

Another strategy to reduce the leakage current and improve relevant properties such as the piezoelectric coefficient  $d_{33}$  is to form a ternary system consisting of the binary solid solution BF-BT and another end member (Figure 12a). Some of these reported additional endmembers are  $\text{Bi}(\text{Mg}_{1/2}\text{Ti}_{1/2})\text{O}_3$  [103, 104],  $\text{LiNbO}_3$  [105, 106],  $\text{Bi}(\text{Mg}_{2/3}\text{Nb}_{1/3})\text{O}_3$  [107] and  $\text{Na}_{1/2}\text{Bi}_{1/2}\text{TiO}_3$  [15, 108, 109]. Introducing small amounts of NBT into BF-BT has been reported to reduce the amount of oxygen vacancies and improve the ferro- and piezoelectric and magnetic properties [15]. However, the number of available studies on  $\text{BiFeO}_3\text{-BaTiO}_3\text{-Na}_{1/2}\text{Bi}_{1/2}\text{TiO}_3$  (BF-BT-NBT) is rather limited and partly with emphasize on the material's magnetic properties [108, 109]. Additionally, there are studies on NBT-BT with small concentrations of BF, which technically report the same ternary system, but due to very different concentrations of the endmembers, the material properties differ strongly from BF-BT [110, 111]. Decent ferro- and piezoelectric properties of the MPB composition of BF-BT with 5 mol% NBT with a remanent polarization  $P_{\text{rem}} = 24.2 \mu\text{C}/\text{cm}^2$ ,  $d_{33} = 183 \text{ pC}/\text{N}$ ,  $T_c = 467 \text{ }^\circ\text{C}$  and enhanced insulating behavior were recently reported by Cheng and coworkers [15]. This renders BF-BT-NBT a promising lead-free ferroelectric material worthy

of further investigation, especially, since quenching BF-BT ceramics, similar to quenching NBT-BT, is frequently used to improve the material's properties (Figure 12b), but the consequences of quenching on BF-BT-NBT have not been reported in literature yet. In the following chapter, the quenching-induced changes in structure and relevant material characteristics are discussed in detail for the NBT-BT and BF-BT systems.

Table 1: Promising doping elements reported for BF-BT. Typically, the doping concentrations vary between 0 and 3 mol%. In most cited studies, different doping concentrations were investigated. The qualitative changes in properties listed in this table refer to the most promising doping concentrations stated in the cited literatures, respectively.

<b>Dopant</b>	<b>Qualitative changes in properties</b>	<b>References</b>
Al	<ul style="list-style-type: none"> <li>Decreased rhombohedral phase fraction, structure becomes more cubic</li> <li>Increase in remanent and maximum polarization</li> </ul>	[112]
Ca	<ul style="list-style-type: none"> <li>Increase in grain size</li> <li>Improved piezoelectric properties</li> </ul>	[113]
Cu	<ul style="list-style-type: none"> <li>Improved ferroelectric and magnetoelectric properties</li> <li>Acting as sintering aid</li> </ul>	[114, 115]
Eu	<ul style="list-style-type: none"> <li>Decrease in average grain size</li> <li>Influence on ferroelectric properties depending on doping concentration</li> </ul>	[116]
Ga	<ul style="list-style-type: none"> <li>Improved ferroelectric, piezoelectric and dielectric properties</li> </ul>	[117]
Gd	<ul style="list-style-type: none"> <li>Stabilized single rhombohedral phase</li> <li>Decrease in dielectric constant and losses</li> </ul>	[118, 119]
K	<ul style="list-style-type: none"> <li>Increase in rhombohedral distortion</li> <li>More pronounced ferroelectric behavior with increase in coercive field and polarization</li> </ul>	[120]
La	<ul style="list-style-type: none"> <li>Decrease in bulk resistivity</li> <li>Enhanced ferroelectricity</li> <li>Difference between isovalent and donor substitution, with the latter leading to more relaxor-like behavior</li> </ul>	[121-123]
Li	<ul style="list-style-type: none"> <li>Decreased sintering temperature, acting as sintering aid</li> </ul>	[124]

Mg	<ul style="list-style-type: none"> <li>Increased piezoelectric response</li> </ul>	[125]
Mn	<ul style="list-style-type: none"> <li>Improved resistivity and decreased dielectric losses</li> <li>Decrease in defect concentration</li> <li>Enhanced piezo- and ferroelectric properties</li> </ul>	[90, 100, 114, 126-134]
Na	<ul style="list-style-type: none"> <li>Improved piezoelectric properties and high temperature stability</li> </ul>	[135]
Nb	<ul style="list-style-type: none"> <li>Improved resistivity</li> <li>Low remanent but high maximum polarization, beneficial for energy storage</li> </ul>	[94, 101]
Sc	<ul style="list-style-type: none"> <li>Low doping concentrations increase grain size</li> <li>Decrease in oxygen vacancy concentration</li> <li>Improved piezoelectric properties</li> </ul>	[136, 137]
Sm	<ul style="list-style-type: none"> <li>Promotes relaxor behavior</li> <li>Increased energy storage capability</li> </ul>	[102]
Zn	<ul style="list-style-type: none"> <li>Increased rhombohedral distortion and grain size</li> <li>Improved piezoelectric performance</li> </ul>	[138]

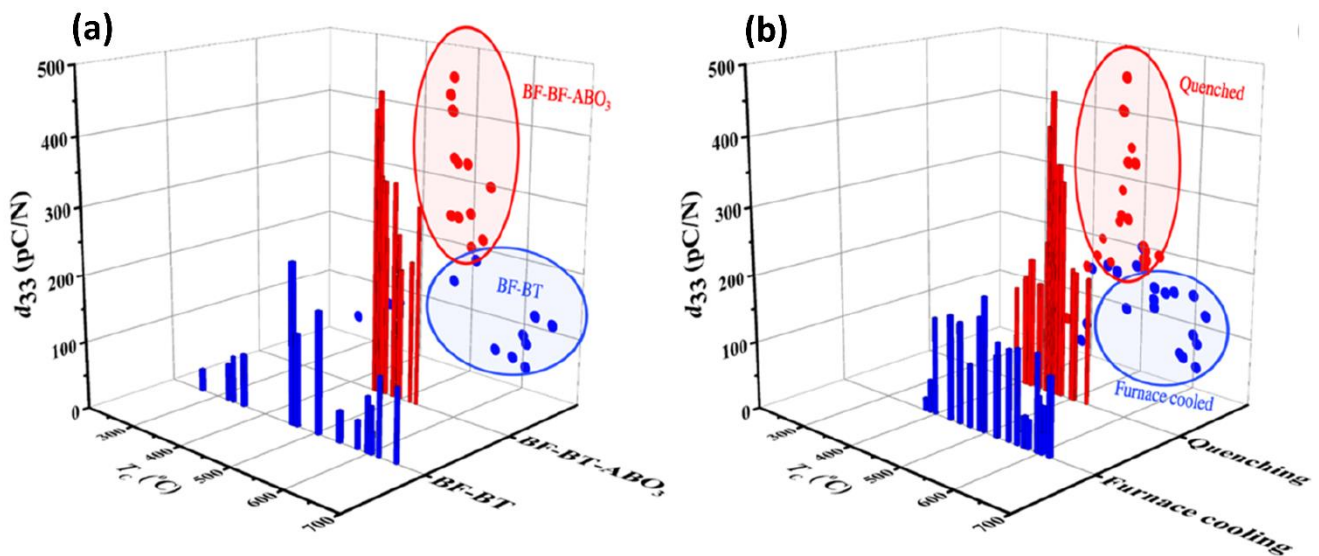


Figure 12: Piezoelectric coefficient,  $d_{33}$ , versus Curie Temperature,  $T_C$ , in BF-BT ceramics with (a) comparison between pure BF-BT and ternary systems and (b) comparison between as sintered or furnace cooled and quenched ceramics (reprinted from [139]).

---

## 2.6 Quenching Lead-free Ferroelectrics

---

Quenching is a well-known method to influence the structural and microstructural properties of metals [140]. Furthermore, quenching non-metallic materials like ceramics is commonly utilized for stabilizing a high-temperature phase under ambient conditions [141], but in contrast to quenching metals, the cooling rate is usually lower due to the smaller fracture toughness of ceramics. Additionally, the influence of quenching on the defect distribution in perovskite-structured oxides like SrTiO<sub>3</sub> or BaTiO<sub>3</sub> has been widely investigated [142]. Quenching La-doped BaTiO<sub>3</sub> from temperatures above 1350 °C results in a significant decrease in resistivity due to enhanced p-type conductivity [143]. A change in ferroelectric and piezoelectric behavior upon quenching was reported for Sr<sub>x</sub>Ba<sub>1-x</sub>Nb<sub>2</sub>O<sub>6</sub> with a reduction in A-site disorder leading to less pronounced relaxor behavior [144]. However, the quenching-induced changes in properties depend on the investigated material system and differ for NBT and BF-based materials as discussed in the following.

A detailed overview on quenched bismuth-based ferroelectrics with perovskite structure is given by K.V. Lalitha and coauthors [14] and serves as main reference for this chapter and the following two subchapters on the quenching-induced changes in the materials investigated in this study.

---

### 2.6.1 Quenching-induced Changes in Na<sub>1/2</sub>Bi<sub>1/2</sub>TiO<sub>3</sub>-BaTiO<sub>3</sub>

---

The first work reporting quenching experiments on NBT-BT by Zang et al. investigated changes in the temperature-dependent dielectric response and the aging effect upon quenching [145]. However, the highest quenching temperature in this study was 600 °C and the material's dielectric behavior was only measured in the unpoled state making the establishment of  $T_{F-R}$  impossible. In 2016, Muramatsu and coworkers reported an increase in the depolarization temperature in pure NBT ceramics when quenching from different high temperatures directly after the sintering step [12].  $T_d$  shows the strongest increase of about 50 °C when the material was quenched from 1100 °C to room temperature in air, assisted by an air fan. Furthermore, the rhombohedral lattice distortion given as  $90^\circ-\alpha_{\text{rhom}}$  is enhanced upon quenching, but without a significant change in the electromechanical properties. Shortly after, a similar enhancement in  $T_d$  was found in Li-doped NBT and NBT-BT of different compositions [87]. Due to this improvement of the application-relevant temperature stability of the poled state by quenching, combined with the lack of

understanding of the underlying mechanisms, the topic became interesting for an increasing number of researchers focusing on different aspects of the quenching mechanism [13, 146].

One of the most widely discussed consequences of quenching NBT-BT ceramics is the change in structural properties. Irrespective of the investigated composition and dopants, an increase in the distortion from the (pseudo-)cubic unit cell has been reported upon quenching, derived from XRD data [13, 87, 147, 148]. For compositions close to the NBT endmember, meaning in the rhombohedral regime of the phase diagram, quenching enhances the rhombohedral distortion [12, 147, 149]. In compositions with higher BT content or ternary systems exhibiting a tetragonal distortion, the tetragonality given as the  $c_T/a_T$ -ratio is increased upon quenching [13, 150]. In Figure 13a, the lattice distortion for rhombohedral and tetragonal phases is given for Li-doped NBT-BT with different BT concentrations with the quenched materials clearly showing enhanced distortions. Not only does quenching alter the average structure, Nagata and coworkers also quantified an increased off-centering, but less fluctuation in the position of the Bismuth-ion in Li-doped NBT (Figure 13b) using pair distribution function [149]. The off-centered state from high temperatures is frozen-in due to the rapid cooling. The increased off-centering of the  $\text{Bi}^{3+}$ -ion and the general increase in lattice distortion is assumed to stabilize a more ordered structure and therefore the ferroelectric state in the relaxor material, which is supported by the dielectric properties of quenched NBT-BT [13].

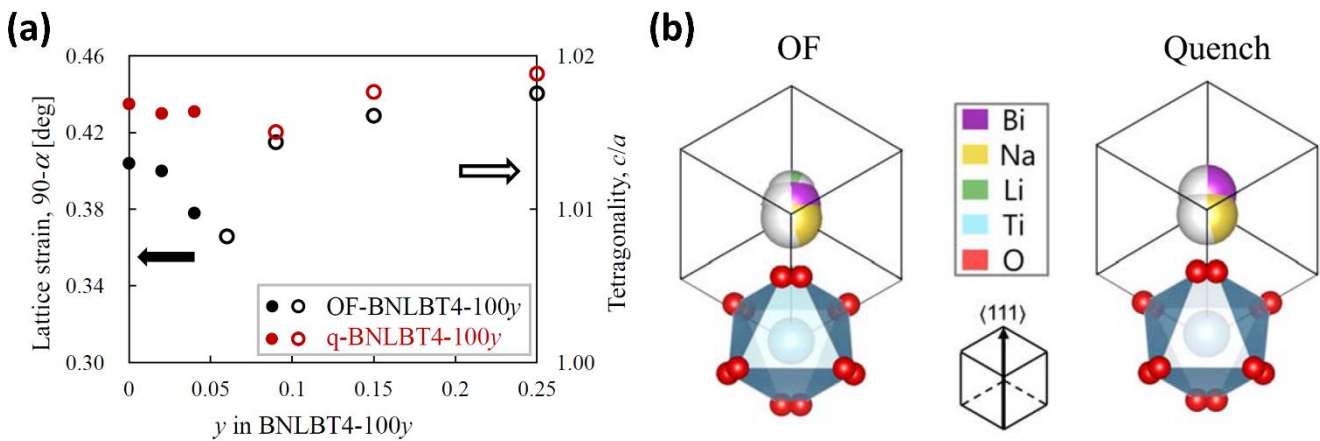


Figure 13: (a) Rhombohedral and tetragonal lattice distortion given as  $90^\circ - \alpha_{\text{rhom}}$  and  $c_T/a_T$ , respectively, for normally sintered (OF) and quenched (q) Li-doped NBT-BT (reprinted from [87] with permission from IOP Publishing). (b) Schematic illustration of the A-site ion with the unit cell of Li-doped NBT using the software VESTA (reprinted from [149]).

Amongst other techniques, K.V. Lalitha et al. utilized the temperature-dependent dielectric properties of normally sintered (furnace cooled, FC) and quenched NBT-BT (here Q1100) with 6 and 9 mol% BT (NBT-6BT and NBT-9BT, respectively) to establish  $T_{F-R}$  and therefore  $T_d$ , but also to propose a stabilized ferroelectric state upon quenching (Figure 14) [13]. Comparing the dielectric spectra of furnace cooled and quenched NBT-6BT and NBT-9BT clearly shows an increase in  $T_{F-R}$  as marked by the dashed line in Figure 14a, b and c, d, respectively. Furthermore, unpoled quenched NBT-9BT also exhibits a clear anomaly in the real part of permittivity similar to the poled materials (Figure 14h), therefore, indicating a transition from relaxor to ferroelectric due to the quenching treatment. In the furnace cooled materials, this is not the case as the materials are in the relaxor state (Figure 14g), suggesting the spontaneous formation of ferroelectric order upon quenching in NBT-9BT.

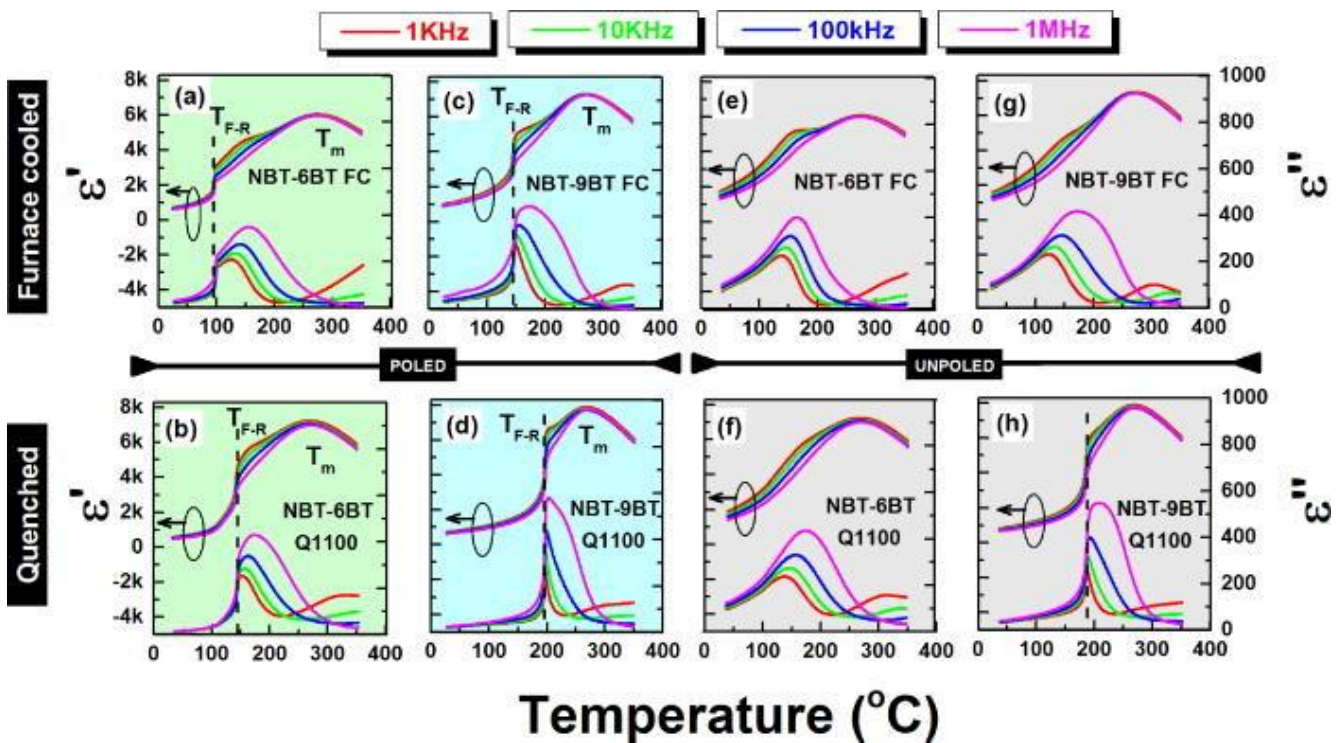


Figure 14: Temperature-dependent real and imaginary part of permittivity for poled and unpoled NBT-6BT FC (a, e), NBT-6BT Q1100 (b, f), NBT-9BT FC (c, g) and NBT-9BT Q1100 (d, h). FC stands for furnace cooled meaning normally sintered while Q1100 means the material was quenched from 1100 °C after the sintering step (reprinted from [13] with permission from AIP Publishing).

In addition, the effect of quenching NBT-BT on its electromechanical properties has been investigated. Several studies state a slight decrease of about 10-15 % in the piezoelectric coefficient  $d_{33}$  around room temperature upon quenching. However, the temperature window in

---

which the material's piezoelectricity can be exploited is extended by the increase in  $T_d$  [13, 87, 151, 152]. The electromechanical coupling factor  $k_{33}$  remains unaltered [87, 151] while the Young's modulus decreases only by 8-10 % in NBT-6BT and NBT-9BT by air-quenching routines [153].

Besides the enhanced off-centering of the  $\text{Bi}^{3+}$ -ion, other possible explanations have been discussed in literature as the reason for the quenching-induced changes in properties, namely residual stress and an enhanced oxygen vacancy concentration [154]. Quenching-induced stresses can cause sample fracture if the cooling rates are fast enough, for example, when quenching NBT-BT in water or oil [155]. Therefore, it was reasonable to assume that lower quenching rates like those realized in air-quenching can cause microfracturing, possibly decreasing the materials fracture strength. However, no evidence of microcracking and only small changes in bending strength compared to furnace cooled ceramics have been found in air quenched samples with quenching rates of 3.85 °C/s [155]. Mathematical modelling of thermal gradients and resulting stress distribution upon quenching cylindrical NBT-BT ceramic samples revealed maximum tensile and compressive stresses of 15 MPa and 8 MPa, respectively [153], with both values being lower than the coercive stress of NBT-BT [156]. Therefore, based on these recent findings, the influence of residual stress and microcracking of NBT-BT ceramics upon air-quenching can be neglected.

Upon slowly cooling from high temperatures, the oxygen vacancy distribution and concentration equilibrates within the material; however, this mechanism is likely to be hindered by fast cooling rates. A quenching rate-dependent increase in bulk conductivity has been reported, suggesting a connection to the oxygen vacancy concentration [153, 157]. Furthermore, an enhanced oxygen vacancy concentration has been reported for quenched Co-doped NBT-BT single crystals based on X-ray photoelectron spectroscopy and electron paramagnetic resonance [154]. However, annealing the ceramics in oxygen atmosphere did not result in significant change in bulk conductivity [158], but annealing at temperatures around 800 °C restores the quenching-induced increase in  $T_{F-R}$  to values characteristic for furnace cooled samples [13]. Therefore, the change in temperature-dependent dielectric and depolarization behavior is unlikely to be connected to an altered oxygen vacancy concentration, even though, quenching seems to enhance the oxygen vacancy concentration.

This leaves the structural changes, namely enhanced lattice distortion and  $\text{Bi}^{3+}$ -ion off-centering as the main responsible mechanisms causing the changes in application-relevant properties upon



---

quenching. Due to that, in the presented study, special emphasis is put on the influence of quenching on the structural properties of NBT-BT.

---

## 2.6.2 Quenching-induced Changes in BiFeO<sub>3</sub>-BaTiO<sub>3</sub>

---

Since the first study was published on air-quenching BF-BT ceramics in 2013 [159], several effects of this thermal treatment on the material have been reported in literature, namely changes in crystal- and microstructure [160, 161] as well as in application-relevant properties such as resistivity, polarization behavior and piezoelectric response [162, 163]. Some of these changes are similar to what quenching does to pure and doped BF [164, 165]; however, since BF is not in the scope of this study, the following paragraphs will only discuss the consequences of quenching BF-BT.

Pure BF-BT exhibits rhombohedral and/or pseudo-cubic symmetry when normally sintered depending on the composition [90, 96]. The structure of quenched BF-BT is partly under debate [14], and reported as a coexistence of rhombohedral and tetragonal phases in water-quenched BF-BT by Lee et al. [166]. However, another study proposes coexisting rhombohedral and pseudo-cubic phases in water-quenched BF-BT with 20 mol% BT [97], but this might be attributed to differences between surface and bulk phase assemblage [14]. Quenching BF-BT results in an enhanced lattice distortion in the rhombohedral and the partly reported tetragonal phases [161] with higher quenching rates resulting in higher distortion from the cubic reference frame [167]. Mn-doped BF-BT of MPB composition exhibits a transition from pseudo-cubic to rhombohedral symmetry by air-quenching [168]. These structural characteristics seem to be closely correlated to the properties of core-shell type microstructure in quenched BF-BT [160]. In as-sintered ceramics exhibiting a core-shell structure (often acceptor-doped BF-BT), the core is typically chemically enriched in the BF-endmember and shows a rhombohedral structure, while the shell is BT-rich and of cubic symmetry. However, quenching causes a rhombohedral distortion in the previously cubic shell and establishes a long-range ferroelectric order [160, 161] as evident from SEM micrographs of etched BF-BT samples (Figure 15) [134]. Since the chemical composition of the two regions does not change upon quenching, the proposed explanation of the mechanism is connected to a nanoscale phase segregation in the shells of the as-sintered material [134].

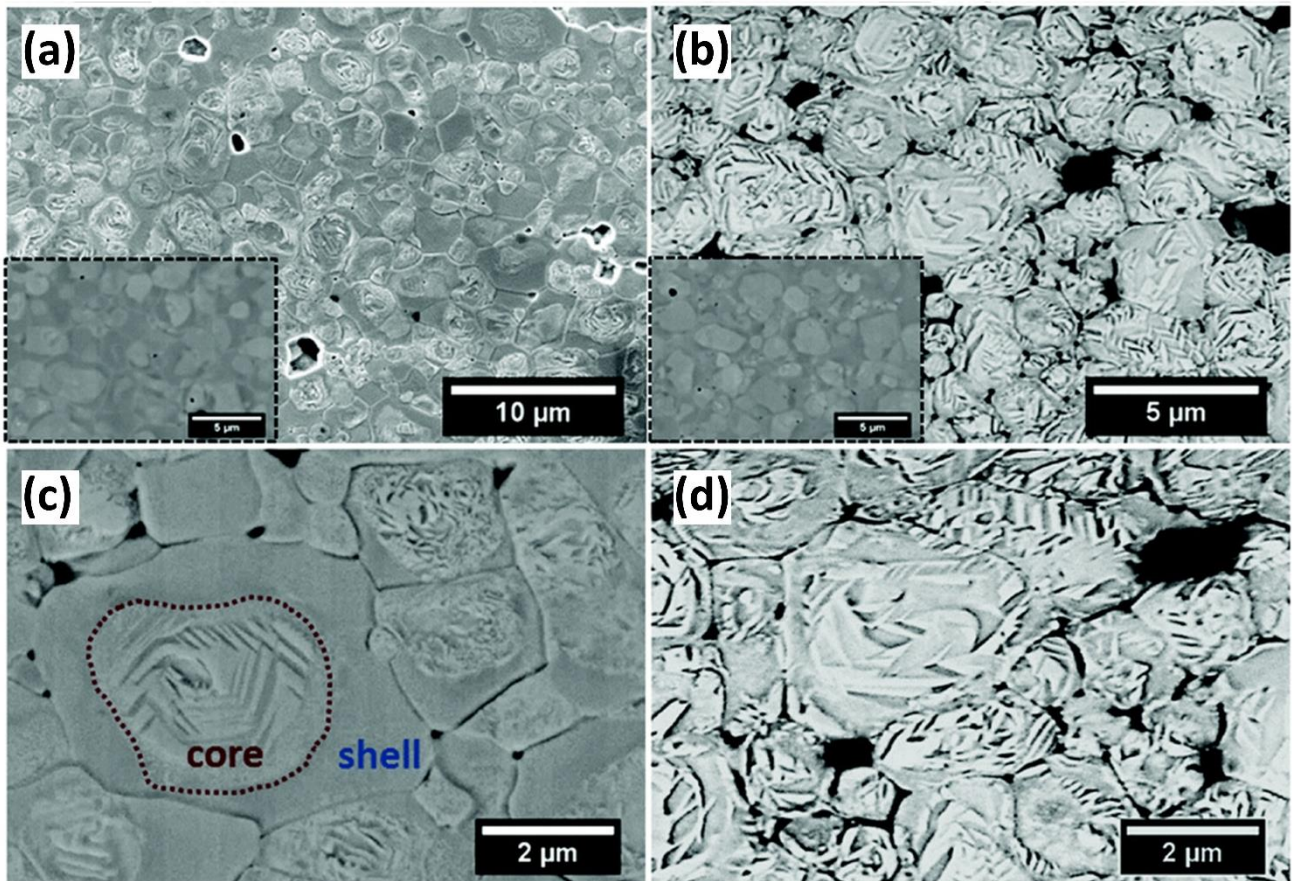


Figure 15: SEM micrographs of etched Mn-doped BF-BT with 25 mol% BT in the as-sintered (a, c) and quenched state (b, d). Reprinted from [134] with permission from the Royal Society of Chemistry.

In addition to the induced structural changes, quenching alters the ferroelectric properties of BF-BT materials, as it increases the remanent polarization and decreases the coercive field [98, 133]. Further changes in polarization hysteresis are a suppression of rounded and more opened  $P(E)$  loops due to an increased resistivity and a pronounced ferroelectric behavior which correlates to the stabilization of a rhombohedral phase upon quenching [97, 163].

Lee et al. carried out a systematic study investigating the influence of different quenching temperatures on structural and electrical properties of BF-BT with 33 mol% BT and partly modified with 1 mol%  $\text{BiGaO}_3$  [167]. Despite also reporting an increased lattice distortion with increasing quenching temperature, the authors observed a strong increase in the direct and indirect piezoelectric coefficient, an only slightly enhanced  $T_c$  when quenching from higher temperatures (Figure 16), and an improved coupling factor,  $k_p$ . Annealing the samples after the quenching treatment resets the properties almost to the as-sintered state. The increase in  $T_c$  established from dielectric measurements is consistent with the increase in depolarization temperature upon quenching [161, 167]. Furthermore, quenching BF-BT results in narrowing of

the main temperature-dependent dielectric peak [167] and in an increase in the permittivity maximum of the first peak in core-shell structured materials, which exhibit two peaks in the dielectric spectrum [134].

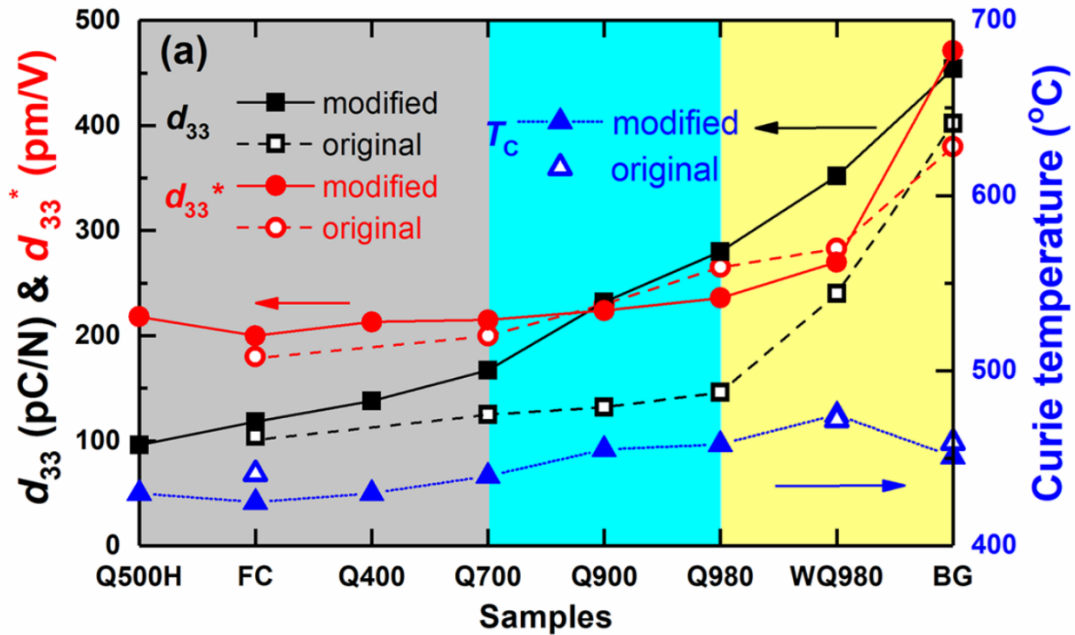


Figure 16: Direct and indirect piezoelectric coefficient and Curie Temperature of BF-BT ceramics with 33 mol% BT as-sintered (FC) and quenched from different temperatures. WQ980 stands for water-quenched and BG for modified with 1 mol% BiGaO<sub>3</sub> and water-quenched. Reprinted from [167] with permission from the American Chemical Society.

The mechanism underlying the quenching-induced changes in BF-BT are not fully understood yet. Similar to quenching NBT-BT, the role of oxygen occupancy in the crystal structure is intensely discussed since quenching stabilizes the ferroelectric domain configuration, which can also be achieved for other ferroelectrics by acceptor-doping, and therefore by implementing oxygen vacancies [14, 169]. Even though a connection between annealing and quenching BF-BT ceramics and the oxygen vacancy concentration within the material is proven by a strong decrease in leakage current caused by the thermal treatment [166], the absence of significant ageing and occurrence of strong structural changes upon quenching render the dominant role of oxygen vacancies questionable [14].

In light of the role of Bi<sup>3+</sup>-ion off-centering in NBT-BT upon quenching [149] and the recent discussion on A-site off-centering in BF-BT-based materials [170], the degree of ion off-centering

---

as a mechanism might be worthwhile investigating with respect to the influence on quenching-induced changes of structure and properties in BF-BT [14].

Despite the fact that the mechanisms responsible for the altered properties of BF-BT upon quenching are not understood yet, the positive effects of this thermal treatment are well established. Therefore, it appears plausible to assume also the rather new and poorly investigated BF-BT-NBT system might benefit from quenching. This alongside the other goals of this work with respect to NBT-BT and understanding the quenching mechanisms in general are outlined in the upcoming chapter.

---

### 3 Aim of the Work

---

As outlined in the previous chapters, quenching can be used to improve application-relevant properties in Bi-based ceramics, while also reflecting in structural changes. For NBT-BT, it has been proposed that quenching stabilizes the ferroelectric order in the unpoled state. However, detailed descriptions of quenching-induced changes in the poled state and in different regions of the phase diagram have not yet been reported in literature. Therefore, chapters 5.1 to 5.3 of this study address the following questions with respect to NBT-BT:

- How does quenching affect the structure in the poled state in comparison to the unpoled state over a broad composition range, and is there a correlation between these structural changes and the piezo- and ferroelectric properties?
- Does quenching influence the fraction of polarized volume, and how does it connect to the dielectric response?
- Since quenching enhances the lattice distortion and promotes a ferroelectric state, is there an impact on the development of the electric field-induced structural changes and the resulting strain contributions?

To answer the first and third question, synchrotron X-ray diffraction experiments were carried out on quenched NBT-BT with 3, 6, 9 and 12 mol% BT, *ex situ* and *in situ* with applied electric field, respectively, and correlated to polarization and strain hysteresis and piezoelectric response. In addition, the microstructure of specimen was investigated for every composition. The temperature-dependent polarized volume was quantified by establishing the material's Young's modulus and applying a composite model, and further connected to the dielectric permittivity.

The second part of the study is focused on deepening the understanding of how introducing NBT into BF-BT changes the structure and electric properties of the material, and how quenching affects this ternary composition. To that end, high resolution X-ray powder diffraction and electric measurements, similar to those performed for NBT-BT, were carried out. In the following main chapter, the methodology used to address the proposed scientific questions will be presented.

---

## 4 Methodology

---

In the following chapter, processing and characterization techniques used in the present study are described in detail. This includes processing conditions for ceramic powders and samples, electrical and structural measurements, and models used for data evaluation.

---

### 4.1 Powder Processing and Manufacturing of Dense Ceramic Samples

---

Both investigated material systems, NBT-BT and BF-BT(-NBT) were synthesized using the solid state reaction method, however, the processing conditions and some aspects of the routine were different as outlined in the respective following subchapters. An outline of the general processing route is provided in Figure 17.

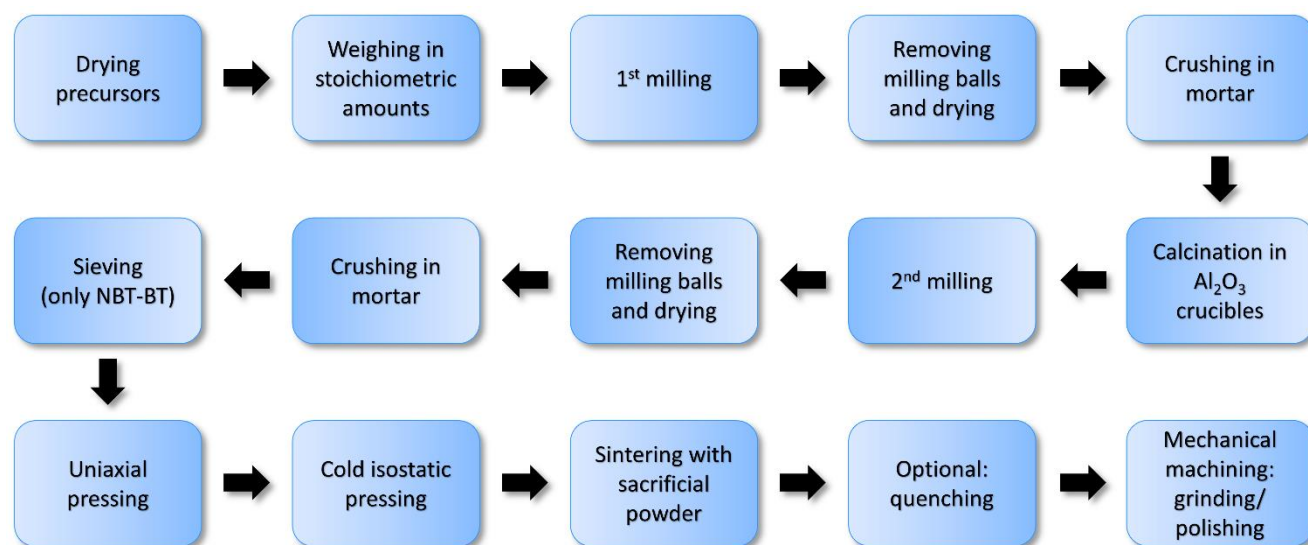


Figure 17: Used solid state reaction processing route to receive polycrystalline ceramic samples.

---

#### 4.1.1 Na<sub>1/2</sub>Bi<sub>1/2</sub>TiO<sub>3</sub>-BaTiO<sub>3</sub> Compositions

---

Ceramic powders of NBT-BT with 3, 6, 9 and 12 mol% BT (labeled as e.g. NBT-3BT for 3 mol% BT) were prepared via solid state reaction method (Figure 17). Precursor powders of Na<sub>2</sub>CO<sub>3</sub> (99.5 %), BaCO<sub>3</sub> (99.8 %), Bi<sub>2</sub>O<sub>3</sub> (99.975 %) and TiO<sub>2</sub> (99.6 %) (all Alfa Aesar, Thermo Fisher Scientific,

Kandel, Germany) were dried in a drying cabinet at 100 °C for approximately 24 h. After that, the powders were weighed in stoichiometric amounts into polyethylene containers. The precursors were mixed with a planetary ball mill at 250 rpm (revolutions per minute) using Y-stabilized ZrO<sub>2</sub> milling balls with a diameter of 3 mm, a powder-to-ball ratio of 1:5, and ethanol as milling medium for 24 h followed by removing the balls and drying. The dried and mixed powders were crushed in a mortar and calcined in Al<sub>2</sub>O<sub>3</sub> crucibles for 3 h at 900 °C with 5 K/min heating and cooling rate to induce the solid state reaction. This was followed by a second milling step with the same parameters as the first. Subsequently, the milling balls were removed from the slurry and the powders were dried, followed by sieving with a mesh size of 160 μm.

Two different geometries of dense ceramic samples were produced: cylindrical pellets and rectangular bars depending on further usage. To process pellet-shaped samples, a pressing die with 15 mm inner diameter was utilized. 0.6 g of ceramic powder was weighed in per pellet and uniaxially pressed with a force of 2 kN to form a green body. Bar-shaped samples were produced using another pressing die with inner dimensions of 38 x 5.3 mm<sup>2</sup>. The height is dictated by the amount of used powder which was 2.1 g per sample. Irrespective of the shape of the green body, an additional compaction step was implemented by cold isostatic pressing (KIP 100E, Paul-Otto Weber GmbH, Remshalden, Germany). This was done by sealing the green bodies in an industrial condom using a vacuum pump and immersing them in silicon oil, after which the samples were subjected to 382 MPa (700 kN) isostatic pressure.

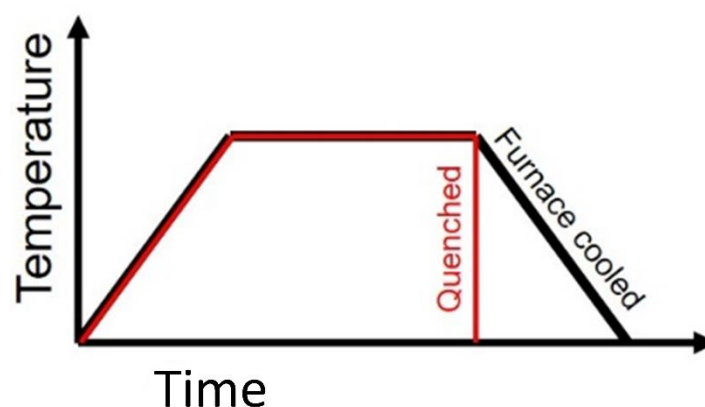


Figure 18: Schematic temperature-time curve for furnace cooled and quenched NBT-BT ceramics.

The compacted green bodies were embedded in sacrificial powder of the same composition to reduce Bi evaporation and sintered in Al<sub>2</sub>O<sub>3</sub> crucibles at 1150 °C for 3h with a heating rate of 5

---

K/min. NBT-BT samples which were slowly cooled down in the furnace are labelled as 'FC' for furnace cooled, while samples which were taken out of the furnace directly after the sintering step at 1150 °C and quickly cooled down to room temperature assisted by a conventional air fan are labelled as 'Q' for quenched (Figure 18). Both sample shapes were ground to remove the surface layers and to receive samples of desired final dimension. Typically, pellets were ground down to 0.6-0.8 mm in thickness with 11-12 mm in diameter, while bars were 3 x 4 x 30 mm<sup>3</sup> after machining.

---

#### 4.1.2 BiFeO<sub>3</sub>-BaTiO<sub>3</sub>(-Na<sub>1/2</sub>Bi<sub>1/2</sub>TiO<sub>3</sub>) Compositions

---

Ceramic BF-BT powders with compositions of 67 and 70 mol% BF and 33 and 30 mol% BT, respectively (BF-33BT and BF-30BT), were prepared via solid state reaction method. Furthermore, based on both BF-BT compositions, ternary systems were synthesized by adding the necessary raw materials for 5 mol% NBT during the weighing step. The resulting stoichiometric compositions are 63.65BF-31.35BF-5NBT and 66.5BF-28.5BT-5NBT and the materials are labelled as BF-33BT+5NBT and BF-30BT+5NBT, respectively.

The drying and weighing of the precursor powders Na<sub>2</sub>CO<sub>3</sub> (99.5%), Bi<sub>2</sub>O<sub>3</sub> (99.975%), BaCO<sub>3</sub> (99.8 %) (Alfa Aesar, Thermo Fisher Scientific, Kandel, Germany), TiO<sub>2</sub> (99.6%) and Fe<sub>2</sub>O<sub>3</sub> (99.9%) (Thermo Fisher Scientific, Kandel, Germany) was done in the same manner as for NBT-BT, but into smaller 100 ml polyethylene bottles. Y-stabilized ZrO<sub>2</sub>-balls with a diameter of 3 mm and ethanol were added before mixing and milling the precursor powders with a roller mill for 24 h. The powder-to-ball ratio was 1:2. Subsequently, the powders were dried, the balls removed and the raw materials manually crushed and further mixed in a mortar for 15 min. After that, the powders were calcined in Al<sub>2</sub>O<sub>3</sub> mortars at 830 °C for 6 h with a heating rate of 5 K/min, followed by a second milling step with the same parameters as the first one. The calcined and milled powders were dried and crushed in a mortar after the milling balls were removed.

Ceramic samples with cylindrical shape of the four BF-BT(-NBT) compositions were produced by compaction in a pressing die with an inner diameter of 10 mm and an applied uniaxial force of 4 kN. Approximately 0.44 g of powder was used per pellet. The subsequent isostatic pressing was performed as described in chapter 4.1.1 and the resulting green bodies were embedded in sacrificial powder of the same composition and sintered in alumina crucibles at 1020 °C for 3 h with a heating rate of 5 K/min followed by slow cooling in the furnace.



---

The resulting sintered ceramic pellets had a diameter of 8 to 8.5 mm and were ground to a thickness between 0.6 and 0.8 mm. An additional quenching step was applied to part of the samples by reheating the ground pellets to 800 °C with a heating rate of 10 K/min in an open alumina crucible. After a dwell time of 30 min, the samples were taken out of the furnace at high temperatures and rapidly cooled down to room temperature assisted by an air fan. Samples that underwent the additional heat treatment are labelled as 'Q' for quenched, while samples that did not undergo the quenching routine are labelled as 'FC' for furnace cooled.

---

## 4.2 Laboratory X-ray Diffraction

---

Two different setups were used for laboratory powder X-ray diffraction (XRD). The diffractometer for carrying out quick measurements with lower resolution was a Bruker D8 diffractometer (Bruker AXS, Karlsruhe, Germany) in Bragg-Brentano symmetry with Cu-K $\alpha_{1,2}$  radiation and a 2 $\theta$  step size of 0.02°. This setup was utilized to check the calcined ceramic powders for a phase-pure perovskite structure and to rule out the existence of any residual precursors. Furthermore, crushed and annealed ceramic powders of sintered pellet-shaped samples were measured to perform LeBail fits to establish the phase composition and the respective lattice parameters. Attaching a high temperature cell (Anton Paar GmbH, Graz, Österreich) to the D8 setup allowed for temperature-dependent experiments.

To receive high resolution powder XRD data of crushed and annealed pellet samples, the powders were also measured by Dr. Kathrin Hofmann with a Stadi P (Stoe & Cie. GmbH, Darmstadt, Germany) diffractometer in transmission geometry using monochromatic Cu-K $\alpha_1$  radiation. The resulting diffraction patterns were refined using the Rietveld method with evaluation software Topas V5 and V6 (Bruker AXS, Karlsruhe, Germany) to establish phase fractions and precise lattice parameters.

---

## 4.3 Microstructure

---

After grinding, pellet-shaped ceramic samples were polished in five consecutive steps using diamond paste with decreasing particle sizes of 15, 6, 3, 1 and ¼  $\mu\text{m}$  in order to perform microstructural investigations and grain size analysis using scanning electron microscopy (SEM).

NBT-BT samples were thermally etched by heating the specimens up to 1000 °C for 10 min to increase the visibility of grain boundaries. Subsequently, gold was sputtered on the sample surfaces to avoid accumulation of charge carriers during microscopy. SEM images were obtained using a Philips XL30FEG (Amsterdam, the Netherlands) in secondary electron (SE) imaging mode. Three dimensional grain sizes were calculated by establishing the average two dimensional grain size of at least 200 grains per composition and multiplying with a numerical factor of 1.56 assuming an isometric grain shape [171].

SEM analysis of BF-BT(-NBT) specimens was performed by Dr. Ann-Katrin Fetzner with a JEOL JSM 7600F microscope (JEOL, Tokyo, Japan) in the backscattered electron (BSE) mode without a previous etching step. The microscope is equipped with an X-Max80 energy-dispersive X-ray spectroscopy (EDS) detector (Oxford Instruments, Abingdon, UK) for chemical analyses.

---

#### 4.4 Density

---

The density of sintered and ground samples was established via the Archimedes method. For that, the sample mass was measured in air ( $m_{\text{air}}$ ) using a hydrostatic scale (BA110S Basic, Sartorius AG, Germany) before immersing the ceramics into distilled water in glass flasks. The flasks were put under vacuum for 20 min. Subsequently, the sample mass was measured in distilled water ( $m_{\text{water}}$ ) with known temperature and therefore known density ( $\rho_{\text{water}}$ ). This allows to calculate the absolute density  $\rho_{\text{abs}}$  of the ceramic materials using equation (10):

$$\rho_{\text{abs}} = \frac{m_{\text{air}} * (\rho_{\text{water}} - \rho_{\text{air}})}{0.99983 * (m_{\text{air}} - m_{\text{water}})} + \rho_{\text{air}} \quad (10)$$

with  $\rho_{\text{air}}$  being the density of air which is assumed to be constant at 0.0012 g/cm<sup>3</sup>. Using the theoretical density ( $\rho_{\text{theo}}$ ) of the respective material established from LeBail fitting the laboratory XRD patterns, the relative density  $\rho_{\text{rel}}$  of a ceramic sample can be calculated following equation (11):

$$\rho_{\text{rel}} = \frac{\rho_{\text{abs}}}{\rho_{\text{theo}}} \quad (11)$$

---

## 4.5 Poling and Piezoelectric Response

---

In order to perform electrical measurements and to pole ceramic samples, applying electrodes is necessary. For that, ground cylindrical pellets of NBT-BT or BF-BT(-NBT) composition were sputtered with silver or platinum, respectively, on top and bottom surfaces forming a plate capacitor with the ceramic acting as the dielectric. The sides of the samples were ground with grinding paper to remove the electrode material there. After that, the samples were annealed at 400 °C for 30 min with a 5 K/min heating rate in a box furnace to relieve the mechanical stresses introduced by grinding and sputtering.

Poling was performed by immersing the sputtered samples into a silicon oil bath and by applying a DC bias field of 6 and 4 kV/mm on NBT-BT and BF-BT(-NBT) materials, respectively, for 20 min at 30 °C. The piezoelectric coefficient  $d_{33}$  was measured on poled pellet-shaped samples with a Berlincourt meter (Piezotest PM300, Singapore) by applying a static force of 2 N and a superimposing oscillating load of 0.25 N with a frequency of 110 Hz.

---

## 4.6 Dielectric Analysis

---

Temperature- and frequency-dependent capacitance  $C_p$  and dielectric loss were measured on electroded, poled and unpoled pellet-shaped samples of all investigated compositions using an impedance analyzer (4192A LF, Hewlett-Packard, CA, USA) with an applied voltage of 1 V. For temperature-dependent measurements, the temperature ranged from room temperature to 500 °C and 650 °C for NBT-BT and BF-BT(-NBT) materials, respectively, while the frequencies ranged from 100 Hz to 1 MHz. Due to the plate capacitor-like sample shape, the dielectric permittivity of the ceramic material can be calculated from the capacitance and the sample geometry following equation (12):

$$\varepsilon' = \frac{C_p * t}{A * \varepsilon_0} \quad (12)$$

with  $t$  being the sample thickness and  $A$  the electrode area. The imaginary part of permittivity can be calculated by multiplying the real part of permittivity with the measured loss tangent,  $\tan \delta$ , as given in equation (13):

$$\varepsilon'' = \varepsilon' * \tan \delta \quad (13)$$

---

## 4.7 Ferroelectric Polarization and Strain Analysis

---

Polarization and strain hysteresis were measured as a function of electric field on electroded cylindrical samples using a modified Sawyer-Tower circuit with a reference capacitor of 10  $\mu\text{C}$  in combination with an optical displacement sensor (D63, Philtec Inc., USA). The electric field was applied with a triangular wave form, a frequency of either 1 or 3 Hz and a field-amplitude of 6 or 8 kV/mm depending on the material. A high voltage amplifier (20/20C, Trek, USA) served as the DC source.

To correlate the calculated strain from electric field-dependent synchrotron measurements described in detail in chapter 4.9 with the macroscopic strain, the latter was measured using the described setup but with step-wise applied electric field. The step size in field amplitude and holding time per step were kept the same as during the synchrotron measurements described in chapter 4.9.

---

## 4.8 Temperature-dependent Young's Modulus and Composite Model

---

A resonance frequency damping analyzer (RFDA-HT1750, IMCE, Genk, Belgium) was used to establish Young's modulus of NBT-BT as a function of temperature with the impulse excitation technique. Bar-shaped samples with a geometry of 3 x 4 x 30 mm<sup>3</sup> were placed in a Ni-wire suspension within a furnace (Figure 19). The wire placement depends on the sample length and needs to be exactly at the nodes of the standing resonance wave of the oscillating sample to not hinder oscillation. A mechanical excitation was caused by hitting the sample lightly with a cylindrical Al<sub>2</sub>O<sub>3</sub> rod on the large face center. The resulting acoustic signal traveled through a tube and was recorded with a microphone placed above the furnace. Sample excitation and recording of the acoustic signal was performed in 30 s intervals. The resonance frequency  $f_R$  was calculated from the acoustic signal via Fast Fourier Transformation by the software provided by the manufacturer. The measurement temperature ranged from room temperature to 800 °C with a heating and cooling rate of 2 K/min and controlled by a thermocouple placed in close proximity to the sample within an Al<sub>2</sub>O<sub>3</sub> ceramic of similar shape and dimension as the measured samples. Only the data from heating curves was used for further evaluation.

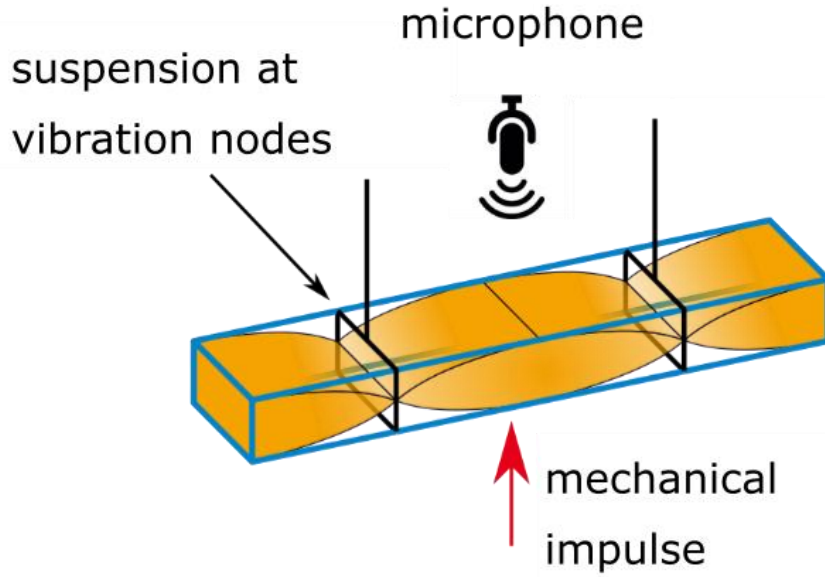


Figure 19: Bar-shaped sample placed in a Ni-wire suspension to measure the resonance frequency with the impulse excitation technique. The elastic mechanical impulse results in an oscillating sample and an acoustic signal which is recorded by a microphone (reprinted in modified form from [172]).

Knowing the sample's mass ( $m$ ), geometry, Poisson's ratio ( $\nu$ ), and resonance frequency ( $f_R$ ) allows calculation of the Young's modulus  $Y$  according to ASTM E1876-99 [173] using equation (14):

$$Y = 0.9465 * \left( \frac{m * l^3 * f_R^2}{b * t^3} \right) * \Psi_f \quad (14)$$

where  $l$  is the sample length,  $b$  is the width,  $t$  is the thickness and  $\Psi_f$  is a correction factor to compensate for flexural vibration and the finite sample thickness.  $\Psi_f$  depends on the sample geometry and the material's Poisson's ratio  $\nu$  and can be calculated with equation (15):

$$\Psi_f = 1 + 6.585(1 + 0.0752\nu + 0.8109\nu^2) \left( \frac{t}{l} \right)^2 - 0.868 \left( \frac{t}{l} \right)^4 - \left[ \frac{8.340(1 + 0.2023\nu + 2.173\nu^2) \left( \frac{t}{l} \right)^4}{1 + 6.338(1 + 0.1408\nu + 1.536\nu^2) \left( \frac{t}{l} \right)^2} \right] \quad (15)$$

For  $\nu$ , a value of 0.27 was taken for all compositions [174]. Due to the sensitivity of the mechanical properties of a polycrystalline ceramic material to the structural changes even on a nanoscale, the temperature-dependent Young's modulus can be utilized to calculate volume fractions of the phases of a two-phase system with known  $Y$ . The assumed two-phase model consists of a

homogeneous matrix phase with spherical inclusions as the second phase, which represents the cubic matrix with polar tetragonal inclusions (PNRs) of a relaxor material as described by the dipolar glass model in chapter 2.4.2.

To be able to calculate the volume fractions of the two phases following a composite model by Weng [175], the temperature-dependent Young's moduli of the cubic phase and the tetragonal phase,  $Y_{\text{cub}}(T)$  and  $Y_{\text{tet}}(T)$ , respectively, need to be established. Both phases are assumed to show a linear decrease with increasing temperature for their respective  $Y$  [176]. In Figure 20, a representative curve for  $Y$  as a function of temperature is displayed, measured for a NBT-12BT FC ceramic. In the low temperature region, where  $Y$  decreases linearly with increasing temperature, the material is assumed to be entirely tetragonal (Figure 20a). Therefore, fitting this temperature interval with a linear function allows to establish  $Y_{\text{tet}}(T)$ . The reported symmetry for NBT-12BT around room temperature is  $P4mm$ , while for the PNRs at elevated temperatures it is  $P4bm$  for all investigated compositions [8, 70]. However, the expected differences in  $Y$  between  $P4mm$  and  $P4bm$  phases are assumed to be negligible, especially in contrast to  $Y$  of the cubic phase [83, 172].  $Y_{\text{cub}}(T)$  was determined for each investigated composition independently in a similar manner by fitting the linear regime at very high temperatures above  $T_B$ , also with a linear function (Figure 20c).

In the mentioned composite model of a matrix material with spherical inclusions [175], the overall bulk modulus of the composite material  $\kappa$  is given as:

$$\kappa = \kappa_M + \frac{\kappa_M c_I}{\frac{3c_M \kappa_M}{3\kappa_M + 4\mu_M} + \frac{\kappa_M}{\kappa_I - \kappa_M}} \quad (16)$$

where  $c_i$  is the volume fraction,  $\kappa_i$  is the bulk modulus and  $\mu_i$  is the shear modulus of the respective phase, indexed with M and I for matrix and inclusions, respectively. Adding up  $c_I$  and  $c_M$  equals 1. Bulk and shear moduli are coupled to  $Y$  and  $\nu$  and can be calculated using equations (17) and (18):

$$\kappa = \frac{Y}{3(1 - 2\nu)} \quad (17)$$

$$\mu = \frac{Y}{2(1 + \nu)} \quad (18)$$

These relations together with the measured  $Y(T)$  and established  $Y_{\text{cub}}(T)$  and  $Y_{\text{tet}}(T)$  allow to calculate the volume fraction of spherical inclusions  $c_i$ , here assumed to be tetragonal PNRs, for NBT-BT compositions.

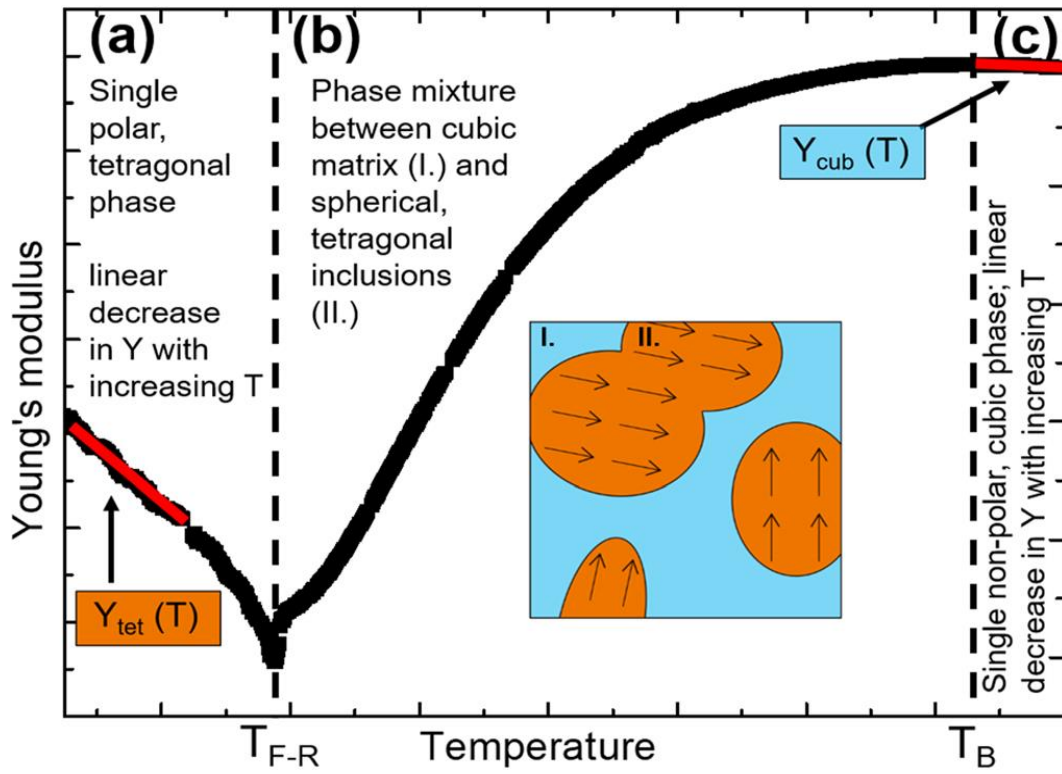


Figure 20: Representative evolution of Young's modulus as a function of temperature here shown from a measurement of NBT-12BT FC. Simplistically, the material undergoes a transition from ferroelectric tetragonal to relaxor with tetragonal polar regions within a cubic matrix at  $T_{F-R}$  and to a paraelectric, entirely cubic state at  $T_B$  upon heating. Reprinted from [177].

---

## 4.9 Synchrotron X-ray Diffraction

---

Synchrotron X-ray diffraction measurements were carried out at two different synchrotrons, namely the Advanced Photon Source (APS) in Lemont, Illinois, USA and the Deutsche Elektronen-Synchrotron (DESY) in Hamburg, Germany. *Ex situ* single shot measurements on poled and unpoled NBT-BT ceramics were carried out at DESY as well as *in situ* electric field-dependent measurements on NBT-3BT FC. Also at the APS, *in situ* electric field-dependent studies were conducted on NBT-6BT and NBT-9BT. Detailed experimental parameters, the respective measurement setups and data processing steps are explained in the following.

---

### 4.9.1 Deutsches Elektronen-Synchrotron

---

The synchrotron X-ray diffraction measurements at DESY were conducted on beamline P02.1 with an incident beam energy of about 59.8 keV corresponding to a wavelength of 0.20718 Å. A 2D 16-in. XRD 1621N ES Series PerkinElmer detector with a resolution of 2048 x 2048 pixels, a pixel size of 200 μm<sup>2</sup> and a sample detector distance of 2180 mm was used to receive two-dimensional diffraction patterns. The beam was focused at one corner of the 2D-detector to maximize the resulting 2θ resolution. Single-shot measurements were performed under ambient conditions on unpoled and poled NBT-BT ceramics with 3, 6, 9 and 12 mol% BT in transmission geometry. The samples were bar-shaped with dimensions of 0.8 x 1 x 7 mm<sup>3</sup> with Ag-electrodes sputtered on the opposing large surfaces with 1 x 7 mm<sup>2</sup> dimensions. Poling was carried out as described for NBT-BT materials in chapter 4.5 about one week prior to the beam time. The poled bars were placed with the poling direction perpendicular to the transmitting beam and parallel to the plate detector as schematically displayed in Figure 21. This allows to collect 2D diffraction patterns which display the poling-induced anisotropy in the sample. In some cases, the X-ray beam also hit the electrode material leading to additional reflections in the diffraction pattern characteristic for elementary silver with cubic  $Fm\bar{3}m$  space group.

Furthermore, *in situ* electric field-dependent measurements were carried out on NBT-3BT FC and NBT-3BT Q with the same experimental setup. For that, the bar-shaped samples were placed in a plastic holder which allows immersing the sample in silicon oil to avoid electrical flashover. Wires were connected to the sputtered electrodes with conductive silver paint to allow for the application of a DC current with a high voltage amplifier. The electric field was applied stepwise



with a step size of 0.14 kV/mm, a holding time per step of 30 s and a maximum field amplitude of about 4.3 kV/mm. The original goal was to apply higher fields, but frequent sample breakdown rendered this impossible. Nevertheless, the measurement was successful and the acquired data meaningful, since the applied field was sufficient to induce the intended electric field response. The data processing was performed as described in chapter 4.9.3. A diffraction pattern of a LaB<sub>6</sub> NIST standard was recorded as reference.

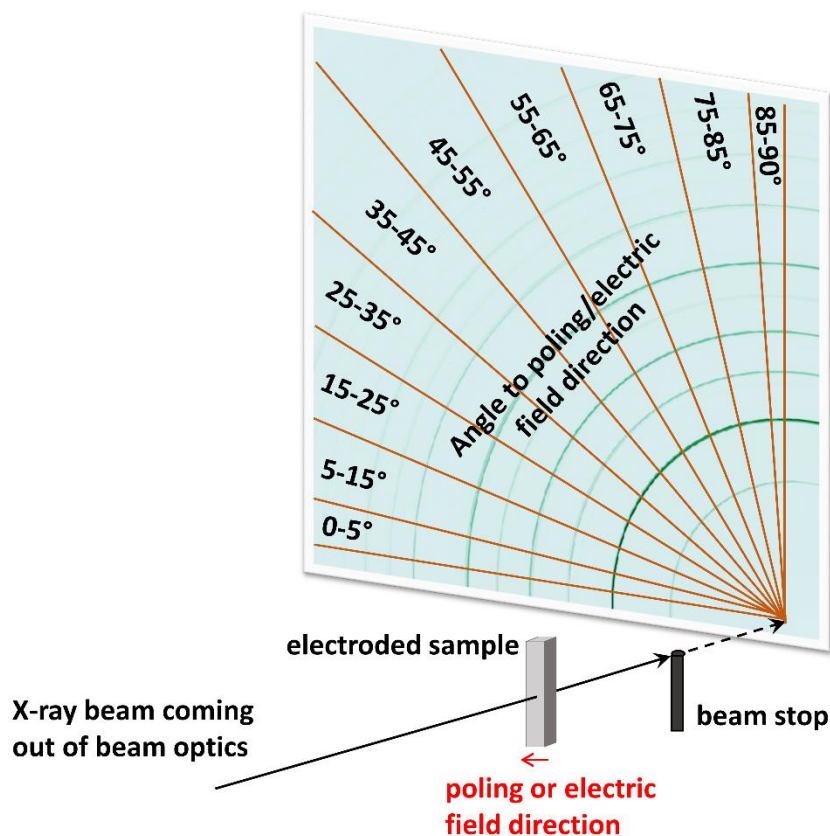


Figure 21: Schematic synchrotron measurement setup for poled samples and *in situ* electric field-dependent measurements as used for diffraction experiments at DESY.

#### 4.9.2 Advanced Photon Source

Furthermore, *in situ* electric field-dependent synchrotron X-ray diffraction experiments were conducted at the 11-ID-C beam line of the Advanced Photon source (APS, Argonne National Laboratory) on NBT-6BT and NBT-9BT furnace cooled and quenched specimens. The wavelength of the incident beam was 0.1173 Å which corresponds to 105.7 keV with a beam size of 0.5 x 0.5

---

mm<sup>2</sup>. The experimental setup was similar to the one used at DESY as depicted in Figure 21, however, the beam was focused at the middle of the PerkinElmer 2D detector with a sample-detector-distance of 2322 mm, resulting in the detection of complete Debye-Scherrer rings, but also in a lower  $2\theta$  resolution. An electric field was applied step-wise to the electroded bar-shaped samples of  $1 \times 1 \times 6.7$  mm<sup>3</sup> with a step size of 0.5 kV/mm, a holding time of 30 s per step and a maximum field amplitude of 6 kV/mm. CeO<sub>2</sub> powder was used as reference material.

---

### 4.9.3 Processing of Synchrotron X-ray Diffraction Data

---

The recorded 2D diffraction patterns from both synchrotrons were divided into 10 sectors and integrated into 1D patterns using DAWN software version 2.15.0 [178]. Each sector ranges over 10° azimuthal angle ( $\Psi$ ) with respect to the poling or *in situ* electric field direction with  $\Psi = 0^\circ$  being parallel to the field and  $\Psi = 90^\circ$  being perpendicular. 2D patterns of DESY single-shot experiments on unpoled samples were integrated from 0 to 90° azimuthal angle, since the material is isotropic, and therefore does not show any angle-dependence in crystal structure in the unpoled state. For the measurements on poled samples, the sectors close-to-parallel and close-to-perpendicular to the field were integrated over 5° azimuthal angle each, from 0 - 5° and from 85 - 90° and referred to as  $\Psi = 2.5^\circ$  and  $\Psi = 87.5^\circ$ , respectively (Figure 21). For the APS measurements, the equivalent sectors were integrated from -5 - 5° and from 85 - 95° and labelled as  $\Psi = 0^\circ$  and  $\Psi = 90^\circ$ , respectively. The sectors between the two extrema were integrated over 5 - 15°, 15 - 25°, etc. and referred to as  $\Psi = 10^\circ$ ,  $\Psi = 20^\circ$  and so forth. Only the first quadrant of the whole ring patterns recorded at APS was used for integration, since the four quadrants are symmetrical, and therefore carry identical information.

The angle-dependent 1D patterns were further evaluated as described in chapters 5.1.3 and 5.3 using OriginPro 2022 for individual peak fitting and Topas V5 and V6 for LeBail fitting and full pattern Rietveld refinements. Individual peak fitting was performed by selecting the respective region of the diffraction patterns and using the 'Multiple Peak Fit' tool with a PseudoVoigt function. Since the diffraction patterns of poled NBT-BT compositions show a strong angle-dependent anisotropy, defining a close to untextured reference state is necessary to refine the patterns without having to use a model to compensate for the anisotropy. This was achieved by weighting the individual azimuthal sectors of the respective patterns with a geometrically necessary weighting factor and summing up the sectors following equation (19) [179]:

---

$$\langle I' \rangle = \sum_{\alpha=0^{\circ}}^{90^{\circ}} I(\alpha) [\cos(\alpha_i) - \cos(\alpha_j)] \quad (19)$$

where  $I'$  is the intensity of the resulting weighted pattern,  $I$  is the intensity of the pattern of the respective azimuthal sector and  $\alpha_i$  and  $\alpha_j$  are the low and high boundaries of the respective azimuthal range.

---

## 5 Results and Discussion

---

The results and discussion part of this thesis is divided into four main chapters each containing individual subchapters. The first three main chapters are focused on the quenching-induced changes in NBT-BT, while in the fourth and last chapter the influence of introducing NBT into BF-BT and subsequent quenching are elucidated.

---

### 5.1 Effect of Quenching on the Structural and Ferroelectric Properties of NBT-BT

---

This chapter focuses on the changes in the structural and ferroelectric properties of NBT-BT upon quenching. Part of the here presented findings are published in Open Ceramics [180], while another publication is currently under preparation. The evaluation of unpoled and poled synchrotron diffraction data discussed in subchapter 5.1.3 was partly done by Julius Körner for his Advanced Research Lab project.

---

#### 5.1.1 Introduction and Motivation

---

Quenching NBT-BT is known to effect the structural characteristics of the material as it increases the lattice distortion from the pseudo-cubic reference frame [12, 13, 87] and promotes an enhanced off-centering of the  $\text{Bi}^{3+}$ -ion [149]. Even though, several recent publications confirmed the quenching-induced strengthening of lattice distortion also for doped materials [151], neither a study on a wider composition range on pure quenched NBT-BT, nor a study revealing the change in phase fractions upon quenching in the unpoled and poled state has been conducted so far.

Therefore, NBT-BT compositions with 3, 6, 9 and 12 mol% BT were synthesized and investigated, putting special emphasize on the structural changes upon quenching. Preliminary low resolution laboratory XRD on crushed and annealed ceramics, carried out at the very start of this project reveal a quenching-induced increase in the rhombohedral lattice distortion in NBT-3BT and in tetragonal distortion in NBT-9BT and NBT-12BT, as apparent from the shift in the  $111_R$  and  $002_T$  reflections, respectively (Figure 22). These results were fitting to the literature and encouraging to do an in-depth structural investigation on the processed compositions.

Furthermore, a thorough composition-dependent description of the alteration of ferroelectric behavior upon quenching NBT-BT has been missing in literature. Therefore, both the structural and ferroelectric studies are combined with the evolution of piezoelectric properties to deepen the understanding of quenching-induced changes in NBT-BT and form the first results and discussion chapter of this thesis.

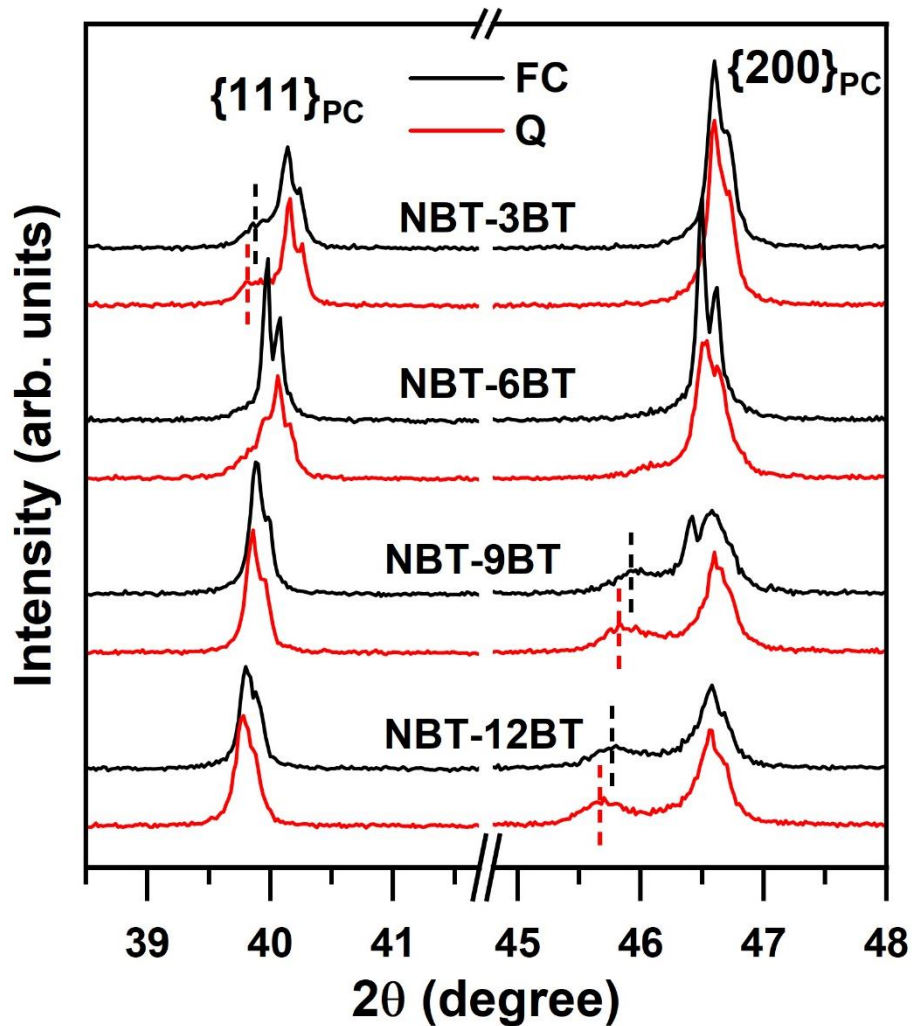


Figure 22: Sections of powder XRD patterns showing the  $\{111\}_{PC}$  and  $\{200\}_{PC}$  reflections of crushed and annealed furnace cooled (black) and quenched (red) NBT-BT ceramics. The dashed vertical lines indicate the approximate position of the  $111_R$  in NBT-3BT and  $002_T$  reflections in NBT-9BT and NBT-12BT.

## 5.1.2 Structural Characteristics of Ceramic Powders

*X-ray diffraction is a valuable tool in the characterization of ferroelectric ceramics – to ensure successful synthesis during powder processing but also to establish the structural properties of sintered ceramics. To this end, XRD was utilized in combination with Rietveld refinement to prove a change in phase composition and an increase in lattice distortion upon quenching.*

Laboratory X-ray diffraction experiments were performed on calcined ceramic powder which was crushed in a mortar. The measurements were carried out as described in chapter 4.2 using a Bruker D8 diffractometer and were conducted to make sure that the solid state synthesis during calcination was successful. All synthesized compositions of NBT-BT show a phase pure perovskite structure as evident from the typical reflections for perovskite materials in the diffraction patterns displayed in Figure 23. This proves the success of the calcination step. Therefore, the powders were used for sintering dense ceramics.

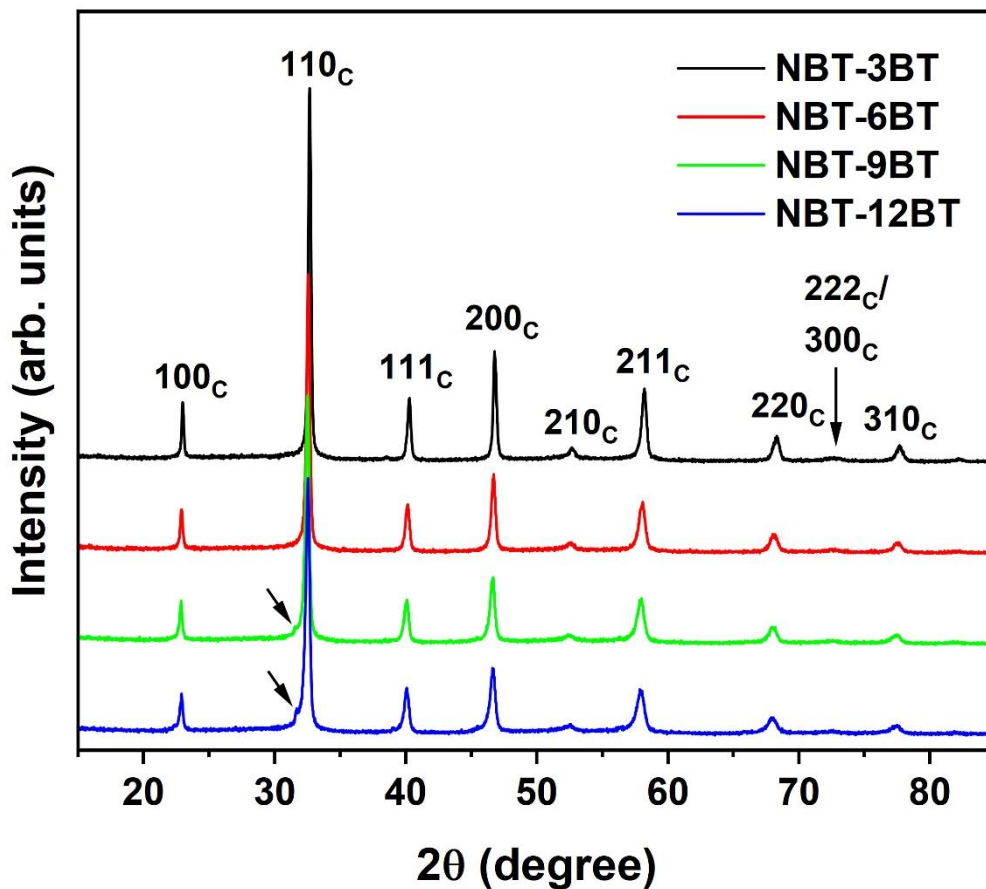


Figure 23: Powder XRD patterns of calcined and crushed NBT-BT. The characteristic perovskite reflections are indexed with respect to a cubic reference frame. The arrows indicate additional reflections due to Tungsten  $K\alpha$ -radiation caused by impurities in the anode material of the diffractometer.

---

To receive high resolution structural data for Rietveld refinement, XRD patterns were collected in transmission geometry with monochromatic Cu  $K\alpha_1$ -radiation on crushed and annealed sintered ceramics (Figure 24a). All the materials feature a phase pure perovskite structure. The diffraction patterns of both NBT-3BT FC and NBT-3BT Q show a clear splitting in the  $\{111\}_{PC}$  reflection, indicating a rhombohedral distortion in the material with the splitting being more pronounced in the quenched sample (Figure 24b). The superlattice reflection (SR) around  $2\theta = 38.3^\circ$  is characteristic for the presence of  $R3c$  phase, since it is related to the doubling of the unit cell due to anti-phase octahedral tilting [57, 181]. The  $\{200\}_{PC}$  reflection of the NBT-3BT materials is symmetrical without any signs of splitting (Figure 24c). The MPB composition NBT-6BT exhibits a small shoulder in the  $\{111\}_{PC}$  reflection indicating a small deviation from the otherwise pseudo-cubic state. Upon quenching, this shoulder gets more pronounced, indicating an increase in the rhombohedral distortion and together with the slightly visible SR, hinting towards an increased rhombohedral phase fraction. Furthermore, an asymmetry and an additional reflection ( $002_T$ ) at the low  $2\theta$  side of the  $\{200\}_{PC}$  reflection is visible for NBT-6BT Q. Since the  $\{200\}_{PC}$  reflection of NBT-6BT FC does not show these features, quenching seems to facilitate the formation of a long-range tetragonal phase detectable with XRD. NBT-9BT and NBT-12BT show similar characteristics in the diffraction patterns. Both materials have a symmetrical singlet as  $\{111\}_{PC}$  reflection and a clearly split  $\{200\}_{PC}$  reflection into  $002_T$  at lower and  $200_T$  at higher  $2\theta$  angles (Figure 24c). For both materials, quenching increases the tetragonal distortion as apparent from the slight shift in peak position of the  $002_T$  and  $200_T$  reflections.

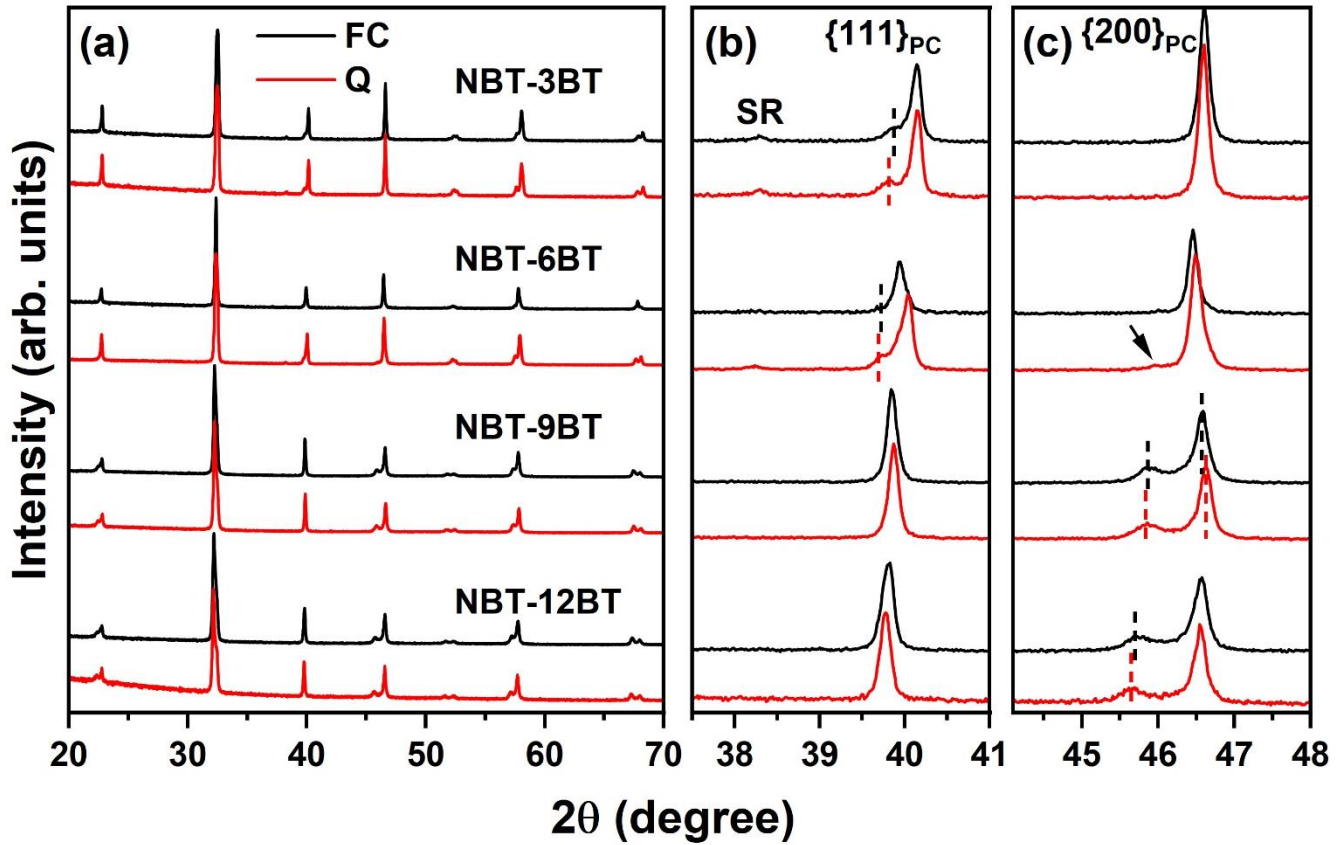


Figure 24: (a) X-ray powder diffraction patterns of furnace cooled and quenched NBT-BT compositions. (b) Enlarged section of the XRD patterns showing the  $\{111\}_{PC}$  reflections. "SR" marks superlattice reflections visible in NBT-3BT and vaguely in NBT-6BT materials. (c) Enlarged sections displaying the  $\{200\}_{PC}$  reflections. Dashed vertical lines indicate the position of relevant peaks.

To enable quantitative statements about the phase assemblage and the crystallographic properties of the respective phases of each material, full-pattern Rietveld refinements were carried out on the XRD patterns using Topas V6. The used structural models were  $R3c$  and  $Pm\bar{3}m$  for NBT-3BT FC and NBT-3BT Q, which is in accordance with literature [181]. Refining with a single-phase rhombohedral model was attempted but did not lead to satisfactory results. An example for a refined pattern, here NBT-3BT FC, is provided in Figure 25. For NBT-6BT FC, the same two-phase model was used while, NBT-6BT Q was refined with  $R3c$  and tetragonal  $P4mm$  phases to account for the tetragonal distortion visible in the diffraction pattern. XRD data does not allow to distinguish between  $P4bm$  and  $P4mm$  phases, since the superlattice reflection caused by the in-phase octahedral tilting in  $P4bm$  is too weak to be observed in conventional laboratory scale XRD. Therefore,  $P4mm$  space group was used for refinement of the tetragonal phase in all NBT-BT compositions exhibiting tetragonal distortion. Both NBT-9BT and NBT-12BT compositions (FC and Q) were refined with a two-phase model of  $P4mm$  and a weakly distorted rhombohedral  $R3m$  phase [67], even though no splitting of the  $\{111\}_{PC}$  reflection can be observed in the respective



diffraction patterns. However, the presence of a rhombohedral phase in these materials was proven by TEM [180].

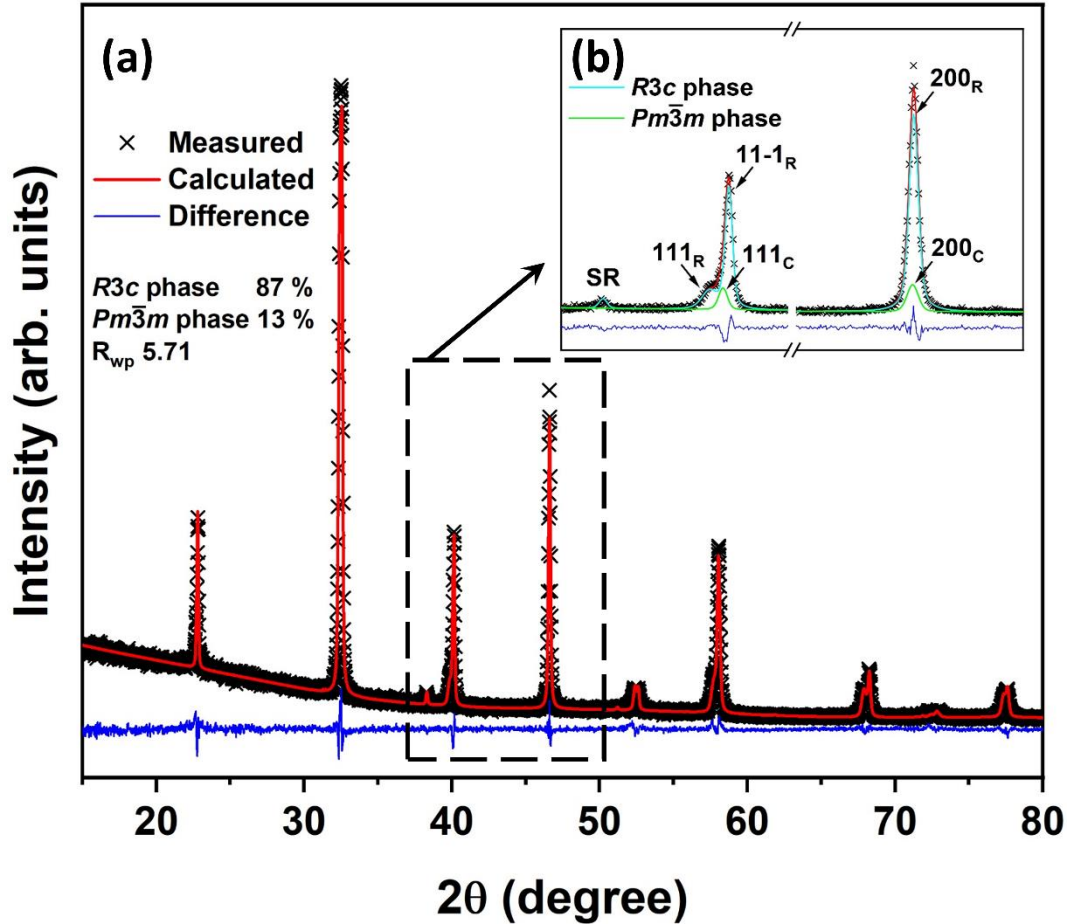


Figure 25: Rietveld refinement of NBT-3BT FC with (a) showing the whole measured XRD pattern, the calculated curve and the difference. The inlay (b) displays the  $\{111\}_{PC}$  and  $\{200\}_{PC}$  reflections with the respective phase contributions.

In Table 2, the phase fractions and lattice parameters with the distortions from the pseudo-cubic state, given as  $90^\circ - \alpha_{\text{rhom}}$  and  $c_{\text{tet}}/a_{\text{tet}} - 1$  for rhombohedral and tetragonal phases, respectively, are listed. As reported in literature [12, 13, 87], quenching enhances the lattice distortion in rhombohedral and tetragonal phases. In NBT-3BT Q, the rhombohedral phase fraction increases from 87 to 91 % upon quenching at the expense of the cubic phase. The effect of quenching on the phase composition is strongest at the MPB. NBT-6BT is transformed from a two-phase system of rhombohedral (32 %) and dominant (pseudo-)cubic symmetry (68 %) to coexisting rhombohedral and tetragonal phases with 68 and 32 %, respectively. NBT-9BT and NBT-12BT exhibit nearly no changes in phase fractions. However, in both materials the distortion of the

dominant  $P4mm$  phase increases similarly from 1.41 to 1.57 % and from 1.67 to 1.82 %, respectively.

Table 2: Refined structural parameters of the high resolution powder XRD data of NBT-BT compositions. The errors given by the refinement software are about 2 % in phase fractions and for the other reported values significantly smaller than the last given digit. C, R and T stand for cubic, rhombohedral and tetragonal, respectively, while  $\eta_{tet}$  describes the tetragonal distortion calculated as  $c_{tet}/a_{tet} - 1$ .  $R_{wp}$  denotes the goodness of fit with lower values indicating less difference between measured and calculated curve.

Material	<i>C-phase</i> /%	<i>R-phase</i> /%	<i>T-phase</i> /%	$a_{cubic}$ /Å	$a_{rhomb}$ /Å	$90^\circ$ - $\alpha_{rhomb}$	$a_{tet}$ /Å	$c_{tet}$ /Å	$\eta_{tet}$ /%	$R_{wp}$
NBT-3BT FC	13	87		3.894	3.892	0.29				5.71
NBT-3BT Q	9	91		3.894	3.893	0.33				5.71
NBT-6BT FC	68	32		3.903	3.903	0.32				6.40
NBT-6BT Q		68	32		3.902	0.33	3.896	3.918	0.56	5.79
NBT-9BT FC		17	83		3.910	0.01	3.895	3.950	1.41	4.96
NBT-9BT Q		16	84		3.909	0.03	3.891	3.952	1.57	5.33
NBT- 12BT FC		16	84		3.914	0.01	3.895	3.960	1.67	5.68
NBT- 12BT Q		13	87		3.916	0.15	3.896	3.967	1.82	4.88

These findings on structural changes in NBT-BT compositions from different regions of the phase diagram (rhombohedral symmetry, MPB and tetragonal symmetry) can be rationalized by the stabilized ferroelectric order upon quenching [13]. The increased fractions of phases with non-cubic symmetry can be interpreted as a larger volume of the material exhibiting a long-range order with a homogeneously distorted symmetry possible to be detected with XRD. This stands in

---

contrast to the short-range order of PNRs, characteristic for relaxors which reflect as a (pseudo-)cubic state in the XRD pattern due to the detection limit of XRD. Therefore, it is plausible to assume that quenching eases the formation of long-range ferroelectric domains, reflecting in an increased phase fraction of rhombohedral and tetragonal phases, depending on the composition.

---

### 5.1.3 Structural Characteristics of Unpoled and Poled Bulk Ceramics

---

*Especially for relaxor materials, the structural properties vary strongly between the unpoled and the poled state. To probe, visualize and quantify the differences, synchrotron X-ray diffraction experiments were carried out on unpoled and poled NBT-BT bulk ceramics, revealing similar phase composition but an enhanced lattice distortion upon quenching in the poled state.*

In Figure 26, the 1D diffraction patterns of unpoled NBT-BT bulk samples, obtained by integrating the 2D from 0 to 90° azimuthal angle, are displayed. Comparing Figure 24 with Figure 26, it becomes apparent that the structural characteristics and the effect of quenching on NBT-BT powder and bulk material are mostly similar. In NBT-3BT, the rhombohedral distortion increases upon quenching, while NBT-6BT only exhibits splitting of the  $\{111\}_{PC}$  reflection in the quenched material (Figure 26b). The XRD pattern of NBT-6BT FC does not feature asymmetry in any reflection, and therefore a (pseudo-)cubic state is assumed. The  $\{200\}_{PC}$  reflection of NBT-6BT Q is broadened hinting towards the presence of a small amount and/or weakly distorted tetragonal phase.

A major difference between powder and bulk, however, is visible for NBT-9BT FC. Its powder XRD pattern (Figure 24c) indicates a clear tetragonal distortion from the splitting of the  $\{200\}_{PC}$  reflection into  $002_T$  and  $200_T$  reflections. This is absent in the bulk, where the  $\{200\}_{PC}$  reflection of NBT-9BT FC is asymmetric with a shoulder towards high  $2\theta$  values, but not clearly split. This suggests a more pseudo-cubic, relaxor state of the material as bulk and more ferroelectric as powder. NBT-9BT Q, on the other hand, has similar structural properties irrespective of powder or bulk. The same is true for NBT-12BT FC and NBT-12BT Q. Also here, quenching enhances the tetragonal distortion also when probing the bulk (Figure 26c).

For the Rietveld refinements of the unpoled NBT-BT bulk diffraction pattern, the same phases for the respective compositions were used as for the powder materials with the exception of NBT-6BT. NBT-6BT FC was refined with a single-phase cubic  $Pm\bar{3}m$  model, since the diffraction pattern did not provide any evidence for the presence of a lower-symmetry phase. Refining NBT-6BT Q

with a two-phase model of  $R3c$  and  $P4mm$  was attempted but did not lead to satisfactory results. Therefore, a three-phase model also including  $Pm\bar{3}m$  was successfully utilized.

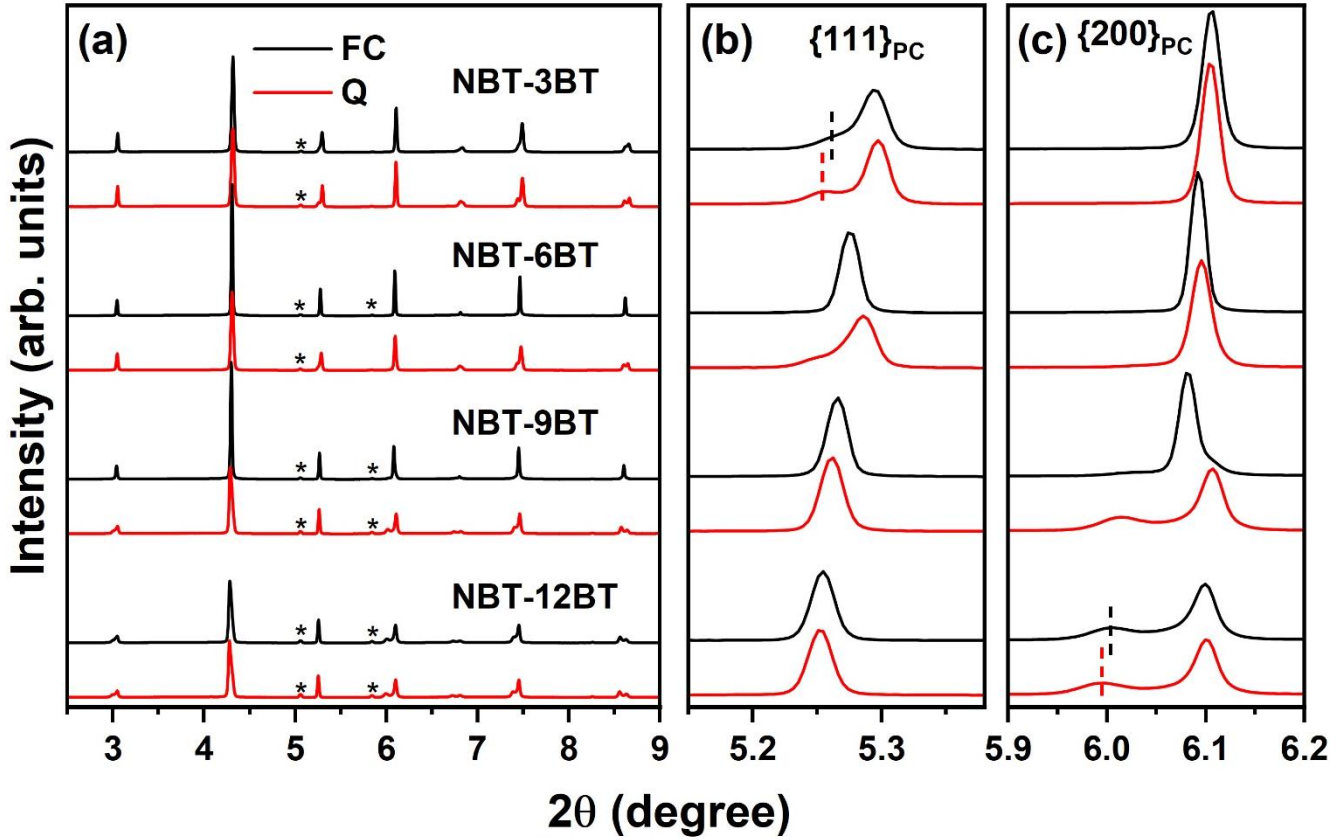


Figure 26: (a) Synchrotron XRD patterns of furnace cooled and quenched NBT-BT bulk ceramics in the unpoled state with enlarged sections of the XRD patterns showing the  $\{111\}_{PC}$  (b) and  $\{200\}_{PC}$  (c) reflections. The asterisks mark contributions from the Ag electrodes.

The resulting structural parameters and phase fractions of the refinements of unpoled samples are listed in Table 3. As expected from the qualitative description, quenching increases the lattice distortion of rhombohedral  $R3c$  and tetragonal  $P4mm$  phases also in the bulk material, however, the distortions, quantified as  $90^\circ - \alpha_{\text{rhom}}$  and  $c_{\text{tet}}/a_{\text{tet}} - 1$ , are more pronounced in the powder material, with the exception of the  $P4mm$  phase in NBT-6BT Q. Stronger distortions from the ideal cubic symmetry are expected close to the surface of a bulk material as well as in powder due to the existence of skin layers in perovskite (relaxor) ferroelectrics most likely caused by the combined effects of oxygen vacancies and a plane stress condition at the material's surface [182]. The fact that the tetragonal phase in NBT-6BT shows a higher distortion in the bulk is probably connected to the usage of a three-phase model and a lower phase fraction of  $P4mm$  in the bulk (11 %) compared to powder (32 %). This allows for an improved positioning of the  $002_{\text{T}}$  and  $200_{\text{T}}$

reflections to precisely model the sides of the  $\{200\}_{PC}$  reflection resulting in a larger difference in  $2\theta$  position of  $002_T$  and  $200_T$ , and therefore an enhanced distortion. The striking differences between the powder and bulk diffraction patterns of NBT-9BT also reflect in the difference in phase fractions of  $R3m$  and  $P4mm$ . In the bulk, the weakly distorted rhombohedral phase is the dominant one. However, this might not represent the phase composition on a nanometer scale but accounts for the suppression of long-range ferroelectric domains in the NBT-9BT FC bulk material, as mentioned earlier. For NBT-9BT Q, NBT-12BT FC and NBT-12BT Q, refinements lead to similar structural characteristics for unpoled bulk compared to powder material.

Table 3: Refined structural parameters of unpoled NBT-BT compositions based on synchrotron XRD measurements. The errors given by the refinement software are about 1 % in phase fractions and for the other reported values significantly smaller than the last given digit.

Material	<i>C-phase</i> /%	<i>R-phase</i> /%	<i>T-phase</i> /%	$a_{cubic}$ /Å	$a_{rhom}$ /Å	$90^\circ$ - $\alpha_{rhom}$	$a_{tet}$ /Å	$c_{tet}$ /Å	$\eta_{tet}$ /%	$R_{wp}$
NBT-3BT FC	17	83		3.894	3.894	0.27				6.53
NBT-3BT Q	9	91		3.894	3.894	0.32				7.88
NBT-6BT FC	100			3.903						7.35
NBT-6BT O	31	58	11	3.901	3.901	0.33	3.892	3.935	1.09	4.04
NBT-9BT FC		65	35		3.910	-0.01	3.898	3.937	1.02	6.61
NBT-9BT O		16	84		3.910	0.03	3.892	3.953	1.55	6.52
NBT- 12BT FC		14	86		3.916	0.02	3.898	3.958	1.55	6.40
NBT- 12BT O		12	88		3.914	-0.03	3.896	3.964	1.74	6.50

In addition to the investigation on unpoled bulk ceramics, diffraction patterns of poled ceramics were collected and evaluated. Full pattern Rietveld refinements were carried out to determine the phase composition and respective lattice parameters of all investigated poled NBT-BT

compositions. For that, the whole 2D azimuthal angle-dependent patterns were weighted and summed up to receive an averaged 1D pattern for each material in the poled state to receive close to untextured 1D XRD reference patterns following equation (19) as described in chapter 4.9.3. This is necessary, since the poled samples are anisotropic, resulting in azimuthal angle-dependent differences in peak intensity and peak position as discussed in detail later in this chapter. The resulting weighted patterns are displayed in Figure 27. The quenching-induced differences in the diffraction patterns in the close to untextured poled state are less prominent compared to the unpoled state. When looking at the  $\{111\}_{PC}$  and  $\{200\}_{PC}$  reflections (Figure 27b and c), a more pronounced peak splitting is visible in  $\{111\}_{PC}$  in NBT-3BT and NBT-6BT, and in  $\{200\}_{PC}$  in all compositions except for NBT-3BT. However, there is no difference in number of reflections or shoulders and no obvious differences in peak intensities between the furnace cooled and the quenched state of the same composition in the poled state.

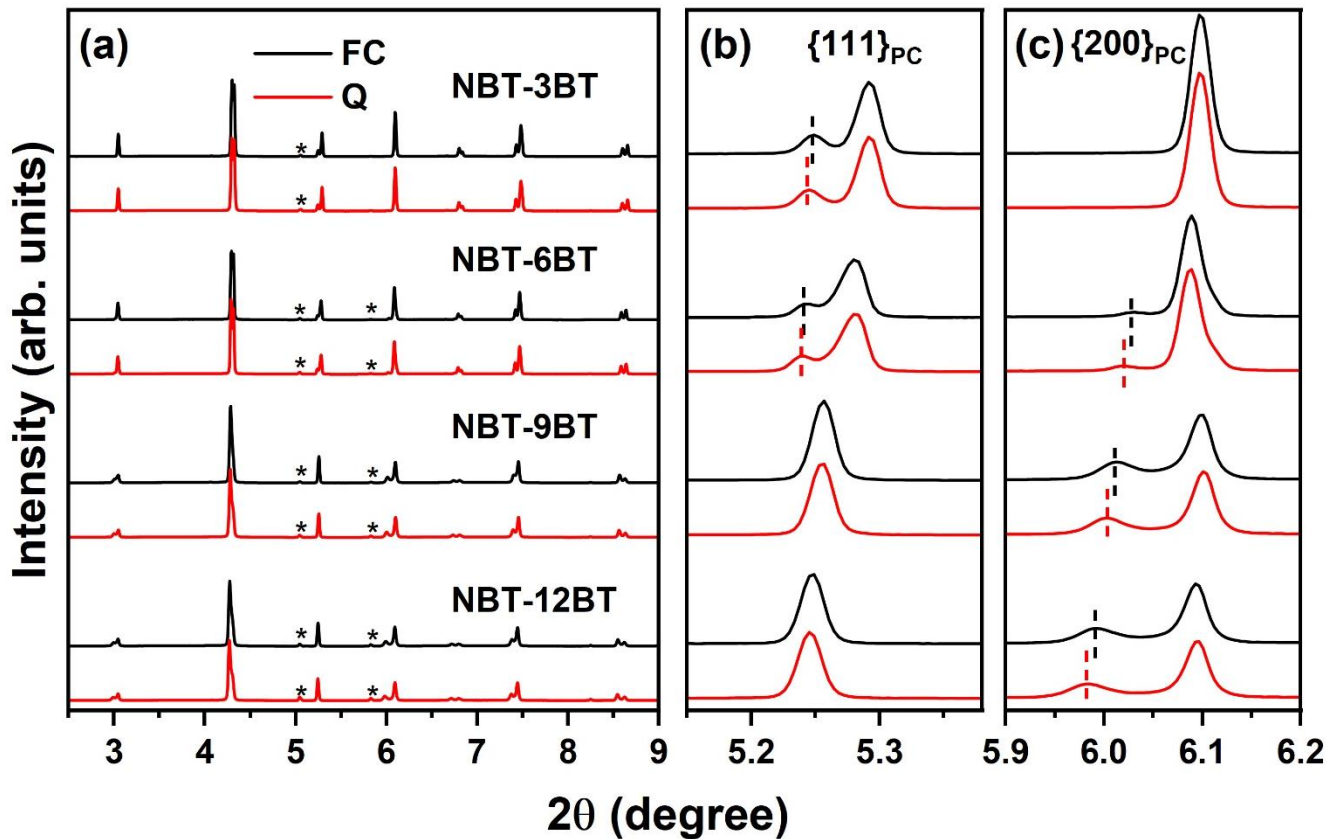


Figure 27: (a) Synchrotron XRD patterns of furnace cooled and quenched NBT-BT bulk ceramics in the poled state, weighted and summed up with respect to the azimuthal angle. Enlarged sections of the XRD patterns showing the  $\{111\}_{PC}$  (b) and  $\{200\}_{PC}$  (c) reflections. The asterisks mark contributions from the Ag electrodes.

---

This qualitative observation of the poled state is also reflected in the structural parameters obtained from the Rietveld refinements listed in Table 4. For NBT-3BT FC and NBT-3BT Q, a single-phase  $R3c$  model gave satisfactory results while for the NBT-6BT compositions a two-phase model of  $R3c$  and  $P4mm$  was used [54]. Patterns of NBT-9BT and NBT-12BT, both in the furnace cooled and quenched states, were refined with  $P4mm$  and  $R3m$  phases also in the poled state [67, 183]. In NBT-3BT and NBT-6BT, the poling-induced phase fractions did not alter upon quenching. Both NBT-6BT FC and NBT-6BT Q exhibit phase fractions of 84 and 16 % of rhombohedral and tetragonal phases, respectively, which is in close agreement with literature values of poled bulk ceramics [76]. In NBT-9BT and NBT-12BT the tetragonal phase fraction is slightly increased by quenching from 87 to 89 % and from 90 to 91 %, respectively. However, this is within the margin of error.

The calculated rhombohedral distortions of the  $R3c$  phase in poled NBT-3BT and NBT-6BT are increased from  $90^\circ - \alpha_{\text{rhom}} = 0.34$  to  $0.36^\circ$  and from  $0.31$  to  $0.34^\circ$ , respectively, by the quenching treatment. An increase in tetragonal distortion of 0.18 to 0.23 % upon quenching was established for the compositions containing the  $P4mm$  phase. Please note that the rhombohedral  $R3m$  phase, which was used to refine NBT-9BT and NBT-12BT compositions alongside with  $P4mm$ , is very weakly distorted and this small distortion does not show a clear trend upon quenching.

The absence of quenching-induced changes in phase fractions in poled NBT-BT can be rationalized since quenching stabilizes the ferroelectric order which is fully accomplished by poling [13]. Therefore, poling the material overwrites the quenching effect by the formation of larger ferroelectric domains that reflect in the established phase fractions. The quenching-enhanced off-centering of the  $\text{Bi}^{3+}$ -ion [149], however, is expected to be retained upon poling which leads to an increased lattice distortion in quenched NBT-BT also in the poled state. The enhanced lattice distortion is most likely the reason for the increase in  $T_{\text{F-R}}$  and  $T_{\text{d}}$  upon quenching, since lattice distortion and depolarization temperature are closely correlated [184].

Table 4: Refined structural parameters of poled NBT-BT compositions based on synchrotron XRD measurements. The errors given by the refinement software are about 1 % in phase fractions and for the other reported values significantly smaller than the last given digit.

	<i>R-phase</i> /%	<i>T-phase</i> /%	$a_{\text{rhom}} / \text{Å}$	$90^\circ\text{-}\alpha_{\text{rhom}}$	$a_{\text{tet}} / \text{Å}$	$c_{\text{tet}} / \text{Å}$	$\eta_{\text{tet}}/\%$	$R_{\text{wp}}$
NBT-3BT FC	100		3.900	0.34			--	3.92
NBT-3BT Q	100		3.900	0.36			--	4.35
NBT-6BT FC	84	16	3.907	0.31	3.894	3.943	1.25	3.35
NBT-6BT Q	84	16	3.907	0.34	3.892	3.949	1.48	3.11
NBT-9BT FC	13	87	3.916	0.01	3.898	3.954	1.42	5.22
NBT-9BT Q	11	89	3.916	0.01	3.896	3.960	1.64	5.09
NBT-12BT FC	10	90	3.920	0.06	3.901	3.965	1.65	4.74
NBT-12BT Q	9	91	3.920	0.04	3.899	3.971	1.83	5.21

In addition to evaluating lattice parameters and phase fractions of the investigated compositions in the poled state, the utilization of a 2D detector allows to visualize and quantify the material's poling-induced anisotropy in crystal structure [185]. The 2D patterns were divided in 10 sectors as described in chapter 4.9.3. All investigated poled materials exhibit dependency in the peak intensities with respect to the angle to the poling field,  $\Psi$ . This crystallographic domain texture is caused by a preferred orientation of the ferroelectric domains and therefore of the unit cells of the material induced by the poling procedure [186]. The peak intensities in a diffraction pattern of certain reflections are proportional to the number of unit cells oriented with the respective axis parallel to the scattering vector. This allows to quantify the degree of texture in a crystallographic phase based on the peak intensities of the critical reflections. Peak splitting as characteristic for a rhombohedrally distorted phase is present in furnace cooled and quenched poled NBT-3BT and NBT-6BT compositions, while splitting in the  $\{200\}_{\text{PC}}$  reflection, which is connected to a tetragonal distortion in NBT-BT compositions, can be observed in furnace cooled and quenched NBT-6BT, NBT-9BT, and NBT-12BT materials in the poled state (Figure S 1, Figure S 2). Figure 28 provides an example of azimuthal angle-dependent peak intensities of the  $\{110\}_{\text{PC}}$ ,  $\{111\}_{\text{PC}}$  and  $\{200\}_{\text{PC}}$  reflections as a consequence of poling-induced texture in NBT-6BT FC. The peak intensities of both



the coexisting rhombohedral and tetragonal phases are highly dependent on the angle to the poling direction, with the reflections corresponding to the long polar axes,  $111_R$  and  $002_T$  of the respective phases, being most intense close-to-parallel ( $2.5^\circ$ ) and nearly absent perpendicular to the poling direction ( $87.5^\circ$ ).

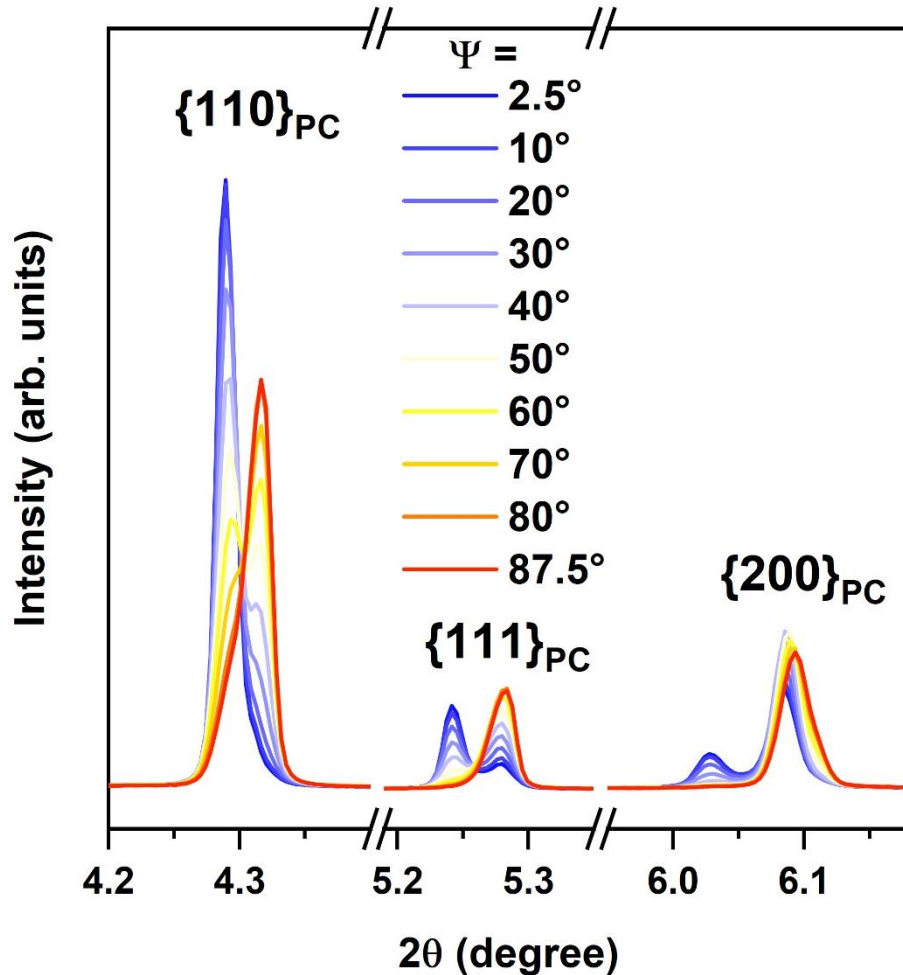


Figure 28: Azimuthal angle-dependent diffraction patterns showing the  $\{110\}_{PC}$ ,  $\{111\}_{PC}$  and  $\{200\}_{PC}$  reflections of poled NBT-6BT FC. A strong angle dependence in the peak intensities is clearly present.

The peak intensities of  $111_R$  and  $11\bar{1}_R$  were established for NBT-3BT and NBT-6BT (FC and Q) and of  $002_T$  and  $200_T$  for NBT-9BT and NBT-12BT (FC and Q). Attempts were made to fit the  $\{200\}_{PC}$  set of reflections of the NBT-6BT materials, but because of the vanishing of the  $002_T$  reflection at higher azimuthal angles and severe overlap of constituting reflections, the fits were unstable leading to untrustworthy results, which are therefore not reported here. For both NBT-6BT materials, three peaks were used to fit the  $\{111\}_{PC}$  reflections to account for the presence of a  $111_T$  reflection due to the coexistence of rhombohedral and tetragonal phases. The split  $\{111\}_{PC}$

reflections of the NBT-3BT compositions and the  $\{200\}_{PC}$  set of reflections of the NBT-9BT and NBT-12BT compositions were fitted using only 2 peaks.

Based on the extracted peak intensities, the texture factors for the distorted rhombohedral and tetragonal phases,  $f_{111}$  and  $f_{002}$ , given in multiples of random distribution (MRD) [187] can be calculated for each azimuthal angle following equation (20) and equation (21), respectively [179, 188-190]:

$$f_{111} = 4 \frac{\frac{I_{111}}{I'_{111}}}{\frac{I_{111}}{I'_{111}} + 3 \frac{I_{11\bar{1}}}{I'_{11\bar{1}}}} \quad (20)$$

$$f_{002} = 3 \frac{\frac{I_{002}}{I'_{002}}}{\frac{I_{002}}{I'_{002}} + 2 \frac{I_{200}}{I'_{200}}} \quad (21)$$

with  $I_{hkl}$  as the integrated hkl peak intensity at the respective angle and  $I'_{hkl}$  as the reference intensity of the respective reflections. Due to the poling-induced phase transformations, the unpoled state of these materials cannot serve as reference. Therefore, the reference state was defined as a weighted average of the respective peak intensities in the poled state [179]:

$$\langle I'_{hkl} \rangle = \int_{\alpha=0}^{\pi/2} I_{hkl}(\alpha) \sin(\alpha) d\alpha \quad (22)$$

This can be written in discrete form as the weighted sum of the respective peak intensities over all angles using equation (23):

$$\langle I'_{hkl} \rangle = \sum_{\alpha=0^\circ}^{90^\circ} I_{hkl}(\alpha) [\cos(\alpha_i) - \cos(\alpha_j)] \quad (23)$$

where  $\alpha_i$  and  $\alpha_j$  are the low and high boundaries of the respective azimuthal range.

In Figure 29, the texture factors of the rhombohedral phase in NBT-3BT and NBT-6BT and of the tetragonal phase in NBT-9BT and NBT-12BT compositions are plotted as a function of azimuthal angle. In NBT-3BT, quenching decreases the poling-induced degree of texture with maximum values for  $f_{111}$  of 2.40 and 2.05 in furnace cooled and quenched NBT-3BT, respectively. Contrastingly, the trend is the opposite in the other compositions with higher BT content. In NBT-6BT Q,  $f_{111}$  has a value of 3.76 MRD at  $\Psi = 2.5^\circ$  which is higher than for NBT-6BT FC (3.27 MRD) and close to the theoretical maximum of 4 [187, 191]. Also in NBT-9BT and NBT-12BT, the tetragonal phase of the quenched materials exhibits a slightly higher degree of texture at low

azimuthal angles, however, the differences are not large with  $f_{002} = 1.25$  (FC) and 1.31(Q) MRD for NBT-9BT and  $f_{002} = 1.19$  and 1.23 MRD for NBT-12BT at  $\Psi = 2.5^\circ$ . This suggests that quenching marginally stabilizes the poling-induced remanent domain configuration in NBT-BT with the exception of NBT-3BT. Due to the only small changes in texture factor values and the composition-dependence of the quenching effect on the crystallographic texture, a clear trend upon quenching cannot be concluded.

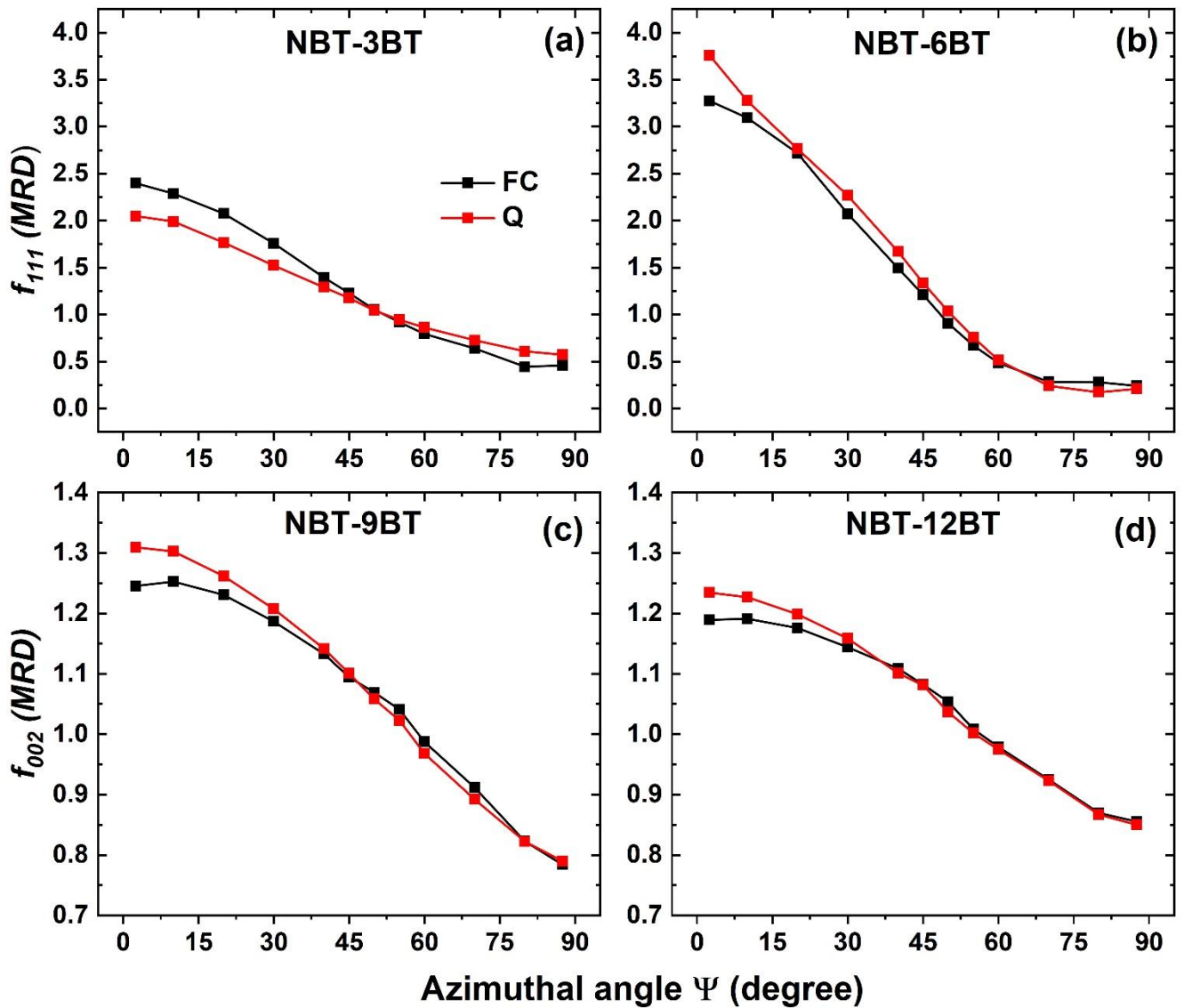


Figure 29: Texture factors as a function of azimuthal angle for the dominant phase of the respective composition.

In contrast to that, the changes in texture factors for different compositions of NBT-BT are much more prominent. Please note that even though the lower values for  $f_{002}$  compared to  $f_{111}$  are likely

---

partly due to a lower degree of remanent texture in the tetragonal phase, the theoretical maximum for a tetragonal system is only 3 and therefore lower than in a rhombohedral system [187, 191], making the absolute texture factors of different phases difficult to compare. However, NBT-3BT shows a lower degree of texture in the rhombohedral phase compared to NBT-6BT, while NBT-9BT exhibits a stronger textured tetragonal phase than NBT-12BT. In other words, the closer the material is to the MPB, the higher the poling-induced remanent texture. This can be rationalized as at the MPB, NBT-BT has coexisting rhombohedral and tetragonal phases exhibiting the respective unit cell distortions. In general, the energy barrier between coexisting phases in a ferroelectric material is dictated by the material's chemical composition and is small directly at the MPB [192]. If the energy barrier between two phases is sufficiently small, in this case between rhombohedral and tetragonal phases in the MPB composition of NBT-6BT, the symmetry of the field-induced phase depends on the orientation of the pseudo-cubic unit cell with respect to the poling field [76, 193, 194]. Combining the possible polar directions of a rhombohedral and a tetragonal system with 8 and 6 polar directions, respectively, allows for a closer alignment of the unit cell's polar vector with the poling field compared to a material in which only one type of unit cell distortion, e.g. rhombohedral or tetragonal, is energetically favorable. This results in a higher degree of ferroelectric domain alignment and less back-switching upon removal of the poling field leading to a higher degree of poling-induced texture in MPB compositions. A similar relationship was found by comparing an MPB and an off-MPB composition of Nb-doped lead zirconate titanate (PZT) [194]. Furthermore, the formation of an intermediate monoclinic phase bridging between rhombohedral and tetragonal symmetries cannot be excluded from the obtained diffraction patterns and the poling-induced peak splitting. This could also favor strong alignment of the polarization vectors with the poling field, leading to high texture factors.

#### 5.1.4 Microstructure and Density

The microstructure of ferroelectric ceramics is severely impacted by the processing route and sintering conditions and highly influential on different material characteristics and properties [195]. Therefore, microstructural investigations and studies on the densities were conducted, comparing furnace cooled and quenched NBT-BT specimen. However, no alteration by the quenching treatment was found.

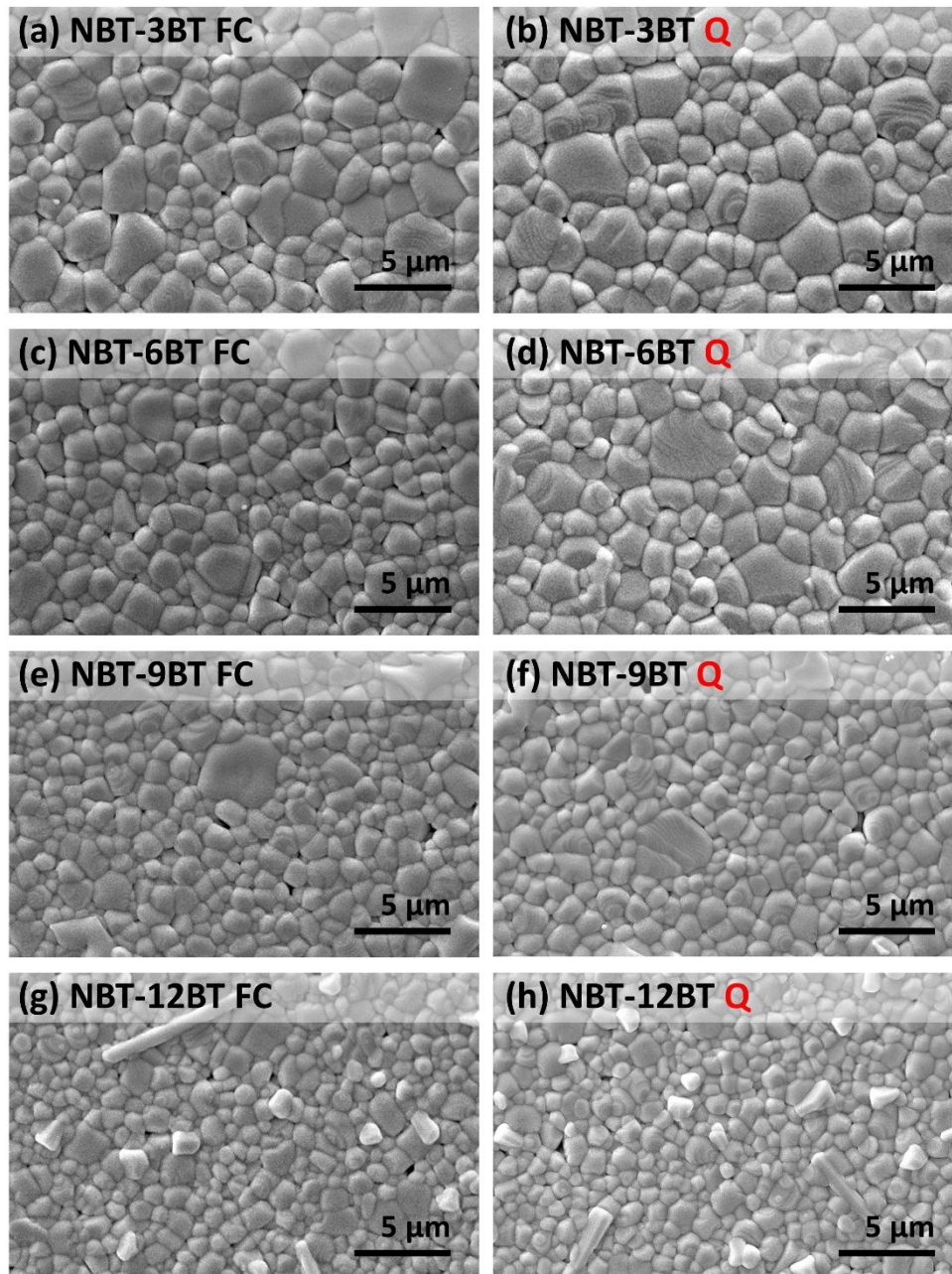


Figure 30: Secondary electron SEM micrographs of polished and thermally etched NBT-BT specimen of all the investigated compositions, furnace cooled and quenched.

All the investigated NBT-BT compositions exhibit a dense polycrystalline microstructure as validated by SEM investigations on polished and thermally etched ceramic specimens (Figure 30). In terms of microstructural features, no difference between furnace cooled and quenched materials can be found. However, the grain size slightly decreases with increase in BT content as visualized in Figure 30 and quantified by a grain size analysis, carried out as described in chapter 4.3. This is in accordance with part of the literature [196, 197] while other works reported no significant composition-dependent change in grain size [172]. In this study, the grain size decreases from  $2.34 \pm 0.33 \mu\text{m}$  for NBT-3BT FC to  $1.28 \pm 0.19 \mu\text{m}$  for NBT-12BT FC (Figure 31). For all the compositions, the grain sizes for furnace cooled and quenched specimen are the same within the margins of error. NBT-6BT exhibits grain sizes of  $1.65 \pm 0.19$  and  $2.07 \pm 0.36$  for FC and Q, respectively. This is in accordance with earlier works that report values ranging between 1.4 and about  $2 \mu\text{m}$  [172, 197, 198].

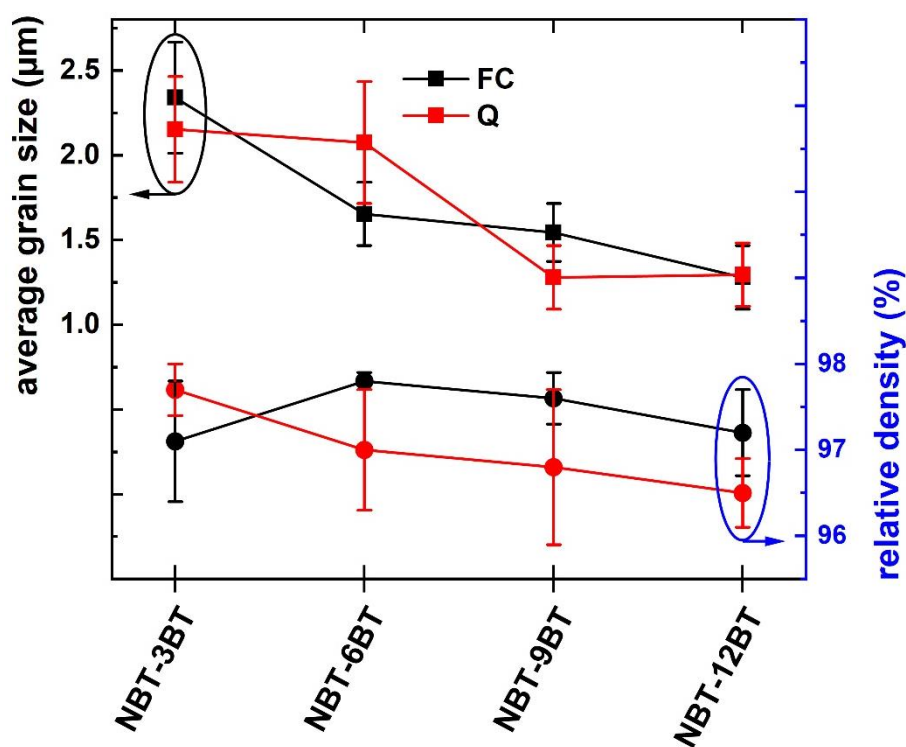


Figure 31: Composition-dependent average grain size and relative density of furnace cooled and quenched NBT-BT ceramics.

All the investigated NBT-BT ceramics exhibit high relative densities between 96 and 98 % (Figure 31). Similar to the grain size, the relative density is not significantly influenced by the quenching treatment. The absence of a significant change in grain size and relative density upon quenching

---

provides evidence that the quenching-induced changes in structural and ferroelectric properties of NBT-BT are not caused or influenced by changes in the microstructure of the material.

---

### 5.1.5 Ferroelectric and Piezoelectric Response

---

*Since quenching influences the structure of NBT-BT, an effect onto the ferroelectric and piezoelectric properties seems likely. Therefore, the piezoelectric response and polarization were established for quenched and furnace cooled NBT-BT compositions, hinting towards a suppression of (ergodic) relaxor behavior upon quenching.*

Polarization and strain curves were measured simultaneously as a function of electric field on as-annealed pellet-shaped NBT-BT samples of all compositions, furnace cooled and quenched, using a Sawyer-Tower circuit and an optical displacement sensor. At least five samples per composition were measured and the data was evaluated. The resulting polarization curves of the first and third electric field cycles are displayed in Figure 32. The maximum applied field was 8 kV/mm for NBT-3BT FC and NBT-3BT Q due to its high coercive field, while it was 6 kV/mm for the other compositions. In Figure 33, the electric field-dependent strain of the first- and third electric field cycle are plotted. All the compositions exhibit saturated polarization and butterfly-shaped strain curves as it is characteristic for ferroelectrics (Figure 32 and Figure 33).

The inflection point, at which the polarization and strain strongly increase, is located at higher electric fields for the quenched materials compared to the furnace cooled references (Figure 32 a-d and Figure 33 a-d). This is especially pronounced in NBT-6BT (Figure 32b and Figure 33b) and was reported before for NBT-9BT [13]. The shift of the inflection point to higher electric fields was rationalized as being connected to a quenching-induced increase in the coercive field due to the stabilization of ferroelectric order upon quenching.

Values for maximum and remanent polarization and coercive field were extracted from the third polarization cycles and plotted in Figure 34. Maximum polarization is defined as the polarization at maximum electric field. Remanent polarization is the respective value, where the electric field is reduced back to zero after reaching the maximum. For the furnace cooled materials, both maximum and remanent polarization decrease monotonously upon increasing the BT amount from  $43 \pm 1 \mu\text{C}/\text{cm}^2$  for NBT-3BT FC to  $32.2 \pm 0.5 \mu\text{C}/\text{cm}^2$  for NBT-12BT FC, and from  $39 \pm 3 \mu\text{C}/\text{cm}^2$  for NBT-3BT FC to  $26.4 \pm 0.2 \mu\text{C}/\text{cm}^2$  for NBT-12BT FC, respectively. With increasing BT content, the coercive field decreases from  $4.56 \pm 0.15 \text{ kV}/\text{mm}$  for NBT-3BT FC to a minimum of

2.76 ± 0.01 kV/mm for NBT-9BT. NBT-12BT FC exhibits a slightly higher coercive field of 3.08 ± 0.07 kV/mm. This is consistent with literature, since the high coercive field of pure NBT is strongly reduced by adding BT [199]. However, by adding more than 10 mol% BT into the structure, the coercive field increases again until it reaches a maximum at 20 mol% which is rationalized as the transition from a modulated structure (containing PNRs) to a non-modulated tetragonal symmetry [59].

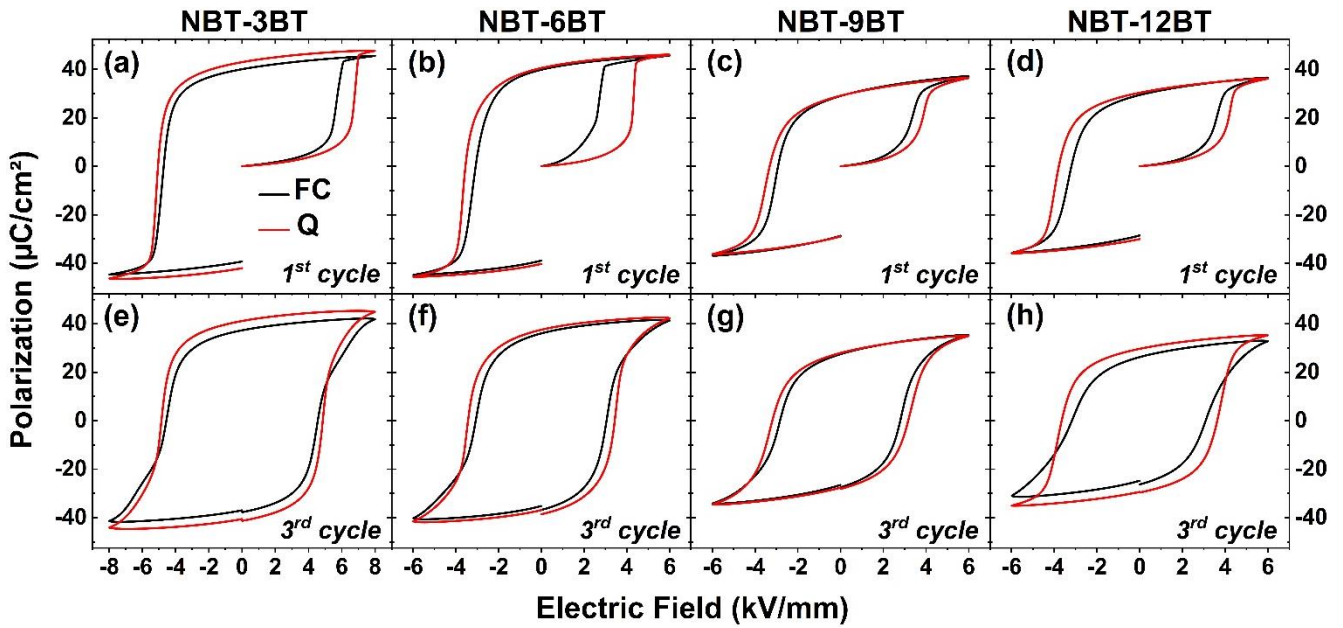


Figure 32: First (a-d) and third (e-h) electric field-dependent polarization cycles of furnace cooled (black) and quenched (red) samples of all investigated NBT-BT compositions measured with a frequency of 1 Hz.

The third polarization cycle of the quenched materials appear more square-shaped than the ones from the furnace cooled materials (Figure 32e-h). Polarization and coercive field values increase in all four compositions upon quenching, however, the changes are only between roughly 5 and 10 %. Nevertheless, they are significant within the margins of error. Typically, ferroelectric softening leads to an increase in polarization but to a decrease in coercive field. On the other hand, ferroelectric hardening causes an increased coercive field but a decrease in polarization, as reported for PZT [200]. Here, in contrast to literature [13], an increase in both polarization values and coercive field are measured in quenched NBT-BT. Therefore, discussing these observations in terms of ferroelectric softening and hardening is most likely not sufficient. However, a correlation with the stabilization of the ferroelectric order upon quenching appears plausible. Even though NBT-BT exhibits non-ergodic relaxor or mainly ferroelectric properties depending on the



composition, quenching might further suppress (ergodic) relaxor behavior and by that, lead to an increase in remanent polarization and coercive field since lower values for both are characteristic for relaxor materials.

Representative third electric field-dependent measurement cycles of strain of all investigated NBT-BT compositions are displayed in Figure 33e-h. From these third electric field cycles, total strain, defined as the difference between the maximum and minimum strain, and negative strain, defined as strain minimum, were extracted (Figure 35a). Quenching increases the total strain and the absolute value of the negative strain. This suggests a correlation to the enhanced lattice distortion and therefore enhanced spontaneous strain upon quenching. Since the strain induced by domain switching (domain switching strain) is proportional to the spontaneous strain [201], this might be the reason for the increase in macroscopically measured strain values. Furthermore, a more pronounced negative strain can be seen as a sign of reduced ergodicity in the material.

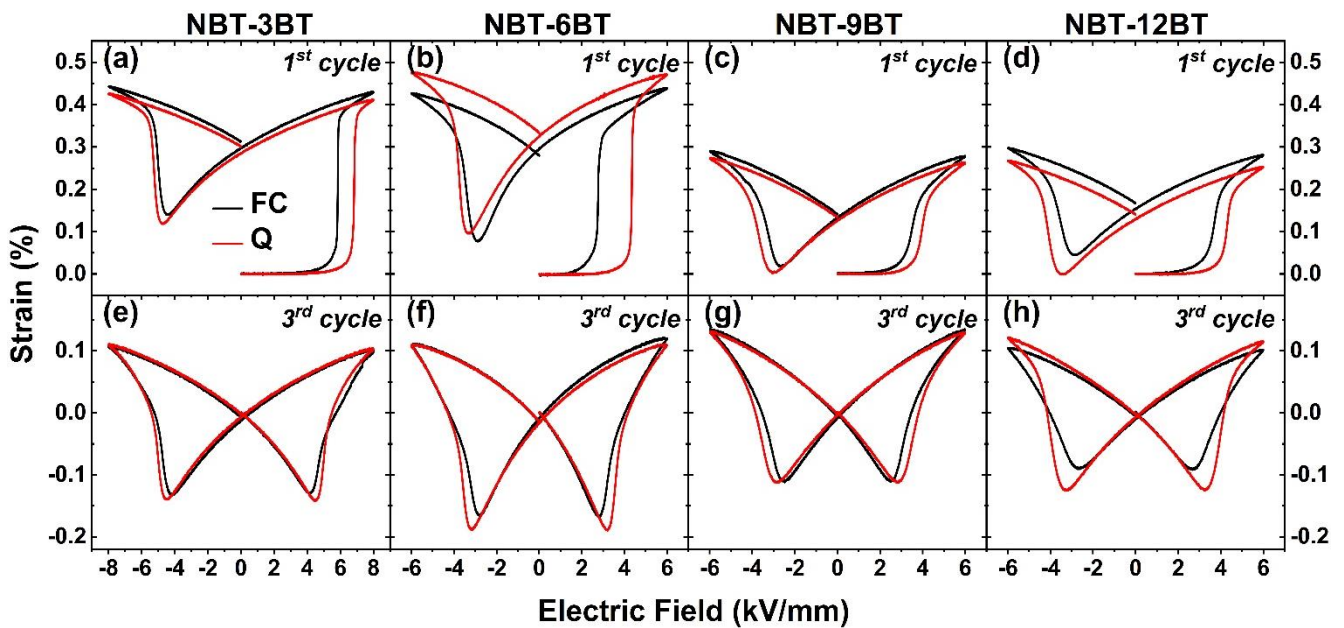


Figure 33: First (a-d) and third (e-h) electric field-dependent strain cycles of furnace cooled (black) and quenched (red) samples of all investigated NBT-BT compositions measured with a frequency of 1 Hz.

The direct piezoelectric coefficient was established using a Berlincourt  $d_{33}$ -meter and is plotted for furnace cooled and quenched NBT-BT materials in Figure 35b. Quenching decreases  $d_{33}$  for all investigated compositions, which is consistent with literature [12, 151, 202]. In this study, the strongest quenching-induced change in  $d_{33}$  in absolute numbers is observed in NBT-6BT, which shows a decrease from  $139 \pm 6$  to  $125 \pm 3$  pC/N upon quenching. Interestingly, quenching shifts

the maximum in  $d_{33}$  from NBT-6BT to NBT-9BT, meaning the piezoelectric properties of NBT-9BT seem to be less affected by the quenching treatment.

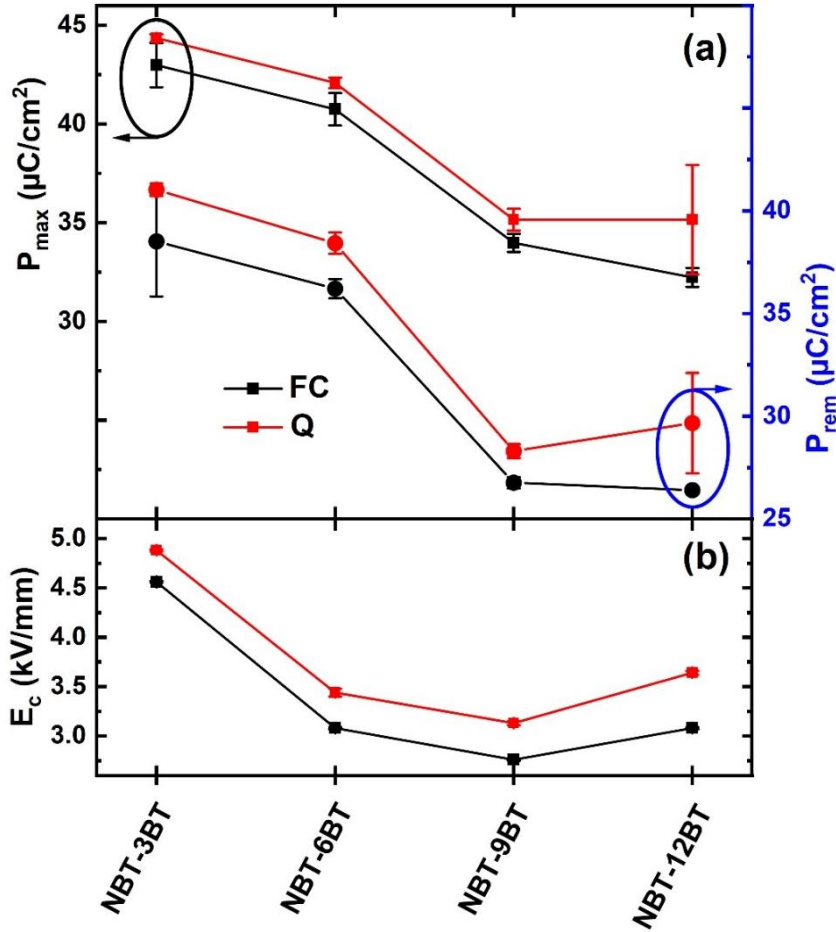


Figure 34: Maximum and remanent polarization (a) and coercive field (b) extracted from electric field-dependent polarization measurements for all investigated NBT-BT compositions.

The decrease in  $d_{33}$  might be connected to a reduction of the extrinsic contributions to the  $d_{33}$ . The piezoelectric response of a ferroelectric material is a combination of intrinsic and extrinsic contributions with intrinsic referring to lattice strain and extrinsic to domain reorientation and domain wall motion [203, 204]. The increase in coercive field upon quenching indicates that higher electric fields meaning more energy is needed for domain reorientation. This could lead to reduced domain wall mobility also at sub-coercive fields and reduce the extrinsic contributions, ultimately being a reason for an overall lower piezoelectric response. However, this is hypothetical and, as stated before, not necessarily connected to classical hardening mechanisms in ferroelectrics.

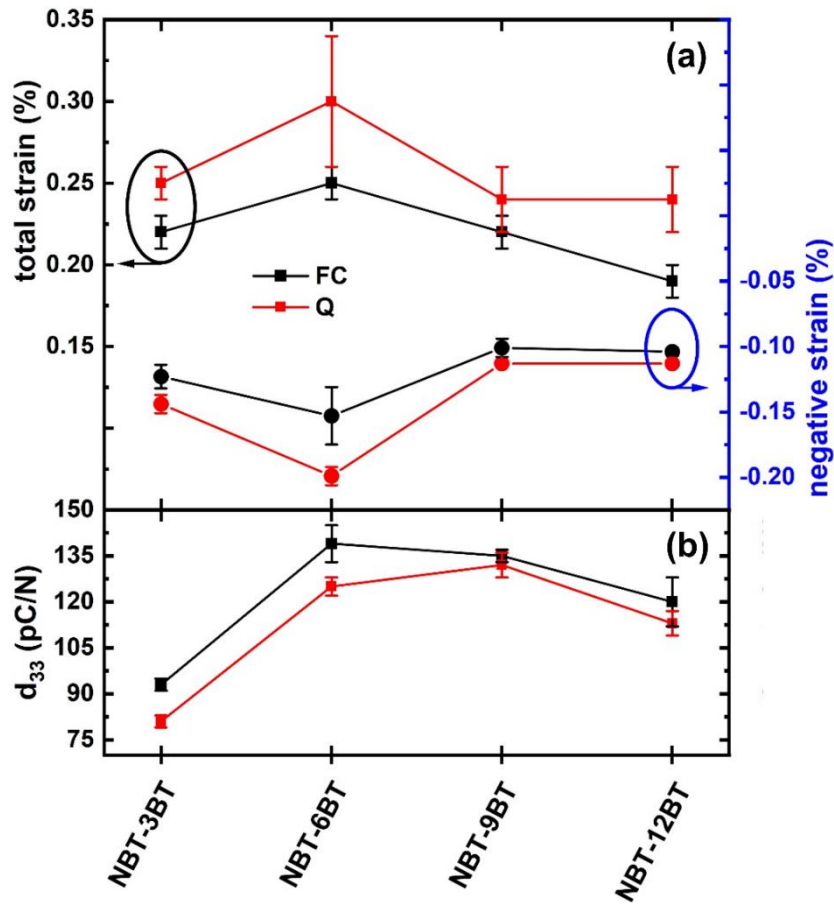


Figure 35: Total and negative strain (a) extracted from electric field-dependent polarization measurements and direct piezoelectric constant,  $d_{33}$  (b), for all investigated NBT-BT compositions.

### 5.1.6 Short Summary

In this chapter, the influence of composition and quenching on the unpoled and poled (*ex situ*) structural, microstructural and ferroelectric properties and piezoelectric coefficient of NBT-BT were elucidated. The grain size slightly decreases with increasing BT content, while the microstructural properties remained unchanged upon quenching, proving that quenching-induced changes in properties are not caused by alterations in the microstructure. The findings presented in this chapter support the hypothesis of a stabilized ferroelectric order and suppression of (ergodic) relaxor characteristics upon quenching.

High resolution laboratory XRD and synchrotron single-shot diffraction experiments were conducted on both poled and unpoled bulk ceramics and correlated with the ferro- and piezoelectric properties. Quenching increases the lattice distortion in all compositions in both

---

powder and bulk samples. The changes in phase fractions are especially pronounced in the MPB composition NBT-6BT, where the material's cubic phase fraction is reduced but also an onset of tetragonal lattice distortion is induced by the quenching treatment. In contrast, quenching does not significantly change the phase composition in poled samples but the quenching-induced increase in lattice distortion is still present in the poled state. Even though quenching stabilizes the ferroelectric order, this effect on the phase composition is overwritten by the poling treatment which completely transforms the material into a ferroelectric. The quenching-induced increase in lattice distortion, most likely caused by the enhanced off-centering of the  $\text{Bi}^{3+}$ -ion [149], however, remains upon poling and might be the reason for the increase in  $T_d$ , since lattice distortion and  $T_d$  correlate in these materials [184].

In addition to that, the poling-induced crystallographic texture in poled materials was quantified. Changes in texture upon quenching are rather small and show different trends in NBT-3BT in contrast to the compositions with a higher BT content. Therefore, a clear influence of quenching on texture cannot be concluded. However, the closer the material composition is to the MPB, the larger the poling-induced texture becomes with NBT-6BT exhibiting the maximum in this study, most likely due to coexisting rhombohedral and tetragonal phases.

Quenching slightly increases polarization, coercive field and total strain as established from ferroelectric hysteresis measurements. The increase in total strain at large applied electric fields might be connected to the increase in lattice distortion, and therefore, the increase in spontaneous strain affects the domain switching strain. The  $d_{33}$  decreases in all compositions upon quenching. This could possibly be attributed to the larger amount of energy needed to move domain walls due to the increase in lattice distortion and coercive field resulting in a reduced extrinsic contribution to the piezoelectric response.

---

## 5.2 Quenching-induced Changes of Polarized Volume in NBT-BT

---

In this chapter, the influence of quenching on the dielectric properties and the volume fraction of polar nanoregions of NBT-BT are examined and discussed. The findings presented here are mostly published in the Applied Physics Letters [177] and minor parts in the Journal of American Ceramic Society [205] and Physical Review Materials [206].

---

### 5.2.1 Introduction and Motivation

---

In addition to the quenching-induced structural changes discussed in the last chapter, quenching NBT-BT also affects the material's dielectric properties and its depolarization temperature,  $T_d$  [13, 87]. In NBT-6BT and NBT-9BT, the relaxor-to-ferroelectric transition temperature,  $T_{F-R}$ , to which  $T_d$  is coupled in NBT-BT, is increased by 40 and 60 °C, respectively, due to the quenching treatment [13]. The frequency dispersion of dielectric permittivity is strongly reduced upon quenching, indicating the stabilization of a ferroelectric state.

The enhanced ferroelectric order also reflects in the more pronounced lattice distortion and phase composition of ferroelectric phases (chapter 5.1). However, the quantitative influence of quenching on the structure on a local level and at elevated temperatures above  $T_{F-R}$  has not been established yet. Even though methods evolving around TEM or piezoresponse force microscopy (PFM) are extremely useful to probe the local structure, they are hardly suitable to establish quantitative changes. Therefore, the number of available methods to quantify the fraction of polarized volume or PNRs in relaxor materials as a function of temperature is very limited with resonance frequency damping analysis (RFDA) and nuclear magnetic resonance (NMR) coming to mind [81-83].

In this study, the sensitivity of the mechanical properties to structural changes were exploited with RFDA to quantify the volume fraction of PNRs in NBT-BT as a function of temperature and correlated with temperature- and frequency-dependent dielectric results. The investigated compositions are NBT-3, 6, 9 and 12BT, representing a rhombohedral, an MPB and two tetragonal compositions, one slightly off and one further away from the MPB, respectively.

First results of frequency-dependent measurements on unpoled NBT-BT samples at room temperature reveal a quenching-induced decrease in the real part of permittivity and in the

frequency dispersion, especially pronounced in NBT-6BT and NBT-9BT (Figure 36). This is fitting to the literature [13] and proves a quantifiable influence of quenching in the materials subject to this study.

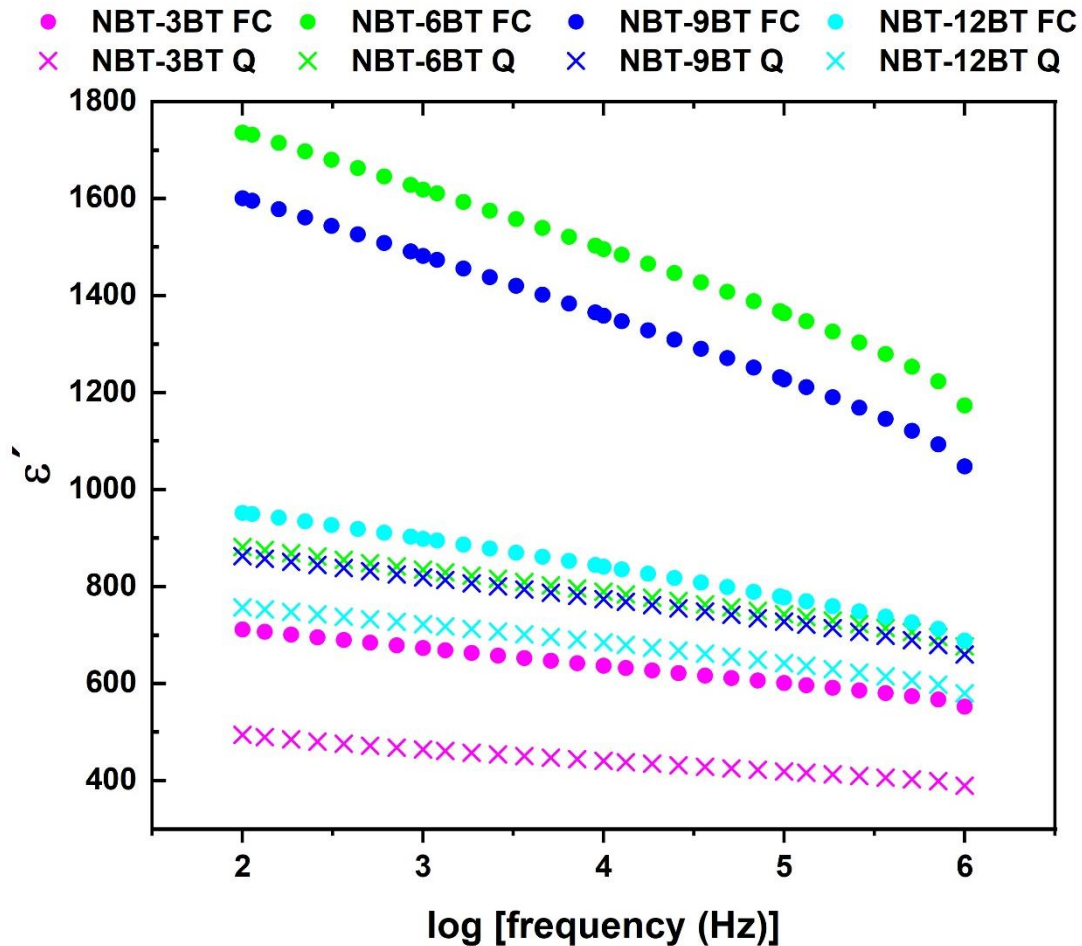


Figure 36: Frequency-dependent permittivity of furnace cooled and quenched NBT-BT samples measured at room temperature in the poled state.

## 5.2.2 Dielectric Analysis

*Evaluation of the real and the imaginary part of the dielectric permittivity provides valuable insight into the properties and nature of phase transitions in ferroelectric and relaxor materials. Since quenching NBT-BT affects the ferroelectric order, temperature-dependent permittivity measurements were carried out to establish the shift in the application-relevant ferroelectric-to-relaxor transition temperature and to understand the influence of quenching on the dielectric characteristics in NBT-BT compositions.*

---

The capacitance and loss tangents were measured on poled pellet-shaped NBT-BT ceramics as a function of temperature at frequencies of  $10^3$ ,  $10^4$ ,  $10^5$  and  $10^6$  Hz. From these parameters, the real and imaginary parts of permittivity were calculated as described in chapter 4.6 and are plotted in Figure 37 as established from the poled state. Measuring two heating and cooling cycles, each from about 25 to 500 °C allows to collect data from the poled and the unpoled state of the material. In Figure 38, the data collected during the second heating cycle, (unpoled) is displayed.

$T_{F-R}$  is defined as the temperature at which  $\epsilon'$  has the steepest increase and was established for all material compositions in the furnace cooled and quenched state. When reaching  $T_{F-R}$ , the frequency dispersion strongly increases in all NBT-BT materials during the first heating cycle due to the transition from the ferroelectric to the relaxor state [16]. In addition to that, the temperature at which permittivity reaches its maximum,  $T_m$ , was derived from the permittivity data (Figure 37 and Figure 38).  $T_{F-R}$  for all investigated NBT-BT compositions is plotted in Figure 39 and exhibits a minimum at the MPB where the material exhibits a more cubic-like structure, which is consistent with literature [172, 207] and can be correlated to the flattening of the free energy landscape [203, 208]. Therefore, the higher  $T_{F-R}$  and by that  $T_d$  in compositions further away from the MPB correlates with the stronger distortion of the crystal lattices from the ideal cubic perovskite structure in these materials.

Furthermore, the quenched samples exhibit higher  $T_{F-R}$  with the difference to the furnace cooled samples of the same composition ranging between 25 to 44 °C. The quenching-induced enhancement in  $T_{F-R}$  is stronger in NBT-6BT and NBT-9BT (44 and 43 °C, respectively), which exhibit relaxor properties in the unpoled state, than in NBT-3BT and NBT-12BT (25 and 33 °C, respectively) that appear more ferroelectric. This increase in  $T_{F-R}$  correlates with the more pronounced lattice distortion upon quenching and is consistent with literature [13, 146]. Based on these findings, quenching, in contrast to Zn-doping [207], does not seem to cause a shift in the composition-dependent position of the MPB, since NBT-6BT is the composition with the lowest  $T_{F-R}$  also in the quenched state and the smallest lattice distortion as confirmed by the structural findings discussed in chapter 5.1. However, the steps of 3 mol% Ba in-between compositions in this study might be too large to detect only a slight shift of the MPB.

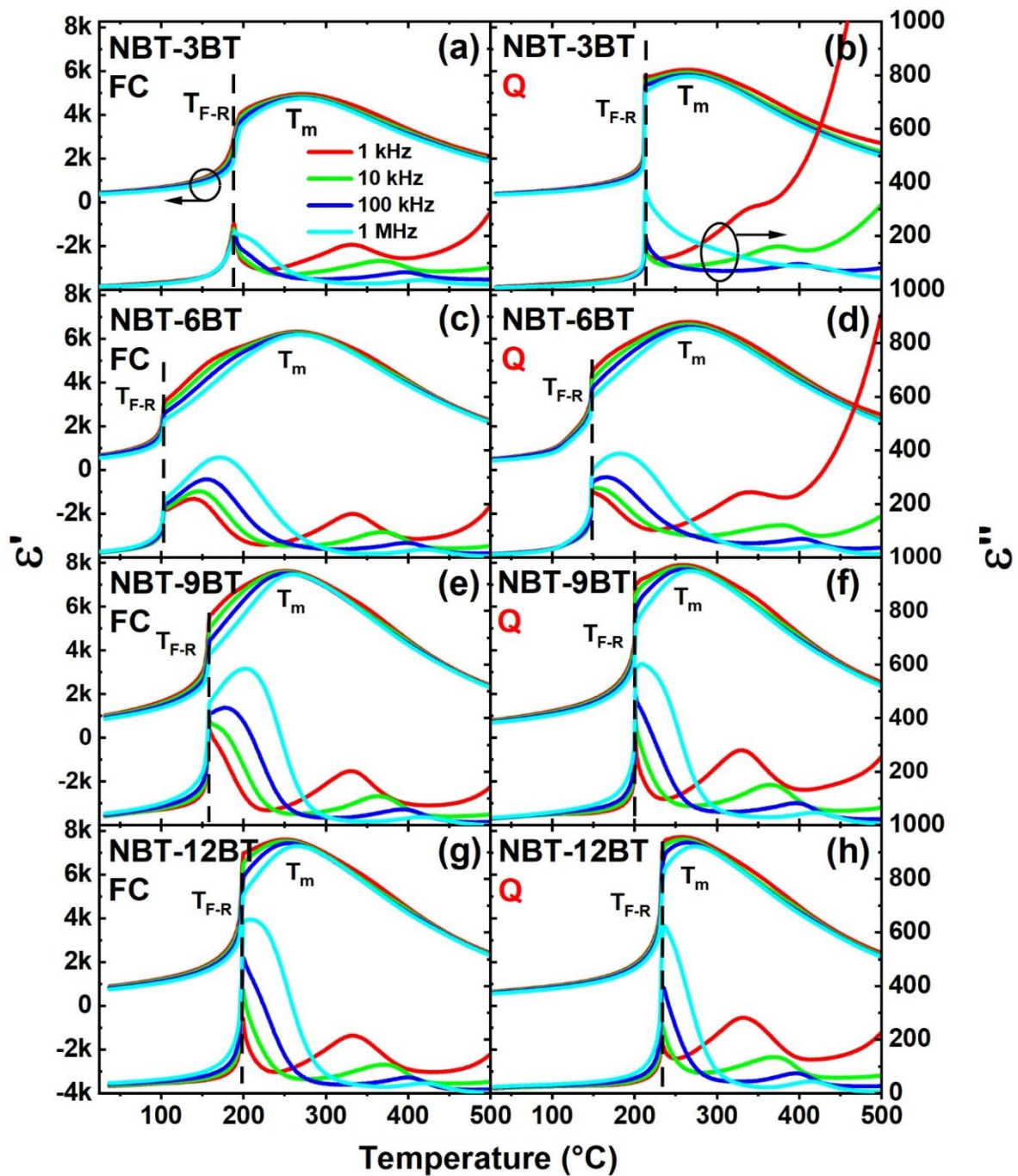


Figure 37: Temperature-dependent permittivity measured at different frequencies on poled furnace cooled and quenched NBT-BT samples.

Due to the ferroelectric nature of NBT-BT in the poled state, all compositions exhibit a clear anomaly at  $T_{F-R}$ . However, there are differences in the unpoled state depending on the composition. NBT-3BT and NBT-12BT that exhibit ferroelectric behavior without poling, exhibit a similar step increase in  $\epsilon'$  around  $T_{F-R}$ , which is valid for both furnace cooled and quenched materials (Figure 38a, b, g and h). NBT-6BT FC and NBT-9BT FC on the other hand (Figure 38c and e), display clearly different behavior with a strong frequency dispersion at lower temperatures



and no clear anomaly, as also reported in literature [13]. Upon quenching, unpoled NBT-6BT exhibits a slight anomaly at around 116 °C and NBT-9BT Q exhibits a steep increase in  $\epsilon'$ , comparable to the poled state (Figure 38f). This further strengthens the argument of a stabilized ferroelectric order [13] and correlates with the quenching-induced structural changes in unpoled bulk NBT-9BT samples (chapter 5.1.3).

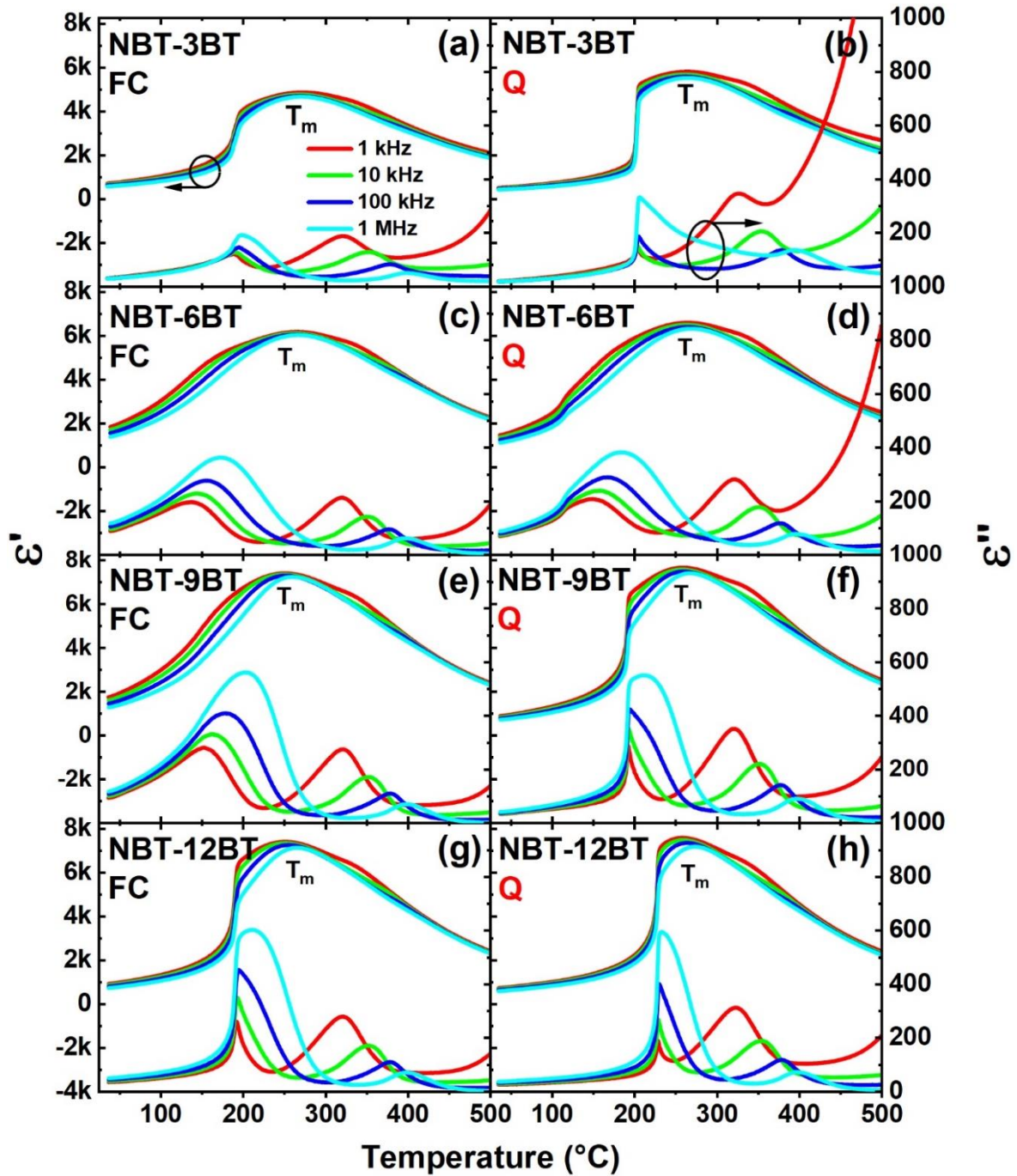


Figure 38: Temperature-dependent permittivity measured at different frequencies on unpoled furnace cooled and quenched NBT-BT samples.

The frequency dispersion in the dielectric response was quantified from the frequency-dependent permittivity measurements at room temperature (Figure 36) as difference between  $\epsilon'$  measured at 100 Hz and  $\epsilon'$  measured at 1 MHz ( $\epsilon'_{100 \text{ Hz}} - \epsilon'_{1 \text{ MHz}}$ ) and is plotted in Figure 39. All the compositions exhibit a clear decrease in frequency dispersion upon quenching, which is especially pronounced for the relaxor compositions NBT-6BT and NBT-9BT, further supporting the hypothesis that quenching introduces or stabilizes a ferroelectric state in NBT-BT.

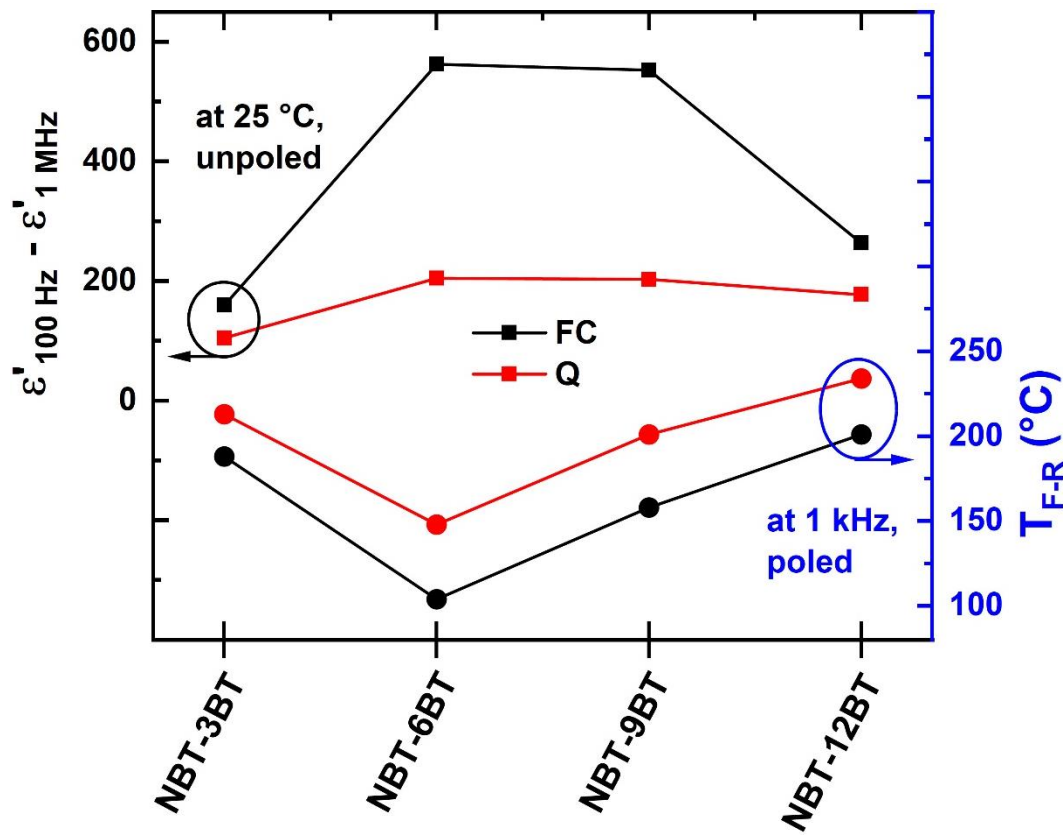


Figure 39: Difference in  $\epsilon'$  measured at 100 Hz and 1 MHz on unpoled samples at room temperature and  $T_{F-R}$  established from temperature-dependent dielectric data measured at 1 kHz on poled samples of NBT-BT.

To establish the influence of quenching on the relaxation dynamics of the relaxor MPB compositions NBT-6BT, Vogel-Fulcher analysis was carried out following equation (9) (chapter 2.4.2). The temperature of the maximum of the imaginary part of permittivity,  $T_m''$ , was obtained from 1 to  $10^6$  Hz from temperature- and frequency-dependent dielectric measurement on NBT-6BT FC and NBT-6BT Q and is plotted in Figure 40. The resulting curves for both materials have similar exponential character, however, for the quenched samples,  $T_m''$  values are shifted to higher

temperatures. Fitting the curves with an exponential function following equation (9), allows to extract the Vogel-Fulcher or static freezing temperature,  $T_{VF}$ , and the activation energy for dipole reorientation,  $E_a$ . The latter coincides within the margins of error with  $24 \pm 3$  and  $26 \pm 5$  meV for NBT-BT FC and NBT-6BT Q, respectively. Therefore, the quenching treatment seems not to influence the threshold energy for dipole reorientation. On the other hand,  $T_{VF}$  increases upon quenching from  $106 \pm 3$  to  $123 \pm 5$  °C. This means the PNRs transform from a dynamic to a static state at higher temperatures, which reflects as an enhanced PNR contrast in temperature-dependent TEM experiments in quenched NBT-6BT [205].

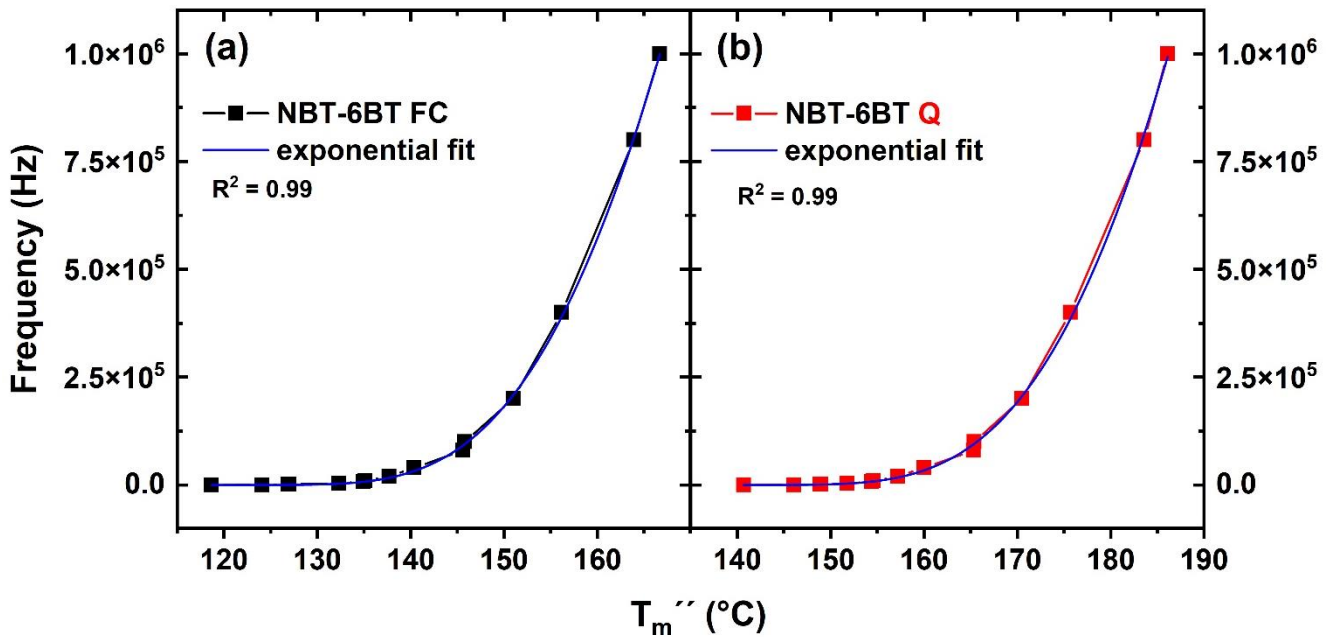


Figure 40: Temperature of the maximum of the imaginary part of permittivity,  $T_m''$  versus frequency plotted for NBT-6BT FC (a) and NBT-6BT Q (b). Blue lines depict the exponential fits of the data which were used to establish Vogel-Fulcher temperature and activation energy.

### 5.2.3 Temperature-dependent Young's Modulus and PNR Volume Fraction

*Utilizing the changes in Young's modulus, established from resonance frequency damping analysis, in combination with a simple composite model allows for quantification of the polarized volume as a function of temperature. In this study, it was applied to calculate the increase in polar nanoregions volume fraction upon quenching in NBT-BT at elevated temperatures.*

The Young's modulus,  $Y$ , is a fundamental mechanical property of a material describing the relation between tensile or compressive stress and axial strain in the linear regime. One method

---

to measure  $Y$  also as a function of temperature is resonance frequency damping analysis (RFDA) which is explained in detail in chapter 4.8. Even though the focus of this study is not on the mechanical properties of ceramics, the temperature-dependent evolution of  $Y$  is still of interest. Due to the direct connection between  $Y$  and the interatomic forces in a material,  $Y$  is sensitive to structural changes even on a nanoscale, as it is the case when PNRs are forming or vanishing. Therefore, the temperature-dependent evolution of PNR volume fraction was computed for furnace cooled and quenched NBT-BT using  $Y$ , which was established by RFDA on unpoled rectangular ceramics together with a composite model [83, 172, 175].

In Figure 41, representative curves of  $Y$  and PNR volume fraction against temperature are plotted for all the investigated NBT-BT materials. Three samples were measured per composition to ensure reproducibility. Both the curves of NBT-3BT FC and NBT-3BT Q feature similar characteristics (Figure 41a). With increasing temperature,  $Y$  decreases linearly until it reaches a sharp minimum at 161 and 178 °C for NBT-3BT FC and NBT-3BT Q, respectively. Even though this minimum indicates the transition from the ferroelectric to the relaxor state, the temperatures do not coincide with  $T_{F-R}$  established from dielectric measurements on poled samples.  $T_{F-R}$  is marked in Figure 41 as vertical dashed lines. In the NBT-BT compositions which also show a temperature-induced transition from ferroelectric to relaxor properties in the unpoled state, poling shifts this transition to higher temperatures. This is due to the poling-induced domain orientation which increases the internal electric field and by that the energy barrier to terminate the ferroelectric structures [172]. Therefore,  $T_{F-R}$  established from dielectric measurements on poled samples is higher than the temperature at which the sharp minimum of  $Y$  of the respective compositions is located.

Upon further increase in temperature,  $Y$  increases monotonously which is directly connected to the PNR volume fraction. In the simplified relaxor model with tetragonal PNRs within a cubic matrix (chapter 4.8), the PNRs possess a lower  $Y$  than the cubic matrix.  $Y$  of both phases is assumed to decrease linearly with increasing temperature. However, the overall  $Y$  of the bulk material increases since the volume fraction of PNRs (lower  $Y$ ) decreases, while the volume fraction of the cubic matrix increases (higher  $Y$ ) with increasing temperature. Also, in the present study, an anomaly in the evolution of  $Y$  around 410 °C with unclear origin is detected in both NBT-3BT FC and NBT-3BT Q. In literature, the onset of a transition from tetragonal to cubic symmetry was suggested as physical cause behind the anomaly [56], while others connected a similar phenomenon in PMN to a development of quasi-static PNRs [172, 209]. The calculated PNR volume fraction has a similar trend for NBT-3BT FC and NBT-3BT Q, however, the quenched

material exhibits slightly higher values at all temperatures.  $Y$  reaches its maximum at around 730 °C for both, furnace cooled and quenched materials. Vögler et al. interpreted this maximum as  $T_B$ , meaning as the temperature where PNR agglomeration sets in upon cooling [83]. This interpretation can also be found in other literatures on lead-based relaxor materials [210, 211]. On the other hand,  $T_B$  established from dielectric results measured on NBT-3BT single crystals and pure NBT was reported as 421 and 405 °C, respectively [212, 213]. However, the findings presented here contradict these reports since  $Y$  clearly increases until about 730 °C.

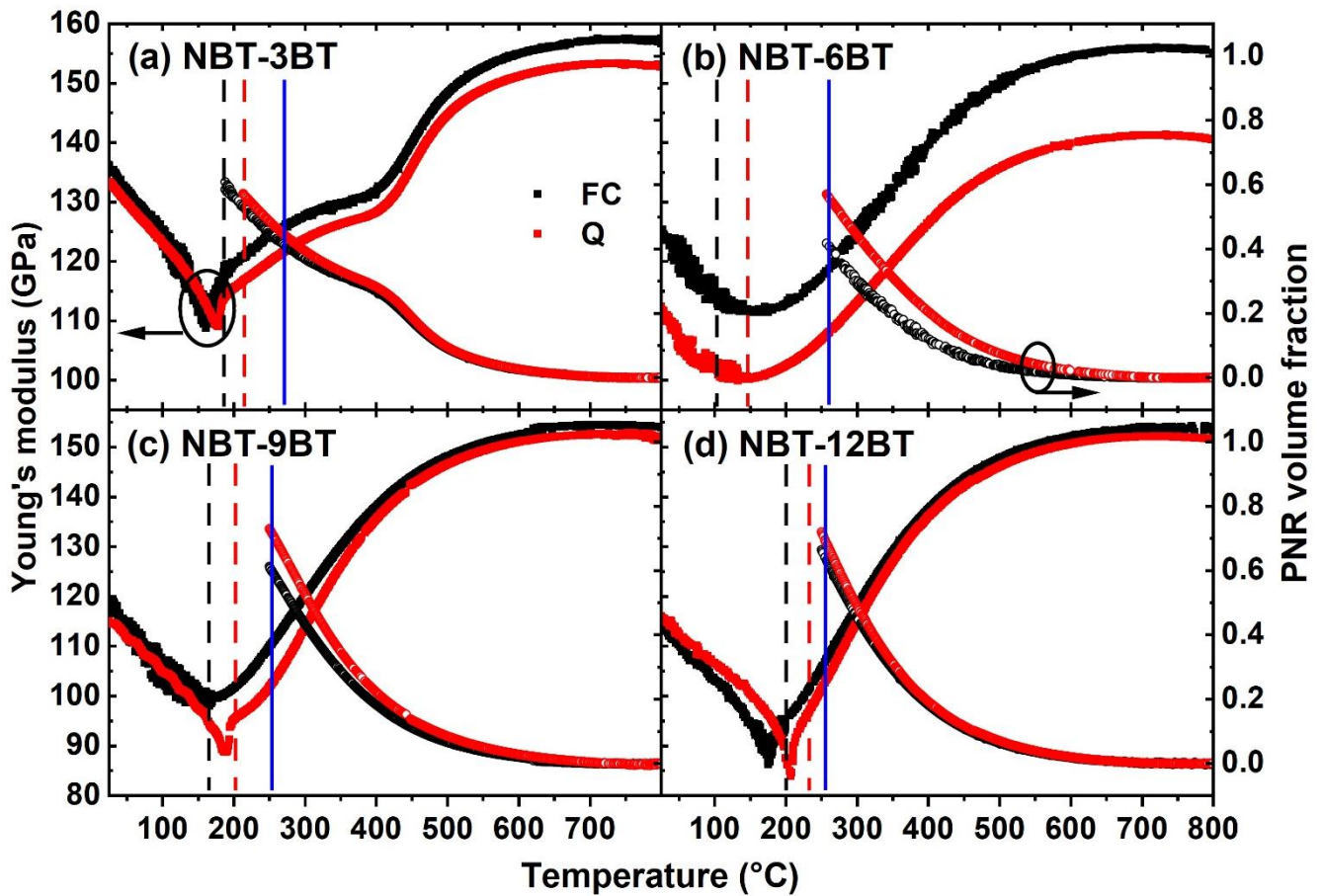


Figure 41: Young's modulus and PNR volume fraction as a function of temperature for all investigated NBT-BT compositions, unpoled, FC and Q. The vertical black and red dashed lines indicate  $T_{F-R}$  for FC and Q, respectively, while the blue solid lines mark  $T_m$ .  $T_m$  for FC and Q samples does not deviate more than 8 °C and therefore, only one line per chemical composition is plotted.

Calculating the PNR volume fraction with the method presented here is only possible at temperatures, wherein solely tetragonal PNRs with  $P4bm$  symmetry are present. For NBT-6BT and the other investigated compositions with higher BT content, this is not the case at temperatures slightly above  $T_{F-R}$ . The shoulder in the temperature-dependent dielectric spectrum

---

with strong frequency dispersion between  $T_{F-R}$  and  $T_m$  has been interpreted as being caused by the vanishing of rhombohedral PNRs with  $R3c$  symmetry [79, 83]. This means, at temperatures above the mentioned shoulder, only tetragonal PNRs should be present. Therefore, in this study, the PNR volume fraction was calculated above  $T_m$  for NBT-6BT, NBT-9BT and NBT-12BT.

The  $Y$  curves of NBT-6BT FC and NBT-6BT Q do not exhibit a sharp minimum since both materials are in the relaxor state when unpoled, and therefore do not exhibit a temperature-induced ferroelectric to relaxor transition. The difference in  $Y$  between the furnace cooled and the quenched sample is much more pronounced in NBT-6BT compared to the other compositions (Figure 41b and Figure 42). In NBT-6BT, quenching decreases  $Y$  at 30 °C from  $123 \pm 1$  to  $115 \pm 6$  GPa and can be correlated to the distinct structural changes that encompass an enhanced lattice distortion and a change in phase composition (chapter 5.1) [153]. Furthermore, the quenching treatment causes an increase in PNR volume fraction at all temperatures above  $T_m$  in NBT-6BT (Figure 41b).

The temperature-dependent  $Y$  curves of NBT-9BT FC and NBT-9BT Q feature a striking difference (Figure 41c). While a sharp minimum is absent in the furnace cooled material, the quenched material exhibits this feature. This indicates the presence of a ferroelectric to relaxor transition and therefore the stabilization of a ferroelectric order in NBT-9BT, already in the unpoled state upon quenching as consistent with literature [13] and the structural and dielectric findings of this study (chapters 5.1.3 and 5.2.2, respectively).  $Y$  is slightly lowered and the PNR volume fraction is enhanced by the quenching treatment as apparent from the representative curve plotted in Figure 41c. However,  $Y$  at 30 °C is comparable for NBT-9BT FC and NBT-9BT Q within the margins of error when averaged over three samples (Figure 42).

Irrespective of furnace cooled or quenched state of the samples, the  $Y$  curves of NBT-12BT exhibit a sharp minimum (Figure 41d), meaning a ferroelectric to relaxor transition upon heating, consistent with the dielectric results (Figure 38g and h). Also here, the position of the minimum is shifted to lower temperatures compared to the  $T_{F-R}$  established from the dielectric results of poled samples. Upon quenching,  $Y$  is slightly shifted to higher values at room temperature and lower values at elevated temperatures. However, the change in  $Y$  at 30 °C is barely outside of the margins of error (Figure 42). NBT-12BT Q shows a slightly higher PNR volume fraction compared to NBT-12BT FC.

PNR volume fraction of all the investigated NBT-BT compositions at 300 °C is plotted in Figure 42. The arbitrary temperature of 300 °C was chosen to compare the different compositions and the

furnace cooled and quenched state, because it is above  $T_m$  for all compositions and therefore only tetragonal PNRs should be present in all materials. Quenching increases the PNR volume fraction for all the investigated compositions, however, in NBT-3BT and NBT-12BT, it is still similar within the margins of error. In the two compositions NBT-6BT and NBT-9BT, which are at and close to the MPB, respectively, the PNR volume fraction is increased significantly from 0.31 to 0.43 and from 0.45 to 0.50 at 300 °C. This means, especially directly at the MPB, quenching strongly influences the local structure of the material also at elevated temperatures, requiring an increase in PNR size and/or in number density. This can be correlated to the global structural changes established with XRD, meaning the influence of quenching on the phase composition and the lattice distortion of the present phases, which leads to the stabilization of ferroelectric order at room temperature [13] and plausibly also to an increase in the coherence length of PNRs.

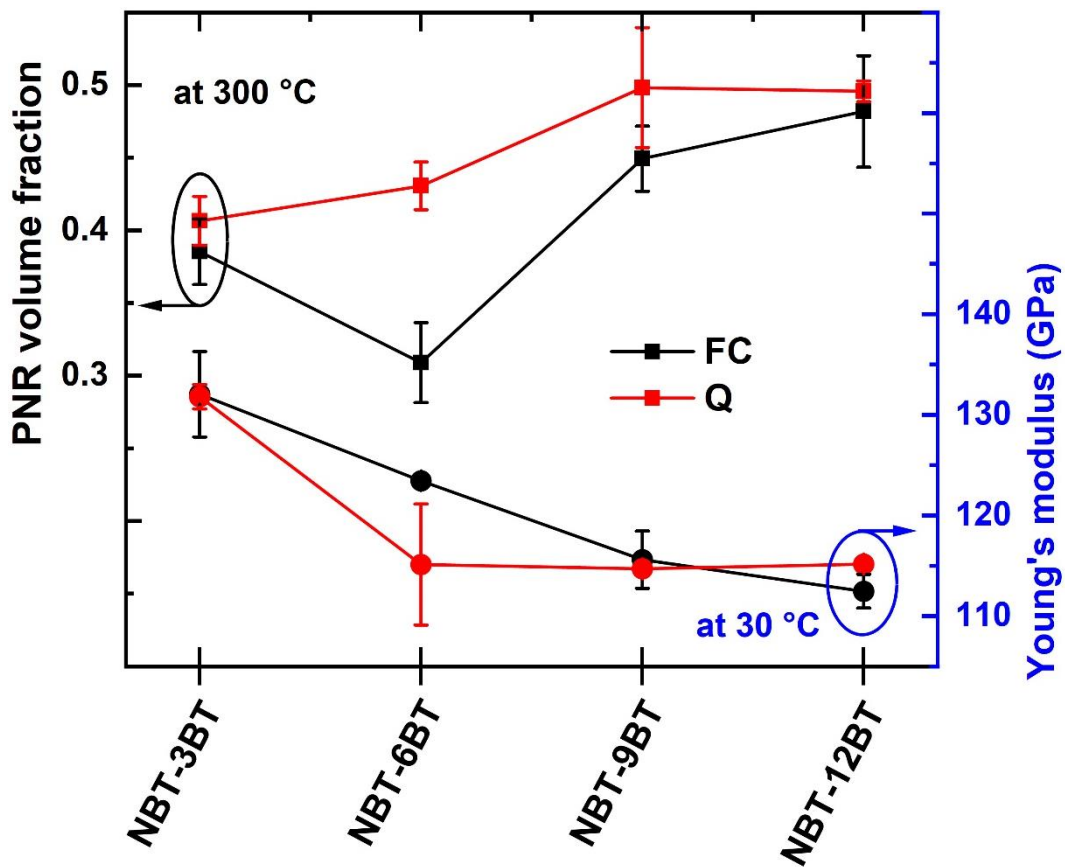


Figure 42: Composition-dependent PNR volume fraction at 300 °C and Young's modulus at 30 °C of unpoled NBT-BT.

Furthermore, in all the investigated NBT-BT compositions, quenching does not change the maximum in  $Y$  and therefore, arguably, does not change  $T_B$ . Also  $T_B$  is similar for all compositions,

---

furnace cooled and quenched, within a range of 708 to 743 °C, consistent with the results by Vögler et al. [83].

---

#### 5.2.4 Short Summary

---

Frequency- and temperature-dependent dielectric measurements were carried out on furnace cooled and quenched NBT-BT with 3, 6, 9 and 12 mol% BT and correlated to the temperature-dependent Young's modulus established from resonance frequency damping analysis. Furthermore, the sensitivity of the mechanical properties to structural changes were utilized to apply a composite model and calculate the PNR volume fraction as a function of temperature from  $Y$  at elevated temperatures.

Typically for a more ferroelectric and less relaxor-like behavior, NBT-BT exhibits a reduced frequency dispersion of the permittivity at room temperature especially at and close to the MPB upon quenching. In addition, Vogel-Fulcher analysis was performed for NBT-6BT FC and NBT-6BT Q and the freezing temperature was extracted. The quenching treatment increases  $T_{VF}$  by 17 °C, meaning the PNRs remain static up to higher temperatures.

The findings based on RFDA underline the fact that quenching has the strongest effect at the MPB. While NBT-6BT is the only composition in which  $Y$  at 30 °C is decreased, the PNR volume fraction above  $T_m$  has the most pronounced increase in the MPB composition from 0.31 to 0.43 at 300 °C. This increase in PNR volume fraction can be correlated to the enhanced non-cubic distortions at the MPB upon quenching, based on the XRD findings. Most likely, the enhanced lattice distortion causes all of the following: the stabilized ferroelectric state at temperatures below  $T_{F-R}$ , the shift in  $T_{F-R}$  and the enhanced PNR volume fraction at higher temperatures, while the reason for the enhanced lattice distortion in quenched NBT-BT might be the more pronounced off-centering of the  $\text{Bi}^{3+}$ -ion [149].

Furthermore, the existence of an anomaly in the temperature-dependent dielectric spectrum and a sharp minimum in  $Y$ , with both phenomena indicating a ferroelectric to relaxor transition in unpoled NBT-9BT Q, proves the quenching-induced stabilization of ferroelectric order since these features are missing in unpoled NBT-9BT FC. In general, all the here presented findings further strengthen the hypothesis of a stabilized ferroelectric state upon quenching.



---

## 5.3 Electric Field-dependent *in situ* Diffraction on Quenched NBT-BT

---

In this chapter, the electric field-induced structural changes in NBT-BT and the influence of quenching upon this structural response are discussed. Besides, different strain contributions are extracted and quantified from the structural data obtained from synchrotron X-ray diffraction at the Advanced Photon Source and at the Deutsche Elektronensynchrotron. Part of the here presented findings are published in the Journal of Materiomics [214].

---

### 5.3.1 Introduction and Motivation

---

The influence of quenching on the structure of NBT and NBT-BT in the unpoled state has been studied by several groups with an enhanced lattice distortion as consistent observation irrespective of the exact composition [12, 13, 87, 151]. As discussed in chapter 5.1.3 of this study, in addition to unpoled NBT-BT, bulk ceramics in the poled state were investigated, also exhibiting an increased lattice distortion, but no significant change in phase composition upon quenching. Since poling introduces a long-range ferroelectric order in NBT-BT compositions, which are at or close to the MPB and therefore exhibit relaxor characteristics, the quenching-induced stabilization of the ferroelectric order gets ‘overwritten’ by the poling treatment. However, due to the pronounced structural differences between furnace cooled and quenched NBT-BT in the virgin state, but similar phase composition after poling, the electric field-induced structural changes in the material must be different.

To that end, electric field-dependent *in situ* synchrotron X-ray diffraction experiments were carried out on furnace cooled and quenched NBT-6BT and NBT-9BT bulk ceramics at the Advanced Photon Source (APS) and on furnace cooled and quenched NBT-3BT at the Deutsche Elektronensynchrotron (DESY). The obtained structural data was utilized to establish field-induced texture, changes in phase fractions and extract different strain contributions, which are characteristic for ferroelectric materials under the influence of an applied electric field. The calculated strains were correlated to macroscopically measured field-induced strain. Based on these findings, the differences between compositions, and also between furnace cooled and quenched NBT-BT are highlighted.

---

### 5.3.2 Qualitative Description

---

*Qualitatively describing the field-induced changes in peak position, intensity, asymmetries and splitting of reflections serves as first step to extract information on the material's structure from diffraction patterns recorded at a certain applied field. All the investigated compositions exhibit field-induced structural phenomena which are less pronounced and/or shifted to higher applied fields in quenched NBT-BT compared to furnace cooled ceramics.*

The 2D diffraction patterns collected during the two beam times at APS and at DESY were recorded and further processed as described in chapter 4.9. Please note that the  $2\theta$  resolution of the data obtained at APS is lower compared to the DESY data. As a consequence, parts of the evaluation performed for the DESY data were not possible or unreliable for the APS data.

The electric field-dependent evolution of peak profiles for the  $\{111\}_{PC}$  and  $\{200\}_{PC}$  reflections of NBT-3BT FC and NBT-3BT Q is depicted in Figure 43 with the scattering vector close to parallel with respect to the applied field. These experiments were carried out at DESY. The electric field was applied stepwise with a step size of about 0.14 kV/mm and a holding time of 30 s at each step. Several samples of both NBT-3BT FC and NBT-3BT Q were measured, however, electric field amplitudes of more than about 4.3 – 4.4 kV/mm resulted in destruction of the samples caused by electrical breakdown. The decreased dielectric breakdown strength of ceramics during synchrotron experiments compared to laboratory experiments is most likely connected to the highly-ionizing synchrotron radiation which might affect charge carrier mobility within the material.

Due to the rhombohedral symmetry of NBT-3BT both in the poled and unpoled state [54],  $\{111\}_{PC}$  is split into two reflections, namely  $111_R$  and  $11\bar{1}_R$  also before an electric field is applied (Figure 43a and Figure 44c). Please note that the superlattice reflection (SR) characteristic for the presence of  $R3c$  phase in the *in situ* NBT-3BT data overlapped with a reflection caused by the Ag-electrode and hence was not interpreted. In NBT-3BT FC, both the intensity of the  $111_R$  reflection and the distance between  $111_R$  and  $11\bar{1}_R$  increase strongly, while the intensity of the  $11\bar{1}_R$  decreases around 3.2 kV/mm in field direction. This change in peak position indicates a field-induced increase in the rhombohedral distortion, which occurs simultaneously with a domain switching event reflecting in a change in peak intensity. At the same field amplitude, the  $\{200\}_{PC}$  reflection starts to exhibit broadening and a very slight asymmetry with shoulder towards lower  $2\theta$  angles (Figure 43b and Figure 44d). Even though NBT-3BT is in the rhombohedral regime of the phase diagram and known to exhibit  $R3c$  symmetry both in the poled and unpoled state [54],

the asymmetry in the  $\{200\}_{PC}$  reflection under high applied electric fields suggests not only an elongation but also a distortion of unit cells in the  $[100]_c$  direction, as known from tetragonal symmetries. In the remanent poled state, there is no asymmetry in the  $\{200\}_{PC}$  reflection present nor any other sign of a unit cell distortion other than of rhombohedral nature (Figure 27c). Therefore, this field-induced distortion in  $[100]_c$  direction appears as reversible and only observable with *in situ* experiments.

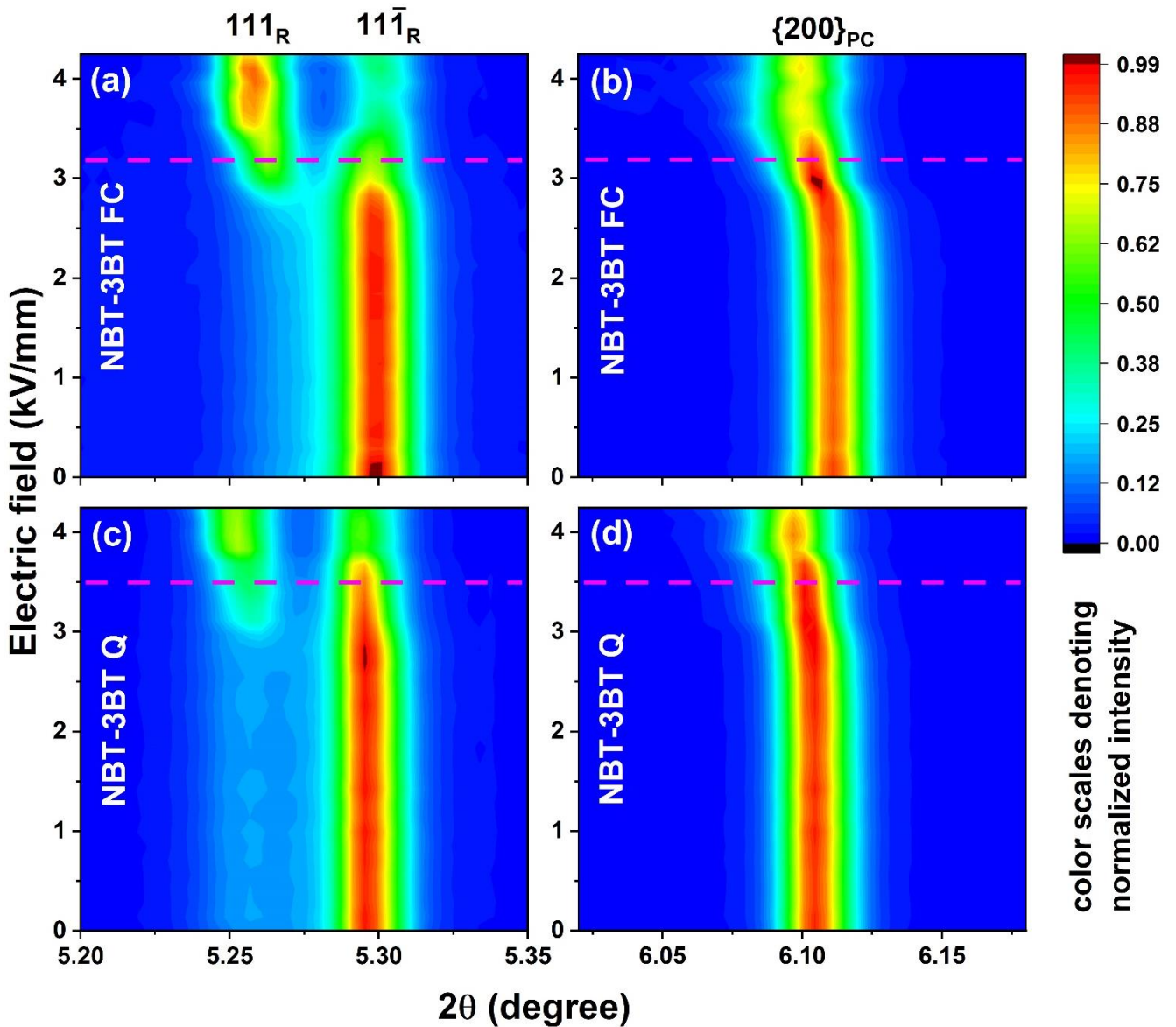


Figure 43: *In situ* synchrotron X-ray diffraction patterns of NBT-3BT FC and NBT-3BT Q during application of electric field, starting from the unpoled state collected parallel to the applied field vector ( $\Psi = 2.5^\circ$ ). (a) and (b) depict the evolution of the  $\{111\}_{PC}$  and  $\{200\}_{PC}$  profiles of NBT-3BT FC upon application of electric field, respectively. (c) and (d) depict the same for NBT-3BT Q. Horizontal dashed lines mark a strong shift in intensities of  $111_R$  and  $111_{\bar{R}}$  reflections and the broadening and onset of asymmetry in the  $\{200\}_{PC}$  reflection.

---

NBT-3BT Q exhibits similar behavior as NBT-3BT FC upon application of an electric field, meaning an increase in rhombohedral distortion, domain reorientation and a slight asymmetry in the  $\{200\}_{PC}$  reflection beyond a certain field threshold (Figure 43c and d). However, the change in peak intensities of the  $111_R$  and  $11\bar{1}_R$  (Figure 43c and Figure 44e) and the broadening of the  $\{200\}_{PC}$  reflection (Figure 43d and Figure 44f) are less pronounced. Furthermore, the electric field strength necessary to induce these structural phenomena is about 3.5 kV/mm and by that around 0.3 kV/mm higher than for NBT-3BT FC. This correlates with the increased coercive field upon quenching as apparent from the ferroelectric hysteresis experiments (chapter 5.1.5). However, the electric field values established with the synchrotron experiments are lower than the coercive field values from the laboratory measurements. The latter are at 4.6 and 4.9 kV/mm for NBT-3BT FC and NBT-3BT Q, respectively, and by that 1.4 kV/mm higher than the electric field amplitude required to cause an onset of structural changes during synchrotron experiments. This might also be connected to the effect of the synchrotron radiation on the ferroelectric material, possibly lowering the electric field strength necessary to reorient the ferroelectric domains.

Similar to the remanent poled state (Figure S 1a and b), NBT-3BT FC and NBT-3BT Q exhibit a strong anisotropy at high applied electric fields. Figure 44a and b depict primary sets of reflections for different azimuthal angles at 4.2 kV/mm for NBT-3BT FC and NBT-3BT Q, respectively. The strong angle dependence of peak intensities provides evidence for pronounced domain texture induced by the application of electric field. Furthermore, an elongation of the unit cell into the direction of the applied field arises from the angle-dependent  $2\theta$ -position of the  $\{200\}_{PC}$  reflection. A quantitative description of the field-induced texture is provided in chapter 5.3.3.

Experiments on furnace cooled and quenched NBT-6BT and NBT-9BT ceramics were performed at the APS with a stepwise-applied electric field with a step size of 0.5 kV/mm and a maximum field amplitude of 6 kV/mm. Figure 45 depicts the evolution of the  $\{111\}_{PC}$  and  $\{200\}_{PC}$  reflections in addition to the SR characteristic for  $R3c$  phase of NBT-6BT FC and NBT-6BT Q parallel to the applied electric field. NBT-6BT FC exhibits symmetric singlets as  $\{111\}_{PC}$  and  $\{200\}_{PC}$ , no SR and therefore (pseudo-)cubic symmetry when probed in the bulk (Figure 45a and b and Figure 46c and d), as reported in literature [76, 215] and consistent with other results from this study (chapter 5.1.3). Between 1.5 and 2.0 kV/mm, the SR caused by the anti-phase tilting of  $R3c$  phase appears, which is accompanied by splitting in both the  $\{111\}_{PC}$  and  $\{200\}_{PC}$  reflections (Figure 45a and b, dashed magenta line). In general, the SR could also be caused by the presence of monoclinic

$Cc$  phase, however, within the detection limits of the diffraction experiments, no evidence could be observed. Therefore, the onset of peak splitting and appearance of the SR are interpreted as a phase transition from (pseudo-)cubic to rhombohedral and tetragonal as consistent with literature reports [76]. Earlier studies observed the same phase transition in NBT-7BT around 1.6 kV/mm also using *in situ* X-ray diffraction experiments [60] and at about 2.3 kV/mm in NBT-6BT as derived from thermometry data [216]. Further increase in electric field amplitude results in a shift in relative peak intensities in the  $\{111\}_{PC}$  and  $\{200\}_{PC}$  doublets at roughly 5 kV/mm, which is most likely connected to a domain switching event.

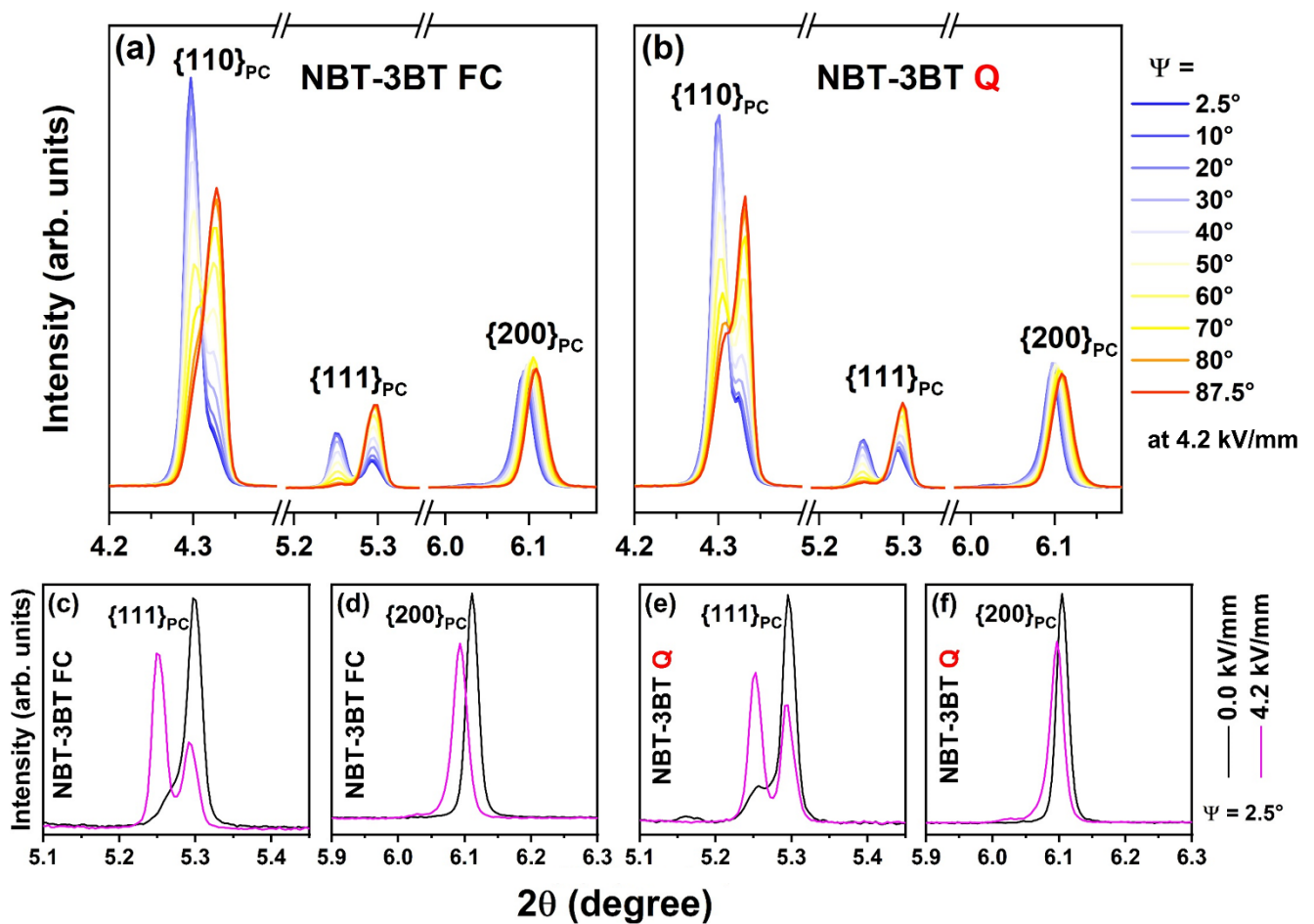


Figure 44: Excerpts of 1D diffraction patterns of NBT-3BT FC visualizing the strong angle dependence in peak intensities at an applied electric field of 4.2 kV/mm (a) and contrasting the reflection profiles of  $\{111\}_{PC}$  (c) and  $\{200\}_{PC}$  (d) reflections at 0 and 4.2 kV/mm parallel to the applied field direction. (b), (e) and (f) depict the same for NBT-3BT Q.

Consistent with results discussed in chapter 5.1, NBT-6BT Q features an asymmetry in the  $\{111\}_{PC}$  reflection and a SR already in the initial state (Figure 45c), however, there is no splitting or

asymmetry in the  $\{200\}_{PC}$  reflection (Figure 45d and Figure 46f). This corroborates the existence of a quenching-induced long-range rhombohedral symmetry also in the unpoled material. Between 2.5 and 3.0 kV/mm, splitting in the  $\{111\}_{PC}$  doublet becomes more pronounced, accompanied with a change in the respective peak intensities. Besides, a shoulder at the lower  $2\theta$  side of the  $\{200\}_{PC}$  reflection starts to appear, indicating the onset of tetragonal distortion at this field amplitude. In addition to stabilizing a long-range ferroelectric order, quenching also shifts the threshold at which the phase transition and accompanied domain reorientation set in, to higher electric field amplitudes in NBT-6BT.

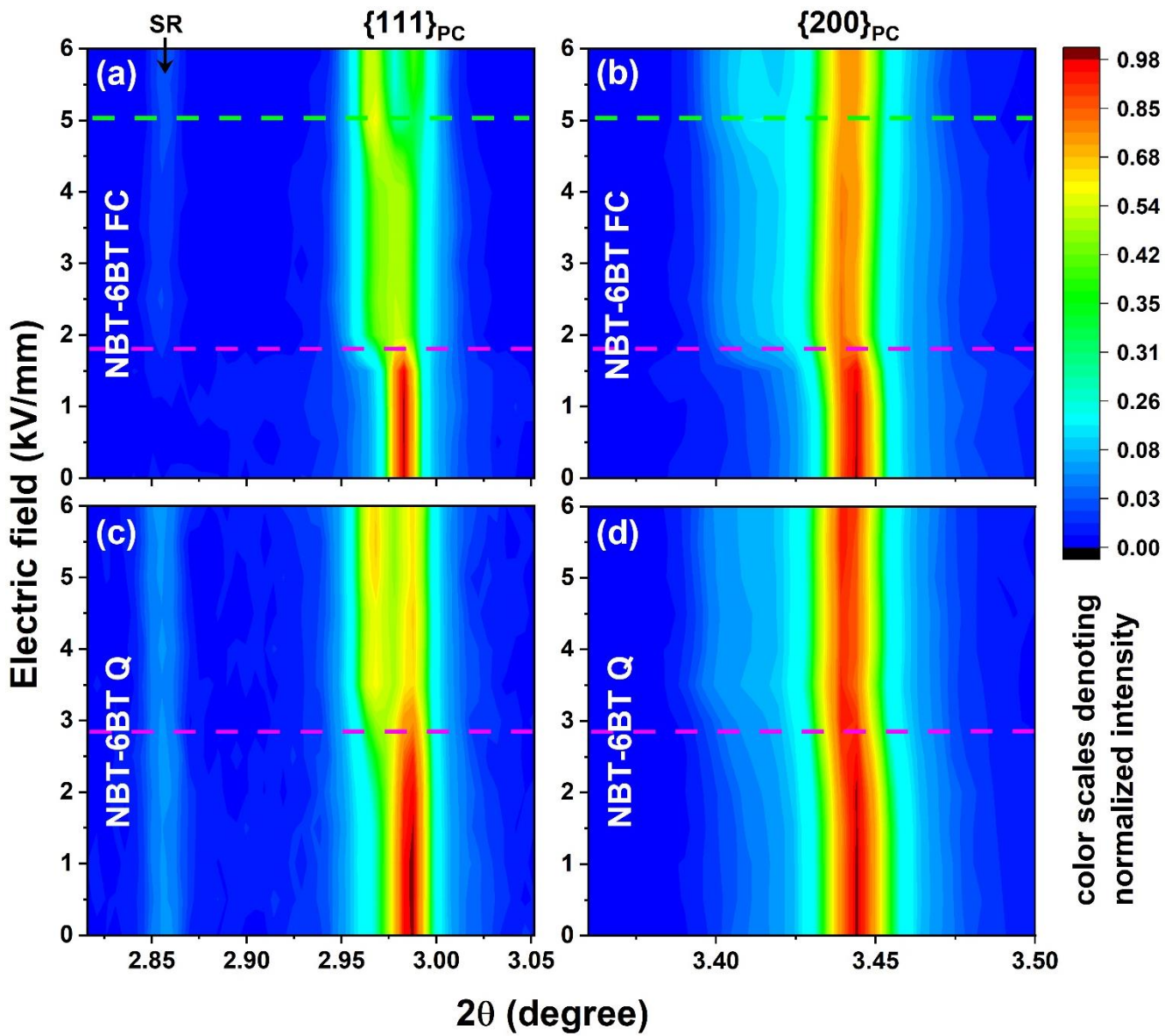


Figure 45: *In situ* synchrotron X-ray diffraction patterns of NBT-6BT FC and NBT-6BT Q during application of electric field, starting from the unpoled state collected parallel to the applied field vector ( $\Psi = 0^\circ$ ). (a) and (b) depict the evolution of the  $\{111\}_{PC}$  and  $\{200\}_{PC}$  profiles of NBT-6BT FC upon application of electric

field, respectively. (c) and (d) depict the same for NBT-6BT Q. SR marks the superlattice reflection in (a) and (c). Horizontal dashed lines mark the appearance of new reflections (magenta) or pronounced intensity change of existing reflections (green).

Both NBT-6BT FC and NBT-6BT Q exhibit significant angle dependence in peak intensities of split reflections (Figure 46a and b), however, the dependence appears to be weaker than in the remanent poled state (Figure 28 and Figure S 1c and d). Most likely, this is not actually the case, but results from the lower  $2\theta$  resolution of the APS compared to the DESY data. The lower  $2\theta$  resolution causes difficulties in separating neighboring reflections with little distance resulting in peak overlap and potentially in a less pronounced signature of texture in the collected diffraction patterns.

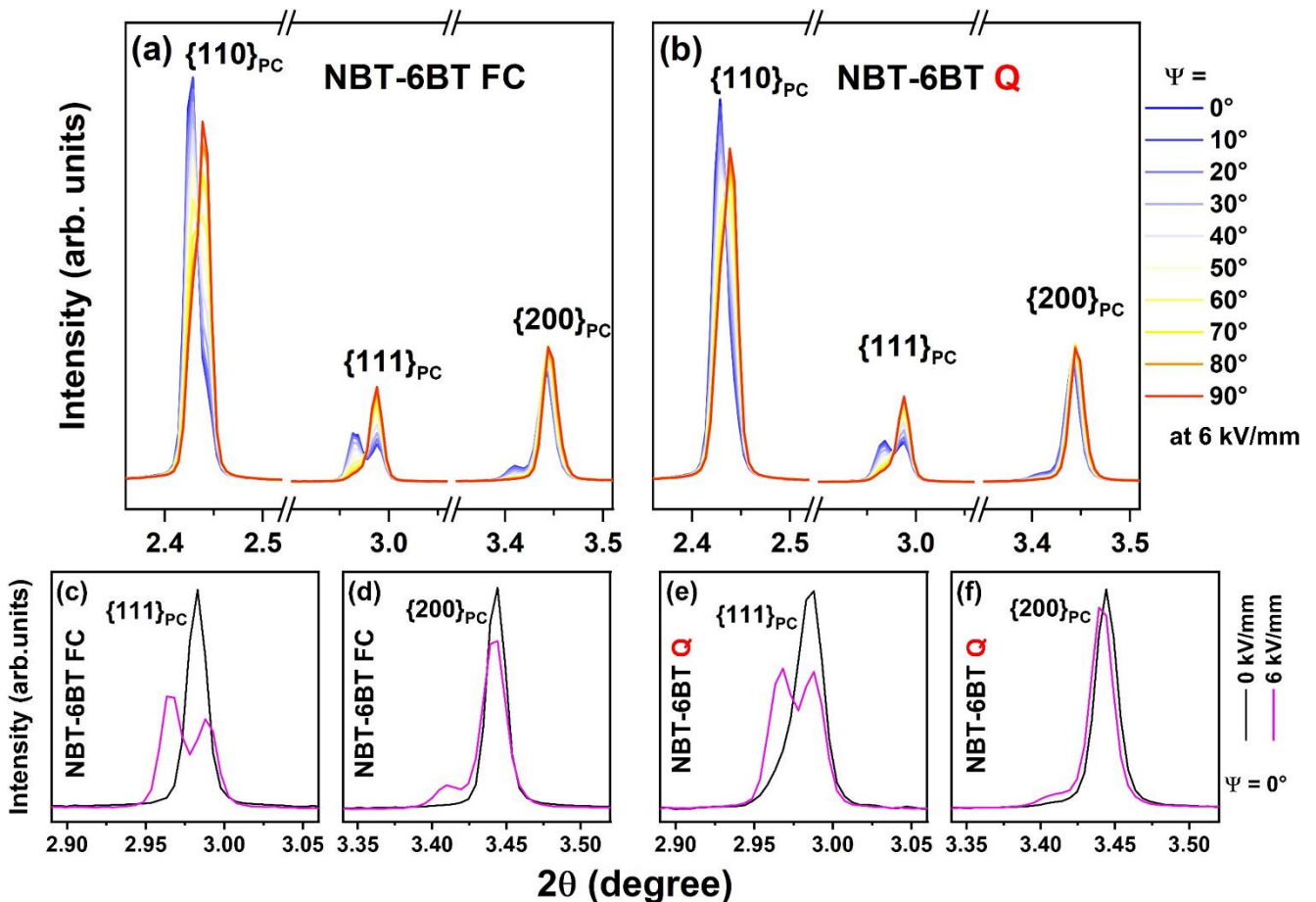


Figure 46: Excerpts of 1D diffraction patterns of NBT-6BT FC visualizing the strong angle dependence in peak intensities at an applied electric field of 6 kV/mm (a) and contrasting the reflection profiles of  $\{111\}_{PC}$  (c) and  $\{200\}_{PC}$  (d) reflections at 0 and 6 kV/mm parallel to the applied field direction. (b), (e) and (f) depict the same for NBT-6BT Q.

---

Figure 47 contrasts the electric field-dependent evolution of  $\{111\}_{PC}$  and  $\{200\}_{PC}$  profiles of NBT-9BT and NBT-9BT Q. Before application of an electric field, the  $\{200\}_{PC}$  reflection is weakly split into two reflections,  $002_T$  and  $200_T$ , while the  $\{111\}_{PC}$  is a singlet, which indicates the presence of a tetragonal phase in NBT-9BT FC [70]. Between 0.5 and 1.0 kV/mm, the splitting in the  $\{200\}_{PC}$  reflection becomes more enhanced and the intensity of the  $002_T$  reflection increases (Figure 47b). Upon further increase in electric field amplitude to about 5.5 kV/mm, an additional peak shoulder appears at the low  $2\theta$  side of the  $200_T$ , so between  $002_T$  and  $200_T$ , also visible in Figure 48d. This suggests the presence of a second phase besides the dominant tetragonal phase. This additional reflection cannot be observed in the remanent poled state of NBT-9BT FC (Figure 27c and Figure S 2a), suggesting a reversible nature of the phenomenon causing the additional reflection.

The  $\{111\}_{PC}$  reflection remains a singlet at all applied fields for both – NBT-9BT FC and NBT-9BT Q (Figure 47a and c). In contrast to the furnace cooled material, NBT-9BT Q exhibits a clear splitting in  $\{200\}_{PC}$  even before an electric field was applied, as consistent with results in chapter 5.1.3. Upon field application, no sudden changes in peak intensities or peak positions are observed, in contrast to NBT-9BT FC and NBT-6BT compositions. Only a gradual shift in the relative peak intensities of the  $002_T$  and  $200_T$  reflections with increasing electric field is visible, which can be interpreted as gradual domain reorientation. These findings indicate an absence of prominent field-induced changes in the structure of NBT-9BT Q and therefore correlate with dielectric results (chapter 5.2.2). This further underlines the presence of a quenching-induced ferroelectric state in NBT-9BT Q and is in accordance with earlier reports [13].



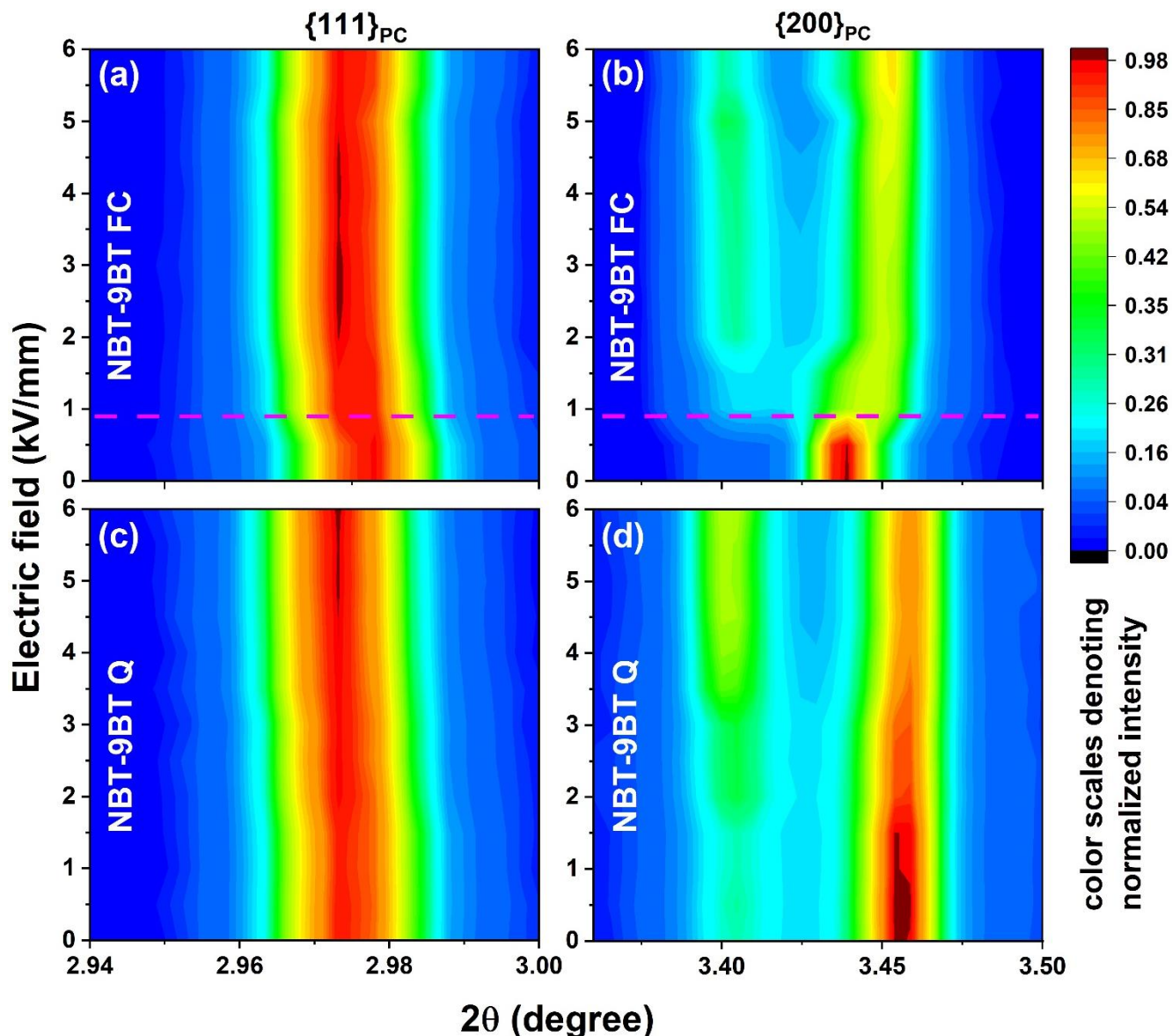


Figure 47: *In situ* synchrotron X-ray diffraction patterns of NBT-9BT FC and NBT-9BT Q during application of electric field, starting from the unpoled state collected parallel to the applied field vector ( $\Psi = 0^\circ$ ). (a) and (b) depict the evolution of the  $\{111\}_{PC}$  and  $\{200\}_{PC}$  profiles of NBT-9BT FC upon application of electric field, respectively. (c) and (d) depict the same for NBT-9BT Q. The horizontal dashed magenta line indicates a phase transformation.

Also in NBT-9BT ceramics, the application of an electric field induces crystallographic texture as depicted in Figure 48a and b for NBT-9BT FC and NBT-9BT Q, respectively, at 6 kV/mm. However, the difference in the respective relative peak intensities for different azimuthal angles is not as pronounced as for NBT-3BT or NBT-6BT (Figure 44 and Figure 46) which is fitting to the data collected during *ex situ* experiments on poled ceramics at DESY (chapter 5.1.3). Based on the data shown in this chapter, quantitative calculations were performed to deepen the understanding of the field-induced structural changes in NBT-BT and are presented in the following chapter.

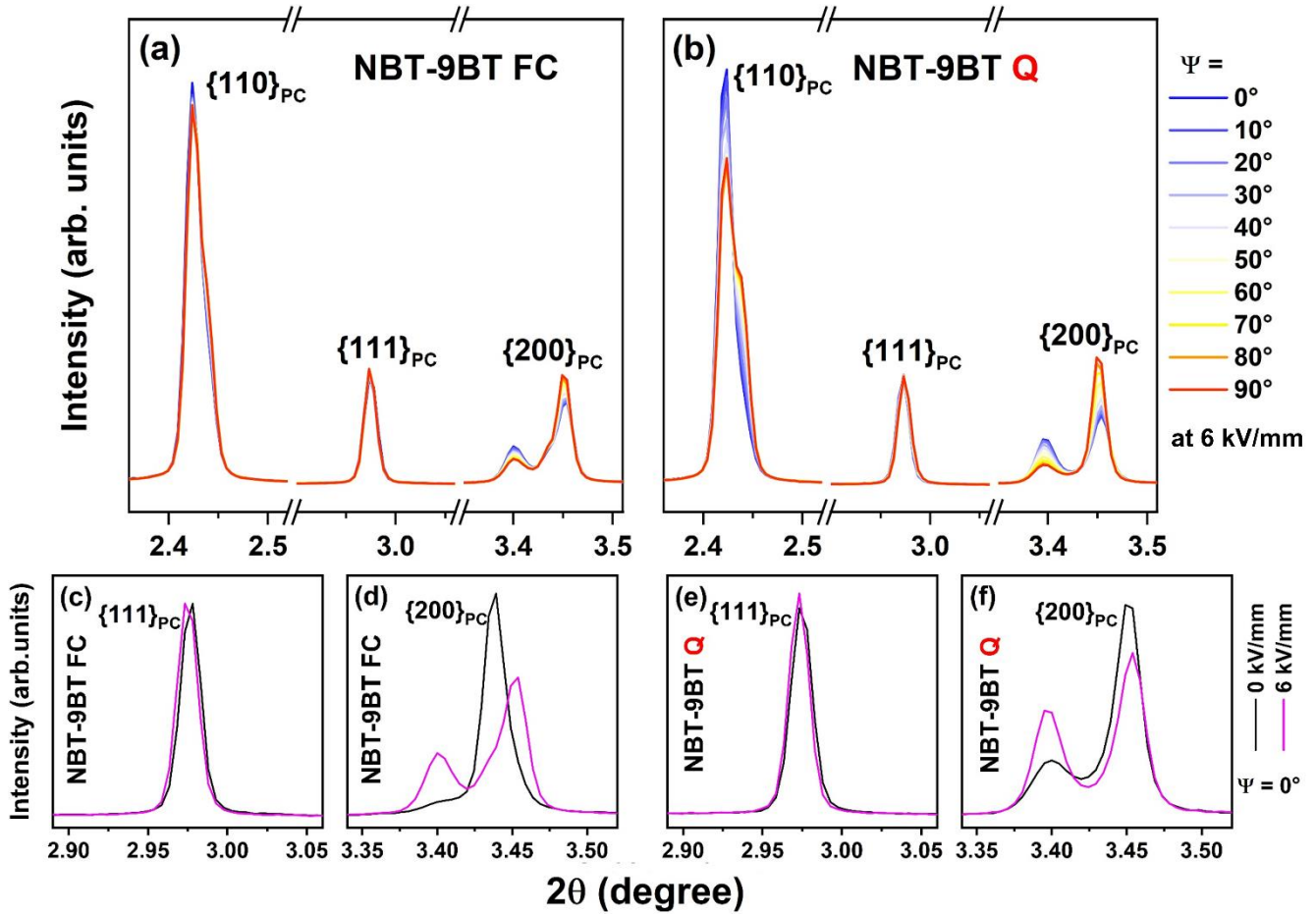


Figure 48: Excerpts of 1D diffraction patterns of NBT-9BT FC visualizing the strong angle dependence in peak intensities at an applied electric field of 6 kV/mm (a) and contrasting the reflection profiles of  $\{111\}_{PC}$  (c) and  $\{200\}_{PC}$  (d) reflections at 0 and 6 kV/mm parallel to the applied field direction. (b), (e) and (f) depict the same for NBT-9BT Q.

### 5.3.3 Quantitative Texture and Rietveld Analysis

*Quantitatively evaluating electric field-dependent structural data allows to extract texture factors describing the crystallographic anisotropy and volume fractions of the phases present in the material. The onset of domain texture and changes in phase composition are shifted to higher electric fields upon quenching NBT-BT.*

The texture factor  $f_{111}$  as a quantity for the crystallographic texture in the rhombohedral phase was calculated following equations (20) and (23) and using the integrated peak intensities of the  $111_R$  and  $11\bar{1}_R$  reflections for NBT-3BT FC and NBT-3BT Q. In Figure 49,  $f_{111}$  is plotted as a function of azimuthal angle for relevant electric field amplitudes. Values close to 1 indicate a random orientation of unit cells, which is the case for NBT-3BT FC up to electric fields of about 2.8 kV/mm (Figure 49a). Upon further increase in electric field, the material exhibits an increasing degree of texture with a maximum value of  $f_{111} = 2.84$  MRD at 3.82 kV/mm close-to parallel to the electric

field vector. This is a higher texturing than in the remanent state where  $f_{111} = 2.40$  MRD parallel to the poling field direction for the same material. A higher degree of texture measured *in situ* compared to *ex situ* is plausible since a fraction of ferroelectric domains will reorient upon removal of the electric field.  $f_{111}$  close-to parallel to the applied field decreases at 4.25 kV/mm to 2.66 MRD, which might be due to the beginning of dielectric breakdown, because the last data was collected at this field amplitude before the sample broke down.

For NBT-3BT Q,  $f_{111}$  starts to deviate significantly from values around 1 MRD at about 3.1 kV/mm. With further increase in field amplitude, the induced texturing becomes stronger, but is less pronounced compared to NBT-3BT FC. The maximum value for NBT-3BT Q is  $f_{111} = 2.33$  MRD at 3.82 kV/mm with the scattering vector close-to parallel to the electric field. Therefore, quenching NBT-3BT appears to hinder electric field-induced domain reorientation resulting in a lower texture factor for NBT-3BT Q compared to NBT-3FC at the same field amplitude.

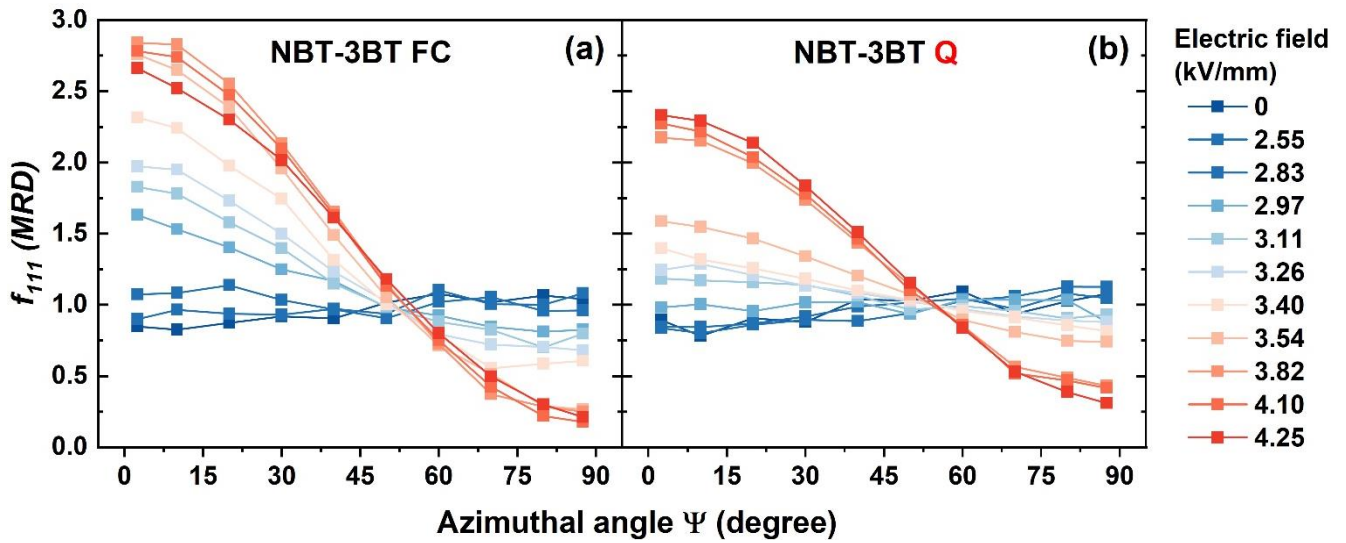


Figure 49: Texture factor,  $f_{111}$ , in MRD for NBT-3BT FC (a) and NBT-3BT Q (b) as a function of azimuthal angle for different applied electric fields.

Due to the lower  $2\theta$  resolution of the APS data, resulting in difficulties in single peak fitting and a lower reliability of the obtained intensity values, texture analysis for NBT-6BT and NBT-9BT materials was not performed in as much detail as for NBT-3BT.  $f_{111}$  and  $f_{002}$  were calculated for NBT-6BT and NBT-9BT following equations (20) and (21), respectively, furnace cooled and quenched, at the maximum field amplitude of 6 kV/mm (Figure 50). The data integrated from  $\Psi =$

40 – 50° ( $\Psi = 45^\circ$ ) of the respective 2D diffraction pattern was used as reference to calculate the texture factors.

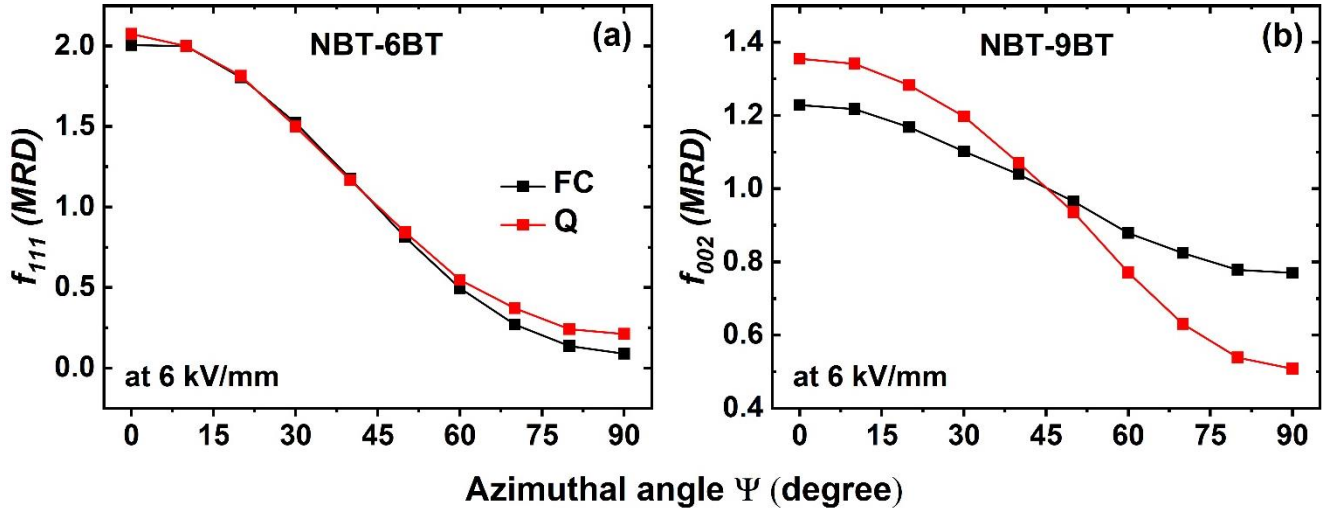


Figure 50: Calculated texture factors at 6 kV/mm applied electric field based on the peak fitting approach for the rhombohedral phase of NBT-6BT FC and NBT-6BT Q (a) and the tetragonal phase of NBT-9BT FC and NBT-9BT Q (b) using the  $45^\circ$  data as reference.

To fit the  $\{111\}_{PC}$  profiles of NBT-6BT FC and NBT-6BT Q of the APS data, only two peaks were used and interpreted as  $111_R$  and  $11\bar{1}_R$ , while for the higher resolved DESY single shot data three peaks were fitted as described in chapter 5.1.3. This leads to lower  $f_{111}$  values for the *in situ* data presented in this chapter with maxima of 2.00 and 2.07 MRD for NBT-6BT FC and NBT-6BT Q, respectively, parallel to the applied electric field (Figure 50a). This slight difference between furnace cooled and quenched is not of significance due to the low resolution, severe peak overlap and therefore rather large expected errors.

For NBT-9BT, the difference in  $f_{002}$  is larger between furnace cooled and quenched material with maxima of 1.23 and 1.35 MRD, respectively, at  $\Psi = 0^\circ$  (Figure 50b). The degree of crystallographic texture at 6 kV/mm is higher in NBT-9BT Q at all azimuthal angles compared to NBT-9BT FC and the difference is more pronounced than in the poled remanent state (Figure 29c). This indicates an increased domain switching fraction in the tetragonal phase of the quenched sample upon application of electric field. A possible explanation are the different conditions of formation of the tetragonal phase in NBT-9BT FC and NBT-9BT Q. While the long-range tetragonal order and therefore tetragonal ferroelectric domains are electric field-induced in NBT-9BT FC (Figure 47b), a strong tetragonal distortion and hence tetragonal phase is already present in the initial state of

NBT-9BT Q. Because of that, the tetragonal phase in NBT-9BT Q might be more susceptible to field induced-texturing.

Rietveld refinements were carried out for all compositions investigated with *in situ* synchrotron experiments and for all applied electric field amplitudes to extract volume fractions of the respective phases present (Figure 51). For NBT-3BT data, the same weighting approach to receive a reference pattern with negligible texture was applied as described in chapter 5.1.3. By that, the usage of a model compensating for anisotropy in the material is not necessary, limiting the refineable parameters. For NBT-6BT and NBT-9BT, whole diffraction patterns at  $\Psi = 45^\circ$  were used for refinement. The phase fractions established by this simpler approach do not account for the grain-scale heterogeneity reported for NBT-BT materials resulting in an orientation-dependent phase evolution [217]. Nevertheless, this simplification seems appropriate due to the lower resolution of the APS data and was successfully applied as reported by different research groups for PZT materials [218-220] and recently for NBT-BT [221].

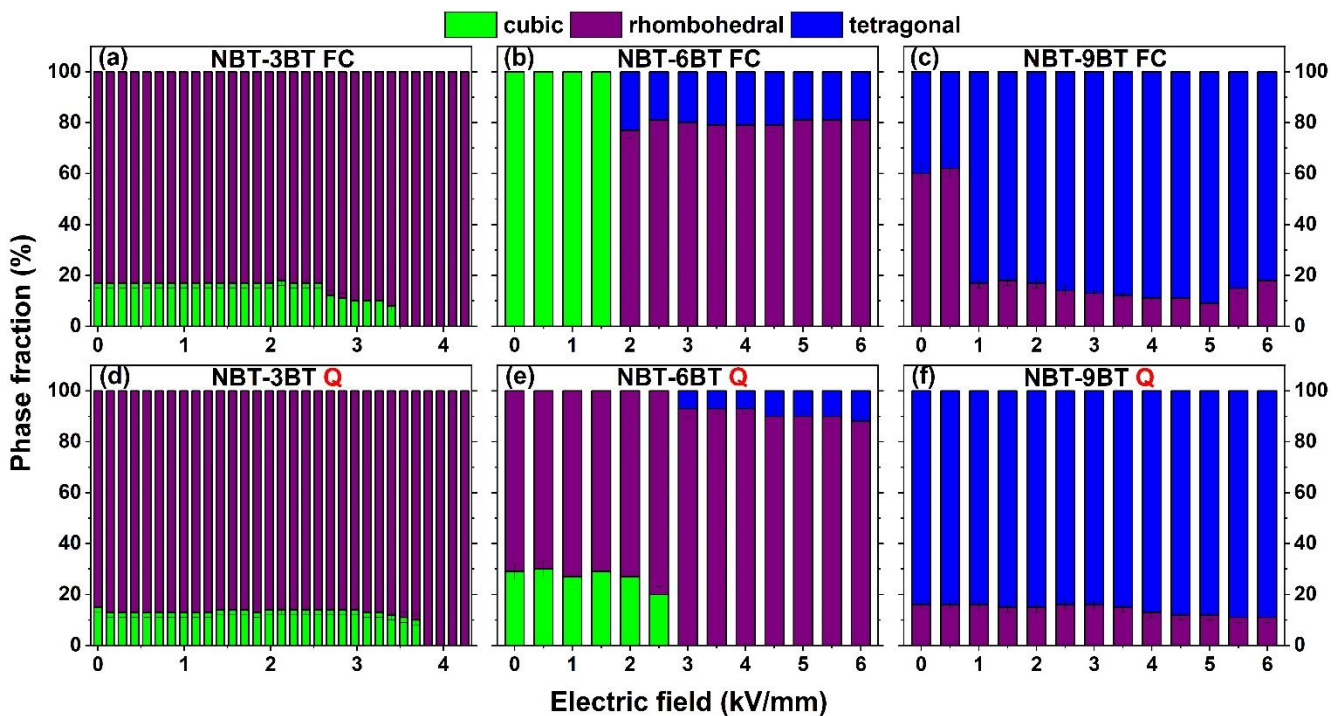


Figure 51: Phase fractions as a function of electric field obtained using Rietveld refinement.

In accordance with the single shot synchrotron X-ray diffraction data (chapter 5.1.3) and literature [181], NBT-3BT FC and NBT-3BT Q were refined using a two phase model of  $R3c$  and  $Pm\bar{3}m$  phases in the initial unpoled state. A single phase  $R3c$  model was tried but did not result in satisfactory

---

fits. Up to applied electric fields of 2.55 kV/mm, the phase fractions of NBT-3BT FC stay constant within the margins of error with 83 % of  $R3c$  and 17 % of  $Pm\bar{3}m$  phases (Figure 51a). This is consistent with the phase fractions obtained by refining the single shot data of unpoled bulk material (Table 3), confirming good reproducibility of the refinements. Upon further increasing the electric field, the cubic phase fraction vanishes in a two stage event. At about 2.69 kV/mm,  $Pm\bar{3}m$  phase volume decreases to 12 % and at 3.40 kV/mm to 8 %. The rhombohedral single phase state is established at 3.54 kV/mm and remains until 4.25 kV/mm, above which the sample experienced dielectric breakdown. NBT-3BT Q exhibits a similar phase evolution under the application of electric field, however, the vanishing of the cubic phase is more abrupt and takes place at a higher field amplitude (Figure 51d). Up to 3.26 kV/mm, the  $R3c$  and  $Pm\bar{3}m$  phase fractions are constant at 85 - 87 % and 13 - 15 %, respectively. By increasing the electric field to 3.68 kV/mm, the cubic phase fraction decreases to 10 %, while the rhombohedral increases to 90 %. At electric fields above 3.68 kV/mm, NBT-3BT Q also transforms into a single  $R3c$  phase system which remains unchanged upon further increasing field amplitude. This quenching-induced enhancement in the necessary electric field strength to induce a rhombohedral single phase state is coupled with domain reorientation as reflecting in the raw data recorded parallel to the applied field (Figure 43). Furthermore, it correlates with the increase in coercive field upon quenching (Figure 34).

In the initial state, NBT-6BT FC does not display any sign of non-cubic distortion within the detection limit of the X-ray diffraction experiments and was therefore refined using a single-phase  $Pm\bar{3}m$  model (Figure 51b). Between 1.5 and 2.0 kV/mm, the material transforms from cubic into a two-phase state with coexisting rhombohedral and tetragonal phases with respective phase fractions of 77 and 23 %. The chosen phases for refinement were  $R3c$  and  $P4mm$  in accordance with literature [60, 76, 80]. The  $R3c$  phase fraction slightly increases upon further increase in electric field amplitude and reaches 81 % at the maximum applied field of 6 kV/mm. This is in rather close agreement with a very recent study reporting phase fractions for normally sintered NBT-6BT and NBT-7BT of 92 and 79 % for rhombohedral phase and of 8 and 21 % for tetragonal phase, respectively, at 6 kV/mm established from refining *in situ* synchrotron XRD data [221].

Since NBT-6BT Q already exhibits a rhombohedral distortion in the initial state (Figure 45c), a two-phase model of  $R3c$  and  $Pm\bar{3}m$  was used for refinement (Figure 51e). This quenching-induced lowering of average symmetry and therefore change in phase composition in NBT-6BT is in agreement with the structural results obtained from *ex situ* XRD data (chapter 5.1) and with literature [12]. The stabilized long-range ferroelectric order [13], resulting in a deviation from the

---

cubic average structure upon quenching, can be correlated to the enhanced off-centering of the  $\text{Bi}^{3+}$ -ion reflecting in increased lattice distortion [149]. In contrast to the unpoled single shot data measured at DESY, using a three-phase model also containing  $P4mm$  phase did not improve the refinement results. This difference is probably connected to the lower  $2\theta$  resolution of the *in situ* APS data, making the small tetragonal distortion in the material impossible to resolve. Upon applying an electric field of 2.5 kV/mm, the  $R3c$  phase fraction in NBT-6BT Q increases to 80 %, before the cubic phase vanishes and the material transforms into a two-phase system of  $R3c$  and  $P4mm$  phases between 2.5 and 3.0 kV/mm with fractions of 93 and 7 %, respectively. With further increasing the electric field amplitude, the  $P4mm$  phase fraction slightly increases to 12 % at 6 kV/mm while the  $R3c$  phase fraction decreases to 88 %.

Both NBT-9BT FC and NBT-9BT Q were refined with a two-phase model of rhombohedral  $R3m$  and tetragonal  $P4mm$  phases (Figure 51c and f) [85]. Even though there is no signature of a rhombohedral distortion in the respective diffraction patterns (Figure 47a and c), the presence of a weakly distorted rhombohedral phase was proven by TEM findings [180]. Furthermore, using a single-phase tetragonal model did not lead to satisfactory fits for both NBT-9BT FC and NBT-9BT Q irrespective of the applied electric field. Refining the initial state of NBT-9BT FC resulted in volume fractions of 60 and 40 % for  $R3m$  and  $P4mm$  phases, respectively. Between electric field amplitudes of 0.5 and 1.0 kV/mm, the tetragonal phase fraction increases strongly to 83 %. Upon further field increase, the increase in  $P4mm$  phase fraction reaches a maximum of 91 % at a field amplitude of 5 kV/mm. However, at the maximum field amplitude of 6 kV/mm, the rhombohedral phase fraction has increased to 18 %, while the tetragonal phase fraction decreased to 82 %. This corresponds to the emerging peak shoulder between the  $002_{\text{T}}$  and  $200_{\text{T}}$  reflections (Figure 47b).

Fitting to the similar phase composition of NBT-9BT Q in the unpoled and in the poled state (Table 3 and Table 4), there are no strong changes in the refined phase fractions upon application of electric field for this material (Figure 51f). The volume fraction of  $P4mm$  phase increases from 84 to 89 % between the virgin state and an applied field amplitude of 6 kV/mm, while the  $R3m$  phase fraction decreases from 16 to 11 %. This quantifies the absence of a field-induced phase transition as expected from the evolution of peak profiles (Figure 47c and d) and corroborates the stabilization of ferroelectric order upon quenching [13].

For all the compositions of NBT-BT investigated in this study with *in situ* electric field-dependent and *ex situ* synchrotron XRD in the poled and unpoled state, the differences in phase fractions between the *in situ* state at high electric fields and the poled remanent state are negligible expect

---

for NBT-9BT FC (Figure 51 and Table 4). NBT-9BT FC has a 5 % higher rhombohedral phase fraction at an applied electric field of 6 kV/mm than in the remanent poled state. This difference is not large, however, might be caused by the fact that with increasing electric field, the unit cell orientation plays a more pronounced role in determining the direction of the polarization vector and by that, the nature of the distortion of the unit cell compared to the chemical composition of the material. Hinterstein et al. claimed for a NBT-BT materials with coexisting rhombohedral and tetragonal phases an ideal phase ratio of  $\frac{8}{14}$  to  $\frac{6}{14}$  or 57.1 to 42.9 %, respectively [76]. These numbers are established from the possible orientation directions of the polarization vectors which are 8 and 6 for rhombohedral and tetragonal symmetries, respectively. Therefore, the phase fractions of NBT-9BT might evolve towards this ideal ratio with increasing electric field. NBT-9BT FC might be more susceptible to this effect than the other investigated compositions since it has the lowest coercive field (Figure 34) or the lower coercive field may indicate a higher sensitivity to field-induced changes in the material. These post-coercive field-induced structural changes towards the ideal ratio might be reversible, explaining the difference in phase composition between the *in situ* and the *ex situ* poled state. Furthermore, the onset of peak asymmetry in the  $\{200\}_{PC}$  reflection of NBT-3BT FC and NBT-3BT Q at high applied electric fields (Figure 43b and d), hinting towards a slight tetragonal distortion, further strengthens the hypothesis of a field-induced phase evolution towards the mentioned ratio. However, this small hint of a tetragonal distortion in NBT-3BT data with scattering vectors close to parallel to the electric field, did not reflect in the observed phase fractions established from the averaged data. For all other compositions except for NBT-9BT FC, the same phase fractions in the *in situ* and in the *ex situ* poled state indicate an absence of significant structural changes and no restoration of the zero-field state upon removal of electric field which corresponds to the non-ergodic nature of NBT-based materials [72, 222]. Furthermore, quenching hinders (NBT-9BT) or shifts (NBT-3BT and NBT-6BT) the electric field-induced phase changes to higher electric fields, consistent with the qualitative synchrotron data evaluation and the coercive fields measured with ferroelectric hysteresis measurements (chapter 5.1.5).



---

### 5.3.4 Volumetric Strain Calculation for NBT-6BT and NBT-9BT

---

*Phase transformations for example caused by applying an electric field to a ferroelectric can result in strain due to differences in unit cell volume between the initial and the electric field-induced phase or phases. This strain contribution can be derived from phase fractions and unit cell parameters of the present phases, revealing a significant decrease in volumetric strain upon quenching NBT-BT.*

Phase transformation or volumetric strain,  $\varepsilon_V$ , is neither the only mechanism contributing to the overall strain in ferroelectrics nor necessarily the dominant one [60], however, it is simple to calculate once the phase composition of a material is determined and does not require high  $2\theta$  resolution as it is the case for the NBT-6BT and NBT-9BT data. For these materials, the approach described here to extract the contribution of volumetric to the overall strain is of particular interest [179], since NBT-6BT and NBT-9BT exhibit an electric field-induced relaxor to ferroelectric transition. The volumetric strain contribution can be calculated for every electric field step using equation (24):

$$\varepsilon_V = \frac{1}{3} [(V_{\text{field}} - V_{\text{initial}})/V_{\text{initial}}] \quad (24)$$

where  $V_{\text{field}}$  and  $V_{\text{initial}}$  are the average unit cell volumes at a certain applied field and in the initial state before an electric field was applied, respectively [60, 179]. The average unit cell volume,  $V$ , is calculated as the weighted sum of unit cell volumes of the coexisting phases. This means, exemplarily for NBT-6BT FC after the phase transition, equation (24) can be specified to equation (25):

$$\varepsilon_V = \frac{1}{3} [(PF_R \cdot V_R) + (PF_T \cdot V_T) - V_C]/V_C \quad (25)$$

where  $PF$  is the phase fraction of the respective phase,  $V_R$  and  $V_T$  are the unit cell volume of the rhombohedral and tetragonal phases at a certain electric field, respectively, and  $V_C$  is the unit cell volume of cubic phase in the initial state. While the phase fractions used for calculating  $\varepsilon_V$  were established from Rietveld refinements of the  $\Psi = 45^\circ$  data, the volume fractions were calculated using the lattice parameters of the respective phase averaged throughout the whole orientation space [179]. For example, the rhombohedral lattice parameter  $a_R$  was calculated following equation (26):

$$a_R = \int_{\alpha=0}^{2\pi} a(\alpha) \sin(\alpha) d\alpha \quad (26)$$

---

or written in discrete form:

$$a_R = \sum_{\alpha=0^\circ}^{90^\circ} a(\alpha) [\cos(\alpha_i) - \cos(\alpha_j)] \quad (27)$$

where  $\alpha_i$  and  $\alpha_j$  are the low and high boundaries of the respective azimuthal range. The azimuthal angle-dependent lattice parameters of the phases present at each electric field step were established by performing LeBail fits on the respective 1D diffraction patterns.

To correlate the calculated volumetric strains, macroscopic strain measurements were performed with the same electric field step size and frequency as the *in situ* diffraction experiments as described in chapter 4.7. Calculated volumetric and measured macroscopic strain are plotted in Figure 52 as a function of electric field for furnace cooled and quenched NBT-6BT and NBT-9BT. Even though the measurement frequency for these experiments is about 0.017 Hz and therefore orders of magnitudes lower compared to the macroscopic strain measurements with 1 Hz presented in Figure 33, the observed trends are the same and even the absolute strain values are comparable. The quenching-induced delay in electric field response, which reflects also as an increase in coercive field upon quenching in the 1 Hz measurements (Figure 34), can be observed as an enhanced switching field in the macroscopic strain measurements with step-wise applied field (Figure 52) and was previously reported for NBT-9BT [13]. The inflection point of the strain curve is interpreted as switching field and shifts by 0.5 and 1.0-1.5 kV/mm for NBT-6BT and NBT-9BT, respectively, upon quenching (Figure 52). The maximum strain achieved at 6 kV/mm is higher for NBT-6BT Q compared to NBT-6BT FC with 0.47 and 0.42 %, respectively, but it is slightly lower for NBT-9BT Q compared to NBT-9BT FC with 0.30 and 0.31 %, respectively. This is in agreement with the maximum strain curves of the first strain cycle for these materials measured with 1 Hz (Figure 33b and c). Therefore, there is no consistent trend, as to whether quenching increases or decreases the maximum strain achievable by applying an electric field to a virgin sample.

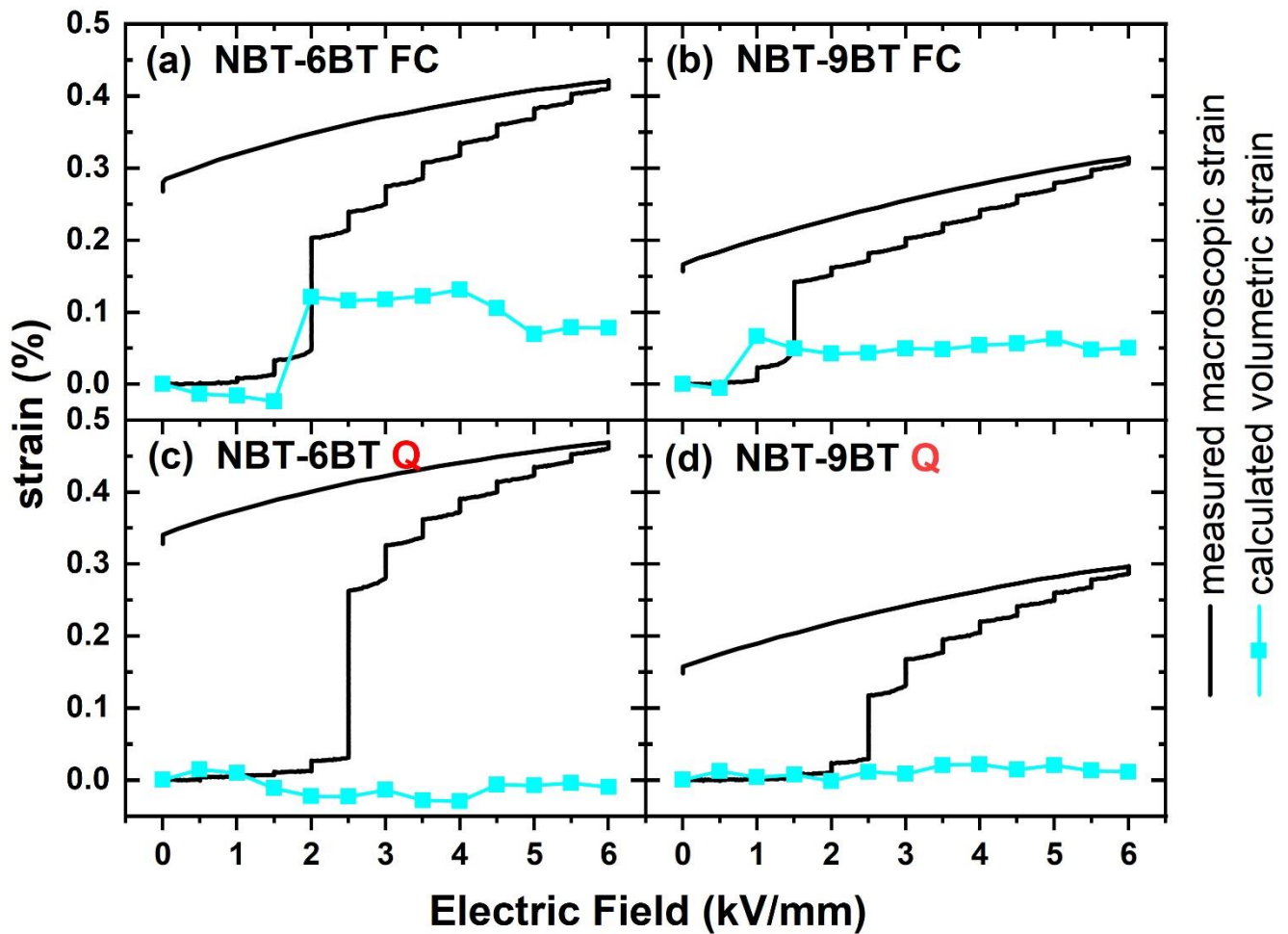


Figure 52: Measured macroscopic strain and calculated volumetric strain,  $\epsilon_v$ , as a function of applied electric field for (a) NBT-6BT FC, (b) NBT-9BT FC, (c) NBT-6BT Q and (d) NBT-9BT Q.

Due to the relaxor-to-ferroelectric transformation, both NBT-6BT FC and NBT-9BT FC exhibit an increase in  $\epsilon_v$  to about 0.12 and 0.07 % at 2.0 and 1.0 kV/mm, respectively. The electric field amplitudes at which the volumetric strain sets in are consistent with the field steps at which the respective pronounced phase transformations occur (Figure 51b and c). The  $\epsilon_v$  values for NBT-6BT FC are in close agreement with literature values for NBT-7BT showing volumetric strain contribution of 0.10 and 0.11 at 1.6 and 2.0 kV/mm, respectively [60]. For NBT-9BT FC, there is about a 0.5 kV/mm off-set in electric field amplitude between the inflection point of the macroscopic strain measurement and the calculated  $\epsilon_v$ . As mentioned in chapter 5.3.2, this difference between the laboratory and the synchrotron experiments might arise from the influence of the sample being exposed to a high energy X-ray beam during the latter. In contrast to the furnace cooled materials, NBT-6BT Q and NBT-9BT Q do not exhibit a sudden rise in  $\epsilon_v$  even though a comparable increase in macroscopic strain can be observed for both, furnace cooled and quenched materials. Regardless of the applied electric field, the quenched samples exhibit overall

---

low values for  $\varepsilon_V$ . The absence of a field-induced phase transition in NBT-9BT Q plausibly reflects in  $\varepsilon_V$  values close to zero. In the case of NBT-6BT Q, an electric field-induced phase transition is present (Figure 51e), however, the material does not exhibit an inflection in  $\varepsilon_V$ . This can be rationalized as the quenching-induced ferroelectric order altering the phase transformation sufficiently to result in negligible  $\varepsilon_V$  values in both NBT-6BT Q and NBT-9BT Q.

The results presented here, which indicate that quenching NBT-BT causes negligible volumetric strain values under the influence of an electric field, are consistent with the other results of this study and with prior research [13]. The weakening or even absence of electric field-induced structural changes in NBT-BT by the quenching treatment resulting in low  $\varepsilon_V$  values that are observed in this study can be rationalized by the enhanced off-centering of the  $\text{Bi}^{3+}$ -ion which is correlated to an increased lattice distortion in quenched samples compared to furnace cooled ones [49, 149]. Additional studies revealed a freezing-in of the defect distribution from a high-temperature state which alters the equilibrium oxygen vacancy concentration in NBT-BT upon quenching [13, 158]. Both quenching-induced phenomena, the increased  $\text{Bi}^{3+}$ -ion off-centering and the non-equilibrated oxygen vacancy concentration might lead to a consolidation of the structure and by that, promote the spontaneous formation of a ferroelectric domain state and long-range order in the material. Ultimately, this could lead to an absence of electric field-induced volumetric strain and a delayed onset or even absence of phase transformation upon application of an electric field in quenched NBT-BT.

---

### 5.3.5 Lattice and Domain Switching Strain Calculations for NBT-3BT

---

*In addition to the already discussed volumetric strain, two other strains contribute to the macroscopically measured total strain, namely lattice or intrinsic and domain switching or extrinsic strain. In the following, these are presented and evaluated for furnace cooled and quenched NBT-3BT.*

As described in chapter 2.3, applying an electric field of sufficient strength to a ferroelectric material results in unit cell expansion and domain reorientation into the direction of electric field. Both mechanisms cause strain and also reflect in the diffraction pattern of the respective material [185, 188, 223]. Unit cell extension causes a shift in d-spacing and therefore a change in  $2\theta$  position of the reflection of the respective lattice plane in the XRD pattern and is referred to as intrinsic or lattice strain. Domain and by that unit cell reorientation results in an anisotropic distribution of

unit cell orientation and consequently in an azimuthal angle dependence of peak intensities. This strain contribution is called extrinsic or domain switching strain [186].

The intrinsic strain contribution can be described as the weighted sum of the strains resulting from the change in d-spacing of each individual lattice plane. This linear strain contribution,  $\varepsilon_{\text{hkl}}$ , from one hkl lattice plane is calculated following equation (28):

$$\varepsilon_{\text{hkl}} = \frac{d_{\text{hkl,field}} - d_{\text{hkl,initial}}}{d_{\text{hkl,initial}}} \quad (28)$$

with  $d_{\text{hkl,field}}$  and  $d_{\text{hkl,initial}}$  as the hkl lattice spacings during application of a certain electric field amplitude and before field application, respectively [188, 224]. The lattice spacings were calculated from the respective peak positions following Bragg's law [225]. Peak positions were determined by single-peak fitting with a Pseudo-Voigt peak shape function of the data collected with the scattering vector close-to-parallel to the electric field ( $\Psi = 2.5^\circ$ ). The total lattice strain,  $\varepsilon_{\text{intrinsic}}$ , for a ceramic material can then be calculated as a weighted sum of the different hkl lattice strains according to equation (29):

$$\varepsilon_{\text{intrinsic}} = \sum_{\text{hkl}} f_{\text{hkl}} \cdot m_{\text{hkl}} \cdot \varepsilon_{\text{hkl}} / \sum_{\text{hkl}} f_{\text{hkl}} \cdot m_{\text{hkl}} \quad (29)$$

where  $f_{\text{hkl}}$  is the texture factor quantifying the domain orientation density in MRD in direction of the applied electric field and  $m_{\text{hkl}}$  is the planar multiplicity of the respective hkl crystallographic plane [188, 226]. In some literatures  $f_{\text{hkl}}$  is labelled as  $T_{\text{hkl}}$ . However, both labellings refer to the same quantity, the texture factor.  $f_{111}$  can be calculated following equation (20) for the rhombohedrally distorted NBT-3BT based on peak intensity values obtained from single peak fitting. For hkl reflections which remain singlets in the diffraction pattern of a material with rhombohedral symmetry, e.g. {200},  $f_{\text{hkl}} = 1$  [191, 227].

The domain switching strain,  $\varepsilon_{\text{non-180}}$ , which is linked to non-180° domain wall motion in a ferroelectric material can be calculated following equation (30):

$$\varepsilon_{\text{non-180}} = \eta \int_{\alpha=0}^{2\pi} [\Delta f_{\text{hkl}\alpha}(\alpha) \cdot \cos^2(\alpha)] \sin(\alpha) d\alpha \quad (30)$$

with  $\eta$  (in some literatures denoted as  $S$ ) as the spontaneous strain of the ferroelectric phase,  $\Delta f_{\text{hkl}} = f_{\text{hkl}} - 1$  and  $\alpha$  as the angle to the electric field direction [187, 188]. The trigonometric functions serve as geometrically necessary weighting factors of the respective azimuthal region.  $\eta_{\text{rhom}}$  and

$\eta_{tet}$  for rhombohedral and tetragonal phases are defined as  $\eta_{rhomb} = \frac{\sqrt{2}c_{rhomb}}{2\sqrt{3}a_{rhomb}} - 1$  and  $\eta_{tet} = \frac{c_{tet}}{a_{tet}} - 1$  with  $c$  and  $a$  as the lattice parameters of the respective phase, for the rhombohedral phase in hexagonal notation [60, 76].

Volumetric, lattice and domain switching strain contributions were calculated for every electric field step as described above and summed up for NBT-3BT FC and NBT-3BT Q (Figure 53a and b).  $\epsilon_{non-180}$  is derived for the rhombohedral material with  $f_{111} - 1$  as  $\Delta f_{hkl}$  (Figure 49). In both, the furnace cooled and quenched NBT-3BT,  $\epsilon_V$  is the smallest contribution to the summed up electric field-induced strain with 0.07 and 0.02 % at 4.25 kV/mm, respectively. This can be rationalized by the small changes in phase fractions upon application of electric field from a two-phase mixture of dominant rhombohedral and cubic phase to single rhombohedral phase (Figure 51). Also in NBT-3BT, quenching strongly reduces  $\epsilon_V$  values as consistent with results on NBT-6BT and NBT-9BT (Figure 52).

Similar to  $\epsilon_V$ , significantly lower  $\epsilon_{intrinsic}$  values are observed for NBT-3BT Q compared to NBT-3BT FC with 0.08 and 0.20 % at 4.25 kV/mm, respectively, however, not only at high applied fields but at all investigated electric field steps. Therefore, quenching might not only hinder electric field-induced phase transitions in NBT-BT, resulting in strongly reduced volumetric strain, but also restrict the change in lattice spacing causing lower intrinsic or lattice strain contribution. Nevertheless, the reduction, both in  $\epsilon_V$  and  $\epsilon_{intrinsic}$  upon quenching might be linked, since for both strain contributions the change in d-spacing during field application is critical, in the former as change in unit cell volume. Since quenching enhances the off-centering but also reduces the fluctuation in the off-centering of the  $Bi^{3+}$ -ion [149], the initial distortion and unit cell parameters might be stabilized and less affected by the application of an electric field compared to furnace cooled NBT-BT.

The  $\epsilon_{non-180}$  values of NBT-3BT FC and NBT-3BT Q exhibit similar maxima, even though the electric field-induced texture is stronger in NBT-3BT FC (Figure 49). This gets compensated by the overall enhanced rhombohedral distortion,  $\eta_{111}$ , in NBT-3BT Q. The maximum in  $\epsilon_{non-180}$  for NBT-3BT FC is observed at 3.96 kV/mm with 0.21 % while in NBT-3BT Q,  $\epsilon_{non-180}$  increases to 0.20 % at the highest measured field amplitude of 4.39 kV/mm. Likely, if the sample would not have experienced dielectric breakdown,  $\epsilon_{non-180}$  would have increased further. Quenching seems to not have a strong influence on the domain switching strain in NBT-3BT. However, the inflection

point of  $\epsilon_{\text{non-180}}$  is shifted slightly from 2.83 to 3.11 kV/mm upon quenching, as consistent with qualitative observations (Figure 43) and the onset of crystallographic texturing (Figure 49).

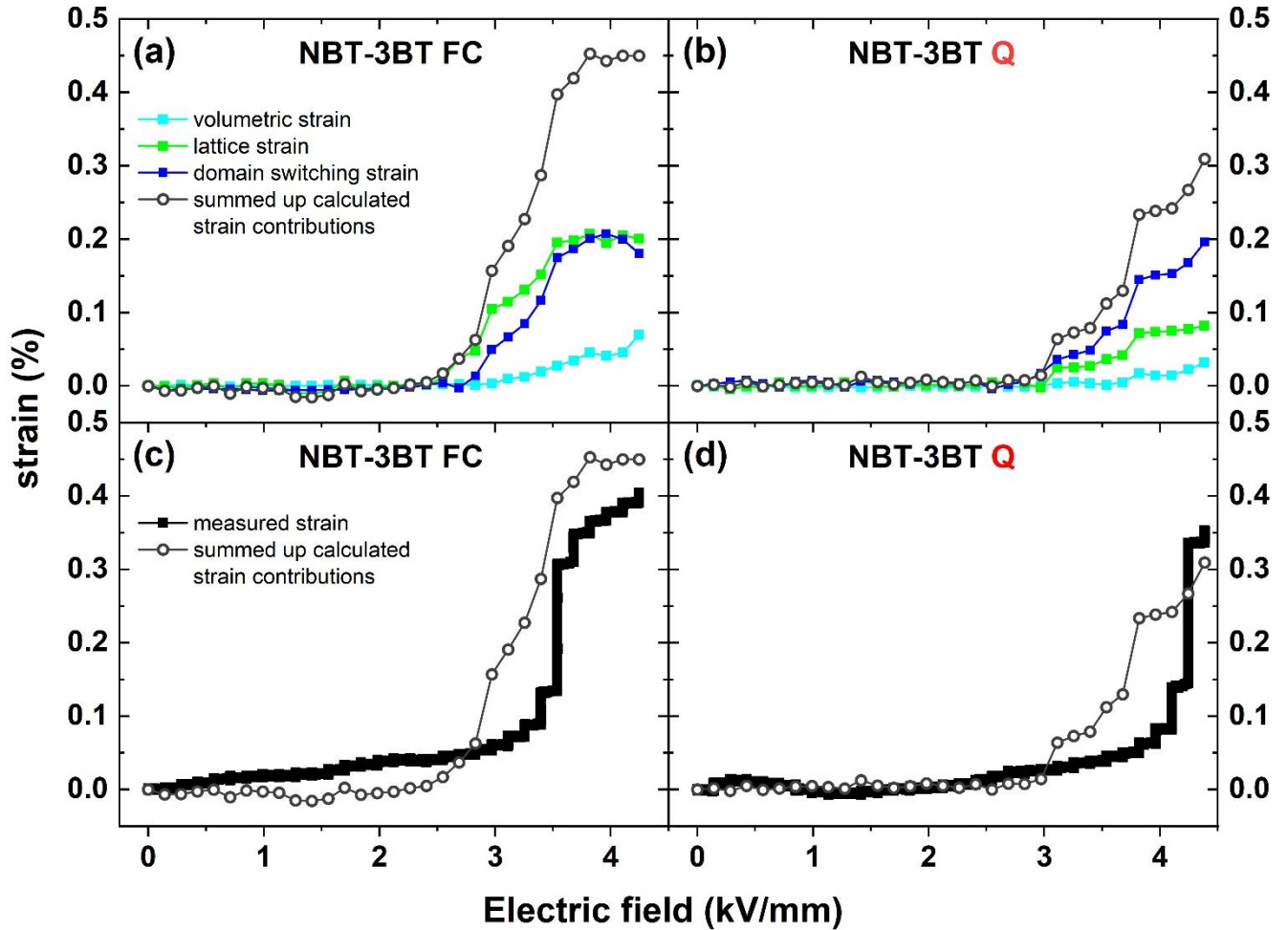


Figure 53: Calculated strain contributions and the comparison between measured and summed up calculated strain as a function of electric field for NBT-3BT FC (a, c) and NBT-3BT Q (b, d).

The three calculated strain contributions are summed up and compared to macroscopically measured strains of NBT-3BT FC and NBT-3BT Q (Figure 53c and d). The macroscopic strain values were obtained with an optical displacement sensor in a laboratory setup and the same electric field steps and holding times per step as during the synchrotron experiments were applied. For both materials, the strain values calculated from synchrotron diffraction data show an inflection point at lower electric fields compared to the directly measured strain. The reason for this is most likely the influence of the high energy X-ray beam as discussed earlier. For NBT-3BT FC, the calculated strains sum up to a value of 0.45 % at 4.25 kV/mm and therefore overestimate the actual strain. The measured strain reaches only 0.40 % at the same electric field

---

amplitude. The trend is opposite for the quenched material with 0.31 and 0.35 % for calculated and measured strains at 4.39 kV/mm, respectively. However, the domain switching might not be saturated at that field amplitude in NBT-3BT Q making the differently obtained strain values difficult to compare. Furthermore, considering the numerous assumptions being made to calculate the different strain contributions, the misfits between calculated and directly measured strains of 0.05 and 0.04 % for NBT-3BT FC and NBT-3BT Q, respectively, seem acceptable.

---

### 5.3.6 Short Summary

---

Electric field-dependent synchrotron X-ray diffraction experiments were carried out on furnace cooled and quenched NBT-3BT, NBT-6BT and NBT-9BT at DESY and APS. In addition to qualitative data evaluation, the degree of field-induced crystallographic texture and field-dependent phase fractions were established and utilized to quantify the different strain contributions in a ferroelectric material. The *in situ* experiments revealed an increase in electric field-amplitude necessary to induce structural changes in quenched NBT-BT like increase in unit cell distortion or change in relative peak intensities. This observation in the diffraction patterns is supported quantitatively by Rietveld refinements and strain calculations and correlates with an increase in coercive field upon quenching.

Calculating texture factors reveals a lower degree of crystallographic texture in NBT-3BT Q compared to NBT-3BT FC at the same applied fields and a lower maximum of induced texture. At 6 kV/mm, texture degree in the rhombohedral phase in NBT-6BT is the same for furnace cooled and quenched samples while the texturing in the dominant tetragonal phase in NBT-9BT Q is more pronounced than in NBT-9BT FC. The lack of a consistent trend makes interpretation challenging, however, the different behavior of NBT-3BT, NBT-6BT and NBT-9BT regarding to the influence of quenching on texturing might be connected to the different phase assemblages of the three compositions.

Due to the stabilized ferroelectric state, the field-induced phase transition in quenched NBT-BT is weakened, leading to strongly reduced volumetric strain values. Furthermore, lattice and domain switching strains were calculated for NBT-3BT with the first being reduced in NBT-3BT Q compared to NBT-3BT FC, which can be correlated to the enhanced but more consistent Bi<sup>3+</sup>-ion off-centering upon quenching [149]. This plausibly supports a more distorted but more resilient structure which might experience less change in lattice spacing and by that lower lattice strains



---

upon application of electric field. Even though texturing is lower in NBT-3BT Q, the domain switching strains are comparable for furnace cooled and quenched NBT-3BT due to the higher spontaneous strain in the quenched material. Comparing the calculated strains with measured strains from a laboratory setup validate the calculations but also reveal an offset in field amplitude of the inflection points of strains calculated from synchrotron data and strains measured in the lab. The high energy X-rays in the synchrotron might influence the material and shift the respective material response to lower electric field amplitudes.

In addition to the presented findings on the influence of quenching on the electric field-dependent structural characteristics of NBT-BT, two phenomena support the hypothesis that the nature of unit cell distortion and thereby phase assemblage of the perovskite material is increasingly dictated by unit cell orientation instead of chemical composition if the applied field is sufficiently strong [76, 193]. These phenomena are the asymmetry in the  $\{200\}_{\text{PC}}$  reflection in both NBT-3BT FC and NBT-3BT Q and the increase in rhombohedral phase fraction in NBT-9BT FC at high applied electric fields. Both compositions are well within the rhombohedral and tetragonal regions of the phase diagram, respectively [54], however, large electric fields cause the onset of tetragonal distortion in NBT-3BT in direction of the applied field and an increase in the assumingly less stable rhombohedral phase in NBT-9BT FC.

---

## 5.4 Effect of Introducing $\text{Na}_{1/2}\text{Bi}_{1/2}\text{TiO}_3$ and Quenching on $\text{BiFeO}_3\text{-BaTiO}_3$

---

In this chapter, the change in structural and electrical properties of BF-BT upon forming a ternary system with NBT and subsequent quenching are elucidated. The findings presented here are currently being prepared for publication.

---

### 5.4.1 Introduction and Motivation

---

The  $\text{BiFeO}_3\text{-BaTiO}_3$  system is a well-known ferroelectric material which is suitable for high-temperature applications [90, 91]. Quenching BF-BT ceramics from high temperatures, either directly after the sintering step or more commonly by reheating and subsequent quenching, impacts the material's structure and enhances application-relevant properties such as resistivity and piezoelectric response [161, 162]. Several research groups have studied the quenching-induced effects on pure, doped and ternary BF-BT compositions, considering the formation of secondary phases, effects on the microstructure (core-shell features) and on application-relevant properties, for example coercive field or  $d_{33}$  (chapter 2.6.2) [14]. Some dopants like Mn and La [90, 123], and ternary systems like  $\text{BiFeO}_3\text{-BaTiO}_3\text{-Bi}(\text{Mg}_{1/2}\text{Ti}_{1/2})\text{O}_3$  [103, 104] are well investigated. However, there is only a limited number of recent studies on the ternary BF-BT-NBT system. Even though, the presented properties such as remanent polarization,  $d_{33}$  and  $T_c$  are promising, especially when introducing 5 mol% NBT into an MPB composition of BF-BT [15], no study has reported on the influence of quenching on the BF-BT-NBT system with BF and BT as the dominant endmembers. By introducing only small percentages of NBT, the material mainly resembles BF-BT, so quenching can be expected to still impact its properties, especially, because NBT is affected by quenching as well. The lack of quenching studies on this relatively new ternary composition presents a promising opportunity to investigate the quenching mechanics and further improve an already promising lead-free candidate material.

Due to the difficulties with secondary phases and achieving desirable ferro- and piezoelectric properties when synthesizing BF-BT ceramics, initial experiments were conducted in the research group of Dr. David Hall at the University of Manchester to benefit from their expertise. However, the first produced batches had an inhomogeneous microstructure and inferior properties. Therefore, the results presented here originate from a batch manufactured at the Technical

University of Darmstadt after the research visit had ended. Nevertheless, the knowledge acquired during the research stay was utilized and of paramount importance for the processing procedure.

#### 5.4.2 Phase Purity, Microstructure and Density

*Phase-pure synthesis of BF-based material systems is challenging, including BF-BT. Therefore, it is critical to check the phase purity, microstructure and density of the calcined ceramic powders and sintered bulk ceramics to optimize processing conditions and validate a successful processing route.*

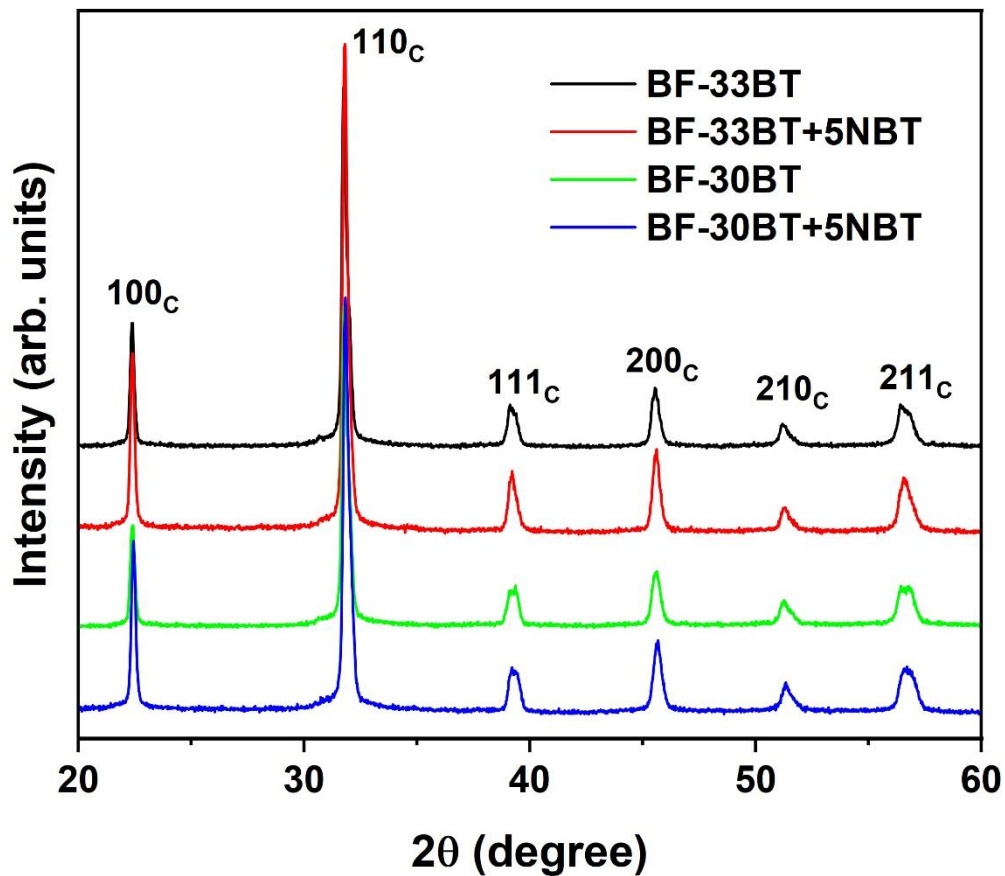


Figure 54: Powder XRD patterns of calcined and crushed BF-BT(-NBT) compositions. The characteristic perovskite reflections are indexed with respect to a cubic reference frame.

Laboratory XRD patterns of calcined and crushed BF-BT(-NBT) compositions synthesized with optimized precursor purity, milling and calcination parameters of 830 °C for 6 h are depicted in Figure 54 with the reflections indexed with respect to a cubic symmetry. All four compositions exhibit a pure perovskite structure without any signs of secondary phases, validating the

---

successful solid state synthesis. The  $111_c$  reflection appears asymmetric in BF-33BT+5NBT and weakly split in the other materials, which can be interpreted as a sign of rhombohedral distortion. The first processed BF-BT(-NBT) batches exhibited strong microstructural inhomogeneities, but optimizing milling and sintering conditions lead to a tremendous improvement in the microstructural appearance. Figure 55 depicts SEM micrographs of furnace cooled and quenched polished specimens of all investigated BF-BT(-NBT) compositions, while in Figure 56 micrographs of furnace cooled specimens with higher magnification are displayed. Please note that, in contrast to the experiments with NBT-BT, quenching was performed by reheating a furnace cooled sample to 800 °C for 30 min followed by rapidly cooling the ceramic in air assisted by a conventional air fan.

The SEM micrographs presented in this section were collected by Dr. Ann-Katrin Fetzer. No microstructural changes were observed upon quenching in any of the investigated compositions, and all specimens display a dense microstructure without large pores. BF-33BT exhibits a weak core-shell structure in few grains while it is more pronounced in BF-30BT (Figure 55a, b, e and f and Figure 56a and c). The cores, which appear lighter in BSE mode are enriched in the BF-endmember, while the darker shells are rich in BT. This chemical heterogeneity is confirmed by energy dispersive X-ray spectroscopy (EDS) and similar core-shell type structures have been reported before for BF-BT ceramics [134, 228]. Adding NBT into BF-BT seems to slightly reduce the abundance of core-shell structures in BF-33BT but increase it in BF-30BT (Figure 55c and g and Figure 56b and d). At the moment, this contrasting behavior cannot be explained with certainty, but it might be connected to problems with the milling procedure. The microstructure was significantly improved by adding a processing step, meaning crushing the material in a mortar after the roller milling. Nevertheless, further optimization of the milling procedure might be necessary individually for each material to avoid the formation of core-shell structures in all the investigated compositions. However, this was beyond the scope and the time frame of this study. Therefore, the abundance of core-shell structures is difficult to interpret since these features are very sensitive to changes in the processing route, especially in the milling procedure in BF-BT materials [229].

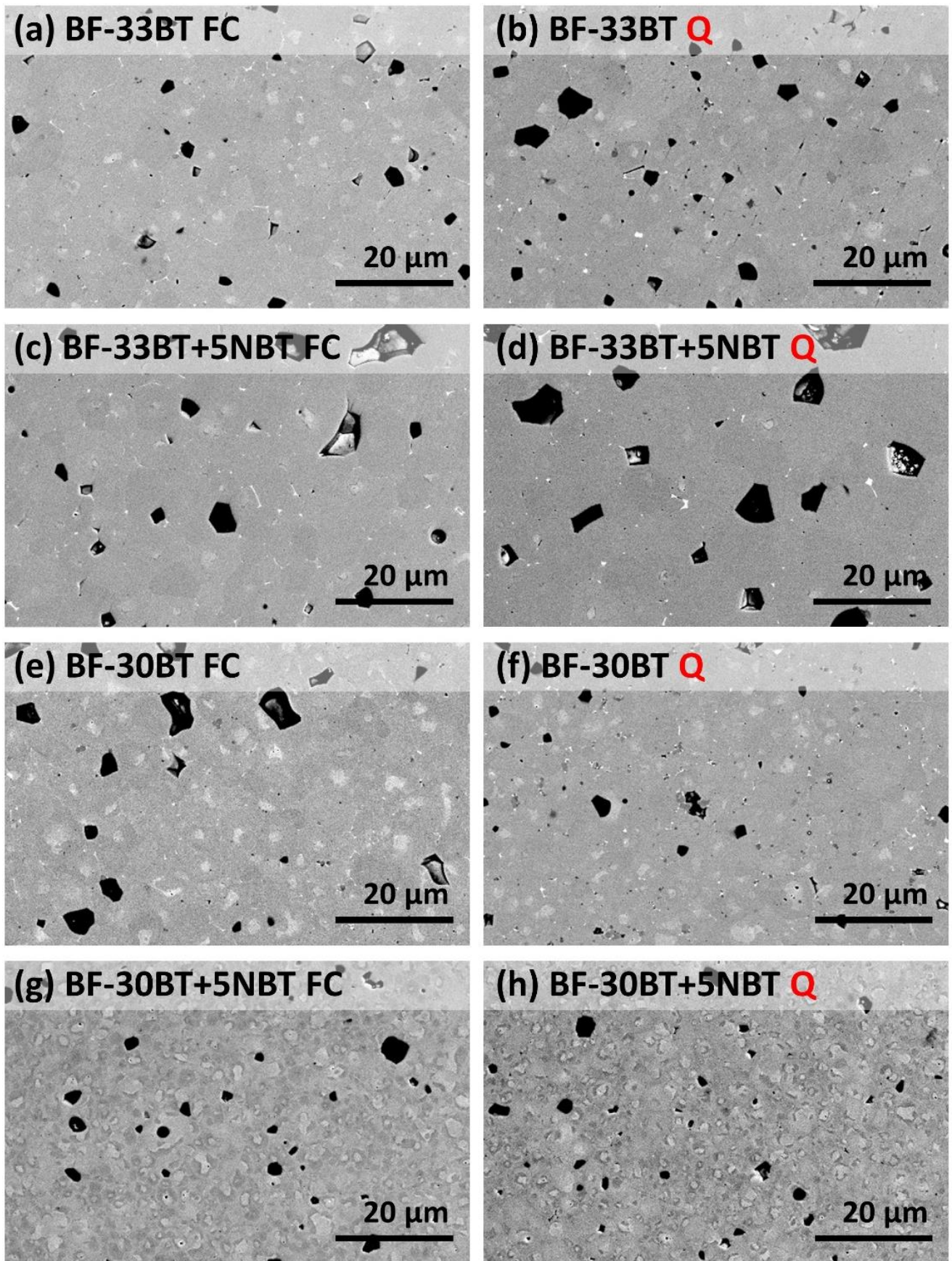


Figure 55: SEM micrographs of polished BF-BT(-NBT) specimens of all investigated compositions, furnace cooled and quenched, collected in BSE mode.

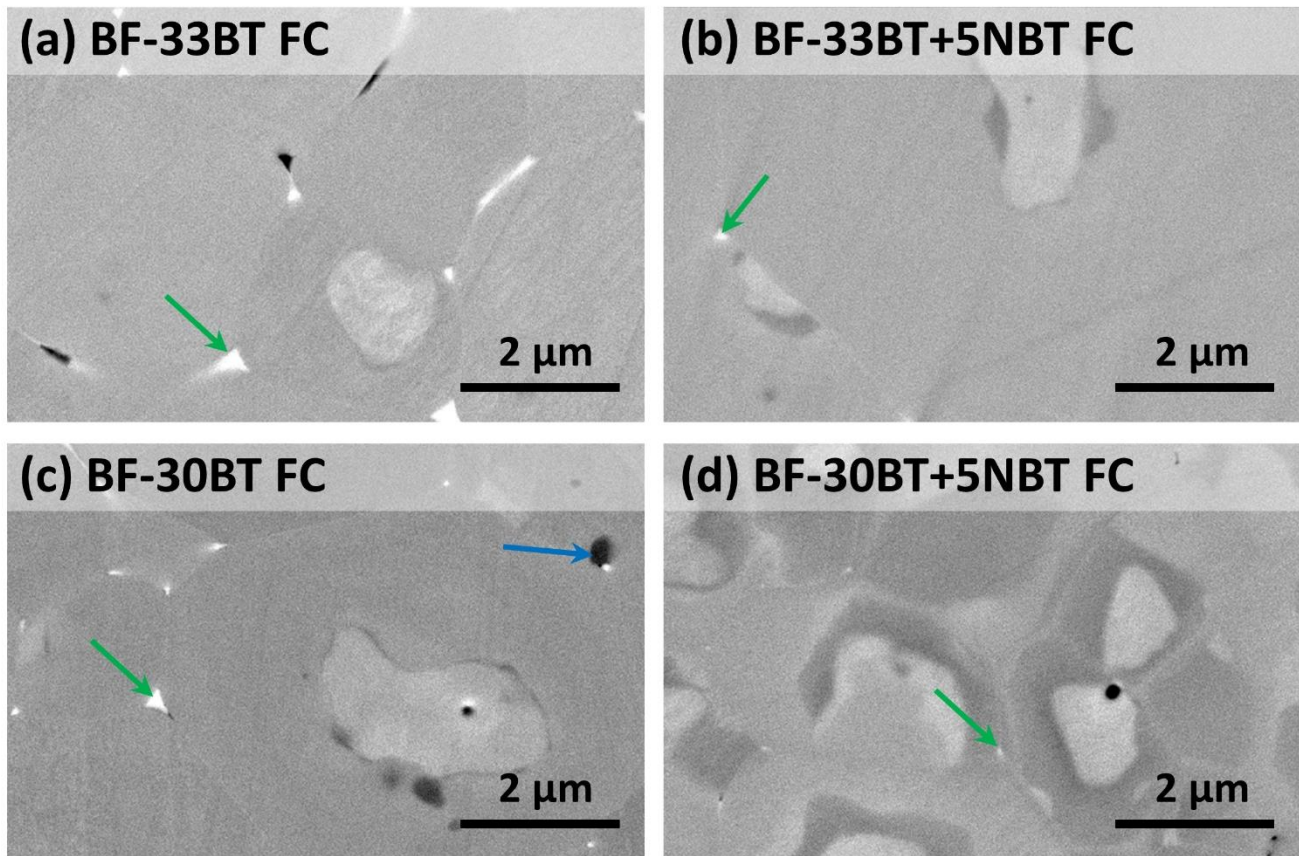


Figure 56: SEM micrographs of polished BF-BT(-NBT) specimens of all investigated compositions, furnace cooled and quenched, collected in BSE mode with higher magnification. The green arrows mark a Bi-rich phase while the blue arrow marks a local enrichment in Ba and Ti.

At the grain boundaries of all the compositions, small amounts of a Bi-rich phase are present possibly due to formation of a liquid phase during the sintering process, appearing very bright in the micrographs in BSE mode (Figure 56, green arrows). Furthermore, small inclusions that appear as dark in BSE mode are abundant in all the compositions but are most prominent in the pure BF-BT (Figure 56c, blue arrow). These inclusions are enriched in lighter elements for the respective site of the perovskite unit cell, meaning in Ba and Ti.

Absolute densities were established using the Archimedes method for furnace cooled and quenched ceramics. Relative densities, calculated from the absolute densities and the unit cell parameters extracted from high resolution structural data (chapter 5.4.3), ranged from 96 to 98 % for all samples without a significant trend upon introducing NBT. Also the quenching procedure did not influence the material's density.

### 5.4.3 Structural Analysis of Sintered Ceramics

*High resolution X-ray powder diffraction experiments were carried out to establish structural changes in BF-BT upon introducing NBT and subsequent quenching. Introducing NBT promotes a more cubic structure, while quenching increases the rhombohedral distortion and/or phase fraction.*

XRD patterns of BF-BT(-NBT) ceramics of all investigated compositions, furnace cooled and quenched, were collected using crushed and annealed samples. Lower resolution patterns with Cu  $K\alpha_{1,2}$  radiation were initially obtained to confirm phase purity after sintering, followed by higher resolution measurements using monochromatic Cu  $K\alpha_1$  radiation. Dr. Kathrin Hofmann conducted the high-resolution experiments, and the resulting diffraction patterns are presented in Figure 57. All compositions exhibit a phase-pure perovskite structure with slight asymmetries to full splitting in the  $\{111\}_{PC}$  but no sign of splitting in the  $\{200\}_{PC}$  reflection.

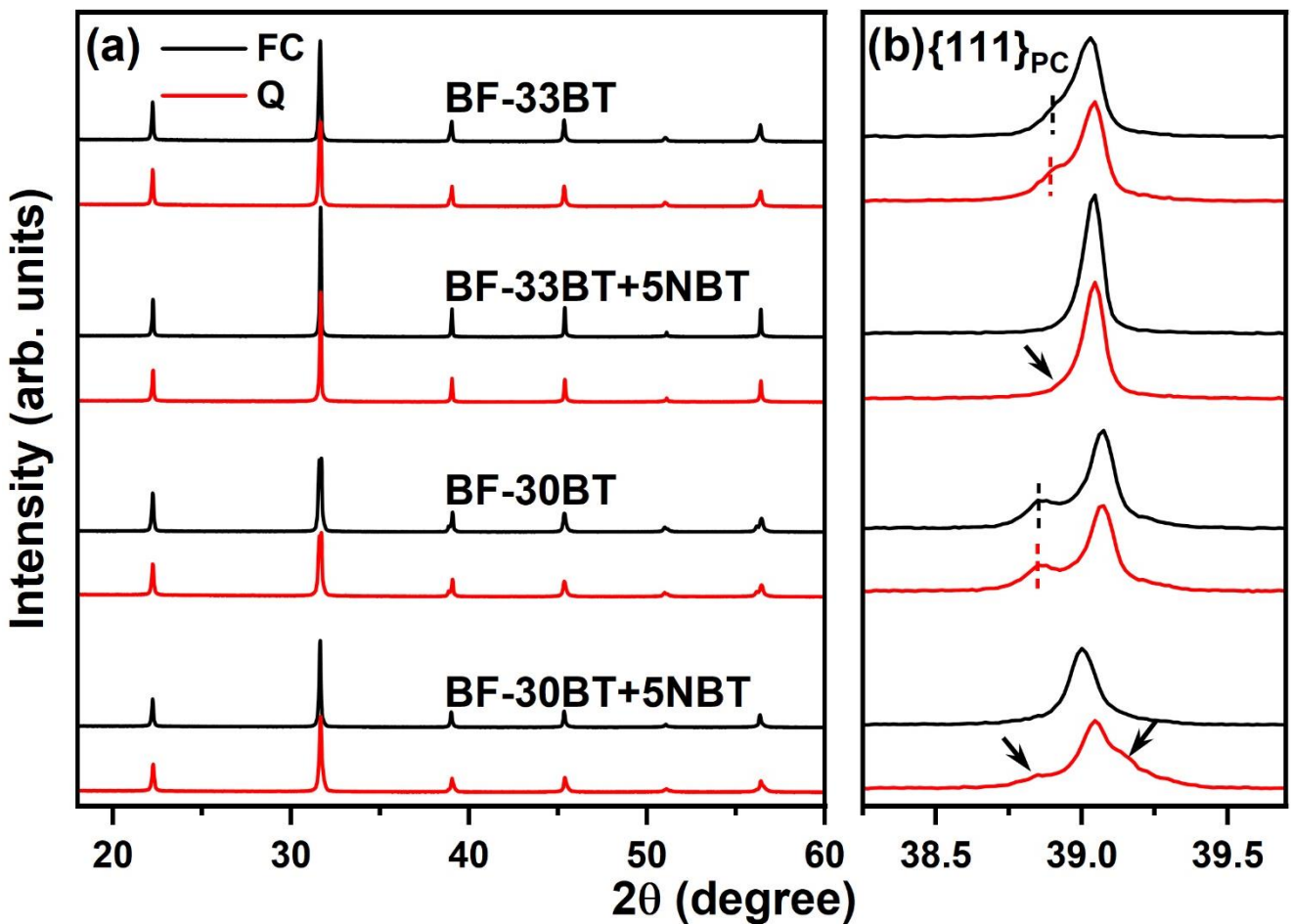


Figure 57: (a) X-ray powder diffraction patterns of furnace cooled and quenched BF-BT(-NBT) compositions. (b) Enlarged section of the XRD patterns showing the  $\{111\}_{PC}$  reflections.

---

The clear shoulder of the  $\{111\}_{PC}$  reflection of BF-33BT FC towards lower  $2\theta$  angles indicates a rhombohedral distortion (Figure 57b). In literature, this composition is reported as pseudo-cubic but ferroelectric [90], while others noted a small rhombohedral distortion of the structure [91, 166]. These differences are likely due to different processing conditions and/or the resolution of the XRD experiments. Quenching BF-33BT causes the shoulder to become marginally more pronounced, while adding 5 mol% NBT to this composition, results in the shoulder vanishing, but a slight asymmetry in the  $\{111\}_{PC}$  reflection remains. In literature, BF-BT-NBT with 1-5 mol% NBT added into BF-33BT is described as pseudo-cubic, however, the resolution of the diffraction patterns appears to be low and the structural investigation is not detailed [15]. Also in BF-33BT+5NBT, quenching causes a slightly more pronounced asymmetry in the  $\{111\}_{PC}$  reflection (Figure 57b, black arrow), indicating an increased rhombohedral distortion and/or a higher rhombohedral phase fraction upon quenching.

The effect of quenching and adding NBT with and without subsequent quenching upon BF-30BT follows similar trends compared to the effect on BF-33BT. However, the diffraction patterns of BF-30BT FC exhibit a clear splitting in the  $\{111\}_{PC}$  reflection into  $111_R$  and  $11\bar{1}_R$ , indicating a larger rhombohedral distortion and/or enhanced phase fraction. This is plausible and in accordance with literature since BF-30BT is closer to the rhombohedral endmember, BF, of the solid solution [90]. The splitting in  $\{111\}_{PC}$  is barely enhanced but rather similar in BF-30BT Q compared to BF-30BT FC (Figure 57b, dashed lines). Upon adding 5 mol% NBT, the splitting vanishes but an asymmetry remains in the  $\{111\}_{PC}$  reflection of BF-30BT+5NBT FC, which becomes strongly enhanced upon quenching, with shoulders developing on both sides of the reflection (Figure 57b, black arrows). This increase in lattice distortion upon quenching could be related to the more pronounced off-centering of the  $\text{Bi}^{3+}$ -ion, which was reported for pure NBT [149]. Given the high Bi-content of the investigated compositions, it is plausible that a similar mechanism to that observed in NBT-BT is in place in BF-BT-NBT.

Rietveld refinements were carried out on the XRD patterns depicted in Figure 57 using a two-phase model consisting of cubic  $Pm\bar{3}m$  and rhombohedral  $R3c$  phases, as is consistent with literature on BF-BT [160]. Relevant refinement parameters are listed in Table 5. Quenching BF-33BT increases the rhombohedral phase fraction from 66 to 81 % and enhances the rhombohedral distortion, given as  $90^\circ - \alpha_{\text{rhom}}$  from  $0.11^\circ$  to  $0.13^\circ$ . These enhanced non-cubic characteristics are similar to the behavior of NBT-BT and have been reported previously for BF-BT materials [161, 167]. However, in this study, quenching does not affect the structural properties of BF-30BT within the error margins of the refinement. Since the change in lattice distortion upon quenching



is dictated by quenching temperature and rate [161, 166, 168], it might be the case that in the study presented here, the quenching rates were not fast enough to strongly influence the already distorted structure of BF-30BT.

Table 5: Refined structural parameters of the high-resolution powder XRD data of BF-BT(-NBT) compositions. The errors given by the refinement software are about 1 % in phase fractions, about  $0.003^\circ$  for  $90^\circ\text{-}\alpha_{\text{rhom}}$  and for the other reported values significantly smaller than the last given digit. C and R stand for cubic and rhombohedral, respectively.

	<i>C-phase</i> /%	<i>R-phase</i> /%	$a_{\text{cubic}} / \text{\AA}$	$a_{\text{rhom}} / \text{\AA}$	$90^\circ\text{-}\alpha_{\text{rhom}}$	$R_{\text{wp}}$
BF-33BT FC	34	66	3.993	3.996	0.11	4.49
BF-33BT Q	19	81	3.991	3.995	0.13	4.48
BF-33BT+5NBT FC	65	35	3.992	3.991	0.00	5.13
BF-33BT+5NBT Q	56	44	3.991	3.992	0.00	4.47
BF-30BT FC	4	96	3.988	3.994	0.21	5.30
BF-30BT Q	4	96	3.987	3.994	0.21	4.88
BF-30BT+5NBT FC	61	39	3.994	3.989	0.19	4.79
BF-30BT+5NBT Q	60	40	3.991	3.985	0.33	4.73

The addition of 5 mol% NBT into BF-BT results in a strong increase in cubic phase fraction from 34 to 65 % and from 4 to 61 % for BF-33BT and BF-30BT, respectively (Table 5). Furthermore, the rhombohedral distortion becomes zero within the margins of error for BF-33BT+5NBT FC and decreases for BF-30BT+5NBT FC. Both aspects, the increase in cubic phase fraction and decrease in rhombohedral distortion can be rationalized by the increased disorder on the A-site of the perovskite unit cell possibly introducing a more relaxor-like behavior with reduced long-range ordering upon forming a ternary composition with NBT [230, 231]. On the other hand, quenching the ternary compositions results in a 9 % increase in rhombohedral phase fraction for BF-33BT+5NBT Q and in enhanced rhombohedral distortion for BF-30BT+5NBT Q. This hints towards a corroborated ferroelectric long-range order upon quenching.

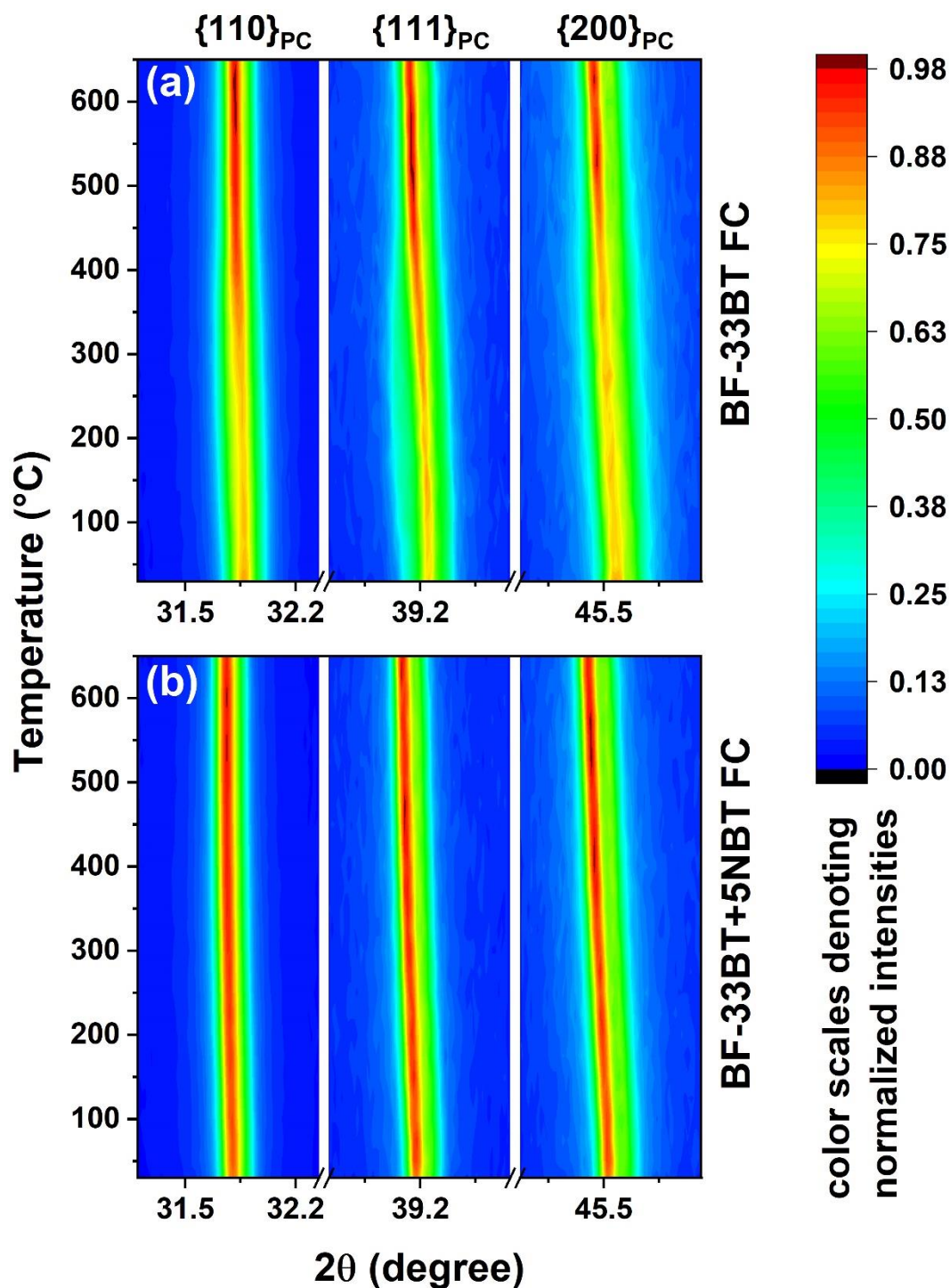


Figure 58: Temperature-dependent X-ray powder diffraction pattern profile evolution of  $\{110\}_{PC}$ ,  $\{111\}_{PC}$  and  $\{200\}_{PC}$  reflections for BF-33BT FC (a) and BF-33BT+5NBT FC (b). Intensities were normalized for each reflection profile individually.

Temperature-dependent XRD experiments were conducted on crushed and annealed powder samples of BF-33BT FC and BF-33BT+5NBT FC (Figure 58). Please note that the diffraction patterns obtained from these experiments have a lower resolution compared to those depicted in Figure 57, leading to a cubic appearance of BF-33BT+5NBT FC at all temperatures studied (Figure

---

58b). The rhombohedral distortion disappears roughly between 350 and 400 °C, while the broadening in the  $\{200\}_{\text{PC}}$  profile, caused by the coexistence of cubic and rhombohedral phases, vanishes between about 400 and 450 °C. This suggests that during heating, the rhombohedral distortion decreases to values close to zero before the rhombohedral phase completely disappears, and the material becomes truly cubic.

---

#### 5.4.4 Dielectric Analysis

---

*Permittivity and loss tangents were measured as a function of temperature to elucidate the effect of introducing NBT and subsequent quenching onto the electrical properties of BF-BT materials. BF-BT-NBT exhibits a strong reduction in dielectric loss over a large temperature range compared to pure BF-BT.*

Temperature-dependent dielectric measurements were carried out on poled cylindrical ceramic samples of all the investigated BF-BT(-NBT) compositions. BF-30BT Q could not be poled due to very high leakage currents during the poling process. The real part of permittivity,  $\epsilon'$ , and the loss tangents,  $\tan \delta$ , of these materials are plotted in Figure 59 for different measurement frequencies and temperatures ranging between room temperature and 650 °C. Figure 60 depicts the differences in the dielectric properties of BF-33BT and BF-30BT upon quenching and adding 5 mol% NBT and subsequent quenching. Two equivalent heating and cooling cycles were performed successively to measure the material properties also after complete depolarization, however, no significant differences between the first and second heating cycles were recognized.

All the compositions show an increase in maximum permittivity upon quenching (Figure 59 and Figure 60a and c), potentially caused by higher conductivity at elevated temperatures [134, 232]. In addition, the respective permittivity maxima are shifted to higher temperatures by the quenching treatment. This phenomenon has been reported before for BF-BT materials and correlated to the quenching-induced structural changes, with a higher distortion being connected to a higher temperature at which the ferroelectric transforms into the paraelectric state ( $T_c$ ) [233]. This connection between changes in structure and the dielectric maximum is supported by the temperature-dependent structural findings for BF-33BT FC. BF-33BT FC loses the rhombohedral distortion and turns cubic at around 400 °C, which is roughly the temperature of the dielectric maximum (Figure 59a).

The pure furnace cooled BF-BT compositions exhibit high dielectric losses above about 100 °C, especially at low measurement frequencies, indicating an increase in electrical conductivity upon heating (Figure 59a and e) [234]. Quenching shifts the inflection point in  $\tan \delta$  measured at 1 kHz

---

by about 50 °C to higher temperatures for BF-33BT, while it has the opposite effect on BF-30BT (Figure 60b and d), which cannot be explained. Adding 5 mol% NBT into BF-33BT leads to a significant shift in the inflection point of  $\tan \delta$  measured at 1 kHz by about 260 °C to roughly 360 °C (Figure 60b) indicating a significant decrease in conductivity in the intermediate temperature range as consistent with earlier reports [15]. Furnace cooled and quenched BF-33BT+5NBT both exhibit strong frequency dispersion in  $T_m$  (Figure 59 c and d), significantly more pronounced than in BF-33BT, which is typical for relaxor ferroelectrics [22].

The effects of introducing NBT into BF-30BT are similar to those observed for BF-33BT, including a significant shift of high-loss behavior to higher temperatures and a stronger frequency dispersion in  $T_m$ . However, all BF-30BT compositions exhibit a second maximum, shoulder, or anomaly in the dielectric spectrum, most prominently in the 1 kHz data. In BF-30BT FC, the first broad maximum around 380 °C appears at about the same temperature as the shoulder of the main permittivity peak in BF-30BT Q at 490 °C (Figure 59 e and f, black arrows). Earlier reports on BF-BT correlated these phenomena with distinct contributions from the core and the shell regions of grains to the dielectric spectrum, with the lower temperature maximum or shoulder being connected to the shell and the second maximum to the core [134, 228]. This reasoning appears plausible for the current study as well, since the core-shell features are weakly developed in the BF-33BT-related but clearly present in the BF-30BT-related materials (Figure 55 and Figure 56) leading to the anomalies in the dielectric spectra of the latter.

In BF-30BT+5NBT FC, the maximum in permittivity at about 390 °C (Figure 59g, black arrow) is likely caused mainly by the shell contributions. Quenching enhances the contribution to the dielectric spectrum from the core region of the grains, resulting in a permittivity maximum at 490 °C, which can be attributed to the core regions with a shoulder caused by the BT-rich shells of the ceramic grains (Figure 59h, black arrow), even though the overall microstructure was not affected by the quenching treatment (Figure 55). However, the strong increase in rhombohedral distortion upon quenching BF-30BT+5NBT might stabilize the rhombohedral phase up to higher temperatures, leading to a higher maximum in permittivity at the eventual transition to a cubic symmetry (Figure 60c). In literature, the BF-rich core region of the BF-BT grains is associated with the presence of a rhombohedrally distorted phase [134] which supports the correlation between an enhanced rhombohedral distortion and a pronounced signature of core regions in the dielectric spectrum. Furthermore, a significantly enhanced rhombohedral domain contrast together with the characteristic  $\frac{1}{2} \{000\}$  SR in the core region was confirmed by TEM analyses carried out by Dr. Ann-Katrin Fetzner on the BF-BT-based materials subject to the study presented here (Figure S 3).

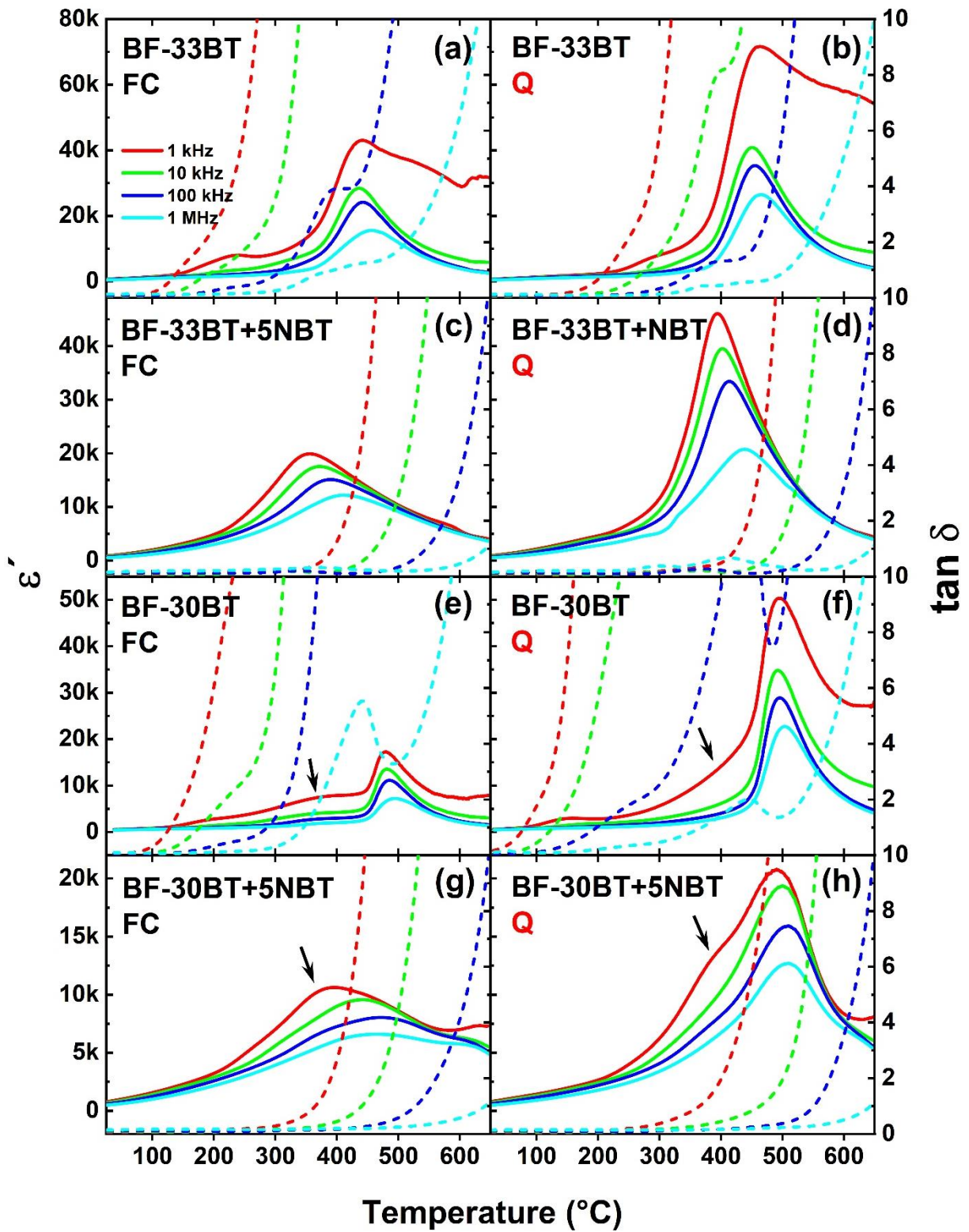


Figure 59: Temperature-dependent permittivity and loss tangents measured at different frequencies on poled furnace cooled and quenched BF-BT(-NBT) ceramics.

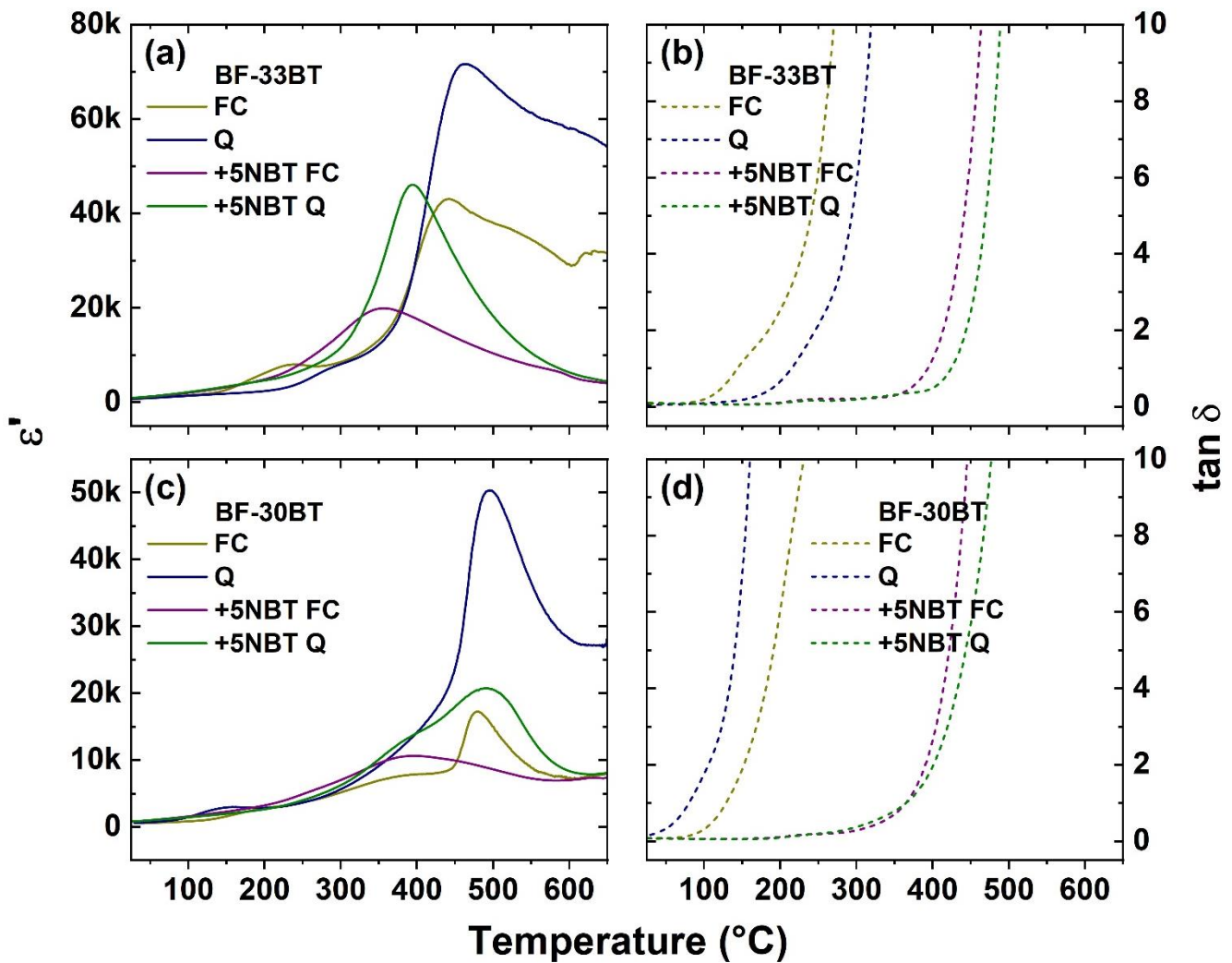


Figure 60: Comparison of temperature-dependent permittivity and loss tangents measured at 1 kHz for furnace cooled and quenched BF-33BT with and without 5 mol% NBT (a and b) and the same for BF-30BT-related materials, respectively (c and d).

#### 5.4.5 Ferroelectric Polarization and Strain Analysis and Piezoelectric Properties

*The influence of introducing NBT into BF-BT and subsequent quenching on electrical characteristics and therefore relevant properties for application were determined by measuring polarization and strain, as well as the piezoelectric coefficient. The polarization and strain response of BF-BT-NBT reveals a partly ergodic relaxor behavior, while quenching suppresses the ergodicity, leading to an increase in remanent polarization and  $d_{33}$ .*

Figure 61 and Figure 62 display the first and third cycles of electric field-dependent polarization and strain measurements, respectively, for BF-BT(-NBT) compositions in both the furnace cooled and quenched state. The maximum amplitude of the bipolar electric field was 6 kV/mm, and the measurement frequency was 3 Hz. Hysteresis measurements for BF-30BT Q were not possible due

to high leakage currents and eventual breakdown of the respective samples. Figure 63 depicts values extracted from hysteresis measurements of at least five samples per furnace cooled and three samples per quenched composition, including error ranges.

In this study, quenching in air from 800 °C does not significantly influence the polarization and strain behavior of BF-33BT (Figure 61a and e, Figure 62a and e and Figure 63). Lee et al. reported strong changes in the hysteresis behavior upon water-quenching [167], while recently Wang et al. witnessed a slight decrease in remanent polarization after air-quenching BF-33BT from temperatures in the range of 600-1000 °C [168]. This suggests that the quenching rates achieved in this study were not high enough to induce changes in ferroelectric properties of BF-33BT. Introducing 5 mol% NBT into BF-33BT increases the maximum polarization and decreases the coercive field relative to pure BF-33BT (Figure 61b and f and Figure 63c and e). Furthermore, it increases the total strain and causes a partly sprout-shaped strain response, which is, in extreme form, typical for ergodic relaxor behavior [235]. However, the strain curve of the third cycle is more like a hybrid between sprout and butterfly shape (Figure 62f). This suggests a partly reversible field-induced polarization switching and resulting strain, which was not observed in earlier reports on BF-BT-NBT, while the increase in maximum polarization is consistent with literature [15].

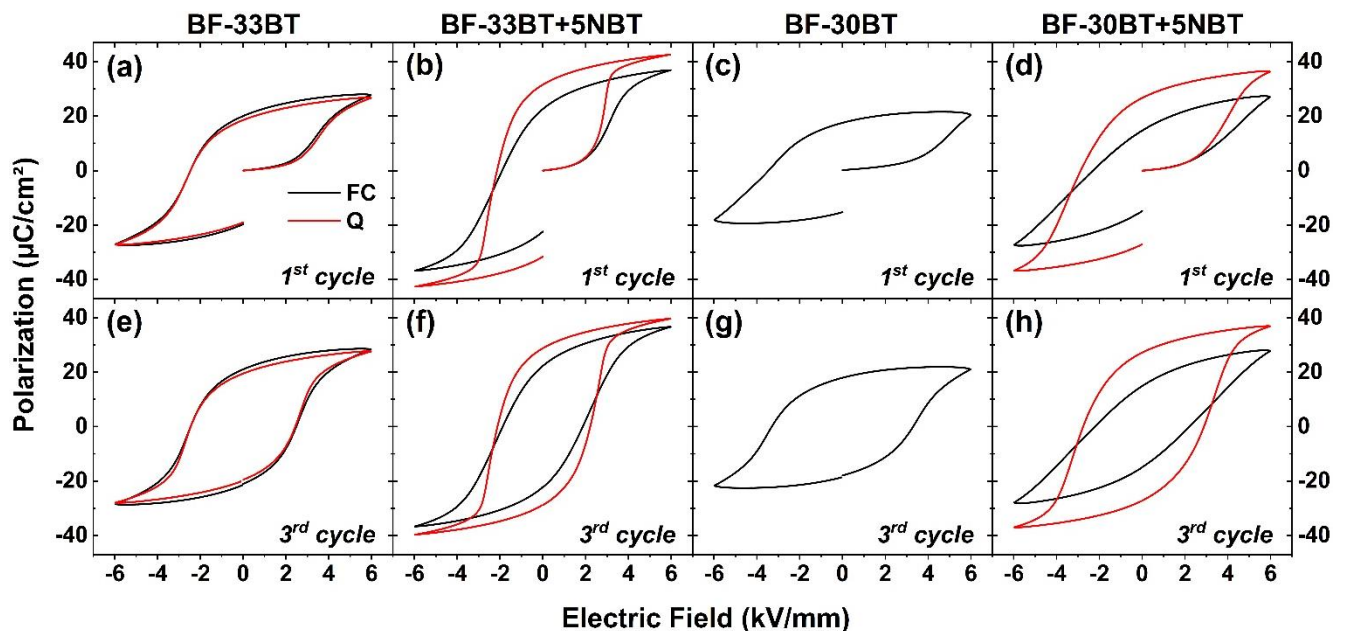


Figure 61: First (a-d) and third (e-h) electric field-dependent polarization cycles of furnace cooled (black) and quenched (red) samples of all investigated BF-BT(-NBT) compositions measured with a frequency of 3 Hz.

Quenching BF-33BT+5NBT leads to a more square-shaped polarization loop with an increase in remanent polarization, coercive field, and significantly enhanced negative strain values (Figure 61f and Figure 62f). These trends are consistent with the quenching-induced changes in ferroelectric properties of NBT-BT compositions (chapter 5.1.5). However, in BF-33BT+5NBT Q, the third cycle of the strain response exhibits an ideal butterfly shape, which is clearly different from the sprout-butterfly hybrid shape of the furnace cooled reference. This results in a strongly increased absolute negative strain value of -0.164 % compared to -0.075 for BF-33BT+5NBT FC (Figure 63b) and suggests a reduced ergodic and more non-ergodic relaxor behavior with stabilized ferroelectric domain state upon quenching. Similar behavior, described as quenching-circumvented ergodicity, was observed for ternary NBT-BT-based compositions including either  $K_{0.5}Na_{0.5}NbO_3$  or  $AgNbO_3$  [236, 237] and rationalized as being connected to the enhanced off-centering of the  $Bi^{3+}$ -ion [149].

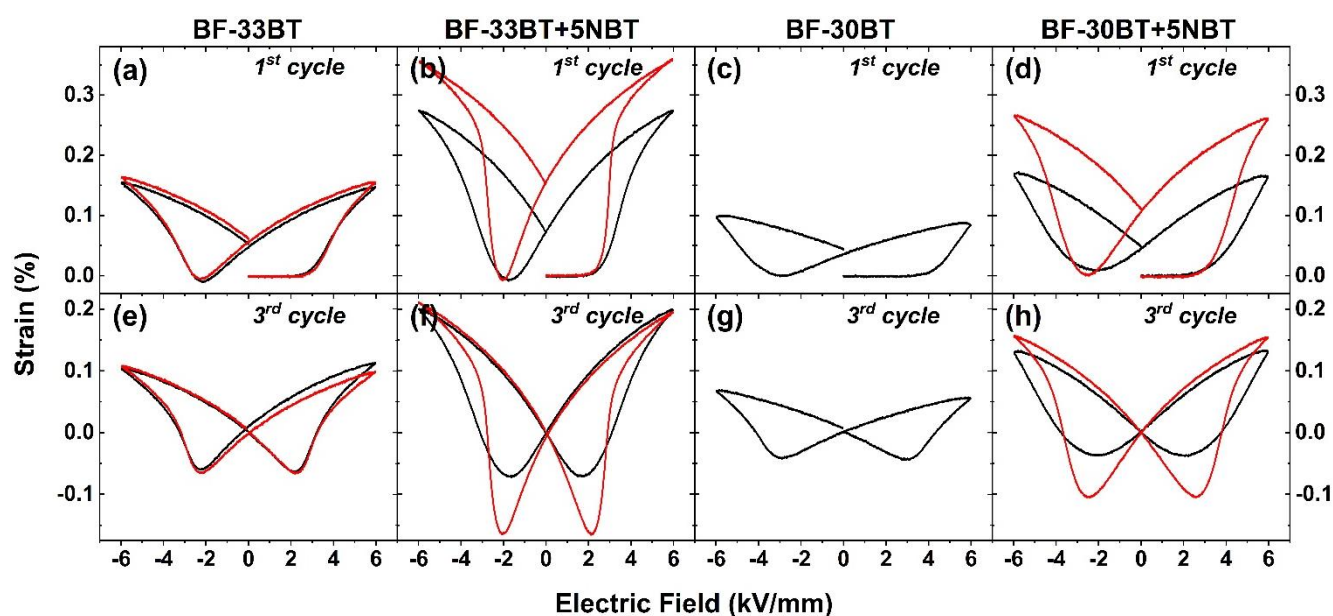


Figure 62: First (a-d) and third (e-h) electric field-dependent strain cycles of furnace cooled (black) and quenched (red) samples of all investigated BF-BT(-NBT) compositions measured with a frequency of 3 Hz.

Introducing NBT into BF-30BT causes similar changes in ferroelectric properties as for BF-33BT, however, the overall polarization and strain values remain lower (Figure 63). The quenching effects on BF-30BT+5NBT also exhibit the same trends as for BF-33BT+5NBT, meaning an increase in strain, remanent and maximum polarization and coercive field.



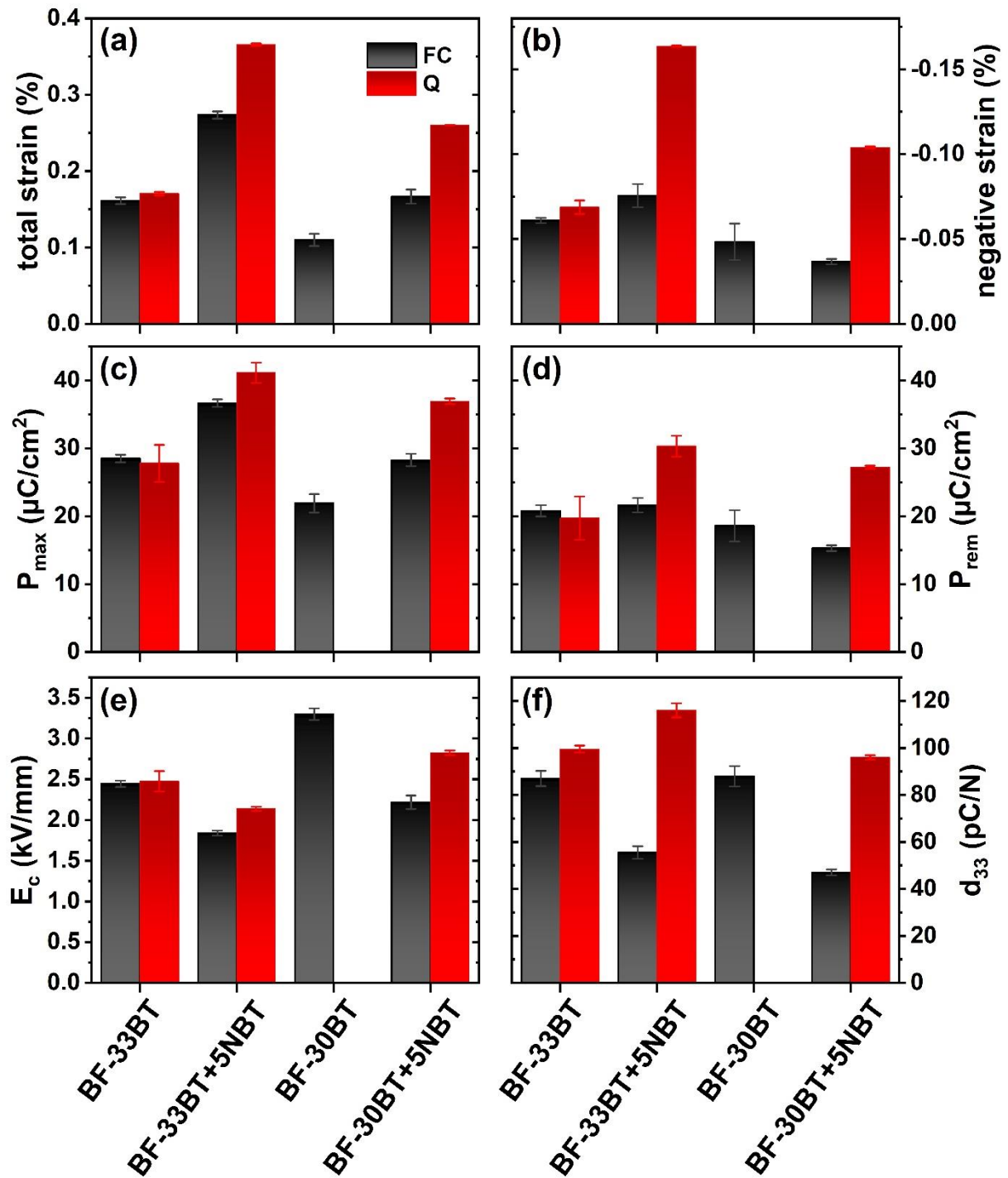


Figure 63: Total (a) and negative strain (b), maximum,  $P_{max}$ , (c) and remanent polarization,  $P_{rem}$ , (d), coercive field,  $E_c$ , (e) and  $d_{33}$  (f) for all investigated BF-BT(-NBT) compositions, furnace cooled and quenched.

In addition to evaluating the ferroelectric hysteresis, the direct piezoelectric coefficient,  $d_{33}$ , was measured on poled samples of all the investigated BF-BT(-NBT) materials except for BF-30BT Q, as poling this composition was not possible due to the high leakage currents and electrical breakdowns. Quenching BF-33BT slightly increases  $d_{33}$  from 87 to 100 pC/N, while introducing 5

---

mol% NBT in the same composition results in a decrease in  $d_{33}$  to 56 pC/N (Figure 63f). This stands in contrast to literature, where the  $d_{33}$  of BF-33BT was increased from 81 to 183 pC/N by forming a ternary composition with 5mol % NBT [15]. Possibly, this is caused by differences in the processing route or not precisely identical compositions, but nevertheless, the opposing trend is difficult to rationalize. In the present study, however, the effects of forming a ternary composition with NBT on the electric field-induced strain and the  $d_{33}$  are consistent. The tendency to a sprout-shaped strain loop indicates lower remanence in the field-induced state, also reflecting in lower  $d_{33}$  after poling.

The quenching treatment increases the  $d_{33}$  of BF-33BT+5NBT by 107 % to a value of 116 pC/N due to the suppression of the partly ergodic behavior of the material upon quenching, which also reflects in the increased remanent polarization and negative strain (Figure 63). As consistent with the development of ferroelectric properties, the influence of introducing NBT into BF-30BT and subsequent quenching is similar to that for the BF-33BT-based material. The  $d_{33}$  decreases from 88 to 47 pC/N upon adding 5mol% NBT and increases to 96 pC/N for BF-30BT+5NBT Q.

---

#### 5.4.6 Short Summary

---

The study presented here focuses on the effect of introducing 5 mol% NBT into BF-BT and subsequent quenching, as this ternary composition has promising properties but has not been extensively researched [15]. The first experiments were conducted in Manchester in David Hall's research group, due to their expertise in processing BF-BT-based ceramics. Processing conditions were optimized after the initial batches exhibited distinct microstructural inhomogeneities.

BF-33BT-based materials show a weak core-shell structure, which is more pronounced in BF-30BT, especially in BF-30BT+5NBT with a BF-rich core and BT-rich shell. However, there are no differences in microstructure between furnace cooled and quenched samples. All compositions show a phase-pure perovskite structure established from XRD. Pure BF-BT exhibits rhombohedrally distorted structure, while the addition of NBT into BF-BT promotes a symmetry close to cubic. On the other hand, quenching increases the non-cubic distortion and/or the rhombohedral phase fraction, as established with Rietveld refinements.

The dielectric results indicate that quenching increases the conductivity of BF-BT materials at elevated temperatures and shifts the permittivity maximum to higher temperatures. The addition

---

of NBT leads to a decrease in dielectric losses over a wide temperature range and shifts the inflection point of  $\tan \delta$  by up to 260 °C to 360 °C. The dielectric spectra of BF-30BT and BF-30BT+5NBT, both in the furnace cooled and quenched states, exhibited signatures of distinct core and shell contributions, consistent with the microstructural findings.

In this study, the quenching-induced changes in ferroelectric polarization and strain response for pure BF-BT are negligible. However, introducing NBT strongly increases total strain, maximum polarization, and decreases the coercive field. Furnace cooled BF-BT-NBT materials exhibit a hybrid between sprout- and butterfly-shaped strain loops, while quenching the ternary compositions leads to well-defined butterfly-shaped strain loops and increased polarization and coercive field. These findings can be rationalized as pronounced relaxor behavior and partly ergodic relaxor properties upon introducing NBT into BF-BT. Quenching the ternary compositions results in the suppression of the partly present ergodicity, reflecting in an increase in remanent polarization, negative strain,  $d_{33}$ , and rhombohedral distortion. The explanation for that might be similar to the quenching-related phenomena in NBT-BT and also connected to the enhanced off-centering of the  $\text{Bi}^{3+}$ -ion.

---

## 6 Summary and Perspective

---

The study presented here provides an enhanced understanding of the quenching-induced changes in the structural and electrical characteristics of lead-free Bi-based piezoceramics. The two chosen material systems were four compositions of NBT-BT, which span different phase regions of the respective phase diagram, and two compositions of BF-BT with and without the introduction of NBT. Besides investigating the material systems with respect to the effects of quenching, the composition-dependent behavior is elucidated.

All the quenching-induced changes in the structural and electrical properties of NBT-BT are most pronounced at and close to the MPB, where the material exhibits non-ergodic relaxor behavior in the furnace cooled state. Quenching NBT-BT increases the lattice distortion in all the investigated compositions, as confirmed by high resolution X-ray powder diffraction and synchrotron diffraction on bulk samples. The increased lattice distortion can be correlated to the more pronounced  $\text{Bi}^{3+}$ -ion off-centering [149]. Furthermore, quenching alters the fractions of crystallographic phases present in the unpoled state, validated by Rietveld refinements, especially at the MPB, with a strong decline in cubic phase volume due to the quenching-induced stabilization of the ferroelectric order. This suppression of relaxor-like behavior also reflects in a decrease in frequency dispersion of the dielectric response. Quenching induces an increase in PNR volume fraction above  $T_m$  at and close to the MPB, as established by temperature-dependent Young's modulus and a composite model. This increase may be due to the enhanced non-cubic distortions and is consistent with the change in phase composition at room temperature. The spontaneous transition from relaxor to ferroelectric in unpoled NBT-9BT upon quenching [13] is reflected in a sharp minimum in the Young's modulus, as well as in the structural and dielectric results.

Although the phase composition of poled samples is not influenced by quenching, the enhanced lattice distortion remains, which is likely the reason for the observed increase in  $T_d$  upon quenching [184]. A quenching-induced increase in  $T_{F-R}$  and, thereby, in  $T_d$ , was established for all NBT-BT compositions by measuring the dielectric properties of poled samples as a function of temperature. Additionally, remanent poling-induced domain texture was evaluated and, irrespective of furnace cooled or quenched, found to be largest at the MPB, consistent with findings on lead-based materials, due to the phase coexistence and, therefore, easier alignment of the polarization vectors with the electric poling field [194].

---

Ferroelectric hysteresis experiments revealed an increase in polarization, coercive field, and total strain in NBT-BT upon quenching, possibly due to the increase in lattice distortion, and therefore, increased spontaneous strain and polarizability. However, the  $d_{33}$  is decreased in quenched NBT-BT, which might be connected to the increase in coercive field and stabilization of the ferroelectric state hindering domain wall mobility, leading to a lower extrinsic contribution to the small field response. Furthermore, onset of electric field-induced structural changes is shifted to higher field amplitudes in quenched NBT-BT compared to the furnace cooled reference material, which was established from *in situ* synchrotron XRD studies. This shift is reflected in the change in phase fractions, unit cell parameters, and the calculated strain contributions. Since quenching NBT-BT stabilizes the ferroelectric state and, by that, a phase composition close to the poled state of the respective material, the field-induced phase changes are smaller, leading to a strong reduction in volumetric strain.

Introducing 5 mol% NBT into BF-BT at and near the MPB results in a less distorted perovskite structure and reduced dielectric losses over a wide temperature range. BF-BT-NBT exhibits partially ergodic relaxor behavior, as evidenced by the hysteresis response and correlates with decreased  $d_{33}$  values. Quenching the ternary compositions suppresses ergodicity, leading to an increased negative strain, remanent polarization, and up to 107 % increase in  $d_{33}$  compared to the furnace-cooled reference. In the BF-BT-based materials studied, quenching enhances the rhombohedral distortion, indicating a similar physical mechanism to that observed in NBT-BT, with the enhanced off-centering of the  $\text{Bi}^{3+}$ -ion being the primary factor.

The findings presented in this study provide insight into the effect of quenching on the structure and on field-induced structural changes in NBT-BT on a global level. However, alterations on a local scale as a function of electric field remain unrevealed. In future studies, *in situ* electric field-dependent pair distribution function analysis could improve the understanding of local-scale changes in the field-induced structural response upon quenching. Furthermore, elucidating the structural transformations during thermally-induced depolarization could provide practical insight into the correlation between phase stability and the increase in  $T_a$  in quenched NBT-BT.

For application relevance, the long-time stability of the enhanced properties is important and could be established by a fatigue study with electric-field cycling at elevated temperatures. However, during the duration of the present work, no signs of deterioration of the quenching-induced changes were observed. Generally, due to the negligible changes in Young's modulus and rather small decrease in  $d_{33}$  upon quenching NBT-BT, it is rendered as a suitable and easy-to-use

---

method to increase the depolarization temperature and, by that, enhance the temperature range for application. In the new BF-BT-NBT material system, quenching helps to improve the application relevant  $d_{33}$  while retaining the beneficial impact on resistivity and strain response upon introducing NBT into BF-BT. Since air-quenching does not require severe alteration of the solid state processing route, it appears as a highly useful method to assist bringing lead-free piezoceramics into application.

## 7 Supplementary Material

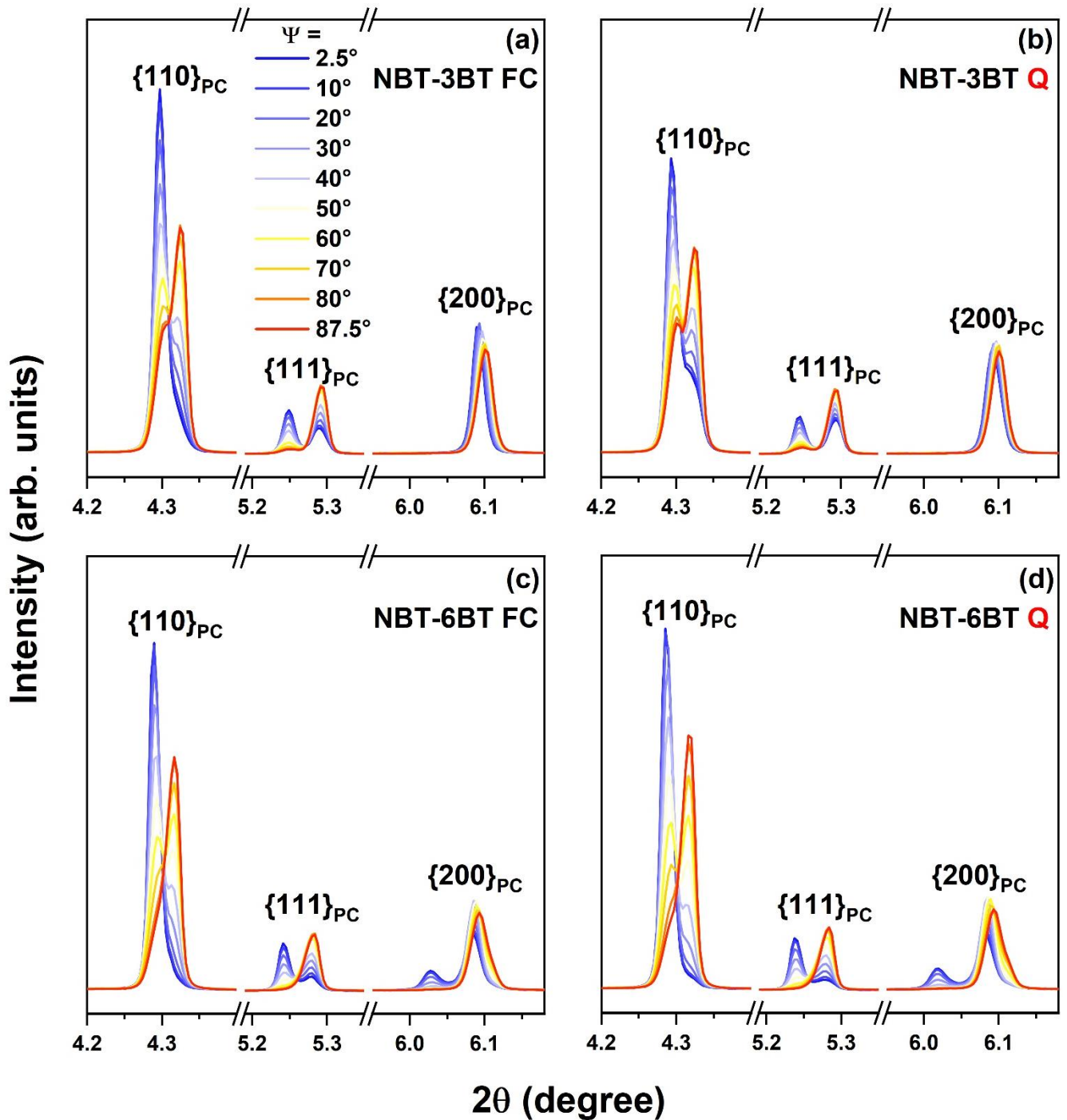


Figure S 1: Azimuthal angle-dependent diffraction patterns showing the  $\{110\}_{PC}$ ,  $\{111\}_{PC}$  and  $\{200\}_{PC}$  reflections of poled (a) NBT-3BT FC, (b) NBT-3BT Q, (c) NBT-6BT FC and (d) NBT-6BT Q.

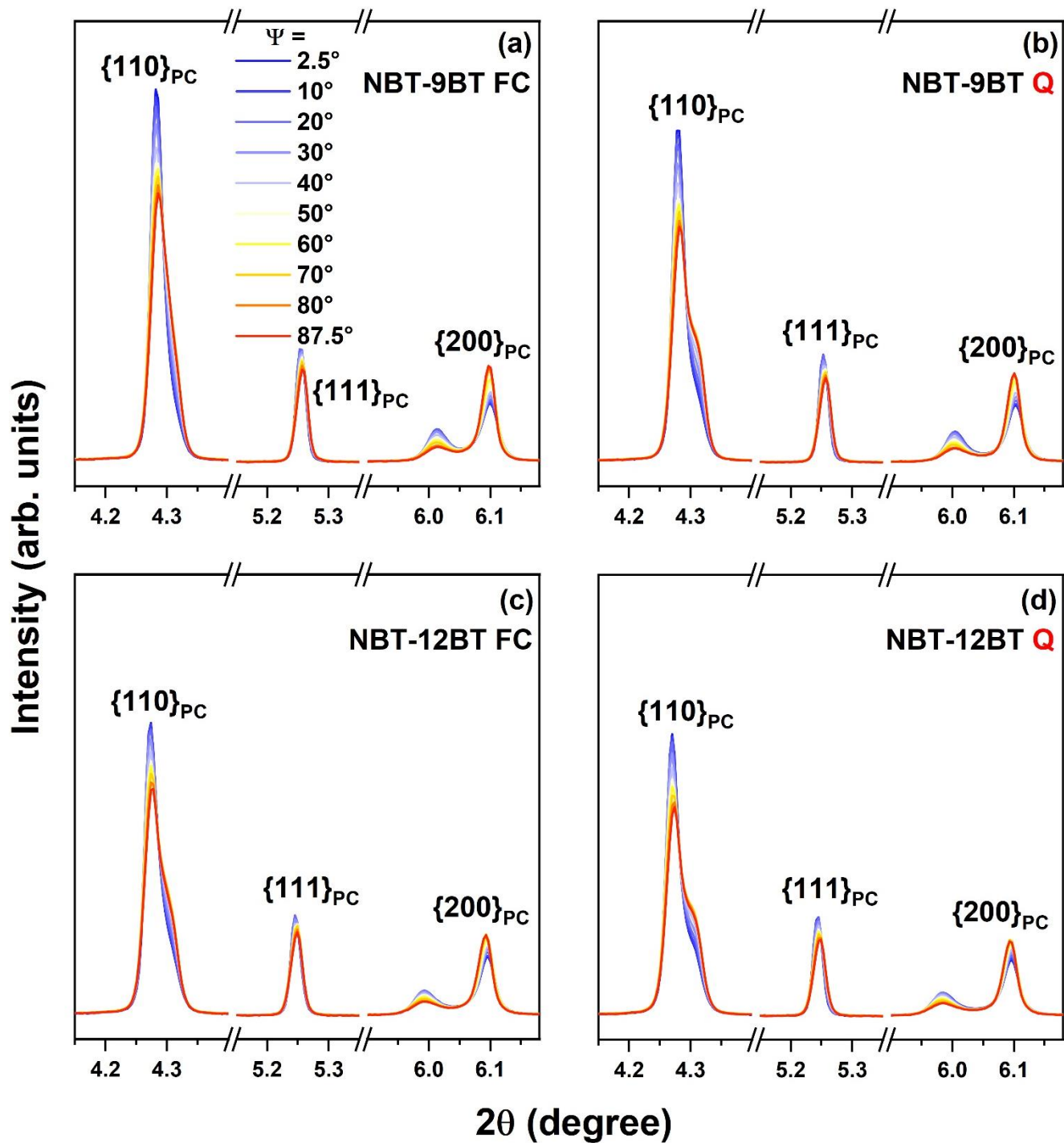


Figure S 2: Azimuthal angle-dependent diffraction patterns showing the  $\{110\}_{PC}$ ,  $\{111\}_{PC}$  and  $\{200\}_{PC}$  reflections of poled (a) NBT-9BT FC, (b) NBT-9BT Q, (c) NBT-12BT FC and (d) NBT-12BT Q.



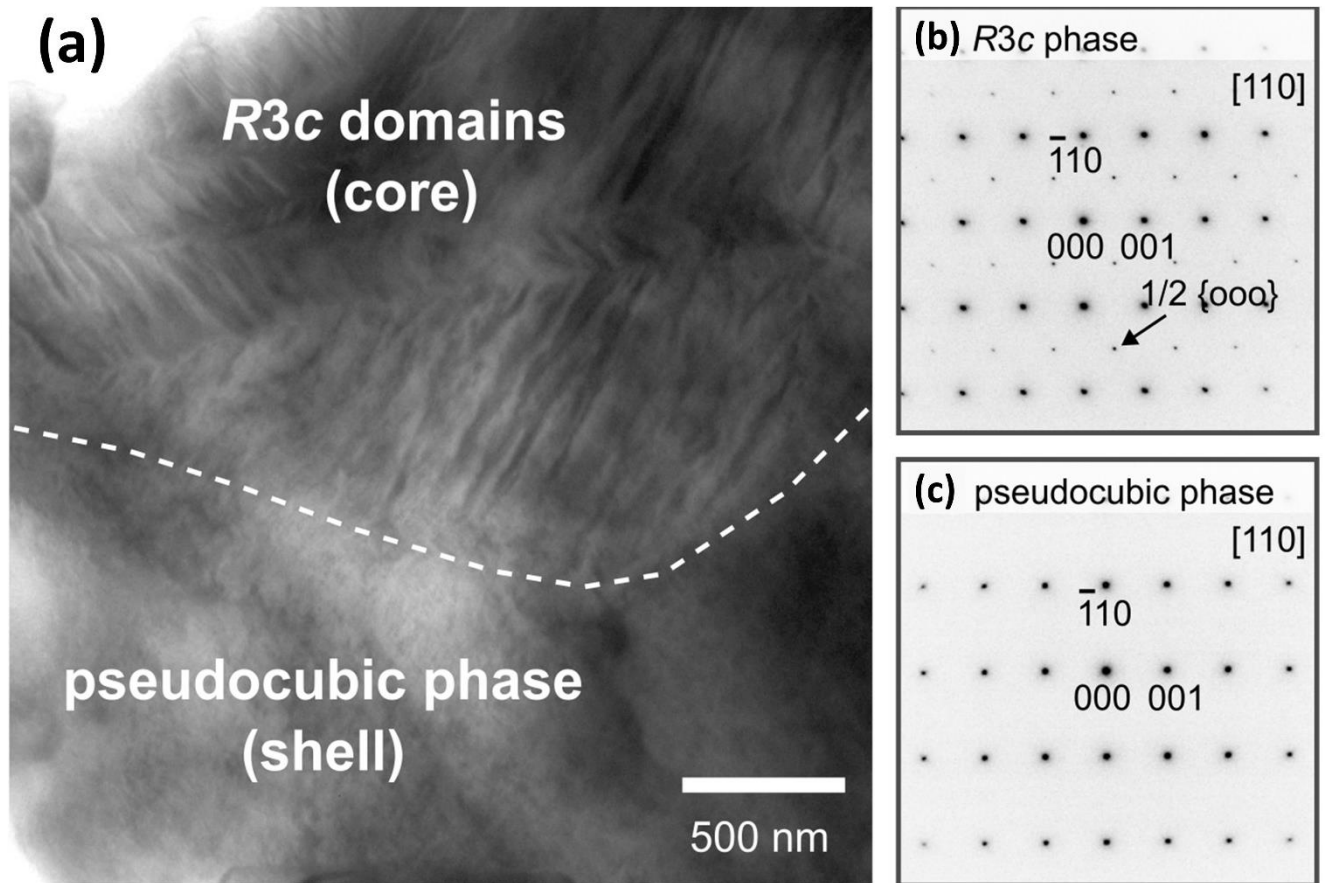


Figure S 3: (b) TEM micrograph of a grain in 67BF-33BT+5NBT Q. (c) and (d) SAED patterns, depicting  $1/2\ \{000\}$  SR for the *R3c* phase, while SR are absent from the pseudocubic phase.

Table S 1: Refined structural parameters of NBT-3BT FC based on *in situ* electric field-dependent synchrotron XRD measurements. The errors given by the refinement software are about 1 % in phase fractions and for the other reported values significantly smaller than the last given digit. The lattice parameters for the rhombohedral phase are given for a unit cell in hexagonal notation. C = cubic, R = rhombohedral.

Electric field /kVmm <sup>-1</sup>	C-phase /%	R-phase /%	a <sub>cubic</sub> /Å	a <sub>rhomb</sub> /Å	c <sub>rhomb</sub> /Å	η <sub>rhomb</sub> /%	R <sub>wp</sub>
0.00	17	83	3.894	5.494	13.552	0.697	5.87
0.14	17	83	3.894	5.494	13.552	0.693	5.87
0.28	17	83	3.894	5.495	13.552	0.692	5.98
0.43	17	83	3.894	5.494	13.552	0.694	5.72
0.57	17	83	3.894	5.494	13.552	0.693	5.76
0.71	17	83	3.894	5.494	13.552	0.692	5.73
0.85	17	83	3.894	5.495	13.551	0.688	5.67
0.99	17	83	3.894	5.495	13.551	0.689	5.69
1.13	17	83	3.894	5.495	13.551	0.688	5.67
1.27	17	83	3.894	5.495	13.551	0.688	5.69
1.42	17	83	3.894	5.495	13.551	0.688	5.67
1.56	17	83	3.894	5.495	13.551	0.689	5.66
1.70	17	83	3.894	5.495	13.552	0.690	5.64
1.84	17	83	3.894	5.495	13.552	0.691	5.63
1.98	17	83	3.894	5.494	13.552	0.696	5.63
2.12	18	82	3.894	5.494	13.552	0.698	5.55
2.26	17	83	3.894	5.494	13.553	0.700	5.53
2.41	17	83	3.894	5.494	13.553	0.705	5.50
2.55	17	83	3.894	5.494	13.554	0.719	5.37
2.69	12	88	3.895	5.494	13.554	0.712	5.54
2.83	11	89	3.895	5.494	13.556	0.739	4.95
2.97	10	90	3.895	5.493	13.561	0.797	4.11

3.11	10	90	3.895	5.492	13.565	0.831	3.75
3.26	10	90	3.895	5.492	13.567	0.847	3.67
3.40	8	92	3.895	5.492	13.570	0.863	3.41
3.54	0	100		5.493	13.570	0.857	3.57
3.68	0	100		5.493	13.572	0.867	3.59
3.82	0	100		5.494	13.574	0.878	4.13
3.96	0	100		5.493	13.576	0.905	4.80
4.10	0	100		5.493	13.577	0.902	3.98
4.25	0	100		5.495	13.577	0.871	4.24

Table S 2: Refined structural parameters of NBT-3BT Q based on *in situ* electric field-dependent synchrotron XRD measurements. The errors given by the refinement software are about 1 % in phase fractions and for the other reported values significantly smaller than the last given digit. The lattice parameters for the rhombohedral phase are given for a unit cell in hexagonal notation. C = cubic, R = rhombohedral.

Electric field /kVmm <sup>-1</sup>	C-phase /%	R-phase /%	a <sub>cubic</sub> /Å	a <sub>rhomb</sub> /Å	c <sub>rhomb</sub> /Å	η <sub>rhomb</sub> /%	R <sub>wp</sub>
0.00	15	85	3.894	5.490	13.571	0.906	6.80
0.14	13	87	3.894	5.491	13.569	0.885	6.69
0.28	13	87	3.894	5.491	13.569	0.884	6.69
0.43	13	87	3.894	5.491	13.569	0.884	6.72
0.57	13	87	3.894	5.491	13.569	0.884	6.79
0.71	13	87	3.894	5.491	13.569	0.884	6.67
0.85	13	87	3.894	5.491	13.569	0.885	6.72
0.99	13	87	3.894	5.491	13.569	0.885	6.67
1.13	13	87	3.894	5.491	13.569	0.885	6.73
1.27	13	87	3.894	5.491	13.569	0.885	6.73
1.42	14	86	3.894	5.491	13.569	0.888	6.67
1.56	14	86	3.894	5.491	13.569	0.887	6.69

1.70	14	86	3.894	5.491	13.569	0.887	6.67
1.84	13	87	3.894	5.491	13.569	0.887	6.69
1.98	14	86	3.894	5.491	13.569	0.888	6.64
2.12	14	86	3.894	5.491	13.569	0.888	6.58
2.26	14	86	3.894	5.491	13.569	0.889	6.58
2.41	14	86	3.894	5.491	13.569	0.890	6.57
2.55	14	86	3.894	5.491	13.569	0.891	6.56
2.69	14	86	3.894	5.491	13.569	0.893	6.53
2.83	14	86	3.894	5.491	13.569	0.894	6.47
2.97	14	86	3.894	5.491	13.570	0.900	6.26
3.11	13	87	3.895	5.491	13.571	0.908	6.05
3.26	13	87	3.895	5.491	13.571	0.909	5.97
3.40	12	88	3.895	5.490	13.572	0.914	5.72
3.54	11	89	3.895	5.490	13.571	0.915	5.17
3.68	10	90	3.896	5.490	13.572	0.923	5.12
3.82	0	100		5.491	13.574	0.913	5.51
3.96	0	100		5.491	13.574	0.923	5.34
4.10	0	100		5.491	13.574	0.926	5.38
4.25	0	100		5.491	13.576	0.936	5.91
4.39	0	100		5.491	13.579	0.951	6.55

Table S 3: Refined structural parameters of NBT-6BT FC based on *in situ* electric field-dependent synchrotron XRD measurements. The errors given by the refinement software are about 2 % in phase fractions and for the other reported values significantly smaller than the last given digit. The lattice parameters for the rhombohedral phase are given for a unit cell in hexagonal notation. C = cubic, R = rhombohedral, T = tetragonal.

Electric field /kVmm <sup>-1</sup>	C-phase /%	R-phase /%	T-phase /%	a <sub>cubic</sub> /Å	a <sub>rhomb</sub> /Å	c <sub>rhomb</sub> /Å	a <sub>tet</sub> /Å	c <sub>tet</sub> /Å	η <sub>rhomb</sub> /%	η <sub>tet</sub> /%	R <sub>wp</sub>
0.0	100			3.904							3.89
0.5	100			3.904							3.99
1.0	100			3.904							3.95
1.5	100			3.904							3.85
2.0		77	23		5.513	13.573	3.898	3.932	0.522	0.859	3.66
2.5		81	19		5.513	13.576	3.897	3.936	0.536	1.006	3.78
3.0		80	20		5.513	13.577	3.898	3.935	0.545	0.952	3.77
3.5		79	21		5.512	13.580	3.897	3.934	0.579	0.944	3.81
4.0		79	21		5.512	13.580	3.897	3.934	0.579	0.944	3.84
4.5		79	21		5.511	13.587	3.895	3.936	0.650	1.060	3.42
5.0		81	19		5.507	13.599	3.902	3.938	0.808	0.899	2.65
5.5		81	19		5.507	13.603	3.903	3.941	0.837	0.961	3.04
6.0		81	19		5.506	13.603	3.902	3.941	0.858	1.005	2.69

Table S 4: Refined structural parameters of NBT-6BT Q based on *in situ* electric field-dependent synchrotron XRD measurements. The errors given by the refinement software are about 2 % in phase fractions and for the other reported values significantly smaller than the last given digit. The lattice parameters for the rhombohedral phase are given for a unit cell in hexagonal notation. C = cubic, R = rhombohedral, T = tetragonal.

Electric field /kVmm <sup>-1</sup>	C-phase /%	R-phase /%	T-phase /%	a <sub>cubic</sub> /Å	a <sub>rhomb</sub> /Å	c <sub>rhomb</sub> /Å	a <sub>tet</sub> /Å	c <sub>tet</sub> /Å	η <sub>rhomb</sub> /%	η <sub>tet</sub> /%	R <sub>wp</sub>
0.0	29	71		3.904	5.505	13.598			0.834		2.49
0.5	30	70		3.904	5.505	13.598			0.838		2.50
1.0	27	73		3.904	5.506	13.597			0.824		2.49

1.5	29	71	3.903	5.505	13.598			0.838	2.57	
2.0	27	73	3.903	5.505	13.599			0.856	2.58	
2.5	20	80	3.904	5.506	13.599			0.840	2.75	
3.0		93	7	5.508	13.590	3.902	3.926	0.732	0.605	4.20
3.5		93	7	5.507	13.595	3.905	3.934	0.778	0.748	4.10
4.0		93	7	5.507	13.595	3.905	3.935	0.781	0.779	4.07
4.5		90	10	5.507	13.596	3.904	3.931	0.794	0.712	4.07
5.0		90	10	5.507	13.597	3.905	3.933	0.803	0.725	4.14
5.5		90	10	5.507	13.597	3.905	3.933	0.806	0.727	3.55
6.0		88	12	5.507	13.597	3.906	3.935	0.800	0.743	3.67

Table S 5: Refined structural parameters of NBT-9BT FC based on *in situ* electric field-dependent synchrotron XRD measurements. The errors given by the refinement software are about 2 % in phase fractions and for the other reported values significantly smaller than the last given digit. The lattice parameters for the rhombohedral phase are given for a unit cell in hexagonal notation. R = rhombohedral, T = tetragonal.

Electric field /kVmm <sup>-1</sup>	R-phase /%	T-phase /%	a <sub>rhomb</sub> /Å	c <sub>rhomb</sub> /Å	a <sub>tet</sub> /Å	c <sub>tet</sub> /Å	η <sub>tet</sub> /%	R <sub>wp</sub>
0.0	60	40	5.534	6.776	3.901	3.945	1.143	4.59
0.5	62	38	5.533	6.779	3.901	3.945	1.138	4.62
1.0	17	83	5.539	6.773	3.899	3.947	1.224	3.81
1.5	18	82	5.539	6.773	3.899	3.947	1.226	3.81
2.0	17	83	5.546	6.766	3.897	3.951	1.385	3.33
2.5	14	86	5.548	6.765	3.898	3.951	1.380	3.24
3.0	13	87	5.550	6.764	3.898	3.952	1.394	3.25
3.5	12	88	5.550	6.765	3.898	3.951	1.380	3.17
4.0	11	89	5.551	6.763	3.898	3.951	1.380	2.99
4.5	11	89	5.551	6.763	3.898	3.952	1.390	2.95

5.0	9	91	5.552	6.762	3.897	3.953	1.422	2.78
5.5	15	85	5.544	6.770	3.897	3.953	1.436	2.75
6.0	18	82	5.543	6.771	3.897	3.953	1.455	2.72

Table S 6: Refined structural parameters of NBT-9BT Q based on *in situ* electric field-dependent synchrotron XRD measurements. The errors given by the refinement software are about 2 % in phase fractions and for the other reported values significantly smaller than the last given digit. The lattice parameters for the rhombohedral phase are given for a unit cell in hexagonal notation. R = rhombohedral, T = tetragonal.

Electric field /kVmm <sup>-1</sup>	R-phase /%	T-phase /%	a <sub>rhom</sub> /Å	c <sub>rhom</sub> /Å	a <sub>tet</sub> /Å	c <sub>tet</sub> /Å	η <sub>tet</sub> /%	R <sub>wp</sub>
0.0	16	84	5.544	6.764	3.897	3.956	1.531	4.23
0.5	16	84	5.544	6.764	3.897	3.956	1.531	4.23
1.0	16	84	5.544	6.763	3.897	3.956	1.531	4.16
1.5	15	85	5.544	6.763	3.897	3.956	1.532	4.15
2.0	15	85	5.546	6.764	3.896	3.957	1.556	4.22
2.5	16	84	5.550	6.762	3.896	3.958	1.569	4.35
3.0	16	84	5.550	6.764	3.896	3.958	1.569	4.33
3.5	15	85	5.555	6.759	3.896	3.959	1.608	4.40
4.0	13	87	5.555	6.758	3.896	3.959	1.617	4.00
4.5	12	88	5.556	6.758	3.896	3.960	1.635	3.94
5.0	12	88	5.556	6.758	3.896	3.960	1.644	3.85
5.5	11	89	5.556	6.759	3.896	3.960	1.644	3.85
6.0	11	89	5.556	6.759	3.896	3.960	1.644	3.87

---

---

## List of Tables

---

- Table 1: Promising doping elements reported for BF-BT. Typically, the doping concentrations vary between 0 and 3 mol%. In most cited studies, different doping concentrations were investigated. The qualitative changes in properties listed in this table refer to the most promising doping concentrations stated in the cited literatures, respectively.....24
- Table 2: Refined structural parameters of the high resolution powder XRD data of NBT-BT compositions. The errors given by the refinement software are about 2 % in phase fractions and for the other reported values significantly smaller than the last given digit. C, R and T stand for cubic, rhombohedral and tetragonal, respectively, while  $\eta_{tet}$  describes the tetragonal distortion calculated as  $c_{tet}/a_{tet} - 1$ .  $R_{wp}$  denotes the goodness of fit with lower values indicating less difference between measured and calculated curve.....55
- Table 3: Refined structural parameters of unpoled NBT-BT compositions based on synchrotron XRD measurements. The errors given by the refinement software are about 1 % in phase fractions and for the other reported values significantly smaller than the last given digit.....58
- Table 4: Refined structural parameters of poled NBT-BT compositions based on synchrotron XRD measurements. The errors given by the refinement software are about 1 % in phase fractions and for the other reported values significantly smaller than the last given digit.....61
- Table 5: Refined structural parameters of the high-resolution powder XRD data of BF-BT(-NBT) compositions. The errors given by the refinement software are about 1 % in phase fractions, about  $0.003^\circ$  for  $90^\circ-\alpha_{rhom}$  and for the other reported values significantly smaller than the last given digit. C and R stand for cubic and rhombohedral, respectively. .... 118



---

## List of Figures

---

- Figure 1: Different polarization processes in dielectric materials under applied electric field: electronic, ionic, dipolar and space charge polarization (redrawn after [16]). ..... 4
- Figure 2: Classification of dielectrics and their subgroups with respective relevant properties. .... 5
- Figure 3: Temperature-dependent distortions of a perovskite-structured BaTiO<sub>3</sub> unit cell. All ions of the unit cell are displayed for the cubic state, while for the lower symmetries only the displacement of the Ti<sup>4+</sup>-ion and one possible polarization vector are given. Distortions are exaggerated for better visibility (modified after [16]). ..... 7
- Figure 4: Schematic of the hysteretic ferroelectric behavior of polarization and strain as a function of bipolar electric field. Different idealized stages of the electric field-dependent domain configuration for a tetragonal ferroelectric material are given with the black arrows indicating the direction of the polarization vector for the respective domains (modified after [20]). ..... 9
- Figure 5: Schematic drawing outlining the differences in electric field- and temperature-dependent polarization and temperature-dependent permittivity in normal ferroelectrics (a-c) and relaxors (d-e). Dashed green lines in (d) indicate the dielectric behavior of a poled non-ergodic relaxor (redrawn and modified after [26]). ..... 11
- Figure 6: PNRs (orange) embedded in non-polarized matrix (blue) as proposed by the dipolar glass model. (a) Temperature is slightly below  $T_B$ . The PNRs have a short coherence length and do not interact. (b) Upon further cooling the PNRs grow and interact partly (redrawn after [35]). ..... 13
- Figure 7: The temperature-dependent phase diagram of NBT-xBT with x being the absolute amount BT in moles in the unpoled (a) and in the poled state (b). Besides the present phase, several material-specific temperatures are marked with  $T_{VF}$ : freezing or Vogel-Fulcher temperature,  $T_2$ : rhombohedral  $R3c$  to tetragonal  $P4bm$  phase transition temperature,  $T_m$ : temperature of the dielectric permittivity maximum,  $T_1$ : tetragonal  $P4bm$  to cubic  $Pm3m$  transition temperature,  $T_2'$ : temperature corresponding to the onset of in-phase octahedral tilt,  $T''$ : tetragonal ( $P4mm$ ) to cubic ( $Pm3m$ ) transition temperature,  $T_d$ : depolarization temperature (reprinted from [54] with permission from the American Physical Society). .... 17
- Figure 8: Temperature-dependent real ( $\epsilon'$ ) and imaginary parts ( $\epsilon''$ ) of permittivity of NBT-6BT in the unpoled (a) and poled state (b).  $\epsilon'$  is deconvoluted based on the assumption of two

processes being related to the two types of PNRs being present. The colors denote measurement frequencies: black = 100 Hz, red = 1 kHz, green = 10 kHz, blue = 100 kHz (reprinted from [79] with the permission from AIP Publishing).....	19
Figure 9: Temperature- and composition-dependent phase diagram of the BF-BT solid solution based on dielectric and differential scanning calorimetry measurements. PE stands for paraelectric. (reprinted from [90] with the permission from John Wiley and Sons).....	21
Figure 10: (a) Phase diagram of BF-BT with $T_c$ established from synchrotron X-ray diffraction and dielectric data and (b) composition-dependent direct ( $d_{33}$ ) and converse ( $d_{33}^*$ ) piezoelectric constants (reprinted from [97] with the permission from AIP Publishing).....	22
Figure 11: Temperature-dependent dielectric permittivity $\epsilon'$ for different (1-x)BF-xBT compositions measured at 1 MHz (reprinted from [98] with permission from John Wiley and Sons).....	23
Figure 12: Piezoelectric coefficient, $d_{33}$ , versus Curie Temperature, $T_c$ , in BF-BT ceramics with (a) comparison between pure BF-BT and ternary systems and (b) comparison between as sintered or furnace cooled and quenched ceramics (reprinted from [139]). .....	25
Figure 13: (a) Rhombohedral and tetragonal lattice distortion given as $90^\circ - \alpha_{\text{rhom}}$ and $c_T/a_T$ , respectively, for normally sintered (OF) and quenched (q) Li-doped NBT-BT (reprinted from [87] with permission from IOP Publishing). (b) Schematic illustration of the A-site ion with the unit cell of Li-doped NBT using the software VESTA (reprinted from [149])......	27
Figure 14: Temperature-dependent real and imaginary part of permittivity for poled and unpoled NBT-6BT FC (a, e), NBT-6BT Q1100 (b, f), NBT-9BT FC (c, g) and NBT-9BT Q1100 (d, h). FC stands for furnace cooled meaning normally sintered while Q1100 means the material was quenched from 1100 °C after the sintering step (reprinted from [13] with permission from AIP Publishing). .....	28
Figure 15: SEM micrographs of etched Mn-doped BF-BT with 25 mol% BT in the as-sintered (a, c) and quenched state (b, d). Reprinted from [134] with permission from the Royal Society of Chemistry.....	31
Figure 16: Direct and indirect piezoelectric coefficient and Curie Temperature of BF-BT ceramics with 33 mol% BT as-sintered (FC) and quenched from different temperatures. WQ980 stands for water-quenched and BG for modified with 1 mol% BiGaO <sub>3</sub> and water-quenched. Reprinted from [167] with permission from the American Chemical Society.....	32

---

Figure 17: Used solid state reaction processing route to receive polycrystalline ceramic samples. .....	35
Figure 18: Schematic temperature-time curve for furnace cooled and quenched NBT-BT ceramics. .....	36
Figure 19: Bar-shaped sample placed in a Ni-wire suspension to measure the resonance frequency with the impulse excitation technique. The elastic mechanical impulse results in an oscillating sample and an acoustic signal which is recorded by a microphone (reprinted in modified form from [172]).	42
Figure 20: Representative evolution of Young's modulus as a function of temperature here shown from a measurement of NBT-12BT FC. Simplistically, the material undergoes a transition from ferroelectric tetragonal to relaxor with tetragonal polar regions within a cubic matrix at $T_{F-R}$ and to a paraelectric, entirely cubic state at $T_B$ upon heating. Reprinted from [177].	44
Figure 21: Schematic synchrotron measurement setup for poled samples and <i>in situ</i> electric field-dependent measurements as used for diffraction experiments at DESY.	46
Figure 22: Sections of powder XRD patterns showing the $\{111\}_{PC}$ and $\{200\}_{PC}$ reflections of crushed and annealed furnace cooled (black) and quenched (red) NBT-BT ceramics. The dashed vertical lines indicate the approximate position of the $111_R$ in NBT-3BT and $002_T$ reflections in NBT-9BT and NBT-12BT.	50
Figure 23: Powder XRD patterns of calcined and crushed NBT-BT. The characteristic perovskite reflections are indexed with respect to a cubic reference frame. The arrows indicate additional reflections due to Tungsten $K\alpha$ -radiation caused by impurities in the anode material of the diffractometer.	51
Figure 24: (a) X-ray powder diffraction patterns of furnace cooled and quenched NBT-BT compositions. (b) Enlarged section of the XRD patterns showing the $\{111\}_{PC}$ reflections. "SR" marks superlattice reflections visible in NBT-3BT and vaguely in NBT-6BT materials. (c) Enlarged sections displaying the $\{200\}_{PC}$ reflections. Dashed vertical lines indicate the position of relevant peaks.	53
Figure 25: Rietveld refinement of NBT-3BT FC with (a) showing the whole measured XRD pattern, the calculated curve and the difference. The inlay (b) displays the $\{111\}_{PC}$ and $\{200\}_{PC}$ reflections with the respective phase contributions.	54

---

Figure 26: (a) Synchrotron XRD patterns of furnace cooled and quenched NBT-BT bulk ceramics in the unpoled state with enlarged sections of the XRD patterns showing the $\{111\}_{PC}$ (b) and $\{200\}_{PC}$ (c) reflections. The asterisks mark contributions from the Ag electrodes.....	57
Figure 27: (a) Synchrotron XRD patterns of furnace cooled and quenched NBT-BT bulk ceramics in the poled state, weighted and summed up with respect to the azimuthal angle. Enlarged sections of the XRD patterns showing the $\{111\}_{PC}$ (b) and $\{200\}_{PC}$ (c) reflections. The asterisks mark contributions from the Ag electrodes. ....	59
Figure 28: Azimuthal angle-dependent diffraction patterns showing the $\{110\}_{PC}$ , $\{111\}_{PC}$ and $\{200\}_{PC}$ reflections of poled NBT-6BT FC. A strong angle dependence in the peak intensities is clearly present.....	62
Figure 29: Texture factors as a function of azimuthal angle for the dominant phase of the respective composition.....	64
Figure 30: Secondary electron SEM micrographs of polished and thermally etched NBT-BT specimen of all the investigated compositions, furnace cooled and quenched. ....	66
Figure 31: Composition-dependent average grain size and relative density of furnace cooled and quenched NBT-BT ceramics. ....	67
Figure 32: First (a-d) and third (e-h) electric field-dependent polarization cycles of furnace cooled (black) and quenched (red) samples of all investigated NBT-BT compositions measured with a frequency of 1 Hz.....	69
Figure 33: First (a-d) and third (e-h) electric field-dependent strain cycles of furnace cooled (black) and quenched (red) samples of all investigated NBT-BT compositions measured with a frequency of 1 Hz.....	70
Figure 34: Maximum and remanent polarization (a) and coercive field (b) extracted from electric field-dependent polarization measurements for all investigated NBT-BT compositions.....	71
Figure 35: Total and negative strain (a) extracted from electric field-dependent polarization measurements and direct piezoelectric constant, $d_{33}$ (b), for all investigated NBT-BT compositions.....	72
Figure 36: Frequency-dependent permittivity of furnace cooled and quenched NBT-BT samples measured at room temperature in the poled state.....	75

Figure 37: Temperature-dependent permittivity measured at different frequencies on poled furnace cooled and quenched NBT-BT samples.....	77
Figure 38: Temperature-dependent permittivity measured at different frequencies on unpoled furnace cooled and quenched NBT-BT samples.....	78
Figure 39: Difference in $\epsilon'$ measured at 100 Hz and 1 MHz on unpoled samples at room temperature and $T_{F-R}$ established from temperature-dependent dielectric data measured at 1 kHz on poled samples of NBT-BT.....	79
Figure 40: Temperature of the maximum of the imaginary part of permittivity, $Tm''$ versus frequency plotted for NBT-6BT FC (a) and NBT-6BT Q (b). Blue lines depict the exponential fits of the data which were used to establish Vogel-Fulcher temperature and activation energy. ....	80
Figure 41: Young's modulus and PNR volume fraction as a function of temperature for all investigated NBT-BT compositions, unpoled, FC and Q. The vertical black and red dashed lines indicate $T_{F-R}$ for FC and Q, respectively, while the blue solid lines mark $T_m$ . $T_m$ for FC and Q samples does not deviate more than 8 °C and therefore, only one line per chemical composition is plotted.....	82
Figure 42: Composition-dependent PNR volume fraction at 300 °C and Young's modulus at 30 °C of unpoled NBT-BT. ....	84
Figure 43: <i>In situ</i> synchrotron X-ray diffraction patterns of NBT-3BT FC and NBT-3BT Q during application of electric field, starting from the unpoled state collected parallel to the applied field vector ( $\Psi = 2.5^\circ$ ). (a) and (b) depict the evolution of the $\{111\}_{PC}$ and $\{200\}_{PC}$ profiles of NBT-3BT FC upon application of electric field, respectively. (c) and (d) depict the same for NBT-3BT Q. Horizontal dashed lines mark a strong shift in intensities of $111_R$ and $111_R$ reflections and the broadening and onset of asymmetry in the $\{200\}_{PC}$ reflection.....	88
Figure 44: Excerpts of 1D diffraction patterns of NBT-3BT FC visualizing the strong angle dependence in peak intensities at an applied electric field of 4.2 kV/mm (a) and contrasting the reflection profiles of $\{111\}_{PC}$ (c) and $\{200\}_{PC}$ (d) reflections at 0 and 4.2 kV/mm parallel to the applied field direction. (b), (e) and (f) depict the same for NBT-3BT Q.....	90
Figure 45: <i>In situ</i> synchrotron X-ray diffraction patterns of NBT-6BT FC and NBT-6BT Q during application of electric field, starting from the unpoled state collected parallel to the applied field vector ( $\Psi = 0^\circ$ ). (a) and (b) depict the evolution of the $\{111\}_{PC}$ and $\{200\}_{PC}$ profiles of	

NBT-6BT FC upon application of electric field, respectively. (c) and (d) depict the same for NBT-6BT Q. SR marks the superlattice reflection in (a) and (c). Horizontal dashed lines mark the appearance of new reflections (magenta) or pronounced intensity change of existing reflections (green).....	91
Figure 46: Excerpts of 1D diffraction patterns of NBT-6BT FC visualizing the strong angle dependence in peak intensities at an applied electric field of 6 kV/mm (a) and contrasting the reflection profiles of $\{111\}_{PC}$ (c) and $\{200\}_{PC}$ (d) reflections at 0 and 6 kV/mm parallel to the applied field direction. (b), (e) and (f) depict the same for NBT-6BT Q.....	92
Figure 47: <i>In situ</i> synchrotron X-ray diffraction patterns of NBT-9BT FC and NBT-9BT Q during application of electric field, starting from the unpoled state collected parallel to the applied field vector ( $\Psi = 0^\circ$ ). (a) and (b) depict the evolution of the $\{111\}_{PC}$ and $\{200\}_{PC}$ profiles of NBT-9BT FC upon application of electric field, respectively. (c) and (d) depict the same for NBT-9BT Q. The horizontal dashed magenta line indicates a phase transformation. ....	94
Figure 48: Excerpts of 1D diffraction patterns of NBT-9BT FC visualizing the strong angle dependence in peak intensities at an applied electric field of 6 kV/mm (a) and contrasting the reflection profiles of $\{111\}_{PC}$ (c) and $\{200\}_{PC}$ (d) reflections at 0 and 6 kV/mm parallel to the applied field direction. (b), (e) and (f) depict the same for NBT-9BT Q.....	95
Figure 49: Texture factor, $f_{111}$ , in MRD for NBT-3BT FC (a) and NBT-3BT Q (b) as a function of azimuthal angle for different applied electric fields. ....	96
Figure 50: Calculated texture factors at 6 kV/mm applied electric field based on the peak fitting approach for the rhombohedral phase of NBT-6BT FC and NBT-6BT Q (a) and the tetragonal phase of NBT-9BT FC and NBT-9BT Q (b) using the $45^\circ$ data as reference.....	97
Figure 51: Phase fractions as a function of electric field obtained using Rietveld refinement. ....	98
Figure 52: Measured macroscopic strain and calculated volumetric strain, $\varepsilon_v$ , as a function of applied electric field for (a) NBT-6BT FC, (b) NBT-9BT FC, (c) NBT-6BT Q and (d) NBT-9BT Q. ....	104
Figure 53: Calculated strain contributions and the comparison between measured and summed up calculated strain as a function of electric field for NBT-3FC (a, c) and NBT-3BT Q (b, d). ....	108
Figure 54: Powder XRD patterns of calcined and crushed BF-BT(-NBT) compositions. The characteristic perovskite reflections are indexed with respect to a cubic reference frame. ....	112

Figure 55: SEM micrographs of polished BF-BT(-NBT) specimens of all investigated compositions, furnace cooled and quenched, collected in BSE mode.....	114
Figure 56: SEM micrographs of polished BF-BT(-NBT) specimens of all investigated compositions, furnace cooled and quenched, collected in BSE mode with higher magnification. The green arrows mark a Bi-rich phase while the blue arrow marks a local enrichment in Ba and Ti.	115
Figure 57: (a) X-ray powder diffraction patterns of furnace cooled and quenched BF-BT(-NBT) compositions. (b) Enlarged section of the XRD patterns showing the $\{111\}_{PC}$ reflections. ..	116
Figure 58: Temperature-dependent X-ray powder diffraction pattern profile evolution of $\{110\}_{PC}$ , $\{111\}_{PC}$ and $\{200\}_{PC}$ reflections for BF-33BT FC (a) and BF-33BT+5NBT FC (b). Intensities were normalized for each reflection profile individually. ....	119
Figure 59: Temperature-dependent permittivity and loss tangents measured at different frequencies on poled furnace cooled and quenched BF-BT(-NBT) ceramics. ....	122
Figure 60: Comparison of temperature-dependent permittivity and loss tangents measured at 1 kHz for furnace cooled and quenched BF-33BT with and without 5 mol% NBT (a and b) and the same for BF-30BT-related materials, respectively (c and d).....	123
Figure 61: First (a-d) and third (e-h) electric field-dependent polarization cycles of furnace cooled (black) and quenched (red) samples of all investigated BF-BT(-NBT) compositions measured with a frequency of 3 Hz. ....	124
Figure 62: First (a-d) and third (e-h) electric field-dependent strain cycles of furnace cooled (black) and quenched (red) samples of all investigated BF-BT(-NBT) compositions measured with a frequency of 3 Hz. ....	125
Figure 63: Total (a) and negative strain (b), maximum, $P_{max}$ , (c) and remanent polarization, $P_{rem}$ , (d), coercive field, $E_c$ , (e) and $d_{33}$ (f) for all investigated BF-BT(-NBT) compositions, furnace cooled and quenched. ....	126

---

## List of Abbreviations and Symbols

---

APS	Advanced Photon Source
DESY	Deutsches Elektronensynchrotron
EU	European Union
FC	Furnace cooled
MPB	Morphotropic phase boundary
NMR	Nuclear magnetic resonance
PC	Pseudo-cubic
PFM	Piezoresponse force microscopy
PNR	Polar nanoregion
Q	Quenched
RFDA	Resonance frequency damping analysis
RoHS	Restriction of Hazardous Substances
SEM	Scanning electron microscopy
SR	Superlattice reflection
TEM	Transmission electron microscopy
XRD	X-ray diffraction

### Materials

BF	$\text{BiFeO}_3$
BF-BT	$\text{BiFeO}_3\text{-BaTiO}_3$
BF-BT-NBT	$\text{BiFeO}_3\text{-BaTiO}_3\text{-Na}_{1/2}\text{Bi}_{1/2}\text{TiO}_3$
BT	$\text{BaTiO}_3$
NBT	$\text{Na}_{1/2}\text{Bi}_{1/2}\text{TiO}_3$
NBT-BT	$\text{Na}_{1/2}\text{Bi}_{1/2}\text{TiO}_3\text{-BaTiO}_3$



---

PLZT	$(\text{Pb,L a})(\text{Zr,T i})\text{O}_3$
PMN	$\text{Pb}(\text{Mg}_{1/3}\text{Nb}_{2/3})\text{O}_3$
PMT-PT	$\text{Pb}(\text{Mg}_{1/3}\text{Nb}_{2/3})\text{O}_3\text{-PbTiO}_3$
PZT	$\text{Pb}(\text{Zr,T i})\text{O}_3$

## Symbols

$A$	Sample area
$a, b, c$	Lattice parameters of a unit cell
$b$	Sample width
$C$	Curie constant
$c_i$	Volume fraction of a PNRs or cubic matrix phase
$C_p$	Capacitance
$d_{33}$	Piezoelectric charge coefficient
$d_{hkl}$	D-spacing
$D_i$	Dielectric displacement
$d_{ijk}$	Piezoelectric tensor
$E_a$	Activation energy
$E_c$	Coercive electric field
$E_j$	External electric field
$E_k$	Applied electric field
$f$	Frequency
$f_{hkl}$	Texture factor
$f_o$	Cut-off frequency of the distribution of relaxation time
$f_R$	Resonance frequency
$I_{hkl}$	Reflection intensity
$k_B$	Boltzmann constant

---

$k_p$	Electromechanical coupling factor
$l$	Sample length
$m$	Sample mass
$m_{\text{air}}$	Sample mass measured in air
$m_{\text{hkl}}$	Planar multiplicity of a hkl lattice plane
$m_{\text{water}}$	Sample mass measured in water
$PF$	Phase fraction from Rietveld refinement
$P_i$	Macroscopic polarization
$p_i$	Pyroelectric constant
$P_{\text{max}}$	Maximum polarization
$P_{\text{rem}}$	Remanent polarization
$S_{\text{rem}}$	Remanent strain
$t$	Sample thickness
$T$	Temperature
$T''_m$	Temperature of the maximum of the imaginary part of permittivity
$\tan \delta$	Dielectric loss tangent
$T_B$	Burns temperature
$T_c$	Curie temperature
$T_d$	Depolarization temperature
$T_{\text{F-R}}$	Ferroelectric-to-relaxor transition temperature
$T_m$	Temperature of the maximum of the real part of permittivity
$T_{\text{VF}}$	Static freezing temperature or Vogel-Fulcher temperature
$V$	Unit cell volume
$Y$	Young's modulus
$Y_{\text{cub}}$	Young's modulus of the cubic phase
$Y_{\text{tet}}$	Young's modulus of the tetragonal phase

---

$\alpha_{\text{rhom}}$ in $90^\circ$ - $\alpha_{\text{rhom}}$	Non- $90^\circ$ angle in a rhombohedral unit cell
$\epsilon'$	Real part of the permittivity
$\epsilon''$	Imaginary part of the permittivity
$\epsilon_{\text{hkl}}$	Contribution from an hkl lattice plane
$\epsilon_{\text{intrinsic}}$	Intrinsic strain contribution
$\epsilon_{\text{non-180}}$	Domain switching strain contribution
$\epsilon_0$	Permittivity of free space
$\epsilon_r$	Relative permittivity
$\epsilon_V$	Volumetric or phase transformation strain
$\eta_{\text{rhom}}$	Rhombohedral distortion
$\eta_{\text{tet}}$	Tetragonal distortion
$\theta$	Diffraction angle
$\kappa_i$	Bulk modulus
$\mu_i$	Shear modulus
$\nu$	Poisson's ratio
$\rho_{\text{abs}}$	Absolute sample density
$\rho_{\text{air}}$	Density of air
$\rho_{\text{rel}}$	Relative sample density
$\rho_{\text{theo}}$	Theoretical sample density
$\rho_{\text{water}}$	Density of water
$\sigma_{\text{jk}}$	Applied stress
$\chi_{\text{ij}}$	Dielectric susceptibility
$\Psi$	Angle to the poling field, azimuthal angle
$\Psi_f$	correction factor for calculation Young's modulus

---

## Literature

---

- [1] M.E. Lines, A.M. Glass, Principles and applications of ferroelectrics and related materials, Oxford classic texts in the physical sciences, (1977), pp. xiii, 680 p.
- [2] L. Cross, R. Newnham, History of ferroelectrics, *Ceramics and civilization* 3 (1987) 289-305.
- [3] N. Izyumskaya, Y.-I. Alivov, S.-J. Cho, H. Morkoç, H. Lee, Y.-S. Kang, Processing, structure, properties, and applications of PZT thin films, *Critical reviews in solid state and materials sciences* 32(3-4) (2007) 111-202.
- [4] A.J. Bell, O. Deubzer, Lead-free piezoelectrics—The environmental and regulatory issues, *MRS Bulletin* 43(8) (2018) 581-587.
- [5] J. Rödel, J.-F. Li, Lead-free piezoceramics: Status and perspectives, *MRS Bulletin* 43(8) (2018) 576-580.
- [6] T. Rojac, A. Bencan, B. Malic, G. Tutuncu, J.L. Jones, J.E. Daniels, D. Damjanovic, D.J. Green, BiFeO<sub>3</sub> Ceramics: Processing, Electrical, and Electromechanical Properties, *Journal of the American Ceramic Society* 97(7) (2014) 1993-2011.
- [7] T. Tou, Y. Hamaguti, Y. Maida, H. Yamamori, K. Takahashi, Y. Terashima, Properties of (Bi<sub>0.5</sub>Na<sub>0.5</sub>)TiO<sub>3</sub>-BaTiO<sub>3</sub>-(Bi<sub>0.5</sub>Na<sub>0.5</sub>)(Mn<sub>1/3</sub>Nb<sub>2/3</sub>)O<sub>3</sub> Lead-Free Piezoelectric Ceramics and Its Application to Ultrasonic Cleaner, *Jpn J Appl Phys* 48(7) (2009).
- [8] T. Takenaka, K. Maruyama, K. Sakata, (Bi<sub>1/2</sub>Na<sub>1/2</sub>)TiO<sub>3</sub>-BaTiO<sub>3</sub> System for Lead-Free Piezoelectric Ceramics, *Jpn J Appl Phys* 1 30(9b) (1991) 2236-2239.
- [9] C.W. Ahn, C.-H. Hong, B.-Y. Choi, H.-P. Kim, H.-S. Han, Y. Hwang, W. Jo, K. Wang, J.-F. Li, J.-S. Lee, A brief review on relaxor ferroelectrics and selected issues in lead-free relaxors, *J Korean Phys Soc* 68(12) (2016) 1481-1494.
- [10] M. Davies, E. Aksel, J.L. Jones, Enhanced High-Temperature Piezoelectric Coefficients and Thermal Stability of Fe- and Mn-Substituted Na<sub>0.5</sub>Bi<sub>0.5</sub>TiO<sub>3</sub> Ceramics, *Journal of the American Ceramic Society* 94(5) (2011) 1314-1316.
- [11] J. Zhang, Z. Pan, F.F. Guo, W.C. Liu, H.P. Ning, Y.B. Chen, M.H. Lu, B. Yang, J. Chen, S.T. Zhang, X.R. Xing, J. Rodel, W.W. Cao, Y.F. Chen, Semiconductor/relaxor 0-3 type composites without thermal depolarization in Bi<sub>0.5</sub>Na<sub>0.5</sub>TiO<sub>3</sub>-based lead-free piezoceramics, *Nat Commun* 6 (2015).
- [12] H. Muramatsu, H. Nagata, T. Takenaka, Quenching effects for piezoelectric properties on lead-free (Bi<sub>1/2</sub>Na<sub>1/2</sub>)TiO<sub>3</sub> ceramics, *Jpn J Appl Phys* 55(10) (2016).
- [13] K.V. Lalitha, J. Koruza, J. Rodel, Propensity for spontaneous relaxor-ferroelectric transition in quenched (Na<sub>1/2</sub>Bi<sub>1/2</sub>)TiO<sub>3</sub>-BaTiO<sub>3</sub> compositions, *Appl Phys Lett* 113(25) (2018).
- [14] L.K. Venkataraman, B. Wang, P. Ren, D.A. Hall, T. Rojac, Quenching effects and mechanisms in bismuth-based perovskite ferroelectrics, *Open Ceramics* (2022) 100259.
- [15] S. Cheng, B.P. Zhang, L. Zhao, K.K. Wang, Enhanced insulating and piezoelectric properties of BiFeO<sub>3</sub>-BaTiO<sub>3</sub>-Bi<sub>0.5</sub>Na<sub>0.5</sub>TiO<sub>3</sub> ceramics with high Curie temperature, *Journal of the American Ceramic Society* 102(12) (2019) 7355-7365.
- [16] A.J. Moulson, J.M. Herbert, *Electroceramics materials, properties, applications*, Second edition. ed. (1990).
- [17] K. Uchino, *Ferroelectric devices*, CRC press (2018).

- 
- [18] R.E. Newnham, Properties of materials: anisotropy, symmetry, structure, Oxford University Press on Demand (2005).
- [19] D. Damjanovic, Ferroelectric, dielectric and piezoelectric properties of ferroelectric thin films and ceramics, Rep Prog Phys 61(9) (1998) 1267-1324.
- [20] F.H. Schader, Mechanical stability of the electromechanical properties and phase transitions in lead-containing and lead-free ferroelectrics, (2016).
- [21] G. Smolenskii, V. Isupov, \* SEGNETOELEKTRICHESKIE SVOISTVA TVERDYKH RASTVOROV STANNATA BARIYA V TITANATE BARIYA, Zhurnal Tekhnicheskoi Fiziki 24(8) (1954) 1375-1386.
- [22] L.E. Cross, Relaxor Ferroelectrics, Ferroelectrics 76(3-4) (1987) 241-267.
- [23] A.A. Bokov, Z.-G. Ye, Dielectric Relaxation in Relaxor Ferroelectrics, J Adv Dielectr 02(02) (2012).
- [24] R.A. Cowley, S.N. Gvasaliya, S.G. Lushnikov, B. Roessli, G.M. Rotaru, Relaxing with relaxors: a review of relaxor ferroelectrics, Adv Phys 60(2) (2011) 229-327.
- [25] L.E. Cross, Relaxor Ferroelectrics: An Overview, Ferroelectrics 151(1) (1994) 305-320.
- [26] G.A. Samara, The relaxational properties of compositionally disordered ABO<sub>3</sub> perovskites, J Phys-Condens Mat 15(9) (2003) R367-R411.
- [27] V.V. Shvartsman, D.C. Lupascu, Lead-Free Relaxor Ferroelectrics, Journal of the American Ceramic Society 95(1) (2012) 1-26.
- [28] R.J.D. Tilley, Perovskites Structure–Property Relationships, (2016).
- [29] G.A. Smolenskii, V.A. Isupov, A.I. Agranovskaya, N.N. Krainik, New Ferroelectrics of Complex Composition .4., Sov Phys-Sol State 2(11) (1961) 2651-2654.
- [30] G. Smolenskii, A. Agranovskaya, Dielectric polarization and losses of some complex compounds, Zhur. Tekh. Fiz. 28 (1958).
- [31] V. Kirillov, V. Isupov, Relaxation polarization of PbMg<sub>1/3</sub>Nb<sub>2/3</sub>O<sub>3</sub> (PMN)-A ferroelectric with a diffused phase transition, Ferroelectrics 5(1) (1973) 3-9.
- [32] N. Setter, L.E. Cross, The Contribution of Structural Disorder to Diffuse Phase-Transitions in Ferroelectrics, J Mater Sci 15(10) (1980) 2478-2482.
- [33] D. Viehland, J.F. Li, S.J. Jang, L.E. Cross, M. Wuttig, Dipolar-Glass Model for Lead Magnesium Niobate, Physical Review B 43(10) (1991) 8316-8320.
- [34] N. Novak, R. Pirc, M. Wencka, Z. Kutnjak, High-resolution calorimetric study of Pb (Mg<sub>1/3</sub> Nb<sub>2/3</sub>) O<sub>3</sub> single crystal, Phys Rev Lett 109(3) (2012) 037601.
- [35] G.A. Samara, Ferroelectricity revisited - Advances in materials and physics, Solid State Phys 56 (2001) 239-458.
- [36] V. Westphal, W. Kleemann, M. Glinchuk, Diffuse phase transitions and random-field-induced domain states of the “relaxor” ferroelectric PbMg<sub>1/3</sub> Nb<sub>2/3</sub> O<sub>3</sub>, Phys Rev Lett 68(6) (1992) 847.
- [37] Y. Imry, S.-k. Ma, Random-field instability of the ordered state of continuous symmetry, Phys Rev Lett 35(21) (1975) 1399.
- [38] V.V. Shvartsman, W. Kleemann, T. Łukasiewicz, J. Dec, Nanopolar structure in Sr<sub>x</sub> Ba<sub>1-x</sub> Nb<sub>2</sub> O<sub>6</sub> single crystals tuned by Sr/Ba ratio and investigated by piezoelectric force microscopy, Physical review B 77(5) (2008) 054105.

- 
- [39] H. Takenaka, I. Grinberg, S. Liu, A.M. Rappe, Slush-like polar structures in single-crystal relaxors, *Nature* 546(7658) (2017) 391-+.
- [40] J. Koruza, L. Kodumudi Venkataraman, B. Malič, Lead-free perovskite ferroelectrics, *Magnetic, Ferroelectric, and Multiferroic Metal Oxides* (2018), pp. 51-69.
- [41] J. Wu, Z. Fan, D. Xiao, J. Zhu, J. Wang, Multiferroic bismuth ferrite-based materials for multifunctional applications: ceramic bulks, thin films and nanostructures, *Progress in Materials Science* 84 (2016) 335-402.
- [42] N.A. Hill, *Why are there so few magnetic ferroelectrics?*, ACS Publications, (2000), pp. 6694-6709.
- [43] S.M. Selbach, T. Tybell, M.-A. Einarsrud, T. Grande, Phase transitions, electrical conductivity and chemical stability of BiFeO<sub>3</sub> at high temperatures, *J Solid State Chem* 183(5) (2010) 1205-1208.
- [44] Y. Doshida, H. Shimizu, Y. Mizuno, H. Tamura, Investigation of High-Power Properties of (Bi,Na,Ba)TiO<sub>3</sub> and (Sr,Ca)<sub>2</sub>NaNb<sub>5</sub>O<sub>15</sub> Piezoelectric Ceramics, *Jpn J Appl Phys* 52(7) (2013).
- [45] K. Shibata, R. Wang, T. Tou, J. Koruza, Applications of lead-free piezoelectric materials, *MRS Bulletin* 43(8) (2018) 612-616.
- [46] M. Slabki, L.K. Venkataraman, T. Rojac, J. Rodel, J. Koruza, Thermal stability of the electromechanical properties in acceptor-doped and composite-hardened (Na<sub>1/2</sub>Bi<sub>1/2</sub>)TiO<sub>3</sub>-BaTiO<sub>3</sub> ferroelectrics, *J Appl Phys* 130(1) (2021).
- [47] S. Gorfman, P.A. Thomas, Evidence for a non-rhombohedral average structure in the lead-free piezoelectric material Na<sub>0.5</sub>Bi<sub>0.5</sub>TiO<sub>3</sub>, *J Appl Crystallogr* 43 (2010) 1409-1414.
- [48] E. Aksel, J.S. Forrester, J.L. Jones, P.A. Thomas, K. Page, M.R. Suchomel, Monoclinic crystal structure of polycrystalline Na<sub>0.5</sub>Bi<sub>0.5</sub>TiO<sub>3</sub>, *Appl Phys Lett* 98(15) (2011).
- [49] E. Aksel, J.S. Forrester, J.C. Nino, K. Page, D.P. Shoemaker, J.L. Jones, Local atomic structure deviation from average structure of Na<sub>0.5</sub>Bi<sub>0.5</sub>TiO<sub>3</sub>: Combined x-ray and neutron total scattering study, *Physical Review B* 87(10) (2013).
- [50] A.R. Paterson, H. Nagata, X. Tan, J.E. Daniels, M. Hinterstein, R. Ranjan, P.B. Groszewicz, W. Jo, J.L. Jones, Relaxor-ferroelectric transitions: Sodium bismuth titanate derivatives, *MRS Bulletin* 43(8) (2018) 600-606.
- [51] V. Shuvaeva, D. Zekria, A. Glazer, Q. Jiang, S. Weber, P. Bhattacharya, P. Thomas, Local structure of the lead-free relaxor ferroelectric (K x Na 1- x) 0.5 Bi 0.5 Ti O 3, *Physical Review B* 71(17) (2005) 174114.
- [52] V. Dorcet, G. Trolliard, A transmission electron microscopy study of the A-site disordered perovskite Na<sub>0.5</sub>Bi<sub>0.5</sub>TiO<sub>3</sub>, *Acta Mater* 56(8) (2008) 1753-1761.
- [53] J. Rödel, W. Jo, K.T.P. Seifert, E.M. Anton, T. Granzow, D. Damjanovic, Perspective on the Development of Lead-free Piezoceramics, *Journal of the American Ceramic Society* 92(6) (2009) 1153-1177.
- [54] G. Das Adhikary, B. Mahale, B.N. Rao, A. Senyshyn, R. Ranjan, Depoling phenomena in Na<sub>0.5</sub>Bi<sub>0.5</sub>TiO<sub>3</sub>BaTiO<sub>3</sub>: A structural perspective, *Physical Review B* 103(18) (2021) 184106.
- [55] C. Ma, H.Z. Guo, X.L. Tan, A New Phase Boundary in (Bi<sub>1/2</sub>Na<sub>1/2</sub>)TiO<sub>3</sub>-BaTiO<sub>3</sub> Revealed via a Novel Method of Electron Diffraction Analysis, *Advanced Functional Materials* 23(42) (2013) 5261-5266.

- 
- [56] F. Cordero, F. Craciun, F. Trequattrini, E. Mercadelli, C. Galassi, Phase transitions and phase diagram of the ferroelectric perovskite  $(\text{Na}_{0.5}\text{Bi}_{0.5})(1-x)\text{Ba}_x\text{TiO}_3$  by anelastic and dielectric measurements, *Physical Review B* 81(14) (2010).
- [57] R. Ranjan, A. Dwiwedi, Structure and dielectric properties of  $(\text{Na}_{0.5}\text{Bi}_{0.5})(1-x)\text{Ba}_x\text{TiO}_3$ :  $0 \leq x \leq 0.10$ , *Solid State Commun* 135(6) (2005) 394-399.
- [58] J.E. Daniels, W. Jo, J. Rodel, J.L. Jones, Electric-field-induced phase transformation at a lead-free morphotropic phase boundary: Case study in a 93% $(\text{Bi}_{0.5}\text{Na}_{0.5})\text{TiO}_3$ -7%  $\text{BaTiO}_3$  piezoelectric ceramic, *Appl Phys Lett* 95(3) (2009).
- [59] B.N. Rao, D.K. Khatua, R. Garg, A. Senyshyn, R. Ranjan, Structural crossover from nonmodulated to long-period modulated tetragonal phase and anomalous change in ferroelectric properties in the lead-free piezoelectric  $\text{Na}_{1/2}\text{Bi}_{1/2}\text{TiO}_3$ - $\text{BaTiO}_3$ , *Physical Review B* 91(21) (2015).
- [60] N.H. Khansur, M. Hinterstein, Z.Y. Wang, C. Groh, W. Jo, J.E. Daniels, Electric-field-induced strain contributions in morphotropic phase boundary composition of  $(\text{Bi}_{1/2}\text{Na}_{1/2})\text{TiO}_3$ - $\text{BaTiO}_3$  during poling, *Appl Phys Lett* 107(24) (2015).
- [61] C. Ma, X. Tan, Phase diagram of unpoled lead-free  $(1-x)(\text{Bi}_{1/2}\text{Na}_{1/2})\text{TiO}_3$ - $x\text{BaTiO}_3$  ceramics, *Solid State Commun* 150(33-34) (2010) 1497-1500.
- [62] C. Ma, H.Z. Guo, S.P. Beckman, X.L. Tan, Creation and Destruction of Morphotropic Phase Boundaries through Electrical Poling: A Case Study of Lead-Free  $(\text{Bi}_{1/2}\text{Na}_{1/2})\text{TiO}_3$ - $\text{BaTiO}_3$  Piezoelectrics, *Phys Rev Lett* 109(10) (2012).
- [63] B. Wylie-van Eerd, D. Damjanovic, N. Klein, N. Setter, J. Trodahl, Structural complexity of  $(\text{Na}_{0.5}\text{Bi}_{0.5})\text{TiO}_3$ - $\text{BaTiO}_3$  as revealed by Raman spectroscopy, *Physical Review B* 82(10) (2010).
- [64] F. Pforr, K.C. Meyer, M. Major, K. Albe, W. Donner, U. Stuhr, A. Ivanov, Relaxation of dynamically disordered tetragonal platelets in the relaxor ferroelectric  $0.964\text{Na}_{1/2}\text{Bi}_{1/2}\text{TiO}_3$ - $0.036\text{BaTiO}_3$ , *Physical Review B* 96(18) (2017).
- [65] F. Pforr, M. Major, W. Donner, U. Stuhr, B. Roessli, Influence of tetragonal platelets on the dielectric permittivity of  $0.964\text{Na}_{1/2}\text{Bi}_{1/2}\text{TiO}_3$ - $0.036\text{BaTiO}_3$ , *Physical Review B* 94(1) (2016).
- [66] J.E. Daniels, W. Jo, J. Rodel, D. Rytz, W. Donner, Structural origins of relaxor behavior in a  $0.96(\text{Bi}_{1/2}\text{Na}_{1/2})\text{TiO}_3$ - $0.04\text{BaTiO}_3$  single crystal under electric field, *Appl Phys Lett* 98(25) (2011).
- [67] K.V. Lalitha, M. Hinterstein, K.Y. Lee, T.N. Yang, L.Q. Chen, P.B. Groszewicz, J. Koruza, J. Rodel, Spontaneous ferroelectric order in lead-free relaxor  $\text{Na}_{1/2}\text{Bi}_{1/2}\text{TiO}_3$ -based composites, *Physical Review B* 101(17) (2020).
- [68] N. Kumar, X. Shi, M. Hoffman, Spontaneous relaxor to ferroelectric transition in lead-free relaxor piezoceramics and the role of point defects, *Journal of the European Ceramic Society* 40(6) (2020) 2323-2330.
- [69] G.O. Jones, P.A. Thomas, Investigation of the structure and phase transitions in the novel A-site substituted distorted perovskite compound  $\text{Na}_{0.5}\text{Bi}_{0.5}\text{TiO}_3$ , *Acta Crystallogr B* 58 (2002) 168-178.
- [70] C. Ma, X. Tan, In situ Transmission Electron Microscopy Study on the Phase Transitions in Lead-Free  $(1-x)(\text{Bi}_{1/2}\text{Na}_{1/2})\text{TiO}_3$ - $x\text{BaTiO}_3$  Ceramics, *Journal of the American Ceramic Society* 94(11) (2011) 4040-4044.

- 
- [71] G. Viola, Y. Tian, C. Yu, Y. Tan, V. Koval, X. Wei, K.-L. Choy, H. Yan, Electric field-induced transformations in bismuth sodium titanate-based materials, *Progress in Materials Science* 122 (2021) 100837.
- [72] R. Dittmer, W. Jo, E. Aulbach, T. Granzow, J. Rodel, Frequency-dependence of large-signal properties in lead-free piezoceramics, *J Appl Phys* 112(1) (2012).
- [73] R. Dittmer, W. Jo, K.G. Webber, J.L. Jones, J. Rodel, Local structure change evidenced by temperature-dependent elastic measurements: Case study on Bi<sub>1/2</sub>Na<sub>1/2</sub>TiO<sub>3</sub>-based lead-free relaxor piezoceramics, *J Appl Phys* 115(8) (2014).
- [74] B.N. Rao, R. Ranjan, Electric-field-driven monoclinic-to-rhombohedral transformation in Na<sub>1/2</sub>Bi<sub>1/2</sub>TiO<sub>3</sub>, *Physical Review B* 86(13) (2012).
- [75] B.N. Rao, R. Datta, S.S. Chandrashekar, D.K. Mishra, V. Sathe, A. Senyshyn, R. Ranjan, Local structural disorder and its influence on the average global structure and polar properties in Na<sub>0.5</sub>Bi<sub>0.5</sub>TiO<sub>3</sub>, *Physical Review B* 88(22) (2013).
- [76] M. Hinterstein, L.A. Schmitt, M. Hoelzel, W. Jo, J. Rodel, H.J. Kleebe, M. Hoffman, Cyclic electric field response of morphotropic Bi<sub>1/2</sub>Na<sub>1/2</sub>TiO<sub>3</sub>-BaTiO<sub>3</sub> piezoceramics, *Appl Phys Lett* 106(22) (2015).
- [77] E. Sapper, S. Schaab, W. Jo, T. Granzow, J. Rodel, Influence of electric fields on the depolarization temperature of Mn-doped (1-x)Bi<sub>1/2</sub>Na<sub>1/2</sub>TiO<sub>3</sub>-xBaTiO<sub>3</sub>, *J Appl Phys* 111(1) (2012).
- [78] E.-M. Anton, W. Jo, D. Damjanovic, J. Rödel, Determination of depolarization temperature of (Bi<sub>1/2</sub>Na<sub>1/2</sub>)TiO<sub>3</sub>-based lead-free piezoceramics, *J Appl Phys* 110(9) (2011) 094108.
- [79] W. Jo, S. Schaab, E. Sapper, L.A. Schmitt, H.J. Kleebe, A.J. Bell, J. Rodel, On the phase identity and its thermal evolution of lead free (Bi<sub>1/2</sub>Na<sub>1/2</sub>)TiO<sub>3</sub>-6 mol% BaTiO<sub>3</sub>, *J Appl Phys* 110(7) (2011).
- [80] R. Garg, B.N. Rao, A. Senyshyn, P.S.R. Krishna, R. Ranjan, Lead-free piezoelectric system (Na<sub>0.5</sub>Bi<sub>0.5</sub>)TiO<sub>3</sub>-BaTiO<sub>3</sub>: Equilibrium structures and irreversible structural transformations driven by electric field and mechanical impact, *Physical Review B* 88(1) (2013).
- [81] P.B. Groszewicz, M. Groting, H. Breitzke, W. Jo, K. Albe, G. Buntkowsky, J. Rodel, Reconciling Local Structure Disorder and the Relaxor State in (Bi<sub>1/2</sub>Na<sub>1/2</sub>)TiO<sub>3</sub>-BaTiO<sub>3</sub>, *Sci Rep-Uk* 6 (2016).
- [82] P.B. Groszewicz, H. Breitzke, R. Dittmer, E. Sapper, W. Jo, G. Buntkowsky, J. Rodel, Nanoscale phase quantification in lead-free (Bi<sub>1/2</sub>Na<sub>1/2</sub>)TiO<sub>3</sub>-BaTiO<sub>3</sub> relaxor ferroelectrics by means of Na-23 NMR, *Physical Review B* 90(22) (2014).
- [83] M. Vogler, N. Novak, F.H. Schader, J. Rodel, Temperature-dependent volume fraction of polar nanoregions in lead-free (1-x)(Bi<sub>0.5</sub>Na<sub>0.5</sub>)TiO<sub>3</sub>-xBaTiO<sub>3</sub> ceramics, *Physical Review B* 95(2) (2017).
- [84] L. Li, M.K. Zhu, K.L. Zhou, Q.M. Wei, M.P. Zheng, Y.D. Hou, Delayed thermal depolarization of Bi<sub>0.5</sub>Na<sub>0.5</sub>TiO<sub>3</sub>-BaTiO<sub>3</sub> by doping acceptor Zn<sup>2+</sup> with large ionic polarizability, *J Appl Phys* 122(20) (2017).
- [85] L. Kodumudi Venkataraman, T. Zhu, M.P. Salazar, K. Hofmann, A.I. Waidha, J.C. Jaud, P.B. Groszewicz, J. Rödel, Thermal depolarization and electromechanical hardening in Zn<sup>2+</sup>-doped Na<sub>1/2</sub>Bi<sub>1/2</sub>TiO<sub>3</sub>-BaTiO<sub>3</sub>, *Journal of the American Ceramic Society* 104(5) (2020).



- 
- [86] L.M. Riemer, K.V. Lalitha, X.J. Jiang, N. Liu, C. Dietz, R.W. Stark, P.B. Groszewicz, G. Buntkowsky, J. Chen, S.T. Zhang, J. Rodel, J. Koruza, Stress-induced phase transition in lead-free relaxor ferroelectric composites, *Acta Mater* 136 (2017) 271-280.
- [87] T. Miura, H. Nagata, T. Takenaka, Quenching effects on piezoelectric properties and depolarization temperatures of (Bi<sub>0.5</sub>Na<sub>0.5</sub>)TiO<sub>3</sub>-based solid solution systems, *Jpn J Appl Phys* 56(10) (2017).
- [88] G. Catalan, J.F. Scott, Physics and applications of bismuth ferrite, *Advanced materials* 21(24) (2009) 2463-2485.
- [89] I. Calisir, Lead-free BiFeO<sub>3</sub>-BaTiO<sub>3</sub> High Temperature Piezoceramics, The University of Manchester (United Kingdom) (2019).
- [90] S.O. Leontsev, R.E. Eitel, Dielectric and Piezoelectric Properties in Mn-Modified (1-x)BiFeO<sub>3</sub>-xBaTiO<sub>3</sub> Ceramics, *Journal of the American Ceramic Society* 92(12) (2009) 2957-2961.
- [91] D.W. Wang, G. Wang, S. Murakami, Z.M. Fan, A. Feteira, D. Zhou, S.K. Sun, Q.L. Zhao, I.M. Reaney, BiFeO<sub>3</sub>-BaTiO<sub>3</sub>: A new generation of lead-free electroceramics, *J Adv Dielectr* 8(6) (2018).
- [92] I. Ismailzade, R. Ismailov, A. Alekberov, F. Salaev, Investigation of the magnetoelectric (ME) H effect in solid solutions of the systems BiFeO<sub>3</sub>-BaTiO<sub>3</sub> and BiFeO<sub>3</sub>-PbTiO<sub>3</sub>, *physica status solidi (a)* 68(1) (1981) K81-K85.
- [93] J.-M. Moreau, C. Michel, R. Gerson, W.J. James, Ferroelectric BiFeO<sub>3</sub> X-ray and neutron diffraction study, *J Phys Chem Solids* 32(6) (1971) 1315-1320.
- [94] Z. Yang, B. Wang, Y. Li, D.A. Hall, Enhancement of Nonlinear Dielectric Properties in BiFeO<sub>3</sub>-BaTiO<sub>3</sub> Ceramics by Nb-Doping, *Materials* 15(8) (2022) 2872.
- [95] S. Cheng, L. Zhao, B.-P. Zhang, K.-K. Wang, Lead-free 0.7BiFeO<sub>3</sub>-0.3BaTiO<sub>3</sub> high-temperature piezoelectric ceramics: Nano-BaTiO<sub>3</sub> raw powder leading to a distinct reaction path and enhanced electrical properties, *Ceramics International* 45(8) (2019) 10438-10447.
- [96] M.M. Kumar, A. Srinivas, S. Suryanarayana, Structure property relations in BiFeO<sub>3</sub>/BaTiO<sub>3</sub> solid solutions, *J Appl Phys* 87(2) (2000) 855-862.
- [97] S. Kim, G.P. Khanal, H.-W. Nam, I. Fujii, S. Ueno, C. Moriyoshi, Y. Kuroiwa, S. Wada, Structural and electrical characteristics of potential candidate lead-free BiFeO<sub>3</sub>-BaTiO<sub>3</sub> piezoelectric ceramics, *J Appl Phys* 122(16) (2017) 164105.
- [98] Y.X. Wei, X.T. Wang, J.T. Zhu, X.L. Wang, J.J. Jia, Dielectric, Ferroelectric, and Piezoelectric Properties of BiFeO<sub>3</sub>-BaTiO<sub>3</sub> Ceramics, *Journal of the American Ceramic Society* 96(10) (2013) 3163-3168.
- [99] Y.X. Wei, C.Q. Jin, Y.M. Zeng, X.T. Wang, G. Xu, X.L. Wang, Polar Order Evolutions near the Rhombohedral to Pseudocubic and Tetragonal to Pseudocubic Phase Boundaries of the BiFeO<sub>3</sub>-BaTiO<sub>3</sub> System, *Materials* 8(12) (2015) 8355-8365.
- [100] D.J. Kim, M.H. Lee, J.S. Park, M.H. Kim, T.K. Song, W.J. Kim, K.W. Jang, S.S. Kim, D. Do, Effects of sintering temperature on the electric properties of Mn-modified BiFeO<sub>3</sub>-BaTiO<sub>3</sub> bulk ceramics, *J Korean Phys Soc* 66(7) (2015) 1115-1119.
- [101] T. Wang, L. Jin, Y. Tian, L.L. Shu, Q.Y. Hu, X.Y. Wei, Microstructure and ferroelectric properties of Nb<sub>2</sub>O<sub>5</sub>-modified BiFeO<sub>3</sub>-BaTiO<sub>3</sub> lead-free ceramics for energy storage, *Materials Letters* 137 (2014) 79-81.

- [102] Z.T. Chen, X.Z. Bai, H.L. Wang, J. Du, W.F. Bai, L.L. Li, F. Wen, P. Zheng, W. Wu, L. Zheng, Y. Zhang, Achieving high-energy storage performance in 0.67Bi(1-x)Sm(x)FeO(3)-0.33BaTiO(3) lead-free relaxor ferroelectric ceramics, *Ceramics International* 46(8) (2020) 11549-11555.
- [103] C.R. Zhou, A. Feteira, X. Shan, H.B. Yang, Q. Zhou, J. Cheng, W.Z. Li, H. Wang, Remarkably high-temperature stable piezoelectric properties of Bi(Mg<sub>0.5</sub>Ti<sub>0.5</sub>)O<sub>3</sub> modified BiFeO<sub>3</sub>-BaTiO<sub>3</sub> ceramics, *Appl Phys Lett* 101(3) (2012).
- [104] I. Fujii, R. Mitsui, K. Nakashima, N. Kumada, M. Shimada, T. Watanabe, J. Hayashi, H. Yabuta, M. Kubota, T. Fukui, S. Wada, Structural, Dielectric, and Piezoelectric Properties of Mn-Doped BaTiO<sub>3</sub>-Bi(Mg<sub>1/2</sub>Ti<sub>1/2</sub>)O<sub>3</sub>-BiFeO<sub>3</sub> Ceramics, *Jpn J Appl Phys* 50(9) (2011).
- [105] R.A. Malik, A. Hussain, T.K. Song, W.J. Kim, R. Ahmed, Y.S. Sung, M.H. Kim, Enhanced electromechanical properties of (1-x)BiFeO<sub>3</sub> BaTiO<sub>3</sub>-xLiNbO(3) ceramics by quenching process, *Ceramics International* 43 (2017) S198-S203.
- [106] R.A. Malik, A. Zaman, A. Hussain, A. Maqbool, T.K. Song, W.J. Kim, Y.S. Sung, M.H. Kim, Temperature invariant high dielectric properties over the range 200 degrees C-500 degrees C in BiFeO<sub>3</sub> based ceramics, *Journal of the European Ceramic Society* 38(4) (2018) 2259-2263.
- [107] S. Murakami, D.W. Wang, A. Mostaed, A. Khesro, A. Feteira, D.C. Sinclair, Z.M. Fan, X.L. Tan, I.M. Reaney, High strain (0.4%) Bi(Mg<sub>2/3</sub>Nb<sub>1/3</sub>)O<sub>3</sub>-BaTiO<sub>3</sub>-BiFeO<sub>3</sub> lead-free piezoelectric ceramics and multilayers, *Journal of the American Ceramic Society* 101(12) (2018) 5428-5442.
- [108] Y. Li, N. Jiang, K.H. Lam, Y. Guo, Q. Zheng, Q. Li, W. Zhou, Y. Wan, D. Lin, Structure, ferroelectric, piezoelectric, and ferromagnetic properties of BiFeO<sub>3</sub>-BaTiO<sub>3</sub>-Bi<sub>0.5</sub>Na<sub>0.5</sub>TiO<sub>3</sub> lead-free multiferroic ceramics, *Journal of the American Ceramic Society* 97(11) (2014) 3602-3608.
- [109] Y. Li, Y. Guo, Q. Zheng, K.H. Lam, W. Zhou, Y. Wan, D. Lin, Enhancement in multiferroic and piezoelectric properties of BiFeO<sub>3</sub>-BaTiO<sub>3</sub>-Bi<sub>0.5</sub>Na<sub>0.5</sub>TiO<sub>3</sub> lead-free ceramics with MnO<sub>2</sub> addition by optimizing sintering temperature and dwell time, *Mater Res Bull* 68 (2015) 92-99.
- [110] M. Rawat, K.L. Yadav, Study of structural, electrical, magnetic and optical properties of 0.65BaTiO(3)-0.35Bi(0.5)Na(0.5)TiO(3)-BiFeO<sub>3</sub> multiferroic composite, *Journal of Alloys and Compounds* 597 (2014) 188-199.
- [111] G.-P. Zheng, S. Uddin, X. Zheng, J. Yang, Structural and electrocaloric properties of multiferroic-BiFeO<sub>3</sub> doped 0.94 Bi<sub>0.5</sub>Na<sub>0.5</sub>TiO<sub>3</sub>-0.06 BaTiO<sub>3</sub> solid solutions, *Journal of Alloys and Compounds* 663 (2016) 249-255.
- [112] J.G.L. Peng, J.T. Zeng, L.Y. Zheng, G.R. Li, N. Yaacoub, M. Tabellout, A. Gibaud, A. Kassiba, The interplay of phases, structural disorder and dielectric behavior in Al doped BiFeO<sub>3</sub>-BaTiO<sub>3</sub> ceramics, *Journal of Alloys and Compounds* 796 (2019) 221-228.
- [113] J. Wang, C.R. Zhou, Q.N. Li, L. Yang, J.W. Xu, G.H. Chen, C.L. Yuan, G.H. Rao, Simultaneously enhanced piezoelectric properties and depolarization temperature in calcium doped BiFeO<sub>3</sub>-BaTiO<sub>3</sub> ceramics, *Journal of Alloys and Compounds* 748 (2018) 758-765.
- [114] S. Chandarak, A. Ngamjarurojana, S. Pojprapai, S. Srilomsak, S. Rujirawat, R. Yimnirun, Effects of Mn and Cu Doping on Electrical Properties of 0.75BiFeO(3)-0.25BaTiO(3) Ceramics, *Integr Ferroelectr* 114 (2010) 100-107.
- [115] S.B. Guan, H.B. Yang, G.J. Qiao, Y.Y. Sun, F.M. Qin, H.G. Hou, Effects of Li<sub>2</sub>CO(3) and CuO as Composite Sintering Aids on the Structure, Piezoelectric Properties, and Temperature Stability of BiFeO<sub>3</sub>-BaTiO(3) Ceramics, *J Electron Mater* 49(10) (2020) 6199-6207.

- 
- [116] M.J. Tian, L. Zhou, X. Zou, Q.J. Zheng, L.L. Luo, N. Jiang, D.M. Lin, Improved ferroelectricity and ferromagnetism of Eu-modified BiFeO<sub>3</sub>-BaTiO<sub>3</sub> lead-free multiferroic ceramics, *J Mater Sci-Mater El* 26(11) (2015) 8840-8847.
- [117] S.A. Khan, R.A. Malik, F. Akram, A. Hussain, T.K. Song, W.J. Kim, M.H. Kim, Synthesis and electrical properties of 0.65Bi(1.05)Fe(1-x)Ga(x)O(3)-0.35BaTiO(3) piezoceramics by air quenching process, *Journal of Electroceramics* 41(1-4) (2018) 60-66.
- [118] C. Behera, A.K. Pattanaik, Structural, dielectric and ferroelectric properties of lead free Gd-modified BiFeO<sub>3</sub>-BaTiO<sub>3</sub> solid solution, *J Mater Sci-Mater El* 30(6) (2019) 5470-5477.
- [119] B.S. Kar, M.N. Goswami, P.C. Jana, P.S. Das, Structural and electrical properties of Gd-doped BiFeO<sub>3</sub>:BaTiO<sub>3</sub> (3:2) multiferroic ceramic materials, *J Mater Sci-Mater El* 30(3) (2019) 2154-2165.
- [120] A. Prasatkhetragarn, P. Jantaratana, N. Vittayakorn, B. Yotburut, R. Yimnirun, Ferroelectric and Ferromagnetic Properties of K-doped 0.7BiFeO(3)-0.3BaTiO(3) Multiferroic Ceramics, *Ferroelectrics* 451(1) (2013) 109-115.
- [121] C. Behera, R.N.P. Choudhary, P.R. Das, Structural and electrical properties of La-modified BiFeO<sub>3</sub>-BaTiO<sub>3</sub> composites, *J Mater Sci-Mater El* 25(5) (2014) 2086-2095.
- [122] X.C. Wu, M.J. Tian, Y.Q. Guo, Q.J. Zheng, L.L. Luo, D.M. Lin, Phase transition, dielectric, ferroelectric and ferromagnetic properties of La-doped BiFeO<sub>3</sub>-BaTiO<sub>3</sub> multiferroic ceramics, *J Mater Sci-Mater El* 26(2) (2015) 978-984.
- [123] I. Calisir, A.A. Amirov, A.K. Kleppe, D.A. Hall, Optimisation of functional properties in lead-free BiFeO<sub>3</sub>-BaTiO<sub>3</sub> ceramics through La<sup>3+</sup> substitution strategy, *J Mater Chem A* 6(13) (2018) 5378-5397.
- [124] S.B. Guan, H.B. Yang, Y.Z. Zhao, R. Zhang, Effect of Li<sub>2</sub>CO<sub>3</sub> addition in BiFeO<sub>3</sub>-BaTiO<sub>3</sub> ceramics on the sintering temperature, electrical properties and phase transition, *Journal of Alloys and Compounds* 735 (2018) 386-393.
- [125] L.F. Zhu, B.P. Zhang, S. Li, G.L. Zhao, Large piezoelectric responses of Bi(Fe,Mg,Ti)O<sub>3</sub>-BaTiO<sub>3</sub> lead-free piezoceramics near the morphotropic phase boundary, *Journal of Alloys and Compounds* 727 (2017) 382-389.
- [126] N. Itoh, T. Shimura, W. Sakamoto, T. Yogo, Fabrication and characterization of BiFeO<sub>3</sub>-BaTiO<sub>3</sub> ceramics by solid state reaction, *Ferroelectrics* 356 (2007) 311-315.
- [127] T. Futakuchi, T. Kakuda, Y. Sakai, Multiferroic properties of BiFeO<sub>3</sub>-BaTiO<sub>3</sub> based ceramics, *J Ceram Soc Jpn* 122(1426) (2014) 464-468.
- [128] S. Chandarak, J. Jutimoosik, A. Bootchanont, M. Unruan, P. Jantaratana, S. Priya, S. Srilomsak, S. Rujirawat, R. Yimnirun, Local Structure of Magnetoelectric BiFeO<sub>3</sub>-BaTiO<sub>3</sub> Ceramics Probed by Synchrotron X-Ray Absorption Spectroscopy, *J Supercond Nov Magn* 26(2) (2013) 455-461.
- [129] D.J. Kim, M.H. Lee, J.S. Park, M.H. Kim, T.K. Song, S.W. Kim, W.J. Kim, K.W. Jang, S.S. Kim, D. Do, Ferroelectric and piezoelectric properties of Mn-modified BiFeO<sub>3</sub>-BaTiO<sub>3</sub> ceramics, *Journal of Electroceramics* 33(1-2) (2014) 37-41.
- [130] Z.H. Dai, L. Liu, G.B. Ying, M. Yuan, X.B. Ren, Structural, dielectric and magnetic properties of Mn modified xBiFeO(3)-(1-x) BaTiO<sub>3</sub> ceramics, *J Magn Magn Mater* 434 (2017) 10-13.
- [131] H.W. Joo, D.S. Kim, J.S. Kim, C.I. Cheon, Piezoelectric properties of Mn-doped 0.75BiFeO<sub>3</sub> - 0.25BaTiO<sub>3</sub> ceramics, *Ceramics International* 42(8) (2016) 10399-10404.

- 
- [132] Q. Li, J.R. Cheng, J.G. Chen, Reduced dielectric loss and enhanced piezoelectric properties of Mn modified 0.71BiFeO<sub>3</sub>-0.29BaTiO<sub>3</sub> ceramics sintered under oxygen atmosphere, *J Mater Sci-Mater El* 28(2) (2017) 1370-1377.
- [133] Q. Li, J.X. Wei, T.L. Tu, J.R. Cheng, J.G. Chen, Remarkable piezoelectricity and stable high-temperature dielectric properties of quenched BiFeO<sub>3</sub>-BaTiO<sub>3</sub> ceramics, *Journal of the American Ceramic Society* 100(12) (2017) 5573-5583.
- [134] I. Calisir, D.A. Hall, Chemical heterogeneity and approaches to its control in BiFeO<sub>3</sub>-BaTiO<sub>3</sub> lead-free ferroelectrics, *J Mater Chem C* 6(1) (2018) 134-146.
- [135] Q.L. Fan, C.R. Zhou, Q.L. Li, J.W. Xu, C.L. Yuan, G.H. Chen, Temperature stability of sodium-doped BiFeO<sub>3</sub>-BaTiO<sub>3</sub> piezoelectric ceramics, *J Mater Sci-Mater El* 26(12) (2015) 9336-9341.
- [136] T. Zheng, Z.G. Jiang, J.G. Wu, Enhanced piezoelectricity in (1-x) Bi(1.05)Fe(1-y)A(y)O(3)-xBaTiO(3) lead-free ceramics: site engineering and wide phase boundary region, *Dalton T* 45(28) (2016) 11277-11285.
- [137] S.B. Guan, H.B. Yang, G.W. Liu, G.J. Qiao, R. Zhang, D.D. Chen, M.H. Jiang, Y.Y. Sun, Effect of BiScO<sub>3</sub> doping on the structure and properties of BiFeO<sub>3</sub>-BaTiO<sub>3</sub> piezoelectric ceramics, *Journal of Electroceramics* 43(1-4) (2019) 26-33.
- [138] K. Tong, C.R. Zhou, J. Wang, Q.N. Li, L. Yang, J.W. Xu, W.D. Zeng, G.H. Chen, C.L. Yuan, G.H. Rao, Enhanced piezoelectricity and high-temperature sensitivity of Zn-modified BF-BT ceramics by in situ and ex situ measuring, *Ceramics International* 43(4) (2017) 3734-3740.
- [139] S. Kim, H. Nam, I. Calisir, Lead-Free BiFeO<sub>3</sub>-Based Piezoelectrics: A Review of Controversial Issues and Current Research State, *Materials* 15(13) (2022) 4388.
- [140] A.J. Ardell, Precipitation hardening, *Metallurgical Transactions A* 16(12) (1985) 2131-2165.
- [141] S. Lee, C.A. Randall, Z.K. Liu, Modified phase diagram for the barium oxide-titanium dioxide system for the ferroelectric barium titanate, *Journal of the American Ceramic Society* 90(8) (2007) 2589-2594.
- [142] R. Waser, Bulk conductivity and defect chemistry of acceptor-doped strontium titanate in the quenched state, *Journal of the American Ceramic Society* 74(8) (1991) 1934-1940.
- [143] F.D. Morrison, A.M. Coats, D.C. Sinclair, A.R. West, Charge compensation mechanisms in La-doped BaTiO<sub>3</sub>, *Journal of Electroceramics* 6(3) (2001) 219-232.
- [144] W.-H. Huang, Z. Xu, D. Viehland, Structure-property relationships in strontium barium niobate II. Quenching and annealing effects, *Philosophical Magazine A* 71(2) (1995) 219-229.
- [145] J.D. Zang, W. Jo, J. Rodel, Quenching-induced circumvention of integrated aging effect of relaxor lead lanthanum zirconate titanate and (Bi<sub>1/2</sub>Na<sub>1/2</sub>)TiO<sub>3</sub>-BaTiO<sub>3</sub>, *Appl Phys Lett* 102(3) (2013).
- [146] Z.-T. Li, H. Liu, H.-C. Thong, Z. Xu, M.-H. Zhang, J. Yin, J.-F. Li, K. Wang, J. Chen, Enhanced Temperature Stability and Defect Mechanism of BNT-Based Lead-Free Piezoceramics Investigated by a Quenching Process, *Advanced Electronic Materials* 5(3) (2019).
- [147] K. Eguchi, Y. Takagi, H. Nagata, T. Takenaka, The quenching effects for depolarization temperature of (Bi<sub>0.5</sub>Na<sub>0.5</sub>)TiO(3)ceramics with Mn dopants, *Jpn J Appl Phys* 59(Sp) (2020).
- [148] J. Yin, H. Tao, Y.X. Zhang, J.H. Han, Y.L. Huang, Z.T. Li, X.M. Zhang, J.G. Wu, Advances in tuning the "d(33) proportional to 1/T-d" bottleneck: simultaneously realizing large d(33) and high T-d in Bi<sub>0.5</sub>Na<sub>0.5</sub>TiO<sub>3</sub>-based relaxor ferroelectrics, *J Mater Chem A* 8(18) (2020) 9209-9217.

- 
- [149] H. Nagata, Y. Takagi, Y. Yoneda, T. Takenaka, Correlation between depolarization temperature and lattice distortion in quenched  $(\text{Bi}_{1/2}\text{Na}_{1/2})\text{TiO}_3$ -based ceramics, *Appl Phys Express* 13(6) (2020).
- [150] Y. Takagi, T. Miura, H. Nagata, T. Takenaka, Relation between lattice distortion and depolarization temperature in quenched  $(\text{Bi}_{0.5}\text{Na}_{0.5})\text{TiO}_3$ - $(\text{Bi}_{0.5}\text{Li}_{0.5})\text{TiO}_3$ - $(\text{Bi}_{0.5}\text{K}_{0.5})\text{TiO}_3$  ceramics, *Jpn J Appl Phys* 58 (2019).
- [151] S. Harada, Y. Takagi, H. Nagata, T. Takenaka, Quenching effects on electrical properties of Cu-doped  $(\text{Bi}_{1/2}\text{Na}_{1/2})\text{TiO}_3$ -based solid solution ceramics, *J Mater Res* 36(5) (2021) 1097-1104.
- [152] J. Zhang, R.-X. Wang, L. Li, J.-Y. Wu, Y.-S. Cui, Z.-B. Gu, H. Zhang, M.-W. Zhu, S.-T. Zhang, B. Yang, Highly enhanced thermal stability in quenched  $\text{Na}_{0.5}\text{Bi}_{0.5}\text{TiO}_3$ -based lead-free piezoceramics, *Journal of the European Ceramic Society* 39(15) (2019) 4705-4711.
- [153] M.H. Zhang, P. Breckner, T. Fromling, J. Rodel, K.V. Lalitha, Role of thermal gradients on the depolarization and conductivity in quenched  $\text{Na}_{1/2}\text{Bi}_{1/2}\text{TiO}_3$ - $\text{BaTiO}_3$ , *Appl Phys Lett* 116(26) (2020).
- [154] C. Chen, L. Yang, Z.X. Cheng, S.S. Chang, X.A. Jiang, X.P. Jiang, J.L. Wang, X.K. Huang, X.Y. Gao, G.Z. Dong, H.S. Luo, Y.H. Lyu, J.M. Liu, S.J. Zhang, Optimization of Ferroelectric Ordering and Thermal Stability in  $\text{Na}_{1/2}\text{Bi}_{1/2}\text{TiO}_3$ -Based Lead-Free Single Crystal through Defect Engineering, *Acs Applied Materials & Interfaces* (2021).
- [155] Y. Takagi, H. Nagata, T. Takenaka, Effects of quenching on bending strength and piezoelectric properties of  $(\text{Bi}_{0.5}\text{Na}_{0.5})\text{TiO}_3$  ceramics, *J Asian Ceram Soc* 8(2) (2020) 277-283.
- [156] A. Martin, N.H. Khansur, K.G. Webber, Electric field-induced changes in the ferroelastic behavior of  $(\text{Na}_{1/2}\text{Bi}_{1/2})\text{TiO}_3$ - $\text{BaTiO}_3$ , *Journal of the European Ceramic Society* 38(14) (2018) 4623-4630.
- [157] P.R. Ren, J.L. Wang, Y.K. Wang, K.V. Lalitha, G.Y. Zhao, Origin of enhanced depolarization temperature in quenched  $\text{Na}_{0.5}\text{Bi}_{0.5}\text{TiO}_3$ - $\text{BaTiO}_3$  ceramics, *Journal of the European Ceramic Society* 40(8) (2020) 2964-2969.
- [158] L. Kodumudi Venkataraman, Influence of Quenching and Subsequent Annealing on the Conductivity and Electromechanical Properties of  $\text{Na}_{1/2}\text{Bi}_{1/2}\text{TiO}_3$ - $\text{BaTiO}_3$ , *Materials* 14(9) (2021).
- [159] M.H. Lee, J.S. Park, D.J. Kim, R.C. Kambale, M.H. Kim, T.K. Song, H.J. Jung, S.W. Kim, H.I. Choi, W.J. Kim, S.S. Kim, K.W. Jang, D. Do, Ferroelectric and Piezoelectric Properties of  $\text{BiFeO}_3$ - $\text{BaTiO}_3$  Solid Solution Ceramics, *Ferroelectrics* 452(1) (2013) 7-12.
- [160] I. Calisir, A.K. Kleppe, A. Feteira, D.A. Hall, Quenching-assisted actuation mechanisms in core-shell structured  $\text{BiFeO}_3$ - $\text{BaTiO}_3$  piezoceramics, *J Mater Chem C* 7(33) (2019) 10218-10230.
- [161] D.S. Kim, C.I. Cheon, S.S. Lee, J.S. Kim, Effect of cooling rate on phase transitions and ferroelectric properties in  $0.75\text{BiFeO}_3$ - $0.25\text{BaTiO}_3$  ceramics, *Appl Phys Lett* 109(20) (2016).
- [162] Q. Li, J. Wei, T. Tu, J. Cheng, J. Chen, Remarkable piezoelectricity and stable high-temperature dielectric properties of quenched  $\text{BiFeO}_3$ - $\text{BaTiO}_3$  ceramics, *Journal of the American Ceramic Society* 100(12) (2017) 5573-5583.
- [163] L. Jin, F. Li, S. Zhang, Decoding the fingerprint of ferroelectric loops: comprehension of the material properties and structures, *Journal of the American Ceramic Society* 97(1) (2014) 1-27.
- [164] T. Rojac, M. Kosec, B. Budic, N. Setter, D. Damjanovic, Strong ferroelectric domain-wall pinning in  $\text{BiFeO}_3$  ceramics, *J Appl Phys* 108(7) (2010).

- 
- [165] S.T. Zhang, M.H. Lu, D. Wu, Y.F. Chen, N.B. Ming, Larger polarization and weak ferromagnetism in quenched BiFeO<sub>3</sub> ceramics with a distorted rhombohedral crystal structure, *Appl Phys Lett* 87(26) (2005).
- [166] M.H. Lee, D.J. Kim, J.S. Park, S.W. Kim, T.K. Song, M.H. Kim, W.J. Kim, D. Do, I.K. Jeong, High-Performance Lead-Free Piezoceramics with High Curie Temperatures, *Adv Mater* 27(43) (2015) 6976-82.
- [167] M.H. Lee, D.J. Kim, H.I. Choi, M.-H. Kim, T.K. Song, W.-J. Kim, D. Do, Thermal quenching effects on the ferroelectric and piezoelectric properties of BiFeO<sub>3</sub>-BaTiO<sub>3</sub> ceramics, *ACS Applied Electronic Materials* 1(9) (2019) 1772-1780.
- [168] B. Wang, Y.Z. Li, D.A. Hall, Surface structure and quenching effects in BiFeO<sub>3</sub>-BaTiO<sub>3</sub> ceramics, *Journal of the American Ceramic Society* 105(2) (2022) 1265-1275.
- [169] P. Lambeck, G. Jonker, The nature of domain stabilization in ferroelectric perovskites, *J Phys Chem Solids* 47(5) (1986) 453-461.
- [170] Y. Kuroiwa, S. Kim, I. Fujii, S. Ueno, Y. Nakahira, C. Moriyoshi, Y. Sato, S. Wada, Piezoelectricity in perovskite-type pseudo-cubic ferroelectrics by partial ordering of off-centered cations, *Commun Mater* 1(1) (2020).
- [171] M.I. Mendelson, Average grain size in polycrystalline ceramics, *Journal of the American Ceramic Society* 52(8) (1969) 443-446.
- [172] M. Vögler, *Mechanisches Verhalten von Natrium-Bismut-Titanat Piezokeramiken*, (2018).
- [173] A. International, E1876-99 Standard Test Method for Dynamic Young's Modulus, Shear Modulus, and Poisson's Ratio by Impulse Excitation of Vibration, West Conshohocken, PA; ASTM International, (2001).
- [174] L. Pardo, E. Mercadelli, Á. García, K. Brebol, C. Galassi, Field-induced phase transition and relaxor character in submicrometer-structured lead-free (Bi<sub>0.5</sub>Na<sub>0.5</sub>)<sub>0.94</sub>Ba<sub>0.06</sub>TiO<sub>3</sub> piezoceramics at the morphotropic phase boundary, *IEEE transactions on ultrasonics, ferroelectrics, and frequency control* 58(9) (2011) 1893-1904.
- [175] G.J. Weng, Some Elastic Properties of Reinforced Solids, with Special Reference to Isotropic Ones Containing Spherical Inclusions, *Int J Eng Sci* 22(7) (1984) 845-856.
- [176] J.B. Wachtman, W.E. Tefft, D.G. Lam, C.S. Apstein, Exponential Temperature Dependence of Young's Modulus for Several Oxides, *Phys Rev* 122(6) (1961) 1754-+.
- [177] A. Wohninsland, Fetzer, A.-K. Riaz, A., Kleebe, H.-J., Rödel, J., and Kodumudi Venkataraman, L., Correlation between enhanced lattice distortion and volume fraction of polar nanoregions in quenched Na<sub>1/2</sub>Bi<sub>1/2</sub>TiO<sub>3</sub>-BaTiO<sub>3</sub> ceramics, *Appl Phys Lett* 118(7) (2021).
- [178] J. Filik, A.W. Ashton, P.C.Y. Chang, P.A. Chater, S.J. Day, M. Drakopoulos, M.W. Gerring, M.L. Hart, O.V. Magdysyuk, S. Michalik, A. Smith, C.C. Tang, N.J. Terrill, M.T. Wharmby, H. Wilhelm, Processing two-dimensional X-ray diffraction and small-angle scattering data in DAWN 2, *J Appl Crystallogr* 50 (2017) 959-966.
- [179] J.E. Daniels, W. Jo, J. Rodel, V. Honkimaki, J.L. Jones, Electric-field-induced phase-change behavior in (Bi<sub>0.5</sub>Na<sub>0.5</sub>)TiO<sub>3</sub>-BaTiO<sub>3</sub>-(K<sub>0.5</sub>Na<sub>0.5</sub>)NbO<sub>3</sub>: A combinatorial investigation, *Acta Mater* 58(6) (2010) 2103-2111.
- [180] A.-K. Fetzer, Wohninsland, A., Hofmann, K., Clemens, O., L. Kodumudi Venkataraman, Kleebe, H.-J., Domain structure and phase evolution in quenched and furnace cooled lead-free Na<sub>1/2</sub>Bi<sub>1/2</sub>TiO<sub>3</sub>-BaTiO<sub>3</sub> ceramics, *Open Ceramics* 5 (2021).

- 
- [181] B.N. Rao, M. Avdeev, B. Kennedy, R. Ranjan, Phase boundary at  $x=0.03$  and its anomalous influence on the structure and properties in the lead-free piezoelectric  $(1-x)\text{Na}_{1/2}\text{Bi}_{1/2}\text{TiO}_3-x\text{BaTiO}_3$ , *Physical Review B* 92(21) (2015).
- [182] S. Kong, N. Kumar, S. Checchia, C. Cazorla, J. Daniels, Defect-Driven Structural Distortions at the Surface of Relaxor Ferroelectrics, *Advanced Functional Materials* (2019).
- [183] K.Y. Lee, X. Shi, N. Kumar, M. Hoffman, M. Etter, J. Winter, L.L. da Silva, D. Seifert, M. Hinterstein, The complex structural mechanisms behind strain curves in bismuth sodium titanate-barium titanate, *Appl Phys Lett* 116(18) (2020).
- [184] H. Luo, H. Liu, S. Deng, S. Hu, L. Wang, B. Gao, S. Sun, Y. Ren, L. Qiao, J. Chen, Simultaneously enhancing piezoelectric performance and thermal depolarization in lead-free  $(\text{Bi}, \text{Na}) \text{TiO}_3\text{-BaTiO}_3$  via introducing oxygen-defect perovskites, *Acta Mater* 208 (2021) 116711.
- [185] J.L. Jones, The use of diffraction in the characterization of piezoelectric materials, *Journal of Electroceramics* 19(1) (2007) 69-81.
- [186] J.L. Jones, B.J. Iverson, K.J. Bowman, Texture and anisotropy of polycrystalline piezoelectrics, *Journal of the American Ceramic Society* 90(8) (2007) 2297-2314.
- [187] J.L. Jones, M. Hoffman, K.J. Bowman, Saturated domain switching textures and strains in ferroelastic ceramics, *J Appl Phys* 98(2) (2005).
- [188] A. Pramanick, D. Damjanovic, J.E. Daniels, J.C. Nino, J.L. Jones, Origins of Electro-Mechanical Coupling in Polycrystalline Ferroelectrics During Subcoercive Electrical Loading, *Journal of the American Ceramic Society* 94(2) (2011) 293-309.
- [189] J.L. Jones, E.B. Slamovich, K.J. Bowman, Domain texture distributions in tetragonal lead zirconate titanate by x-ray and neutron diffraction, *J Appl Phys* 97(3) (2005).
- [190] G. Esteves, C.M. Fancher, J.L. Jones, In situ characterization of polycrystalline ferroelectrics using x-ray and neutron diffraction, *J Mater Res* 30(3) (2015) 340-356.
- [191] A. Pramanick, J.E. Daniels, J.L. Jones, Subcoercive Cyclic Electrical Loading of Lead Zirconate Titanate Ceramics II: Time-Resolved X-Ray Diffraction, *Journal of the American Ceramic Society* 92(10) (2009) 2300-2310.
- [192] Y. Ishibashi, M. Iwata, Morphotropic phase boundary in solid solution systems of perovskite-type oxide ferroelectrics, *Jpn J Appl Phys* 37(8B) (1998) L985.
- [193] G. Esteves, C.M. Fancher, S. Röhrig, G.A. Maier, J.L. Jones, M. Deluca, Electric-field-induced structural changes in multilayer piezoelectric actuators during electrical and mechanical loading, *Acta Mater* 132 (2017) 96-105.
- [194] J.W. Zhao, S.D. Funni, E.R. Molina, E.C. Dickey, J.L. Jones, Orientation-dependent, field-induced phase transitions in soft lead zirconate titanate piezoceramics, *Journal of the European Ceramic Society* 41(6) (2021) 3357-3362.
- [195] G. Arlt, The influence of microstructure on the properties of ferroelectric ceramics, *Ferroelectrics* 104(1) (1990) 217-227.
- [196] Y. Sung, J. Cho, T. Song, S. Jeong, J. Song, M. Kim, Composition Dependent Piezoelectric Properties of Pb-free  $(\text{Bi}_{0.5}\text{Na}_{0.5})_{1-x}\text{Ba}_x\text{TiO}_3$  Ceramics, 2007 Sixteenth IEEE International Symposium on the Applications of Ferroelectrics, IEEE, (2007), pp. 692-695.
- [197] C. Xu, D. Lin, K.W. Kwok, Structure, electrical properties and depolarization temperature of  $(\text{Bi}_{0.5}\text{Na}_{0.5})\text{TiO}_3\text{-BaTiO}_3$  lead-free piezoelectric ceramics, *Solid state sciences* 10(7) (2008) 934-940.

- 
- [198] D. Bremecker, M. Slabki, J. Koruza, J. Rödel, Characterization of crystal structure, electrical and electromechanical properties of Mg-doped 0.94 Na<sub>1/2</sub>Bi<sub>1/2</sub>TiO<sub>3</sub>-0.06 BaTiO<sub>3</sub>, *Journal of the European Ceramic Society* (2022).
- [199] B.-J. Chu, D.-R. Chen, G.-R. Li, Q.-R. Yin, Electrical properties of Na<sub>1/2</sub>Bi<sub>1/2</sub>TiO<sub>3</sub>-BaTiO<sub>3</sub> ceramics, *Journal of the European Ceramic Society* 22(13) (2002) 2115-2121.
- [200] M. Morozov, Softening and hardening transitions in ferroelectric Pb (Zr, Ti) O<sub>3</sub> ceramics, EPFL, (2005).
- [201] J.L. Jones, M. Hoffman, J.E. Daniels, A.J. Studer, Direct measurement of the domain switching contribution to the dynamic piezoelectric response in ferroelectric ceramics, *Appl Phys Lett* 89(9) (2006).
- [202] J. Chen, C. Zhou, H. Liu, H. Zhang, Q. Li, C. Yuan, J. Xu, S. Cheng, J. Zhao, G. Rao, A New Strategy for higher T<sub>d</sub> with large and temperature-independent d<sub>33</sub> in BNT-based piezoceramics via quenching induced built-in field, *Journal of Alloys and Compounds* (2022) 166505.
- [203] D. Damjanovic, Contributions to the piezoelectric effect in ferroelectric single crystals and ceramics, *Journal of the American Ceramic Society* 88(10) (2005) 2663-2676.
- [204] Q.M. Zhang, H. Wang, N. Kim, L.E. Cross, Direct Evaluation of Domain-Wall and Intrinsic Contributions to the Dielectric and Piezoelectric Response and Their Temperature-Dependence on Lead-Zirconate-Titanate Ceramics, *J Appl Phys* 75(1) (1994) 454-459.
- [205] A.K. Fetzer, A. Wohninsland, K. Lalitha, H.J. Kleebe, In situ hot-stage TEM of the phase and domain evolution in quenched Na<sub>1/2</sub>Bi<sub>1/2</sub>TiO<sub>3</sub>-BaTiO<sub>3</sub>, *Journal of the American Ceramic Society* 105(4) (2022) 2878-2888.
- [206] A.-K. Fetzer, A. Wohninsland, K. Lalitha, H.-J. Kleebe, Nanoscale polar regions embedded within ferroelectric domains in Na<sub>1/2</sub>Bi<sub>1/2</sub>TiO<sub>3</sub>-BaTiO<sub>3</sub>, *Phys Rev Mater* 6(6) (2022) 064409.
- [207] D. Bremecker, K.V. Lalitha, S. Teuber, J. Koruza, J. Rodel, Influence of Zn<sup>2+</sup> doping on the morphotropic phase boundary in lead-free piezoelectric (1-x)Na<sub>1/2</sub>Bi<sub>1/2</sub>TiO<sub>3</sub>-xBaTiO<sub>3</sub>, *Journal of the American Ceramic Society* 105(2) (2022) 1232-1240.
- [208] G. Liu, L. Kong, Q. Hu, S. Zhang, Diffused morphotropic phase boundary in relaxor-PbTiO<sub>3</sub> crystals: High piezoelectricity with improved thermal stability, *Applied Physics Reviews* 7(2) (2020) 021405.
- [209] M.A. Carpenter, J.F.J. Bryson, G. Catalan, C.J. Howard, Elastic and anelastic relaxations in the relaxor ferroelectric Pb(Mg<sub>1/3</sub>Nb<sub>2/3</sub>)O<sub>3</sub>: I. Strain analysis and a static order parameter, *J Phys-Condens Mat* 24(4) (2012).
- [210] E. Smirnova, A. Sotnikov, S. Ktitorov, H. Schmidt, M. Weihnacht, High temperature acoustic effects in relaxors PbMg<sub>1/3</sub>Nb<sub>2/3</sub>O<sub>3</sub> and PbFe<sub>1/2</sub>Nb<sub>1/2</sub>O<sub>3</sub>, *Proceedings of ISAF-ECAPD-PFM 2012, IEEE*, (2012), pp. 1-4.
- [211] S. Tsukada, S. Kojima, Broadband light scattering of two relaxation processes in relaxor ferroelectric 0.93 Pb (Zn<sub>1/3</sub>Nb<sub>2/3</sub>)O<sub>3</sub>-0.07 PbTiO<sub>3</sub> single crystals, *Physical review B* 78(14) (2008) 144106.
- [212] J. Suchanicz, T. Kruzina, Dielectric properties, thermal expansion and heat capacity of (1-x)Na<sub>0.5</sub>Bi<sub>0.5</sub>TiO<sub>3</sub>-xBaTiO<sub>3</sub> single crystals (x= 0, 0.02, 0.025, 0.0325 and 0.05), *Materials Science and Engineering: B* 178(13) (2013) 889-895.
- [213] A. Kumar, S. Asthana, Investigation on energy storage properties and thermally stable dielectric constant for high temperature electronic device applications in the holmium substituted



---

Na<sub>0.5</sub>Bi<sub>0.5</sub>TiO<sub>3</sub>, *Journal of Materials Science: Materials in Electronics* 32(15) (2021) 20225-20239.

[214] A. Wohninsland, A.-K. Fetzer, R. Broughton, J.L. Jones, K. Lalitha, Structural and microstructural description of relaxor-ferroelectric transition in quenched Na<sub>1/2</sub>Bi<sub>1/2</sub>TiO<sub>3</sub>BaTiO<sub>3</sub>, *J Materiomics* (2022).

[215] W. Jo, J.E. Daniels, J.L. Jones, X.L. Tan, P.A. Thomas, D. Damjanovic, J. Rodel, Evolving morphotropic phase boundary in lead-free (Bi<sub>1/2</sub>Na<sub>1/2</sub>)TiO<sub>3</sub>-BaTiO<sub>3</sub> piezoceramics, *J Appl Phys* 109(1) (2011).

[216] F. Weyland, M. Acosta, M. Vogler, Y. Ehara, J. Rodel, N. Novak, Electric field-temperature phase diagram of sodium bismuth titanate-based relaxor ferroelectrics, *J Mater Sci* 53(13) (2018) 9393-9400.

[217] J. Oddershede, M.J. Hossain, J.E. Daniels, Maximising electro-mechanical response by minimising grain-scale strain heterogeneity in phase-change actuator ceramics, *Appl Phys Lett* 109(9) (2016).

[218] M. Hinterstein, J. Rouquette, J. Haines, P. Papet, M. Knapp, J. Glaum, H. Fuess, Structural Description of the Macroscopic Piezo- and Ferroelectric Properties of Lead Zirconate Titanate, *Phys Rev Lett* 107(7) (2011).

[219] M. Hinterstein, J. Rouquette, J. Haines, P. Papet, J. Glaum, M. Knapp, J. Eckert, M. Hoffman, Structural contribution to the ferroelectric fatigue in lead zirconate titanate ceramics, *Physical Review B* 90(9) (2014) 094113.

[220] L. Fan, J. Chen, Y. Ren, Z. Pan, L. Zhang, X. Xing, Unique piezoelectric properties of the monoclinic phase in Pb (Zr, Ti) O<sub>3</sub> ceramics: large lattice strain and negligible domain switching, *Phys Rev Lett* 116(2) (2016) 027601.

[221] H. Luo, S. Tang, H. Liu, Z. Sun, B. Gao, Y. Ren, H. Qi, S. Deng, H. Huang, J. Chen, Revealing structure behavior behind the piezoelectric performance of prototype lead-free Bi<sub>0.5</sub>Na<sub>0.5</sub>TiO<sub>3</sub>BaTiO<sub>3</sub> under in-situ electric field, *J Materiomics* 8(6) (2022) 1104-1112.

[222] R. Dittmer, D. Gobeljic, W. Jo, V.V. Shvartsman, D.C. Lupascu, J.L. Jones, J. Rödel, Ergodicity reflected in macroscopic and microscopic field-dependent behavior of BNT-based relaxors, *J Appl Phys* 115(8) (2014) 084111.

[223] E.C. Subbarao, M.C. Mcquarrie, W.R. Buessem, Domain Effects in Polycrystalline Barium Titanate, *J Appl Phys* 28(10) (1957) 1194-1200.

[224] J.E. Daniels, A. Pramanick, J.L. Jones, Time-Resolved Characterization of Ferroelectrics Using High-Energy X-Ray Diffraction, *Ieee T Ultrason Ferr* 56(8) (2009) 1539-1545.

[225] W.H. Bragg, W.L. Bragg, The reflection of X-rays by crystals, *Proceedings of the Royal Society of London. Series A, Containing Papers of a Mathematical and Physical Character* 88(605) (1913) 428-438.

[226] J.E. Daniels, T.R. Finlayson, A.J. Studer, M. Hoffman, J.L. Jones, Time-resolved diffraction measurements of electric-field-induced strain in tetragonal lead zirconate titanate, *J Appl Phys* 101(9) (2007).

[227] G. Wang, Z.M. Fan, S. Murakami, Z.L. Lu, D.A. Hall, D.C. Sinclair, A. Feteira, X.L. Tan, J.L. Jones, A.K. Kleppe, D.W. Wang, I.M. Reaney, Origin of the large electrostrain in BiFeO<sub>3</sub>-BaTiO<sub>3</sub> based lead-free ceramics, *J Mater Chem A* 7(37) (2019) 21254-21263.

- 
- [228] D.W. Wang, Z.M. Fan, W.B. Li, D. Zhou, A. Feteira, G. Wang, S. Murakami, S.K. Sun, Q.L. Zhao, X.L. Tan, I.M. Reaney, High Energy Storage Density and Large Strain in Bi(Zn<sub>2</sub>/3Nb<sub>1</sub>/3)O<sub>3</sub>-Doped BiFeO<sub>3</sub>-BaTiO<sub>3</sub> Ceramics, *Acs Applied Energy Materials* 1(8) (2018) 4403-4412.
- [229] B. Wang, C. Fu, X. Liu, B. Xie, D.A. Hall, Microchemical homogeneity and quenching-induced property enhancement in BiFeO<sub>3</sub>-BaTiO<sub>3</sub> ceramics, *Open Ceramics* 13 (2023) 100322.
- [230] G.A. Samara, Relaxor properties of compositionally disordered perovskites: Ba-and Bi-substituted Pb (Zr 1- x Ti x) O<sub>3</sub>, *Physical Review B* 71(22) (2005) 224108.
- [231] D. Wang, Z. Fan, D. Zhou, A. Khesro, S. Murakami, A. Feteira, Q. Zhao, X. Tan, I.M. Reaney, Bismuth ferrite-based lead-free ceramics and multilayers with high recoverable energy density, *J Mater Chem A* 6(9) (2018) 4133-4144.
- [232] M.I. Morozov, M.-A. Einarsrud, T. Grande, Atmosphere controlled conductivity and Maxwell-Wagner relaxation in Bi<sub>0.5</sub>K<sub>0.5</sub>TiO<sub>3</sub>-BiFeO<sub>3</sub> ceramics, *J Appl Phys* 115(4) (2014) 044104.
- [233] D.J. Kim, M.H. Lee, T.K. Song, Comparison of multi-valent manganese oxides (Mn<sup>4+</sup>, Mn<sup>3+</sup>, and Mn<sup>2+</sup>) doping in BiFeO<sub>3</sub>-BaTiO<sub>3</sub> piezoelectric ceramics, *Journal of the European Ceramic Society* 39(15) (2019) 4697-4704.
- [234] K. Härdtl, Electrical and mechanical losses in ferroelectric ceramics, *Ceramics International* 8(4) (1982) 121-127.
- [235] G. Dong, H. Fan, J. Shi, M. Li, Composition-and temperature-dependent large strain in (1-x)(0.8 Bi<sub>0.5</sub>Na<sub>0.5</sub>TiO<sub>3</sub>-0.2 Bi<sub>0.5</sub>K<sub>0.5</sub>TiO<sub>3</sub>)-xNaNbO<sub>3</sub> ceramics, *Journal of the American Ceramic Society* 98(4) (2015) 1150-1155.
- [236] Q. Wei, A. Riaz, S. Zhukov, K. Hofmann, M. Zhu, Y. Hou, J. Rödel, L. Kodumudi Venkataraman, Quenching-circumvented ergodicity in relaxor Na<sub>1/2</sub>Bi<sub>1/2</sub>TiO<sub>3</sub>-BaTiO<sub>3</sub>-K<sub>0.5</sub>Na<sub>0.5</sub>NbO<sub>3</sub>, *Journal of the American Ceramic Society* 104(7) (2021) 3316-3324.
- [237] Q. Hua, P. Ren, J. Wang, Y. Wang, L. Liu, K. Lalitha, D. Hua, G. Zhao, Quenching-induced nonergodicity in ergodic Na<sub>1/2</sub>Bi<sub>1/2</sub>TiO<sub>3</sub>-BaTiO<sub>3</sub>-AgNbO<sub>3</sub> ceramics, *J Mater Sci* 56(33) (2021) 18430-18439.

---

---

## Curriculum Vitae

---

### Personal Data

Name Andreas Georg Wohninsland  
Date and Place of Birth August 26, 1993, Kirchheimbolanden  
Citizenship German



### Education

Since 08/2019 **Doctorate**  
Technical University of Darmstadt  
Department of Materials and Geosciences  
Division: Nonmetallic-Inorganic Materials

08/2021 – 10/2021 **PhD candidate in Materials Science (guest)**  
University of Manchester  
Department of Materials

10/2015 – 09/2018 **Master of Science**  
Heidelberg University  
Institute of Earth Sciences

10/2012 – 09/2015 **Bachelor of Science**  
Heidelberg University  
Institute of Earth Sciences

08/2004 – 03/2012 **Abitur**  
Albert-Einstein-Gymnasium Frankenthal

### Professional Experience

Since 08/2019 **Research Associate**  
Technical University of Darmstadt

---

09/2014 – 07/2019      **Geologist/Working Student**

WST GmbH Eppelheim

12/2018 – 03/2019      **Research Assistant**

Heidelberg University

10/2014 – 03/2015      **Research Assistant**

Heidelberg University

## **Awards**

11/2021      **ICAE Student Award (Talk)**

6th International Conference on Advanced Electromaterials

01/2021      **Best Student Poster Presentation Award - Third Price**

Conference on Electronic Materials and Application

12/2019      **2-min Oral Presentation - Third Price**

IEEE UFFC Ferroelectrics School Beijing

## **Publications**

D. Bremecker, **A. Wahninsland**, S. Teuber, L. Kodumudi Venkataraman, M. Hinterstein, J. Rödel, Texture-based ferroelectric hardening in  $\text{Na}_{1/2}\text{Bi}_{1/2}\text{TiO}_3$ -based piezoceramics, *Phys. Rev. Materials* (2023) (accepted).

Z. Yang, B. Wang, T. Brown, S.J. Milne, A. Feteira, **A. Wahninsland**, L. Kodumudi Venkataraman, Y. Li, D.A. Hall, Re-entrant relaxor ferroelectric behaviour in Nb-doped  $\text{BiFeO}_3$ - $\text{BaTiO}_3$  ceramics, *J Mater Chem C* 11(6) (2023) 2186-2195.

A.K. Fetzer, **A. Wahninsland**, L. Kodumudi Venkataraman, H.J. Kleebe, In situ hot-stage TEM of the phase and domain evolution in quenched  $\text{Na}_{1/2}\text{Bi}_{1/2}\text{TiO}_3$ - $\text{BaTiO}_3$ , *Journal of the American Ceramic Society* 105(4) (2022) 2878-2888.

**A. Wahninsland**, A.-K. Fetzer, R. Broughton, J.L. Jones, L. Kodumudi Venkataraman, Structural and microstructural description of relaxor-ferroelectric transition in quenched  $\text{Na}_{1/2}\text{Bi}_{1/2}\text{TiO}_3\text{BaTiO}_3$ , *J Materiomics* (2022).

---

A.-K. Fetzer, **A. Wahninsland**, L. Kodumudi Venkataraman, H.-J. Kleebe, Nanoscale polar regions embedded within ferroelectric domains in  $\text{Na}_{1/2}\text{Bi}_{1/2}\text{TiO}_3\text{-BaTiO}_3$ , *Phys Rev Mater* 6(6) (2022) 064409.

F. Zhuo, X. Zhou, S. Gao, M. Höfling, F. Dietrich, P.B. Groszewicz, L. Fulanović, P. Breckner, **A. Wahninsland**, B.-X. Xu, Anisotropic dislocation-domain wall interactions in ferroelectrics, *Nat Commun* 13(1) (2022) 6676.

**A. Wahninsland**, A.-K. Fetzer, A. Riaz, H.-J. Kleebe, J. Rödel, L. Kodumudi Venkataraman, Correlation between enhanced lattice distortion and volume fraction of polar nanoregions in quenched  $\text{Na}_{1/2}\text{Bi}_{1/2}\text{TiO}_3\text{-BaTiO}_3$  ceramics, *Appl Phys Lett* 118(7) (2021).

A.-K. Fetzer, **A. Wahninsland**, K. Hofmann, O. Clemens, L. Kodumudi Venkataraman, H.-J. Kleebe, Domain structure and phase evolution in quenched and furnace cooled lead-free  $\text{Na}_{1/2}\text{Bi}_{1/2}\text{TiO}_3\text{-BaTiO}_3$  ceramics, *Open Ceramics* 5 (2021).